Bioceramic nanoparticles for bone regeneration

Citation for published version (APA):

Sutthavas, P. (2023). *Bioceramic nanoparticles for bone regeneration*. [Doctoral Thesis, Maastricht University]. Maastricht University. https://doi.org/10.26481/dis.20231011ps

Document status and date:
Published: 01/01/2023

DOI:
10.26481/dis.20231011ps

Document Version:
Publisher's PDF, also known as Version of record

Please check the document version of this publication:

• A submitted manuscript is the version of the article upon submission and before peer-review. There can be important differences between the submitted version and the official published version of record. People interested in the research are advised to contact the author for the final version of the publication, or visit the DOI to the publisher's website.
• The final author version and the galley proof are versions of the publication after peer review.
• The final published version features the final layout of the paper including the volume, issue and page numbers.

Link to publication

General rights
Copyright and moral rights for the publications made accessible in the public portal are retained by the authors and/or other copyright owners and it is a condition of accessing publications that users recognise and abide by the legal requirements associated with these rights.

- Users may download and print one copy of any publication from the public portal for the purpose of private study or research.
- You may not further distribute the material or use it for any profit-making activity or commercial gain
- You may freely distribute the URL identifying the publication in the public portal.

If the publication is distributed under the terms of Article 25fa of the Dutch Copyright Act, indicated by the "Taverne" license above, please follow below link for the End User Agreement:

www.umlib.nl/taverne-license

Take down policy
If you believe that this document breaches copyright please contact us at:

repository@maastrichtuniversity.nl

providing details and we will investigate your claim.

Download date: 28 Apr. 2024

Bioceramic nanoparticles for bone regeneration

Pichaporn Sutthavas

Bioceramic nanoparticles for bone regeneration
PhD Thesis, Maastricht University, Maastricht, The Netherlands.
ISBN : 978-94-6469-505-2
Cover Art : Pichaporn Sutthavas
Printed by ProefschriftMaken

Bioceramic nanoparticles for bone regeneration

DISSERTATION

To obtain the degree of Doctor at the Maastricht University,
on the authority of the Rector Magnificus, Prof. Dr. Pamela Habibović
in accordance with the decision of the Board of Deans,
to be defended in public
on Wednesday 11th October 2023 at 10:00 hours

by

Pichaporn Sutthavas

Born on 11th December 1984
In Chiangmai, Thailand.

Supervisor:

Prof. Dr. Pamela Habibovic

Co supervisor:

Dr. Sabine van Rijt

Assessment Committee:

Prof. Dr. Martijn van Griensven (Chair)

Dr. Berta Cillero-Pastor

Dr. Florence de Groot, Kuros Bioscience BV.

Prof. Dr. Maarten Honing

Prof. MD. Keita Ito, Eindhoven University of Technology.

Table of Contents

CHAPTER 1

CHAPTER 2

CHAPTER 3

CHAPTER 4

CHAPTER 5

CHAPTER 6

Chapter 1

General Introduction

1. Introduction

Regenerative medicine is an interdisciplinary field that aims to restore diseased or injured tissues and organs to their normal functional state [1]. In order to properly regenerate functional tissue, careful control of the behaviour of native cells and of their surrounding is required. One, relatively simple and inexpensive approach to achieve this, is the use of synthetic biomaterials that can mimic native tissue. In order to be successful, materials used in regenerative medicine need to provide temporary support to damaged tissue and to exert appropriate cues (e.g. chemical, mechanical, topographical) to govern cell behaviour *in vivo*. Synthetic biomaterials such as polymers, metals and ceramics are researched in the context of regeneration of various tissues including bone, cartilage and skin. Over the past decades, there has been increased interest in incorporating nanotechnology in biomaterials design and development, to mimic the nanoscale features of tissues and organs. Nanotechnology concerns the development of materials in the 5 to 200 nm range in at least one dimension [2]. In the context of regenerative medicine, the development of nanoparticles has been of particular interest. Their composition and distinct advantages such as low toxicity, high cellular uptake, and large surface area with tuneable properties, make them highly versatile for many applications in the fields of drug delivery, bio-imaging and theranostics [3] as well as in regenerative medicine [2, 4, 5]. Several recent reviews summarize their great potential for furthering the field of tissue regeneration [6-8]. For example, nanoparticle's inherent optical properties have been used to label (stem) cells for real-time monitoring of cell location and fate. Moreover, nanoparticles have been applied as carriers for the delivery of drugs and signalling molecules such as growth factors or peptides to steer specific regenerative processes [8-10]. This is advantageous because conventional administration of drugs including oral intake or injection often lead to poor drug bio-distribution, and bioactive molecules such as growth factors and peptides generally have short half-lives in biological fluids. Nanoparticles can carry various cargo such as drugs, ions or bioactive molecules within their matrix, protecting them from degradation and, in addition, circumventing issues with limited drug solubility. Many types of nanoparticles have been researched for regenerative medicine applications, including polymeric, calcium phosphate, gold and silica based nanoparticles [11]. This thesis concerns the field of bone regeneration, and for applications in bone, especially nanoparticles based on silica and calcium phosphate have been investigated.

The regeneration of bone defects, resulting from trauma, tumor removal, or diseases such as osteoporosis, remains a big challenge in our aging population. While bone is capable of natural regeneration, large, critical-sized bone defects require intervention, often with use of bone (grafts) substitutes. The gold standard treatment involves the use of a patient’s own bone from elsewhere in the body (autograft). However, autografts have limited availability and complications may occur at the harvest site. Therefore, the development of synthetic materials which can mimic natural bone is the primary focus of research into biomaterials for bone regeneration. Bone is a composite material comprising an organic and an inorganic phase. The inorganic phase of bone consists of calcium phosphate (CaP), in the form of carbonated hydroxyapatite. Moreover, CaP found in natural bone exists in the form of nano-sized apatite with a calcium-to-phosphate (Ca/P) ratio close to that of hydroxyapatite [12, 13]. For this reason, CaP ceramics are a frequently investigated synthetic biomaterial for bone regeneration purposes. In the past decades it has been shown that the chemical phase, crystallinity and porosity of CaP ceramics are important parameters that influence its ability to bind to bone and stimulate bone repair (bioactivity) [14, 15]. Several synthetic CaP are used in the clinic in the form of bone cement, bone filler or coating of (metallic) implants [16, 17]. Pure CaP ceramics are, in contrast to natural bone, intrinsically brittle and therefore not suitable for load-bearing applications [18]. One approach to improve the mechanical properties of ceramic materials is to combine them with metals or polymers to create composite materials. Using ceramics in the nanoparticle size range (e.g. between 20-500 nm), is promising in this regard, since they can be easily incorporated into polymeric scaffolds [19, 20], owing to their easy handling and small size. Such approaches have resulted in the creation of composite materials with improved mechanical properties and bioactivity. For example, addition of ceramic nanoparticles to polymer scaffolds could promote osteointegration, osteoconduction, and osteoinduction processes [21-23]. Indeed, it has been shown that CaP but also silica based nanoparticles can efficiently promote stem cell differentiation e.g., towards specialised bone cells (i.e., osteogenesis), or promote new blood vessel formation (i.e., angiogenesis), both vital processes in bone regeneration [24-26]. Due to these favourable properties, CaP nanoparticles have found widespread use in the bone regeneration field. CaP nanoparticles have also been used as delivery vehicles for therapeutic factors for bone regeneration including antibiotics, anti-inflammatory agents, growth factors, and genetic material [24, 27, 28]. Next to CaP, also mesoporous silica nanoparticles (MSN) and mesoporous bioactive glass nanoparticles (MBG) have received a lot of attention in the bone regeneration field due to their intrinsic bioactivity and drug delivery capabilities. MSN consists of a SiO2 network as the main core structure. Over the last decades, the application of MSN in the bone regeneration field has increased significantly due to their excellent chemical stability, yet easily tuneable surface properties [29]. Degraded silica ions from the network can stimulate bone regenerative processes, especially enhancing blood vessel formation and angiogenesis [30, 31]. MSN can be prepared in different sizes and shapes such as spheres, disks and needles [32-34]. MSN have been used for drug delivery purposes due to their unique structure consisting of hundreds of mesopores, resulting in high surface area and large cargo loading capacity [35]. This morphology enables MSN to absorb or encapsulate large amounts of biomolecules and ions. As such, MSN have been used to deliver a great variety of biomolecules, including osteogenic factors such as bone morphogenetic protein (BMP) and transforming growth factor-β (TGF-β), angiogenic factors such as vascular endothelial growth factor (VEGF), and genetic materials such as DNA and RNA [36, 37]. Unlike purely silicate-based materials, bioactive glasses contain additional calcium and/or phosphorous ions within their silicate network [38]. Bioactive glass has the unique ability to form strong bonds with bone tissue. These occur via interactions with Ca ions within the composite, with an HA layer forming on the glass surface upon contact with body fluid [39]. Therefore, using bioactive glass for bone regeneration has received significant interest over the past decades [40-43]. For example, addition of bioactive glass nanoparticles to a polymeric scaffold can increase its mechanical properties and osteoinductivity [44, 45]. The ability of bioactive glass to form a strong bond with native bone has also been utilized for coating of (metallic) implants used in orthopaedics, dentistry and maxillofacial surgery. While the majority of initially developed bioactive glass nanoparticles were solid spheres, mesoporous bioactive glass (MBG) has been successfully synthesized by adding surfactants during synthesis [46].The mesoporous structure has resulted in the development of bioactive glass nanoparticles for drug and molecule delivery [47].

While bioceramic nanoparticles already consist of inorganic components which are beneficial for bone regeneration, their biological performance can be further improved by incorporating biological additives, such as grow factors, peptides or ions. Especially bioinorganic ions are interesting additives because they are naturally found in the human body and are important for the normal functioning of tissue and organs. In addition, due to their low cost and high stability, the clinical use of bioinorganic ions can overcome many of the disadvantages associated with larger biomolecules such as proteins and growth factors. Several bioinorganic ions such as fluoride, magnesium, strontium, zinc, and copper play important roles in bone regeneration, and systemic deficiency of these ions can hinder bone development and cause malfunctioning of bone repair mechanisms [48-50].

Bioinorganic ions can be delivered either systemically, e.g., by oral administration, or incorporated into other bone graft substitutes. However, proper dose control using these methods is difficult. Bioceramic nanoparticles represent a powerful alternative for therapeutic ion administration because they allow local ion delivery. Local ion delivery can increase therapeutic efficiency and minimize side effects. Moreover, the degradation of ceramic nanoparticles can be modulated to allow controlled and sustained ion release. This allows a much closer control of the therapeutic activity of these ions, which is highly dose-dependent. Due to their small size, nanoparticles are intrinsically taken up by cells via endocytosis. This enables bioceramic nanoparticles to deliver ions within cells rather than in their surrounding environment.

2. Aim and outline for this thesis

The overall aim of this thesis is to study how CaP, MSN and MBG nanoparticle design and administration mode affect their ability to promote bone processes.

Following this introduction, **chapter 2** of this thesis presents an overview of the application of CaP, MSN and MBG nanoparticles in the field of bone regeneration. In this review, a summary is given of each of these nanoparticles in terms of synthesis and their applications. Furthermore, advantages and future perspectives on their (clinical) use in the field of bone regeneration, are provided.

In **chapter 3**, we investigated the effect of nanoparticle shape on their ability to promote osteogenic differentiation of hMSCs. Specifically, round, rice and needle shaped CaP nanoparticles with similar crystallinity and chemical composite were synthesized. Their ability to induce osteogenesis were evaluated on both gene and protein level. Furthermore, their application as nanoparticle suspensions and as nanoparticle based films was explored.

In **chapter 4**, MSN for multiple ion delivery were developed. CaP layers were created onto the MSN surface to allow multiple inorganic ion incorporation and pH responsive ion release. The ability of the developed MSN to effectively stimulate osteogenesis in hMSCs was assessed and compared to direct ion administration in cell culture medium.

In **chapter 5,** different modes of ion incorporation in MSN and MBG were compared in terms of their ability to induce osteogenesis and mineralization of hMSCs. Zinc ions were incorporated in three different locations within MSN; within the matrix, on the surface or in the mesopores. Ion incorporation efficiency, ion release profiles and their ability to increase the ALP activity of hMSCs were investigated.

In **chapter 6**, the feasibility of incorporating multiple bioinorganic ions into nBGs without changing their morphology and structure via laser-doping technology, was investigated. The ability of laser doped nBGs to stimulate osteogenic differentiation in hMSCs was determined, while their ability to induce angiogenesis was analysed using human umbilical vein endothelial cells (HUVECs) culture.

Chapter 7 discusses the general results obtained from the different studies in this thesis. It also provides future perspectives of bioceramic nanoparticles in bone regeneration. In **Chapter 8**, the impact of the main findings of this thesis is discussed.

References

1. A. S. Mao and D. J. Mooney, Proc. Natl. Acad. Sci., 2015, Regenerative medicine: current therapies and future directions, 112, 14452-14459.
2. K. McNamara and S. A. Tofail, Adv. Phys. 2017, Nanoparticles in biomedical applications, 2, 54-88.
3. M. González-Béjar, L. Francés-Soriano and J. Pérez-Prieto, Front. Bioeng. Biotechnol., 2016, Upconversion nanoparticles for bioimaging and regenerative medicine, 4, 47.
4. M. Fathi-Achachelouei, H. Knopf-Marques, C. E. Ribeiro da Silva, J. Barthès, E. Bat, A. Tezcaner and N. E. Vrana, Front. Bioeng. Biotechnol., 2019, Use of nanoparticles in tissue engineering and regenerative medicine, 7, 113.
5. J. Jeevanandam, A. Barhoum, Y. S. Chan, A. Dufresne and M. K. Danquah, Beilstein J. Nanotechnol., 2018, Review on nanoparticles and nanostructured materials: history, sources, toxicity and regulations, 9, 1050-1074.
6. A.-I. Moreno-Vega, T. Gomez-Quintero, R.-E. Nunez-Anita, L.-S. Acosta-Torres and V. Castaño, J. Nanotechnol., 2012, Polymeric and ceramic nanoparticles in biomedical applications, 2012.
7. A. Tautzenberger, A. Kovtun and A. Ignatius, Int. J. Nanomed., 2012, Nanoparticles and their potential for application in bone, 7, 4545.
8. W. Gu, C. Wu, J. Chen and Y. Xiao, Int. J. Nanomed., 2013, Nanotechnology in the targeted drug delivery for bone diseases and bone regeneration, 8, 2305.
9. E. Engel, A. Michiardi, M. Navarro, D. Lacroix and J. A. Planell, Trends Biotechnol., 2008, Nanotechnology in regenerative medicine: the materials side, 26, 39-47.
10. D. Khang, J. Carpenter, Y. W. Chun, R. Pareta and T. J. Webster, Biomed. Microdevices, 2010, Nanotechnology for regenerative medicine, 12, 575-587.
11. M. Pöttler, I. Cicha, H. Unterweger, C. Janko, R. P. Friedrich and C. Alexiou, Nanomed., 2019, Nanoparticles for regenerative medicine, 14, 1929-1933.
12. S. Weiner and H. D. Wagner, Annu. Rev. Mater. Sci., 1998, The material bone: structure-mechanical function relations, 28, 271-298.
13. Z. Wang, Z. Tang, F. Qing, Y. Hong and X. Zhang, Nano., 2012, Applications of calcium phosphate nanoparticles in porous hard tissue engineering scaffolds, 7, 1230004.
14. S. Punj, J. Singh and K. Singh, Ceram. Int., 2021, Ceramic biomaterials: Properties, state of the art and future prospectives, 47, 28059-28074.
15. P. Habibovic and J. Barralet, Acta Biomater., 2011, Bioinorganics and biomaterials: bone repair, 7, 3013-3026.
16. Y. C. Chai, A. Carlier, J. Bolander, S. J. Roberts, L. Geris, J. Schrooten, H. Van Oosterwyck and F. P. Luyten, Acta Biomater., 2012, Current views on calcium phosphate osteogenicity and the translation into effective bone regeneration strategies, 8, 3876-3887.
17. F. Barrère, C. A. van Blitterswijk and K. de Groot, Int. J. Nanomed., 2006, Bone regeneration: molecular and cellular interactions with calcium phosphate ceramics, 1, 317.
18. I. Elgali, O. Omar, C. Dahlin and P. Thomsen, Eur. J. Oral Sci., 2017, Guided bone regeneration: materials and biological mechanisms revisited, 125, 315-337.

19. A. Satpathy, A. Pal, S. Sengupta, A. Das, M. M. Hasan, I. Ratha, A. Barui and S. Bodhak, J. Indian Inst. Sci., 2019, Bioactive nano-hydroxyapatite doped electrospun PVA-chitosan composite nanofibers for bone tissue engineering applications, 99, 289-302.

20. H. Zhou and J. Lee, Acta Biomater., 2011, Nanoscale hydroxyapatite particles for bone tissue engineering, 7, 2769-2781.

21. N. Wang, S. T. Dheen, J. Y. H. Fuh and A. S. Kumar, Bioprinting, 2021, A review of multi-functional ceramic nanoparticles in 3D printed bone tissue engineering, 23, e00146.

22. K. Kim and J. P. Fisher, J. Drug Targeting, 2007, Nanoparticle technology in bone tissue engineering, 15, 241-252.

23. J. Corona-Gomez, X. Chen and Q. Yang, JFB., 2016, Effect of nanoparticle incorporation and surface coating on mechanical properties of bone scaffolds: a brief review, 7, 18.

24. T. J. Levingstone, S. Herbaj, J. Redmond, H. O. McCarthy and N. J. Dunne, Nanomaterials, 2020, Calcium phosphate nanoparticles-based systems for RNAi delivery: Applications in bone tissue regeneration, 10, 146.

25. N. Pajares-Chamorro and X. Chatzistavrou, Acs Omega, 2020, Bioactive glass nanoparticles for tissue regeneration, 5, 12716-12726.

26. A. Bozorgi, M. Khazaei, M. Soleimani and Z. Jamalpoor, Biomater. Sci., 2021, Application of nanoparticles in bone tissue engineering; a review on the molecular mechanisms driving osteogenesis, 9, 4541-4567.

27. F. Bakan, Hydroxyapatite-Advances in Composite Nanomaterials, Biomedical Applications and Its Technological Facets, 2018, Gene delivery by hydroxyapatite and calcium phosphate nanoparticles: a review of novel and recent applications, 157-176.

28. S. van Rijt, K. de Groot and S. C. Leeuwenburgh, Tissue Eng., 2022, Calcium phosphate and silicate-based nanoparticles: history and emerging trends, 28, 461-477.

29. I. I. Slowing, J. L. Vivero-Escoto, B. G. Trewyn and V. S.-Y. Lin, J. Mater. Chem., 2010, Mesoporous silica nanoparticles: structural design and applications, 20, 7924-7937.

30. C. Mao, X. Chen, G. Miao and C. Lin, Biomed. Mater., 2015, Angiogenesis stimulated by novel nanoscale bioactive glasses, 10, 025005.

31. A. A. Gorustovich, J. A. Roether and A. R. Boccaccini, Tissue Eng. Part B Rev., 2010, Effect of bioactive glasses on angiogenesis: a review of *in vitro* and *in vivo* evidences, 16, 199-207.

32. S.-W. Ha, M. Viggeswarapu, M. M. Habib and G. R. Beck Jr, Acta Biomater., 2018, Bioactive effects of silica nanoparticles on bone cells are size, surface, and composition dependent, 82, 184-196.

33. W. Cui, Q. Liu, L. Yang, K. Wang, T. Sun, Y. Ji, L. Liu, W. Yu, Y. Qu and J. Wang, ACS Biomater. Sci. Eng., 2018, Sustained delivery of BMP-2-related peptide from the true bone ceramics/hollow mesoporous silica nanoparticles scaffold for bone tissue regeneration, 4, 211-221.

34. X. Wu, M. Wu and J. X. Zhao, Nanomed. Nanotechnol. Biol. Med., 2014, Recent development of silica nanoparticles as delivery vectors for cancer imaging and therapy, 10, 297-312.

35. S.-H. Wu, C.-Y. Mou and H.-P. Lin, Chem. Soc. Rev, 2013, Synthesis of mesoporous silica nanoparticles, 42, 3862-3875.

36. F. Baino, S. Fiorilli and C. Vitale-Brovarone, Acta Biomater., 2016, Bioactive glass-based materials with hierarchical porosity for medical applications: Review of recent advances, 42, 18-32.
37. Y. Wang, Q. Zhao, N. Han, L. Bai, J. Li, J. Liu, E. Che, L. Hu, Q. Zhang and T. Jiang, Nanomed. Nanotechnol. Biol. Med., 2015, Mesoporous silica nanoparticles in drug delivery and biomedical applications, 11, 313-327.
38. L. L. Hench, J. Mater. Sci.: Mater. Med., 2006, The story of Bioglass®, 17, 967-978.
39. L. L. Hench and H. Paschall, J. Biomed. Mater. Res., 1973, Direct chemical bond of bioactive glass-ceramic materials to bone and muscle, 7, 25-42.
40. J. R. Jones, D. S. Brauer, L. Hupa and D. C. Greenspan, Int. J. Appl. Glass Sci., 2016, Bioglass and bioactive glasses and their impact on healthcare, 7, 423-434.
41. L.-C. Gerhardt and A. R. Boccaccini, Materials, 2010, Bioactive glass and glass-ceramic scaffolds for bone tissue engineering, 3, 3867-3910.
42. Q. Fu, E. Saiz, M. N. Rahaman and A. P. Tomsia, Mater. Sci. Eng., C, 2011, Bioactive glass scaffolds for bone tissue engineering: state of the art and future perspectives, 31, 1245-1256.
43. A. A. El-Rashidy, J. A. Roether, L. Harhaus, U. Kneser and A. R. Boccaccini, Acta Biomater., 2017, Regenerating bone with bioactive glass scaffolds: A review of *in vivo* studies in bone defect models, 62, 1-28.
44. Á. J. Leite and J. Mano, J. Mater. Chem. B, 2017, Biomedical applications of natural-based polymers combined with bioactive glass nanoparticles, 5, 4555-4568.
45. Z. Hong, G. M. Luz, P. J. Hampel, M. Jin, A. Liu, X. Chen and J. F. Mano, J. Biomed. Mater. Res. A, 2010, Mono-dispersed bioactive glass nanospheres: preparation and effects on biomechanics of mammalian cells, 95, 747-754.
46. K. Zheng and A. R. Boccaccini, Adv. Colloid Interface Sci., 2017, Sol-gel processing of bioactive glass nanoparticles: A review, 249, 363-373.
47. M. Erol-Taygun, K. Zheng and A. R. Boccaccini, Int. J. Appl. Glass Sci., 2013, Nanoscale bioactive glasses in medical applications, 4, 136-148.
48. I. Zofková, P. Nemcikova and P. Matucha, CCLM, 2013, Trace elements and bone health, 51, 1555-1561.
49. M. Dermience, G. Lognay, F. Mathieu and P. Goyens, J. Trace Elem. Med. Biol., 2015, Effects of thirty elements on bone metabolism, 32, 86-106.
50. J.-P. Bonjour, J. Am. Coll. Nutr., 2011, Calcium and phosphate: a duet of ions playing for bone health, 30, 438S-448S.

Chapter 2

Bioceramic nanoparticles for bone regeneration

1. Introduction

Traumatic bone defects caused by trauma, or bone cancer removal, are a tremendous health burden in the western population. Bone has the ability to remodel and an intrinsic capacity to regenerate without the formation of scar tissue. However, when a bone defect is larger than 1-2.5 cm in length, this self-healing can fail and external intervention is required [1-3]. Current treatment options for large bone defects often involve implanting patients' own bone, removed from elsewhere in the body (i.e., autograft), to the site of the bone defect. However, there are several complications associated with using autografts, including donor site morbidity and limited graft availability [4, 5]. Therefore, synthetic biomaterials have been proposed as off-the-shelf available bone graft substitutes. Many different biomaterials are being actively researched for this purpose including metals, polymers and ceramic materials or a combination of these materials [4, 6]. In order for these biomaterials to be effective in load bearing applications, they need to provide temporary mechanical support and facilitate new bone formation.

Bone provides structural support and protection for internal organs and serves as a mineral reservoir of the body. It undergoes continuous remodelling to meet the changing mechanical demands, and to maintain the nutritional balance of the body. The 3D structure and a chemical composition with both inorganic and organic components, are responsible for its mechanical strength. Specifically, in native bone, nano-sized hydroxyapatite (HA) crystals are imbedded periodically along the long axes of collagen fibres. These fibres assemble into mineralized collagen fibrils, which are arranged in a staggered array. At the micro level, the fibrils form larger structures called osteons. Osteons consist of layers of mineralized collagen fibrils surrounding a central canal that contains blood vessels and nerves. The bone matrix is populated by several cell types including osteoblasts, osteoclasts, bone lining cells and osteocytes. Osteoclasts are responsible for resorbing and releasing mineral components, such as calcium and phosphate ions from bone matrix, which allows the body to maintain a homeostatic balance of ions. Osteoblasts are differentiated from osteoprogenitor cells and produce new bone matrix. Osteocytes are mature osteoblasts, which can sense mechanical (e.g. changes in mechanical load) and chemical stimuli (e.g. cytokines, chemokines and hormones) within mineralized bone and can respond by producing signalling molecules that regulate bone remodelling. Bone formation in healthy individuals occurs in two ways; membranous ossification and endochondral ossification. In membranous ossification, or direct ossification, mesenchymal stem cells (MSCs) directly differentiate to become osteoblasts. On the other hand, in endochondral ossification or indirect ossification, MSCs differentiate into cartilage first, and are later slowly mineralized by existing osteoblasts or differentiated MSCs. For both routes, the differentiation of MSCs into the osteoblast lineage (i.e., osteogenesis), and mineralization of the extracellular matrix (ECM), are vital. Formation of new vasculature (i.e., angiogenesis) needs to occur simultaneously in order to provide adequate nutrients, growth factors, minerals and oxygen to maintain cell viability.

Thus, the ideal biomaterial should be mechanically strong and have the ability to direct both osteogenesis and angiogenesis for successful bone regeneration. Ceramic-based materials, including alumina (Al_2O_3) and zirconia (ZrO_2), have been heavily researched as synthetic biomaterial alternatives because of their high mechanical strength, which is required for load bearing applications. However, these biomaterials are generally bioinert and cannot actively stimulate bone formation [7]. In contrast, calcium phosphate (CaP) ceramics can support the growth of new bone formation by providing a scaffold for osteoblasts to adhere to and deposit new bone (osteoconductive). Certain compositions of CaP ceramics can also be osteoinductive, meaning that they have the ability to stimulate the differentiation of stem cells into osteoblasts, leading to the formation of new bone tissue. Although CaP ceramics are used for clinical applications, including as dental and orthopaedic implants, they typically cannot be used for load-bearing applications due to their brittle nature.

Over the past decades, the development of ceramics at the nanoscale has received increased interest because of the same size range as CaP apatite found in natural bone [12]. Moreover, ceramic nanoparticles (CNPs) can show improved bioactivity over macro-sized ceramics by providing a larger surface area for cells to interact with. Most frequently used CNPs include CaP, mesoporous bioactive glass (MBG), and mesoporous silica nanoparticles (MSN). Synthesized CaP can exist in various compositions and crystallinity, ranging from highly crystalline hydroxyapatite (HA) to amorphous calcium phosphate (ACP), depending on synthesis process used. The composition, or calcium to phosphate (Ca/P) ratio, and crystallinity effects CaP bioactivity and biodegradation rate.

MBG and MSN are silica-based NPs which mainly consist of a Si-O network. However, while MBG have an additional Ca-O or P-O bond within the Si-O network, MSN consists purely of Si-O bonds. All three CNPs can be synthesized in different shapes and sizes, and can also be post-modified to allow tissue targeting, imaging or attachment to biomaterial scaffolds. CNPs are also often incorporated as fillers in biomaterials, or used as coatings on implants to improve their biological and/or mechanical performance. They have also shown potential as delivery vehicles for therapeutic agents or bioinorganic ions [13, 14]. For example, CNPs have been used for the delivery of growth factors, including bone morphogenetic protein 2 (BMP2), and differentiation supplements, such as dexamethasone (Dex), to promote osteogenesis. Moreover, more recently, CNPs structure have been doped with additional bioinorganic ions, which are trace elements in the human body that play important roles in facilitating new bone (osteogenesis) and new blood vessel (angiogenesis) formation [15, 16]. For example, strontium (Sr) promotes osteoblast proliferation and differentiation via activation of the calcium sensing receptor in osteoblasts [17-19]. Zinc (Zn) and manganese (Mn) are able to stimulate osteoblast proliferation, differentiation and mineralization [20, 21]. Moreover, several ions are known to stimulate angiogenesis such as copper (Cu), magnesium (Mg), cobalt (Co) and boron (B) [22-25]. CNPs synthesis and structure allow for easy incorporation of ions, representing an important advantage for the clinical use of CNPs. Incorporating ions into CNPs thus represents a promising alternative to the use of therapeutic proteins since they are more cost-effective, and have a longer shelf-life.

In this review, we provide a comprehensive summary of CNPs and their use in the bone regeneration field. A brief introduction to the general chemical properties of CaP, MBG, and MSN including their synthesis is provided. Furthermore, recent research concerning the application of each CNP in bone regeneration, including their role as delivery vehicles of drugs and ions, are highlighted.

2. Calcium phosphate nanoparticules (CaPNP)

As earlier mentioned, CaP are frequently researched ceramics for bone regeneration applications because their chemical composition is similar to the inorganic phase of bone and teeth. CaP, or more accurately calcium orthophosphates, are a family of salts consisting of Ca ions and orthophosphoric acid (H_3PO_4). The Ca/P ratio determines their crystal structure and specific physicochemical properties. For example, hydroxyapatite (HA), with Ca/P ratio of 1.67, is extensively investigated for use in bone repair applications due to their close chemical similarity to nano-apatite found in bone matrix. Due to the high stability of HA, it is frequently used as dental and bone defect filler. In contrast, the highly interconnected porous alpha-tricalcium phosphate (TCP) is more soluble in comparison to HA, and can act as a source of Ca and P ions when material degradation is desirable.

Nano-sized needle-shaped apatite crystals as found in bone have inspired the synthesis of HA NPs but also other CaP phases. CaPNP in different sizes, shapes and crystallinity have been synthesized and it has been shown that CaP morphology has a significant effect on their ability to promote bone formation, although the mechanisms are often not completely understood [26-29]. For example, Cai et al. found that human MSCs exposed to 20 nm sized CaPNP led to significantly higher cell proliferation compared to exposure to 80 nm sized and micrometer- sized CaP [27]. This may be due to a more pronounced uptake of smaller NPs, thereby increasing intracellular Ca ion release [29]. Also, crystallinity plays an important role in the degradation of CaPNP, with lower ion release rates observed from particles with higher levels of crystallinity [30]. Interestingly, CaPNP with high crystallinity but low solubility could promote cell adhesion [31, 32].

CaPNP can be synthesized using various methods including wet-chemical precipitation, sol-gel, plasma-spray pyrolysis, and solid-state reactions [33-38]. Wet precipitation is straightforward and cost-efficient because Ca and P salts are highly soluble in water and precipitation occurs instantaneously in basic conditions. However, the precise control over synthesis parameters such as time, pH, concentration, temperature, and precipitation time is required in order to produce CaPNP with consistent size and crystallinity [39]. The sol–gel method involves precursors to undergo hydrolysis and condensation reactions, often in an organic solution. This synthesis method allows high control over the chemical composition (Ca/P ratio), which is important to control the crystallinity of the NPs. However, the particle yield is often low. Plasma-spray pyrolysis is a technique where a precursor solution is injected in nano or micro-sized droplets. Particle formation occurs as the droplet is passed through a plasma flame at a high temperature. The (nano)particle size and crystallinity can be adjusted by modifying synthesis parameters such as type of solvent and temperature. However, one disadvantage of this method is that it is difficult to achieve homogenously sized particles and specialized equipment is needed. Moreover, the high processing temperatures prevent the incorporation of organic compounds.

In solid-state methods, Ca and P precursor salts are mixed and ground into fine powder, which then undergoes high temperature treatment to form CaPNP. This method usually yields well-crystallised CaPNP in large quantities, however, is only suitable for thermally stable CaP phases. Moreover, long exposure to high temperatures causes NPs to agglomerate and melt together, resulting in sintered micro and macro material as the final product [38, 40]. Therefore, the addition of a mechanical process such as milling or grinding is necessary to achieve nano-sized particles [41]. Thus, obtaining homogenous NPs via this method remains challenging [42, 43].

Using the techniques outlined above, CaPNP can be synthesized in many sizes, shapes and crystallinities, as demonstrated in Figure 1. The large diversity in synthesis methods give scientists the advantage to create CaPNP that can be tailored depending on the application.

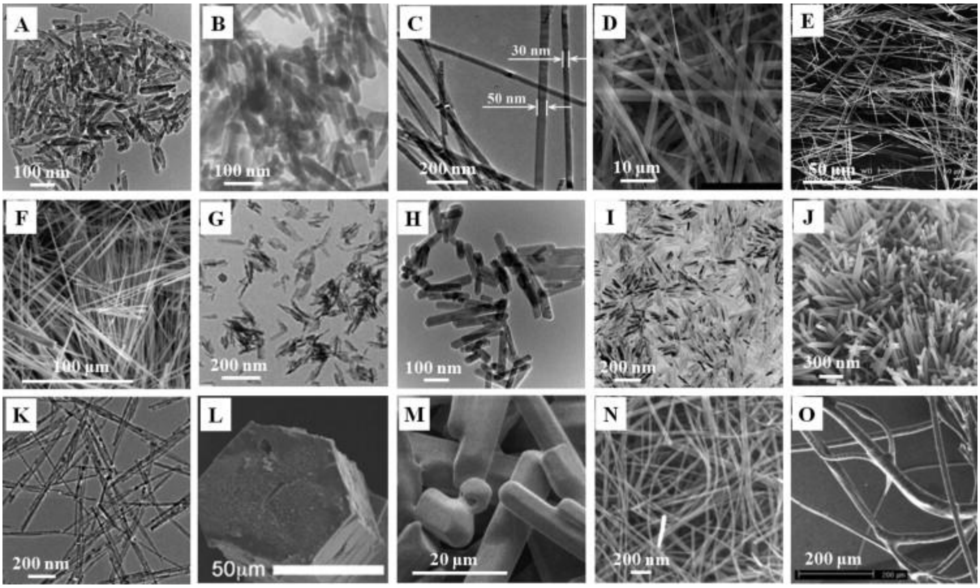

Figure 1: Examples of CaPNP with different morphology and crystallinity: (A) HA nano-needles by wet precipitation [44], (B) HA nanorods by wet precipitation at high temperature [45], (C) nanowires by microwave-assisted hydrothermal method using ATP as phosphorus source [46], (D) OCP fibers by urea hydrolysis method[47], (E) HA whiskers by hydrothermal method using amide as the homogeneous precipitation reagent [48], (F) SrHA whiskers by hydrothermal method using amide as the homogeneous precipitation reagent[49], (G) DCPD whiskers by hydrothermal reactions of Ca-chelated reagent [50], (H) HA nanorods by hydrothermal-microemulsion method [51], (I) HA nanorods by liquid-solid-solution (LSS) [52], (J) HA nanowires using CS as hard template [53], (K) HA nanowires using xonotlite nanowires as precursors [54], (L) millimetre-sized HA whiskers by Cl^-–OH^- ion exchange [55], (M) HA whiskers by solid state method [56] , (N) HA wires by electro-deposition (flux) method [57], and (O) HA fibers by electrospinning technique [57]. Source: Kaili et al. [58].

2.1 Application of CaPNP in the field of bone regeneration

As synthesis methods have improved, the use of CaPNP for bone regeneration applications has rapidly increased in the past decade. While there is a huge variety of medical applications for nanosized CaP, including as bone fillers [59], coatings for dental implants [60], additives in scaffolds for cartilage regeneration [61], drug and gene delivery carriers, and bioimaging [62], here we will focus on the application of CaPNP in thebone regeneration field.

CaPNP coatings on metallic implants is a promising method to promote bone integration between an implant surface and native bone. Coatings based on CaPNP have been used to improve metal implant fixation. Different techniques are currently being used to coat CaPNP onto metallic or polymeric implant surface, such as electrochemical deposition [63], plama-spraying [64] and biomimic deposition [65, 66]. Several studies have shown that coatings prepared from nano-sized HA can improve bone integration [67-69]. For example, Aksakal et al. reported better *in vivo* fixationand osteointegration of nano-sized HA coated metallic screws compared to those coated with CaP microparticles [70]. A few studies have investigated the influence of CaPNP shape on their ability to promote bone regeneration [38–40]. It has been shown that cells can sense topographical cues on 2D surfaces via formation of focal adhesions through integrin receptors, which can promote cell proliferation and differentiation [71]. One such study reported higher upregulation of bone-specific protein osteocalcin (OCN) and alkaline phosphotase (ALP) osteogenic markers when human MSCs were exposed to needle-shaped CaPNPs surface compared to spherical CaPNP surface [38]. Needle-shaped CaPNP can also increase osteogenic protein expression (e.g., Runx2, OPN and OCN) in osteoblasts compared to spherical CaPNP [72]. Also our work demonstrated that CaPNP shape played an important role in their ability to upregulate markers related to osteogenesis [73]. Specifically, Runx2, BMP2, OPN and OCN gene levels were significantly increased when human MSCs were cultured on surfaces prepared from needle-shaped CaPNPs. In contrast, rice- and spherical-shaped CaPNP were less efficient in upregulating these genes.

Similar to bulk CaP ceramics, CaPNP can be implanted directly into the damaged site as bone cement or compressed to form a bulk structure [74-76]. However, bulk materials made by agglomerating CaPNPs often lack the mechanical strength required for weight bearing applications. CaPNP can be added to other (synthetic) biomaterials such as collagen as filler components, which can lead to composite biomaterials with improved mechanical properties [77-79]. For example, it has been demonstrated that by combining collagen with nano-HA, a composite material with high elasticity (0.15–20 GPa), similar to bovine cortical bone (3–30 GPa) could be obtained [80]. In a similar study, Gahawar et al. showed that the addition of HA NPs not only improved the mechanical strength and elasticity of poly(ethylene glycol) (PEG) hydrogels, but also the cell adhesion to the scaffold with increasing nano-HA weight percent [81].

Due to their small size, CaPNP have also been used as delivery carriers for various cargoes, such as antibiotics and anti-inflammatory drugs [82], growth factors and morphologic proteins[83]. Therapeutic molecules can be incorporated in CaP either via co-precipitation or surface adsorption. Since bacterial infections are a major concern in the treatment of bone defects, various antibiotics such as tetracycline and gentamicin have been successfully combined with CaPNP [82, 84, 85].

Crucial growth factors for bone regeneration, such as BMP2 which stimulates osteogenesis and vascular endothelial growth factor (VEGF) which promotes blood vessel formation, have also been incorporated into CaPNP to stimulate bone regeneration [83, 86, 87]. Moreover, CaPNP are also widely used for the delivery of genetic cargo due to the presence of Ca ions, which increases the loading volume for genetic material [88-90]. An advantage of CaPNP over other viral vectors is that they can enhance osteogenesis despite their low transfection efficacy (10–20% compared to 40%-50% for viral vectors). While the mechanism of CaPNP as transfection carriers is not yet fully understood, it has been hypothesized that Ca ions not only intrinsically induce osteogenesis but also aid the transcription process of the delivered genetic material [91]. An extensive overview on CaPNP used for this application can be found in reviews by Bakan [92] and Levingstone *et al*. [93]. Interestingly, the drug loading capacity of CaPNP can also be affected by shape, which is probably related to the dependency of surface area on NP shape. For example, one study showed that platelet-like CaPNP can adsorb 1.3 times higher amount of drugs compared to needle-like NPs of the same weight [94]. Moreover, another study showed that spherical CaPNP have higher drug loading and drug release capacity compared to flaky, square or elongated orthogonal shaped CaPNP [95].

In addition to organic molecules, CaPNP can also be doped with inorganic ions to improve their ability to promote osteogenesis or provide additional functionalities to the materials such as anti-bacterial or anti-inflammatory properties. Inorganic ion substitution in CaP material has been well studied and applied for bone regeneration purposes [97, 98]. Several inorganic ions such as Sr, Zn, Cu, and silver (Ag) have been successfully added to CaPNP without altering the morphology of the NPs. Scaffolds consisting of Sr-CaPNP showed a more pronounced cell adhesion, proliferation, and osteogenic differentiation as demonstrated by the ALP activity of osteoblasts as compared to plain CaPNP [99, 100]. Apart from being doped independently, Sr can also be co-doped along with other ions such as Ag for additional anti-bacterial capability [101]. Zn-doped CaPNP induced higher ALP activity in MSCs, but decreased their mineralization ability in comparison to pure HA NPs [102]. Cu is often used for its antibacterial properties. Cu-doped HA NPs have been shown effective against Staphylococcus aureus (S. aureus), which is commonly associated with bone device-related infections [103].

3. Silica-based nanoparticles

The application of silica-based NPs in the field of bone regeneration has expanded rapidly over the last decade[107]. MBG and MSN have especially found widespread use as drug delivery carriers due to their ordered mesoporous structure. This mesoporous structure provides a large surface area and volume for cargo loading. Moreover, the biocompatibility, easily tuneable porosity, and possibilities for surface functionalization make them interesting candidates for controlled and/or targeted delivery of various cargo.

The difference between MBG and MSN lies in their chemical composition. While MSN consist of pure SiO_2 network, MBG also contain CaO and/or P within their structure. The presence of Ca and/or P ions facilitates the deposition of CaP on to the MBG surface. This deposited CaP layer renders MBG the bone bonding, which is a reason for their name bioactive glass. It is known that Si, Ca and P ions released from MBG and MSN can positively affect osteogenic differentiation of human MSCs and osteoblasts [108-111]. Therefore, controlling the amount of these ions and their release are of primary importance in developing both MBG and MSN for application in the bone regeneration.

3.1 Mesoporous bioactive glass nanoparticles (MBG)

MBG are generally produced using the modified Stöber's method [112]. Introduction of Ca, P and other ions into the silica network is done either via ion absorption or direct introduction during nucleation of the particles. In order to create the mesoporous structure, surfactants such as cetyltrimethyl ammonium bromide (CTAB), P123, and F127 are often used as templates to form a micelle structure directing NP growth. The hydrophilic parts of micelles provide the nucleation sites for siloxane precursors. After the SiO_2 network is formed, the surfactant can be removed, resulting in a NP with a mesoporous structure. Surfactant choice affects the pore size, while the ion precursor greatly affects particle shape, size and morphology of the MBG. In a study comparing 24 mesoporous bioactive glass compositions, only those with at least 60% of SiO_2 content could form an ordered mesoporous structure [113]. Due to the well-known stimulatory effect of Ca on osteogenensis, many researchers have attempted to maximize the amount of Ca within MBG. However, a Ca ratio of more than 20wt% is difficult to achieve, even if high Ca ion concentrations are present during the synthesis process. In addition, higher Ca amount increases the overall particle size and lowers the overall size homogeneity of MBG [114, 115]. The addition of specific ions into the SiO_2 matrix can also affect the pore formation and integrity of the MBG network. For example, Zn and Cu addition led to an increase of the surface area and pore volume [116, 117], while Mg, Zn and Sr doping weakened the overall SiO_2 network structure by expanding the lattice, which led to higher degradation rates [118-120].

3.1.1 Application of MBG in bone regeneration

Thanks to their unique ability to form strong bonds with bone tissue, MBG are researched for bone regeneration applications. The ordered mesoporous structure has also been used for drug delivery applications [126-129]. Examples include the use of MBG for delivery of antibiotic drugs such as vancomycin [130], anti-inflammatory drug ibuprofen [131], but also several examples of gene delivery exist [132-134]. For example, Li et al. demonstrated that amine modified MBG could successfully transfect cells with a green fluorescent protein fusion plasmid [132]. In a study by Kim et al., enlarged pore

MBG were used to transfect rat MSCs with BMP2-pDNA, which significantly improved localized bone regeneration when collagen gels containing the MBG were implanted into a bone defect site [135]. In a similar study it was shown that MBG containing osteogenic growth peptide incorporated within polymer scaffolds led to improved scaffold mineralization, where Ca release from MBG could aid gene transfection [136].

While MBG in their original form can stimulate osteogenesis and angiogenesis, the addition of inorganic ions into MBG (i.e., ion doping) is a popular approach to further enhance their bioactivity such as their osteogenic potential, or add other functionalities, such as anti-bacterial and anti-inflammatory properties [137]. For example, several ions such as Ag, Manganese (Mn), Cerium (Ce), and Cu with known antibacterial properties have been incorporated into MBG. Ag is the most popular ion for this purpose as it is effective against both gram-positive and gram-negative bacteria. Ag can induce reactive oxygen species (ROS) such as OH−, $O^{2-,}$ and H_2O_2 production which causes cell damage [138, 139]. While Ag has been successfully incorporated into solid BG particles, there are limited studies using MBG [140-142]. One such study reported co-doping of Ag and Mn in MBG, which led to reduced *S. carnosus* and *E. coli* growth, while enhancing human osteoblast-like cells (MG-63) proliferation *in vitro* [142]. In contrast to Ag, Ce can be both anti-bacterial and anti-inflammatory, depending on its oxidation state (Ce^{3+} or Ce^{4+}). At high pH, Ce^{3+} acts as an antioxidant [143, 144], while at low pH, Ce^{4+} becomes a pro-oxidant and can induce ROS, leading to anti-bacterial activity [144]. Kurtuldu et al. tested the anti-inflammatory and anti-bacterial activity of Ce containing MBG on RAW 264.7 cells (pro-inflammatory macrophage cells). The study found that RAW 264.7 cells exposed to Ce containing MBG, resulted in decreased nitric oxide release, indicating an anti-inflammatory response and also a reduction in biofilm formation was observed [145]. Han et al., demonstrated that Cu- doped MBG exhibited an antibacterial effect against porphyromonas gingivalis while also promoting migration of human umbilical vein endothelial cells (HUVECs) [146].

In order to achieve successful bone regeneration, the formation of blood vessels to replenish nutrients and oxygen to cells is critical. In addition to Si, several inorganic ions that are known to stimulate angiogenesis such as Cu, magnesium (Mg) and cobalt (Co) have been incorporated into MBG. For example, zebra fish embryos exposed to Cu-MBG led to increased vascularization in comparison with Cu-free MBG [147].

MBG ion doping with bivalent ions such as Sr, Zn, and B can further enhance their osteogenic potential. For example, incorporation of Sr in MBG led to the upregulation of osteogenic gene expression including ALP, osteoprotegerin (OPG) and collagen I (Col I) in osteoblast-like SAOS-2 cells [148]. Zn containing MBG (Zn-MBG) could enhance *in vitro* mineralization, ALP activity, and the production of intracellular protein osteocalcin in rat MSCs in comparison to MBG without Zn [110]. The choice of ion to be incorporated into MBG requires careful consideration, because it may also stimulate other biological processes. For example, B is known to play an important role in bone homeostasis [150]. However, one study showed that B-doped MBG (B-MBG) also reduced the inflammatory response of macrophages in addition lowered formation of osteoblasts compared to non-doped MBG [125, 151]. Moreover, Zheng et al., showed that B-MBG downregulated the expression of pro-inflammatory cytokine expression of IL-1β and IL-6 in comparison to bare MBG.

3.2 Mesoporous silica nanoparticles (MSN)

Unlike MBG, MSN consists of pure silica (Si-O) bonds without additional network modifiers. Generally, MSN synthesis follows the modified Stöber's method, using surfactants as the templating agent similar to that of MBG synthesis [112, 152, 153]. MSN have made a large impact in the drug delivery field, and have been used to carry diverse cargo such as hydrophobic drugs, peptides, proteins, and other nanoparticles within its mesopores [154]. MSN synthesis is very flexible; NP size, mesopore size and internal structure (e.g., hollow or core shell structure) can be adjusted to improve their drug delivery capabilities. For example, hollow MSN exhibited higher loading capacity of antibiotic tetracycline drug and slower release compared to traditional MSN [155]. Moreover, the MSN surface can be further modified for tissue targeting or to allow controlled drug release by using pore gatekeepers. Gatekeepers prevent premature drug release and can be functionalised to be responsive to specific stimuli, such as pH, temperature, light, redox agent or enzymes. The use of gatekeepers for controlled drug delivery from MSN have been comprehensively reviewed by Aznar et al [156].

Another approach to control the release of incorporated cargo is by controlling the degradation of MSN themselves. One method is to dope the silica matrix with metal ions such as Fe, Mn, Mg or Cu. The addition of these ions can accelerate MSN degradation when exposed to specific environments [157-159]. For instance, Fe doped MSN resulted in two-times increased degradation rate compared to that of non-doped MSN in serum-rich environments [157, 160]. Mn-doped hollow MSN (Mn-HMSN) rapidly dissolved in the presence of high concentrations of glutathione (GSH), compared to their non-doped counterpart [158].

Degradation of MSN can also be achieved by incorporation of disulphide bonds (S-S) into the silica network [161,162]. S-S bond cleavage could be triggered by an intracellular redox reaction. Several studies reported the synthesis of MSN with disulphide-bonds to achieve desirable biodegradability without affecting the overall shape of the NPs [163-165]. In one study, S-S MSN was used to improve the delivery of chemotherapeutic drug temozolomide to glioblastoma cancer cells by doubling the amount of drug released [164].

3.2.1 Application of MSN in bone regeneration

Within the field of bone regeneration, MSN have been used for the delivery of several types of molecules to stimulate bone formation including Dex, a corticosteroid drug that stimulates osteogenesis in bone cells, and growth factors such as BMP2 that are important for bone formation. For example, in one study, Dex was loaded within the mesoporous structure and the surface was further modified with chitosan to allow controlled drug release. The NPs were then incorporated into a poly-l-lactic acid scaffold and adipose tissue-derived human MSCs were seeded inside the scaffold. The scaffold with Dex-loaded MSN showed improvement in cell proliferation, osteogenic differentiation and mineralization compared to scaffolds without MSN and scaffolds with non-loaded MSN [166].

Due to their large size, growth factors such as BMP2 cannot be incorporated in the mesoporous system. However, several studies showed successful BMP2 delivery by immobilization on MSN surface [167, 168]. Dual or multiple factor delivery, e.g., by loading both in the mesopores and on the surface, can lead to improved therapeutic outcomes [168, 169]. For example, in one study, a BMP2 peptide was covalently grafted onto the surface of MSN and Dex was loaded into the mesopores. This dual delivery system could significantly increase ALP activity levels, osteogenic proteins expression (RUNX2, OCN) and mineralization in human MSCs in comparison to both control group (bare MSN) and MSN that contained only Dex or only BMP2. Ectopic bone formation in rats was used to evaluate the osteoinductive potential of bare MSN, BMP2-grafted MSN and BMP2-grafted/Dex-loaded MSN. The dual system showed a higher ability to induce ectopic bone formation compared to bare MSN and BMP2-grafted MSN [134]. In a similar study, Sun et al. developed MSN loaded with Dex and surface coated with chitosan and QK peptide, a VEGF mimicking peptide. This dual system improved differentiation of both human MSCs and HUVECs *in vitro* and induced the formation of blood vesicles in chicken embryos (chorioallantoic test) [170]. New bone formation *in vivo* was shown in a rat bone defect model using micro-CT imaging after 8 weeks of treatment, while immunofluorescence staining showed increased expression of CD31 marker in endothelial cells.

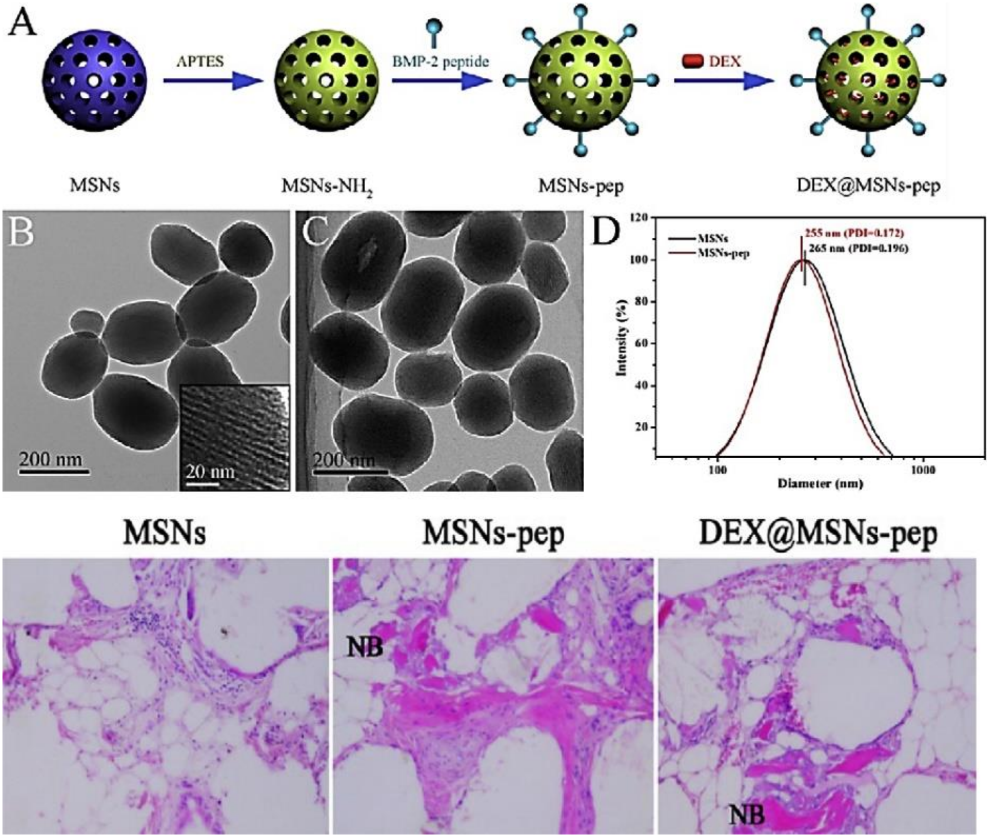

Figure 2: A Schematic illustration of the synthesis method for aminated mesoporous MSN; (B, C) TEM images of mesoporous MSN and BMP2-loaded NPs; (D) the size distribution of SNPs before (black) and after (red) the modification process. (Bottom) The progress of new bone (NB) formation after 3 weeks for unmodified (left), after loading BMP2 growth factor (middle), and after simultaneous loading of both Dex and BMP2 in mesoporous SNPs (right). Figure adapted with permission from [168].

Besides delivery of drugs and small therapeutic molecules, MSN have also been used to effectively deliver genetic materials such as DNA and RNA [171, 172]. For example, Kim et al. incorporated siRNA in hollow MSN to knockdown the Pelkho-1 gene in osteoblast cells. Similarly, Raimundo et al. used MSN coated with poly (ethylenimine) to deliver SOST gene siRNA and osteostatin in an osteoporosis mouse model. They successfully showed SOST gene expression reduction and increased RUNX2 and ALP gene expression and new bone formation *in vivo* [173]. Although not as widely studied as MBG, MSN have also been used for bioinorganic ion delivery. Several reports have demonstrated doping of MSN with ions such as Sr and Zn for bone regeneration [174-176]. Liu et al. showed that MSN containing 6wt% Sr could efficiently promote *in vitro* mineralization and new bone formation *in vivo* compared to non-doped MSN [174]. In our recent study, we showed that MSN containing multiple ions is significantly more efficient in promoting hMSC osteogenesis compared to single ion delivery using MSN [177].

4. Future outlook

CNPs have high potential for use in the bone regeneration field due to their excellent biocompatibity and intrinsic ability to promote bone growth. CNPs have been used to improve the mechanical properties of scaffolds made of other biomaterials, but also as delivery vehicles aiding processes relevant for bone regeneration, such as osteogenesis and angiogenesis. In the past decades, there have been many advancements in their synthesis and (surface) modification methods, offering fine control over material and surface properties. Several studies have shown how material properties such as size, shape and crystallinity, play important roles in CNP ability to promote bone regenerative processes. Moreover, we and others have shown that also their application mode (e.g., as coatings or as injectables) are important for their ability to induce and facilitate tissue regenerative processes. However, the mechanisms that lie behind these observations are currently poorly understood. Future efforts should focus on understanding the role different material parameters including shape, composition and ion release profiles, play in relevant biological processes. This knowledge will help scientists in the field to design better performing nanomaterials capable of efficiently guiding bone formation processes.

Ion doping of CNPs is a promising strategy to improve CNPs biological performance. Incorporating multiple ions could lead to CNPs that are more bioactive or can promote multiple biological processes simultaneously. Indeed, several studies demonstrate that combining multiple ions in one CNP can significantly improve their *in vitro* performance. However, incorporating multiple ions into CNP is often difficult due to interference between ions which can negatively impact particle formation and morphology. Some successful attempts of multiple ion doping into MBG have been demonstrated, albeit in low concentrations. Research into MSN for ion delivery is still in its infancy, however, several papers have shown that MSN surface can be modified with a CaP surface layer for drug delivery purposes [178]. More research is needed to investigate good synthesis methods that allow efficient multiple ion doping, but also what ion combinations aid bone regenerative processes.

For CaPNP in particular, a lot of research has focused on developing methods to control ion doping, crystallinity, and particle degradation. Furthermore, their use as biocompatible gene carriers has been established and validated both in *in vitro* and *in vivo* models. Although much progress has been made, precise control over morphological properties such as shape and size as well as homogeneity in their chemical synthesis, remains a challenge in the synthesis of these NPs. As a consequence, relatively little is known about the importance of these structural properties on their ability to promote *de novo* bone formation, which is important to understand their mode of action, and to increase their impact in the field.

BG has evolved a long way from simple solid glass composites to the structurally more complex MBG, both in synthesis methods and in their application. MBG have shown higher bioactivity than their solid counterpart due to an increased surface area and porosity. Moreover, MBG are biodegradable and the ionic dissolution products of MBG are known to benefit new bone formation, but have also been reported to e.g., induce angiogenesis or prevent bacterial infection. More importantly, their porous structure makes them suitable for drug delivery purposes. Recent years have demonstrated MBG as versatile materials for the delivery and co-delivery of ions, growth factors and small molecules. Therefore, MBG hold great promise as multipurpose tools in bone regeneration and other tissue regeneration fields. To maximize their use as multifunctional drug delivery tools, methods that allow surface modification to provide controlled drug delivery will likely further increase the clinical potential of MBG, but also their use in other fields such as soft tissue regeneration should be more actively explored.

MSN have been extensively used as nanocarriers, particularly for small molecule-, peptide- and gene delivery. Thanks to advancement in silica chemistry, MSN surface and core network can be modified with relative ease in comparison to other CNPs. However, their application in bone regenerative is relatively limited and mainly focuses on establishing their use as drug delivery tools. Research on how ions could be incorporated into MSN to increase their bioactivity and biodegradability is however limited, while successful incorporation of ions could lead to more bioactive MSN. Moreover, their use in other areas, such as in imaging tools, or as components in composites could be explored further to maximally exploit their potential.

References

1. E. H. Schemitsch, J. Orthop. Trauma, 2017, Size matters: defining critical in bone defect size, 31, S20-S22.
2. W. Wang and K. W. Yeung, Bioact. Mater., 2017, Bone grafts and biomaterials substitutes for bone defect repair: A review, 2, 224-247.
3. A. Nauth, E. Schemitsch, B. Norris, Z. Nollin and J. T. Watson, J. Orthop. Trauma, 2018, Critical-size bone defects: is there a consensus for diagnosis and treatment?, 32, S7-S11.
4. P. V. Giannoudis, H. Dinopoulos and E. Tsiridis, Injury, 2005, Bone substitutes: an update, 36, S20-S27.
5. C. G. Finkemeier, JBJS, 2002, Bone-grafting and bone-graft substitutes, 84, 454-464.
6. R. Dimitriou, E. Jones, D. McGonagle and P. V. Giannoudis, BMC medicine, 2011, Bone regeneration: current concepts and future directions, 9, 1-10.
7. P. Kumar, B. S. Dehiya and A. Sindhu, Int. J. Appl. Eng. Res, 2018, Bioceramics for hard tissue engineering applications: A review, 13, 2744-2752.
8. Y. C. Chai, A. Carlier, J. Bolander, S. J. Roberts, L. Geris, J. Schrooten, H. Van Oosterwyck and F. P. Luyten, Acta Biomater., 2012, Current views on calcium phosphate osteogenicity and the translation into effective bone regeneration strategies, 8, 3876-3887.
9. A. Hasan, B. Byambaa, M. Morshed, M. I. Cheikh, R. A. Shakoor, T. Mustafy and H. E. Marei, J. Tissue Eng. Regener. Med., 2018, Advances in osteobiologic materials for bone substitutes, 12, 1448-1468.
10. C. Mao, X. Chen, G. Miao and C. Lin, Biomed. Mater., 2015, Angiogenesis stimulated by novel nanoscale bioactive glasses, 10, 025005.
11. A. A. Gorustovich, J. A. Roether and A. R. Boccaccini, Tissue Eng. Part B Rev., 2010, Effect of bioactive glasses on angiogenesis: a review of *in vitro* and *in vivo* evidences, 16, 199-207.
12. S. J. Kalita, A. Bhardwaj and H. A. Bhatt, Mater. Sci. Eng., C, 2007, Nanocrystalline calcium phosphate ceramics in biomedical engineering, 27, 441-449.
13. A. Z. Wilczewska, K. Niemirowicz, K. H. Markiewicz and H. Car, Pharmacol. Rep., 2012, Nanoparticles as drug delivery systems, 64, 1020-1037.
14. A. H. Faraji and P. Wipf, Bioorg. Med. Chem, 2009, Nanoparticles in cellular drug delivery, 17, 2950-2962.
15. V. M. Schatkoski, T. L. do Amaral Montanheiro, B. R. C. de Menezes, R. M. Pereira, K. F. Rodrigues, R. G. Ribas, D. M. da Silva and G. P. Thim, Ceram. Int., 2021,Current advances concerning the most cited metal ions doped bioceramics and silicate-based bioactive glasses for bone tissue engineering, 47, 2999-3012.
16. S. Bose, G. Fielding, S. Tarafder and A. Bandyopadhyay, Trends Biotechnol., 2013,Understanding of dopant-induced osteogenesis and angiogenesis in calcium phosphate ceramics, 31, 594-605.
17. Z. Saidak and P. J. Marie, Pharmacol. Ther., 2012, Strontium signaling: molecular mechanisms and therapeutic implications in osteoporosis, 136, 216-226.

18. A. A. Gorustovich, T. Steimetz, R. L. Cabrini and J. M. Porto López, J Biomed Mater Res A, 2010, Osteoconductivity of strontium-doped bioactive glass particles: a histomorphometric study in rats, 92, 232-237.
19. E. Gentleman, Y. C. Fredholm, G. Jell, N. Lotfibakhshaiesh, M. D. O'Donnell, R. G. Hill and M. M. Stevens, Biomaterials, 2010, The effects of strontium-substituted bioactive glasses on osteoblasts and osteoclasts *in vitro*, 31, 3949-3956.
20. J. P. O'Connor, D. Kanjilal, M. Teitelbaum, S. S. Lin and J. A. Cottrell, Materials, 2020, Zinc as a therapeutic agent in bone regeneration, 13, 2211.
21. E. M. Lewiecki and P. D. Miller, J Clin Densitom, 2013, Skeletal effects of primary hyperparathyroidism: bone mineral density and fracture risk, 16, 28-32.
22. M. Ziche, J. Jones and P. M. Gullino, J. Natl. Cancer Inst., 1982, Role of prostaglandin E1 and copper in angiogenesis, 69, 475-482.
23. G. f. Hu, J. Cell. Biochem., 1998, Copper stimulates proliferation of human endothelial cells under culture, 69, 326-335.
24. C. Gérard, L.-J. Bordeleau, J. Barralet and C. J. Doillon, Biomaterials, 2010, The stimulation of angiogenesis and collagen deposition by copper, 31, 824-831.
25. C. Giacomelli, M. L. Trincavelli, C. Satriano, Ö. Hansson, D. La Mendola, E. Rizzarelli and C. Martini, Int. J. Biochem. Cell Biol., 2015, Copper (II) ions modulate Angiogenin activity in human endothelial cells, 60, 185-196.
26. Y. Cai, Y. Liu, W. Yan, Q. Hu, J. Tao, M. Zhang, Z. Shi and R. Tang, J. Mater. Chem., 2007, Role of hydroxyapatite nanoparticle size in bone cell proliferation, 17, 3780-3787.
27. Z. Shi, X. Huang, Y. Cai, R. Tang and D. Yang, Acta Biomater., 2009, Size effect of hydroxyapatite nanoparticles on proliferation and apoptosis of osteoblast-like cells, 5, 338-345.
28. N. Li, G. Wu, H. Yao, R. Tang, X. Gu and C. Tu, Dent. Mater. J., 2019, Size effect of nano-hydroxyapatite on proliferation of odontoblast-like MDPC-23 cells, 38, 534-539.
29. X. Yang, Y. Li, X. Liu, R. Zhang and Q. Feng, Stem Cells Int., 2018, *In vitro* uptake of hydroxyapatite nanoparticles and their effect on osteogenic differentiation of human mesenchymal stem cells, 2018.
30. T. Matsumoto, M. Okazaki, M. Inoue, S. Yamaguchi, T. Kusunose, T. Toyonaga, Y. Hamada and J. Takahashi, Biomaterials, 2004, Hydroxyapatite particles as a controlled release carrier of protein, 25, 3807-3812.
31. B. Feng, J. Weng, B. Yang, S. Qu and X. Zhang, Biomaterials, 2004, Characterization of titanium surfaces with calcium and phosphate and osteoblast adhesion, 25, 3421-3428.
32. Q. Hu, Z. Tan, Y. Liu, J. Tao, Y. Cai, M. Zhang, H. Pan, X. Xu and R. Tang, J. Mater. Chem., 2007, Effect of crystallinity of calcium phosphate nanoparticles on adhesion, proliferation, and differentiation of bone marrow mesenchymal stem cells, 17, 4690-4698.
33. A. Fomin, S. Barinov, V. Ievlev, V. Smirnov, B. Mikhailov, E. Belonogov and N. Drozdova, Dock. Chem., 2008, Nanocrystalline hydroxyapatite ceramics produced by low-temperature sintering after high-pressure treatment, 418, 22-25.
34. K. Prakash, R. Kumar, C. Ooi, P. Cheang and K. A. Khor, J. Phys. Chem. B, 2006, Conductometric study of precursor compound formation during wet-chemical synthesis of nanocrystalline hydroxyapatite, 110, 24457-24462.
35. C. Manuel, M. Ferraz and F. Monteiro, Key Eng. Mater., 2003, Synthesis of hydroxyapatite and tricalcium phosphate nanoparticles–preliminary studies, 240, 555-558.

36. K. Ishikawa, E. Garskaite and A. Kareiva, J. Sci. Technol., 2020, Sol–gel synthesis of calcium phosphate-based biomaterials—A review of environmentally benign, simple, and effective synthesis routes, 94, 551-572.
37. J. Xu, K. A. Khor, Z. Dong, Y. Gu, R. Kumar and P. Cheang, Mater. Sci. Eng., A, 2004, Preparation and characterization of nano-sized hydroxyapatite powders produced in a radio frequency (rf) thermal plasma, 374, 101-108.
38. R. R. Rao, H. Roopa and T. Kannan, J. Mater. Sci.: Mater. Med., 1997, Solid state synthesis and thermal stability of HAP and HAP–β-TCP composite ceramic powders, 8, 511-518.
39. M. Ferraz, F. Monteiro and C. Manuel, J. Appl. Biomate. Biomech., 2004, Hydroxyapatite nanoparticles: a review of preparation methodologies, 2, 74-80.
40. B. Fowler, Inorg. Chem., 1974, Infrared studies of apatites. II. Preparation of normal and isotopically substituted calcium, strontium, and barium hydroxyapatites and spectra-structure-composition correlations, 13, 207-214.
41. I. S. Trakhtenberg, A. Rubshtein, E. Volkova, S. Petrova, A. Y. Fishman, R. Zakharov, V. Vykhodets and T. Kurennykh, Inorg. Mater., 2011, Effect of mechanical activation on the morphology and structure of hydroxyapatite, 47, 45-50.
42. M. Otsuka, Y. Matsuda, J. Hsu, J. L. Fox and W. I. Higuchi, Biomater. Biomed. Eng., 1994, Mechanochemical synthesis of bioactive material: Effect of environmental conditions on the phase transformation of calcium phosphates during grinding, 4, 357-362.
43. H. E. Briak-BenAbdeslam, C. Mochales, M. P. Ginebra, J. Nurit, J. A. Planell and P. Boudeville, J Biomed Mater Res A, 2003, Dry mechanochemical synthesis of hydroxyapatites from dicalcium phosphate dihydrate and calcium oxide: A kinetic study, 67, 927-937.
44. K. Lin, J. Pan, Y. Chen, R. Cheng and X. Xu, J Hazard. Matter., 2009, Study the adsorption of phenol from aqueous solution on hydroxyapatite nanopowders, 161, 231-240.
45. S. Manafi and M. R. Rahimipour, Chem Eng Technol, 2011, Synthesis of nanocrystalline hydroxyapatite nanorods via hydrothermal conditions, 34, 972-976.
46. C. Qi, Q.-L. Tang, Y.-J. Zhu, X.-Y. Zhao and F. Chen, Mater. Lett., 2012, Microwave-assisted hydrothermal rapid synthesis of hydroxyapatite nanowires using adenosine 5'-triphosphate disodium salt as phosphorus source, 85, 71-73.
47. X. Lu, Y.-b. Wang, J.-x. Wang, S.-x. Qu, J. Weng, R.-l. Xin and Y. Leng, J. Cryst. Growth, 2006, Calcium phosphate crystal growth under controlled environment through urea hydrolysis, 297, 396-402.
48. H. Zhang and B. W. Darvell, Acta Biomater., 2011, Morphology and structural characteristics of hydroxyapatite whiskers: effect of the initial Ca concentration, Ca/P ratio and pH, 7, 2960-2968.
49. Y. Shen, J. Liu, K. Lin and W. Zhang, Mater. Lett., 2012, Synthesis of strontium substituted hydroxyapatite whiskers used as bioactive and mechanical reinforcement material, 70, 76-79.
50. R. Xin, F. Ren and Y. Leng, Mater. Des., 2010, Synthesis and characterization of nano-crystalline calcium phosphates with EDTA-assisted hydrothermal method, 31, 1691-1694.

51. K. Lin, J. Chang, R. Cheng and M. Ruan, Mater. Lett., 2007, Hydrothermal microemulsion synthesis of stoichiometric single crystal hydroxyapatite nanorods with mono-dispersion and narrow-size distribution, 61, 1683-1687.

52. X. Wang, J. Zhuang, Q. Peng and Y. Li, Adv. Mater., 2006, Liquid–solid–solution synthesis of biomedical hydroxyapatite nanorods, 18, 2031-2034.

53. K. Lin, J. Chang, X. Liu, L. Chen and Y. Zhou, Cryst. Eng. Comm., 2011, Synthesis of element-substituted hydroxyapatite with controllable morphology and chemical composition using calcium silicate as precursor, 13, 4850-4855.

54. K. Lin, X. Liu, J. Chang and Y. Zhu, Nanoscale, 2011, Facile synthesis of hydroxyapatite nanoparticles, nanowires and hollow nano-structured microspheres using similar structured hard-precursors, 3, 3052-3055.

55. E. García-Tuñon, J. Franco, S. Eslava, V. Bhakhri, E. Saiz, F. Giuliani and F. Guitián, J. Am. Ceram. Soc., 2013, Synthesis and Optimization of the Production of Millimeter-Sized Hydroxyapatite Single Crystals by Cl−–OH− Ion Exchange, 96, 759-765.

56. A. C. Taş, J. Am. Ceram. Soc., 2001, Molten salt synthesis of calcium hydroxyapatite whiskers, 84, 295-300.

57. K. Teshima, H. Wagata, K. Sakurai, H. Enomoto, S. Mori, K. Yubuta, T. Shishido and S. Oishi, Cryst. Growth Des., 2012, High-quality ultralong hydroxyapatite nanowhiskers grown directly on titanium surfaces by novel low-temperature flux coating method, 12, 4890-4896.

58. K. Lin, C. Wu and J. Chang, Acta Biomater., 2014, Advances in synthesis of calcium phosphate crystals with controlled size and shape, 10, 4071-4102.

59. M. Bohner, S. Tadier, N. van Garderen, A. de Gasparo, N. Döbelin and G. Baroud, Biomatter, 2013, Synthesis of spherical calcium phosphate particles for dental and orthopedic applications, 3, e25103.

60. A. Choi, B. Ben-Nissan, J. Matinlinna and R. Conway, J. Dent. Res., 2013, Current perspectives: calcium phosphate nanocoatings and nanocomposite coatings in dentistry, 92, 853-859.

61. L. Cheng, S. M. Zhang, P. Chen, S. Huang, R. R. Cao, W. Zhou, J. Liu, Q. Luo and H. Gong, Key Eng. Mater., 2006,Fabrication and characterization of nano-hydroxyapatite/poly (D, L-lactide) composite porous scaffolds for human cartilage tissue engineering, 309, 943-948.

62. A. Tabaković, M. Kester and J. H. Adair, Wiley Interdiscip. Rev. Nanomed. Nanobiotechnol., 2012, Calcium phosphate-based composite nanoparticles in bioimaging and therapeutic delivery applications, 4, 96-112.

63. M. Yousefpour, A. Afshar, X. Yang, X. Li, B. Yang, Y. Wu, J. Chen and X. Zhang, J. Electroanal. Chem., 2006, Nano-crystalline growth of electrochemically deposited apatite coating on pure titanium, 589, 96-105.

64. Y. Han, K. Xu, G. Montay, T. Fu and J. Lu, J. Biomed. Mater. Res., 2002, Evaluation of nanostructured carbonated hydroxyapatite coatings formed by a hybrid process of plasma spraying and hydrothermal synthesis, 60, 511-516.

65. P. Li, J Biomed Mater Res A, 2003, Biomimetic nano-apatite coating capable of promoting bone ingrowth, 66, 79-85.

66. D. V. Vasudev, J. L. Ricci, C. Sabatino, P. Li and J. R. Parsons, J Biomed Mater Res A, 2004, *In vivo* evaluation of a biomimetic apatite coating grown on titanium surfaces, 69, 629-636.

67. J. Yazdani, E. Ahmadian, S. Sharifi, S. Shahi and S. M. Dizaj, Biomed. Pharmacother., 2018, A short view on nanohydroxyapatite as coating of dental implants, 105, 553-557.

68. K. Breding, R. Jimbo, M. Hayashi, Y. Xue, K. Mustafa and M. Andersson, Int. J. Dent., 2014, The effect of hydroxyapatite nanocrystals on osseointegration of titanium implants: an *in vivo* rabbit study, 2014.

69. M. He, Y. Huang, H. Xu, G. Feng, L. Liu, Y. Li, D. Sun and L. Zhang, Acta Biomater., 2021, Modification of polyetheretherketone implants: From enhancing bone integration to enabling multi-modal therapeutics, 129, 18-32.

70. B. Aksakal, M. Kom, H. Tosun and M. Demirel, Eur. J. Orthop., 2014, Influence of micro-and nano-hydroxyapatite coatings on the osteointegration of metallic (Ti6Al4 V) and bioabsorbable interference screws: an *in vivo* study, 24, 813-819.

71. J. Luo, M. Walker, Y. Xiao, H. Donnelly, M. J. Dalby and M. Salmeron-Sanchez, Bioact. Mater., 2021, The influence of nanotopography on cell behaviour through interactions with the extracellular matrix–A review.

72. J. Xu, K. A. Khor, J. Sui, J. Zhang and W. N. Chen, Biomaterials, 2009, Protein expression profiles in osteoblasts in response to differentially shaped hydroxyapatite nanoparticles, 30, 5385-5391.

73. P. Sutthavas, P. Habibovic and S. H. van Rijt, Biomater. Sci., 2021, The shape-effect of calcium phosphate nanoparticle based films on their osteogenic properties, 9, 1754-1766.

74. F.-X. Huber, N. McArthur, J. Hillmeier, H. J. Kock, M. Baier, M. Diwo, I. Berger and P. J. Meeder, Arch Orthop Trauma Surg. , 2006, Void filling of tibia compression fracture zones using a novel resorbable nanocrystalline hydroxyapatite paste in combination with a hydroxyapatite ceramic core: first clinical results, 126, 533-540.

75. M.-P. Ginebra, T. Traykova and J. A. Planell, J Control Release, 2006, Calcium phosphate cements as bone drug delivery systems: a review, 113, 102-110.

76. Z. H. Mok, P. Mylonas, R. Austin, G. Proctor, N. Pitts and M. Thanou, Nanoscale, 2021, Calcium phosphate nanoparticles for potential application as enamel remineralising agent tested on hydroxyapatite discs, 13, 20002-20012.

77. Z. Wang, Z. Tang, F. Qing, Y. Hong and X. Zhang, Nano, 2012, Applications of calcium phosphate nanoparticles in porous hard tissue engineering scaffolds, 7, 1230004.

78. P. Wang, L. Zhao, J. Liu, M. D. Weir, X. Zhou and H. H. Xu, Bone Res., 2014, Bone tissue engineering via nanostructured calcium phosphate biomaterials and stem cells, 2, 1-13.

79. Q. Wu, W.-s. Miao, H.-j. Gao and D. Hui, Nanotechnol. Rev., 2020, Mechanical properties of nanomaterials: A review, 9, 259-273.

80. A. Stanishevsky, S. Chowdhury, P. Chinoda and V. Thomas, J Biomed Mater Res A, 2008, Hydroxyapatite nanoparticle loaded collagen fiber composites: microarchitecture and nanoindentation study, 86, 873-882.

81. A. K. Gaharwar, S. A. Dammu, J. M. Canter, C.-J. Wu and G. Schmidt, Biomacromolecules, 2011, Highly extensible, tough, and elastomeric nanocomposite hydrogels from poly (ethylene glycol) and hydroxyapatite nanoparticles, 12, 1641-1650.

82. K. Madhumathi, Y. Rubaiya, M. Doble, R. Venkateswari and T. Sampath Kumar, Drug Deliv. Transl. Res., 2018, Antibacterial, anti-inflammatory, and bone-regenerative dual-drug-loaded calcium phosphate nanocarriers—*in vitro* and *in vivo* studies, 8, 1066-1077.

83. G. Xie, J. Sun, G. Zhong, C. Liu and J. Wei, J. Mater. Sci.: Mater. Med., 2010, Hydroxyapatite nanoparticles as a controlled-release carrier of BMP-2: absorption and release kinetics *in vitro*, 21, 1875-1880.

84. R. Mukherjee, M. Patra, D. Dutta, M. Banik and T. Basu, Biochim Biophys Acta Gen Subj, 2016, Tetracycline-loaded calcium phosphate nanoparticle (Tet-CPNP): rejuvenation of an obsolete antibiotic to further action, 1860, 1929-1941.

85. D. Tadic, T. Welzel, P. Seidel, E. Wüst, E. Dingeldein and M. Epple, Materialwissenschaft und Werkstofftechnik, 2004, Controlled release of gentamicin from biomimetic calcium phosphate *in vitro*. Comparison of four different incorporation methods, 35, 1001-1005.

86. G. Hulsart-Billström, Q. Hu, K. Bergman, K. B. Jonsson, J. Åberg, R. Tang, S. Larsson and J. Hilborn, Acta Biomater., 2011, Calcium phosphates compounds in conjunction with hydrogel as carrier for BMP-2: a study on ectopic bone formation in rats, 7, 3042-3049.

87. E. Wernike, M.-O. Montjovent, Y. Liu, D. Wismeijer, E. B. Hunziker, K.-A. Siebenrock, W. Hofstetter and F. M. Klenke, Eur Cell Mater, 2010, VEGF incorporated into calcium phosphate ceramics promotes vascularisation and bone formation *in vivo*, 19.

88. H. Jung, S. A. Kim, Y. G. Yang, H. Yoo, S.-J. Lim and H. Mok, Arch. Pharmacal Res. , 2015, Long chain microRNA conjugates in calcium phosphate nanoparticles for efficient formulation and delivery, 38, 705-715.

89. D. Olton, J. Li, M. E. Wilson, T. Rogers, J. Close, L. Huang, P. N. Kumta and C. Sfeir, Biomaterials, 2007, Nanostructured calcium phosphates (NanoCaPs) for non-viral gene delivery: influence of the synthesis parameters on transfection efficiency, 28, 1267-1279.

90. C. M. Curtin, G. M. Cunniffe, F. G. Lyons, K. Bessho, G. R. Dickson, G. P. Duffy and F. J. O'Brien, Adv. Mater., 2012, Innovative collagen nano-hydroxyapatite scaffolds offer a highly efficient non-viral gene delivery platform for stem cell-mediated bone formation, 24, 749-754.

91. I. Roy, S. Mitra, A. Maitra and S. Mozumdar, Int. J. Pharm. , 2003, Calcium phosphate nanoparticles as novel non-viral vectors for targeted gene delivery, 250, 25-33.

92. F. Bakan, Hydroxyapatite-Advances in Composite Nanomaterials, Biomedical Applications and Its Technological Facets, 2018, Gene delivery by hydroxyapatite and calcium phosphate nanoparticles: a review of novel and recent applications, 157-176.

93. T. J. Levingstone, S. Herbaj, J. Redmond, H. O. McCarthy and N. J. Dunne, Nanomaterials, 2020, Calcium phosphate nanoparticles-based systems for RNAi delivery: Applications in bone tissue regeneration, 10, 146.

94. B. Palazzo, M. Iafisco, M. Laforgia, N. Margiotta, G. Natile, C. L. Bianchi, D. Walsh, S. Mann and N. Roveri, Adv. Funct. Mater., 2007, Biomimetic hydroxyapatite–drug nanocrystals as potential bone substitutes with antitumor drug delivery properties, 17, 2180-2188.

95. V. Uskoković and D. P. Uskoković, J. Biomed. Mater. Res. B, 2011, Nanosized hydroxyapatite and other calcium phosphates: chemistry of formation and application as drug and gene delivery agents, 96, 152-191.

96. M. Iafisco, B. Palazzo, M. Marchetti, N. Margiotta, R. Ostuni, G. Natile, M. Morpurgo, V. Gandin, C. Marzano and N. Roveri, J. Mater. Chem., 2009, Smart delivery of antitumoral platinum complexes from biomimetic hydroxyapatite nanocrystals, 19, 8385-8392.

97. V. Mourino, J. P. Cattalini and A. R. Boccaccini, J R Soc Interface, 2012, Metallic ions as therapeutic agents in tissue engineering scaffolds: an overview of their biological applications and strategies for new developments, 9, 401-419.

98. E. Hughes, T. Yanni, P. Jamshidi and L. Grover, Adv. Appl. Ceram., 2015, Inorganic cements for biomedical application: calcium phosphate, calcium sulphate and calcium silicate, 114, 65-76.

99. J. Li, X. Liu, S. Park, A. L. Miller, A. Terzic and L. Lu, J. Biomed. Mater. Res. A, 2019, Strontium-substituted hydroxyapatite stimulates osteogenesis on poly (propylene fumarate) nanocomposite scaffolds, 107, 631-642.

100. M. Frasnelli, F. Cristofaro, V. M. Sglavo, S. Dirè, E. Callone, R. Ceccato, G. Bruni, A. I. Cornaglia and L. Visai, Mater. Sci. Eng., C, 2017, Synthesis and characterization of strontium-substituted hydroxyapatite nanoparticles for bone regeneration, 71, 653-662.

101. Z. Geng, Z. Cui, Z. Li, S. Zhu, Y. Liang, Y. Liu, X. Li, X. He, X. Yu and R. Wang, Mater. Sci. Eng., C, 2016, Strontium incorporation to optimize the antibacterial and biological characteristics of silver-substituted hydroxyapatite coating, 58, 467-477.

102. M. H. Fernandes, M. M. Alves, M. Cebotarenco, I. A. Ribeiro, L. Grenho, P. S. Gomes, M. J. Carmezim and C. F. Santos, Mater. Sci. Eng., C, 2020, Citrate zinc hydroxyapatite nanorods with enhanced cytocompatibility and osteogenesis for bone regeneration, 115, 111147.

103. K. Sahithi, M. Swetha, M. Prabaharan, A. Moorthi, N. Saranya, K. Ramasamy, N. Srinivasan, N. Partridge and N. Selvamurugan, J. Biomed. Nanotechnol., 2010, Synthesis and characterization of nanoscalehydroxyapatite-copper for antimicrobial activity towards bone tissue engineering applications, 6, 333-339.

104. E. Boanini, M. Gazzano and A. Bigi, Acta Biomater., 2010, Ionic substitutions in calcium phosphates synthesized at low temperature, 6, 1882-1894.

105. R. Rosenbrand, D. Barata, P. Sutthavas, R. Mohren, B. Cillero-Pastor, P. Habibovic and S. van Rijt, Int. J. Nanomed., 2018, Lipid surface modifications increase mesoporous silica nanoparticle labeling properties in mesenchymal stem cells, 13, 7711.

106. C. L. Popa, A. Deniaud, I. Michaud-Soret, R. Guégan, M. Motelica-Heino and D. Predoi, J. Nanomater., 2016, Structural and biological assessment of zinc doped hydroxyapatite nanoparticles, 2016.

107. J. R. Jones, D. S. Brauer, L. Hupa and D. C. Greenspan, Int. J. Appl. Glass Sci., 2016, Bioglass and bioactive glasses and their impact on healthcare, 7, 423-434.

108. C. Covarrubias, F. Arroyo, C. Balanda, M. Neira, A. Von Marttens, P. Caviedes, J. P. Rodríguez and C. Urra, J. Nanomater., 2015, The effect of the nanoscale structure of nanobioceramics on their *in vitro* bioactivity and cell differentiation properties, 2015.

109. F. Westhauser, S. Wilkesmann, Q. Nawaz, F. Hohenbild, F. Rehder, M. Saur, J. Fellenberg, A. Moghaddam, M. S. Ali and W. Peukert, J. Biomed. Mater. Res. A, 2021, Effect of manganese, zinc, and copper on the biological and osteogenic properties of mesoporous bioactive glass nanoparticles, 109, 1457-1467.

110. H. Sun, K. Zheng, T. Zhou and A. R. Boccaccini, Pharm., 2021, Incorporation of zinc into binary SiO2-CaO mesoporous bioactive glass nanoparticles enhances anti-inflammatory and osteogenic activities, 13, 2124.

111. M. Shi, Y. Zhou, J. Shao, Z. Chen, B. Song, J. Chang, C. Wu and Y. Xiao, Acta Biomater., 2015, Stimulation of osteogenesis and angiogenesis of hBMSCs by delivering Si ions and functional drug from mesoporous silica nanospheres, 21, 178-189.

112. W. Stöber, A. Fink and E. Bohn, J. Colloid Interface Sci., 1968, Controlled growth of monodisperse silica spheres in the micron size range, 26, 62-69.

113. M. Schumacher, P. Habibovic and S. van Rijt, Bioact. Mater., 2021, Mesoporous bioactive glass composition effects on degradation and bioactivity, 6, 1921-1931.

114. S. L. Greasley, S. J. Page, S. Sirovica, S. Chen, R. A. Martin, A. Riveiro, J. V. Hanna, A. E. Porter and J. R. Jones, J. Colloid Interface Sci., 2016, Controlling particle size in the Stöber process and incorporation of calcium, 469, 213-223.

115. A. Lukowiak, J. Lao, J. Lacroix and J.-M. Nedelec, Chem. Commun., 2013, Bioactive glass nanoparticles obtained through sol–gel chemistry, 49, 6620-6622.

116. M. Bini, S. Grandi, D. Capsoni, P. Mustarelli, E. Saino and L. Visai, J. Phys. Chem. C, 2009, SiO2− P2O5− CaO glasses and glass-ceramics with and without ZnO: relationships among composition, microstructure, and bioactivity, 113, 8821-8828.

117. V. Aina, G. Cerrato, G. Martra, G. Malavasi, G. Lusvardi and L. Menabue, Appl. Surf. Sci., 2013, Towards the controlled release of metal nanoparticles from biomaterials: Physico-chemical, morphological and bioactivity features of Cu-containing sol–gel glasses, 283, 240-248.

118. S. Watts, R. Hill, M. O'donnell and R. Law, J. Non-Cryst. Solids, 2010, Influence of magnesia on the structure and properties of bioactive glasses, 356, 517-524.

119. A. M. El-Kady and A. F. Ali, Ceram. Int., 2012, Fabrication and characterization of ZnO modified bioactive glass nanoparticles, 38, 1195-1204.

120. Y. C. Fredholm, N. Karpukhina, R. V. Law and R. G. Hill, J. Non-Cryst. Solids, 2010, Strontium containing bioactive glasses: glass structure and physical properties, 356, 2546-2551.

121. K. Boldbaatar, K. Dashnyam, J. C. Knowles, H.-H. Lee, J.-H. Lee and H.-W. Kim, Acta Biomater., 2019, Dual-ion delivery for synergistic angiogenesis and bactericidal capacity with silica-based microsphere, 83, 322-333.

122. M. S. Kang, N.-H. Lee, R. K. Singh, N. Mandakhbayar, R. A. Perez, J.-H. Lee and H.-W. Kim, Biomaterials, 2018, Nanocements produced from mesoporous bioactive glass nanoparticles, 162, 183-199.

123. Q. Zhang, Y. Zhang, W. Chen, B. Zhang and S. Wang, Exp. Ther. Med., 2013, Long-term controlled release of 125I-tagged BMP-2 by mesoporous bioactive glass with ordered nanopores, 6, 1443-1448.

124. C. Wu and J. Chang, J Control Release, 2014, Multifunctional mesoporous bioactive glasses for effective delivery of therapeutic ions and drug/growth factors, 193, 282-295.

125. C. Wu, R. Miron, A. Sculean, S. Kaskel, T. Doert, R. Schulze and Y. Zhang, Biomaterials, 2011, Proliferation, differentiation and gene expression of osteoblasts in boron-containing associated with dexamethasone deliver from mesoporous bioactive glass scaffolds, 32, 7068-7078.

126. A. El-Fiqi, T.-H. Kim, M. Kim, M. Eltohamy, J.-E. Won, E.-J. Lee and H.-W. Kim, Nanoscale, 2012, Capacity of mesoporous bioactive glass nanoparticles to deliver therapeutic molecules, 4, 7475-7488.

127. C. H. Kong, C. Steffi, Z. Shi and W. Wang, J. Biomed. Mater. Res. B, 2018, Development of mesoporous bioactive glass nanoparticles and its use in bone tissue engineering, 106, 2878-2887.

128. V. Lalzawmliana, A. Anand, M. Roy, B. Kundu and S. K. Nandi, Mater. Sci. Eng., C, 2020, Mesoporous bioactive glasses for bone healing and biomolecules delivery, 106, 110180.

129. A. El-Fiqi, J.-H. Kim and H.-W. Kim, ACS Appl. Mater. Interfaces, 2015, Osteoinductive fibrous scaffolds of biopolymer/mesoporous bioactive glass nanocarriers with excellent bioactivity and long-term delivery of osteogenic drug, 7, 1140-1152.

130. A. M. El-Kady, M. M. Farag and A. M. El-Rashedi, Eur. J. Pharm. Sci., 2016, Bioactive glass nanoparticles designed for multiple deliveries of lithium ions and drugs: curative and restorative bone treatment, 91, 243-250.

131. A. H. Taghvaei, F. Danaeifar, C. Gammer, J. Eckert, S. Khosravimelal and M. Gholipourmalekabadi, Microporous Mesoporous Mater., 2020, Synthesis and characterization of novel mesoporous strontium-modified bioactive glass nanospheres for bone tissue engineering applications, 294, 109889.

132. X. Li, L. Zhao, Q. Liang, J. Ye, N. Komatsu, Q. Zhang, W. Gao, M. Xu and X. Chen, J. Biomed. Nanotechnol., 2017, Cationic polyarginine conjugated mesoporous bioactive glass nanoparticles with polyglycerol coating for efficient DNA delivery, 13, 280-289.

133. T.-H. Kim, R. K. Singh, M. S. Kang, J.-H. Kim and H.-W. Kim, Acta Biomater., 2016, Inhibition of osteoclastogenesis through siRNA delivery with tunable mesoporous bioactive nanocarriers, 29, 352-364.

134. X. Li, X. Chen, G. Miao, H. Liu, C. Mao, G. Yuan, Q. Liang, X. Shen, C. Ning and X. Fu, J. Mater. Chem. B, 2014, Synthesis of radial mesoporous bioactive glass particles to deliver osteoactivin gene, 2, 7045-7054.

135. T.-H. Kim, R. K. Singh, M. S. Kang, J.-H. Kim and H.-W. Kim, Nanoscale, 2016, Gene delivery nanocarriers of bioactive glass with unique potential to load BMP2 plasmid DNA and to internalize into mesenchymal stem cells for osteogenesis and bone regeneration, 8, 8300-8311.

136. J. Luo, Y. Ling, X. Li, B. Yuan, F. Yu, W. Xie and X. Chen, Rsc Advances, 2015, Combining amphiphilic chitosan and bioglass for mediating cellular osteogenic growth peptide gene, 5, 79239-79248.

137. A. Hoppe, N. S. Güldal and A. R. Boccaccini, Biomaterials, 2011, A review of the biological response to ionic dissolution products from bioactive glasses and glass-ceramics, 32, 2757-2774.

138. Z.-M. Xiu, J. Ma and P. J. Alvarez, Environ. Sci. Technol., 2011, Differential effect of common ligands and molecular oxygen on antimicrobial activity of silver nanoparticles versus silver ions, 45, 9003-9008.

139. D. He, A. M. Jones, S. Garg, A. N. Pham and T. D. Waite, J. Phys. Chem. C, 2011, Silver nanoparticle− reactive oxygen species interactions: application of a charging−discharging model, 115, 5461-5468.

140. K. Zheng, P. Balasubramanian, T. E. Paterson, R. Stein, S. MacNeil, S. Fiorilli, C. Vitale-Brovarone, J. Shepherd and A. R. Boccaccini, Mater. Sci. Eng., C, 2019, Ag modified mesoporous bioactive glass nanoparticles for enhanced antibacterial activity in 3D infected skin model, 103, 109764.

141. S. J. Shih, W. L. Tzeng, R. Jatnika, C. J. Shih and K. B. Borisenko, J. Biomed. Mater. Res. B, 2015, Control of Ag nanoparticle distribution influencing bioactive and antibacterial properties of Ag-doped mesoporous bioactive glass particles prepared by spray pyrolysis, 103, 899-907.

142. A. Nawaz, S. Bano, M. Yasir, A. Wadood and M. A. U. Rehman, Mater. Adv., 2020, Ag and Mn-doped mesoporous bioactive glass nanoparticles incorporated into the chitosan/gelatin coatings deposited on PEEK/bioactive glass layers for favorable osteogenic differentiation and antibacterial activity, 1, 1273-1284.

143. A. Pedone, F. Muniz-Miranda, A. Tilocca and M. C. Menziani, Biomed. Glass., 2016, The antioxidant properties of Ce-containing bioactive glass nanoparticles explained by Molecular Dynamics simulations, 2.

144. A. Pinna, M. T. Baghbaderani, V. V. Hernández, P. Naruphontjirakul, S. Li, T. McFarlane, D. Hachim, M. M. Stevens, A. E. Porter and J. R. Jones, Acta Biomater., 2021, Nanoceria provides antioxidant and osteogenic properties to mesoporous silica nanoparticles for osteoporosis treatment, 122, 365-376.

145. F. Kurtuldu, H. Kaňková, A. Beltrán, L. Liverani, D. Galusek and A. R. Boccaccini, Mater. Today Bio, 2021, Anti-inflammatory and antibacterial activities of cerium-containing mesoporous bioactive glass nanoparticles for drug-free biomedical applications, 12, 100150.

146. J. Han, N. Hassani Besheli, D. Deng, B. A. van Oirschot, S. C. Leeuwenburgh and F. Yang, Tissue Eng. Part C: Methods, 2022, Tailoring Copper-Doped Bioactive Glass/Chitosan Coatings with Angiogenic and Antibacterial Properties.

147. L. B. Romero-Sánchez, M. Marí-Beffa, P. Carrillo, M. Á. Medina and A. Díaz-Cuenca, Acta Biomater., 2018, Copper-containing mesoporous bioactive glass promotes angiogenesis in an *in vivo* zebrafish model, 68, 272-285.

148. S. Fiorilli, G. Molino, C. Pontremoli, G. Iviglia, E. Torre, C. Cassinelli, M. Morra and C. Vitale-Brovarone, Materials, 2018, The incorporation of strontium to improve bone-regeneration ability of mesoporous bioactive glasses, 11, 678.

149. M. Yamaguchi, J. trace elem. exp. med., 1998, Role of zinc in bone formation and bone resorption, 11, 119-135.

150. F. H. Nielsen, Nutrition, 2000, The emergence of boron as nutritionally important throughout the life cycle, 16, 512-514.

151. E. Álvarez, B. González, D. Lozano, A. L. Doadrio, M. Colilla and I. Izquierdo-Barba, Pharm., 2021, Nanoantibiotics Based in Mesoporous Silica Nanoparticles: New Formulations for Bacterial Infection Treatment, 13, 2033.

152. G. S. Attard, J. C. Glyde and C. G. Göltner, Nature, 1995, Liquid-crystalline phases as templates for the synthesis of mesoporous silica, 378, 366-368.

153. A. E. Danks, S. R. Hall and Z. Schnepp, Mater. Horiz., 2016, The evolution of 'sol–gel'chemistry as a technique for materials synthesis, 3, 91-112.

154. Y. Wang, Q. Zhao, N. Han, L. Bai, J. Li, J. Liu, E. Che, L. Hu, Q. Zhang and T. Jiang, Nanomed. Nanotechnol. Biol. Med., 2015, Mesoporous silica nanoparticles in drug delivery and biomedical applications, 11, 313-327.
155. C. X. C. Lin, S. Z. Qiao, C. Z. Yu, S. Ismadji and G. Q. M. Lu, Microporous Mesoporous Mater., 2009, Periodic mesoporous silica and organosilica with controlled morphologies as carriers for drug release, 117, 213-219.
156. E. Aznar, M. Oroval, L. Pascual, J. R. Murguía, R. Martinez-Manez and F. Sancenon, Chem. Rev., 2016, Gated materials for on-command release of guest molecules, 116, 561-718.
157. Y.-K. Peng, Y.-J. Tseng, C.-L. Liu, S.-W. Chou, Y.-W. Chen, S. E. Tsang and P.-T. Chou, Nanoscale, 2015, One-step synthesis of degradable T 1-FeOOH functionalized hollow mesoporous silica nanocomposites from mesoporous silica spheres, 7, 2676-2687.
158. L. Yu, Y. Chen, H. Lin, S. Gao, H. Chen and J. Shi, Small, 2018, Magnesium-engineered silica framework for pH-accelerated biodegradation and DNAzyme-triggered chemotherapy, 14, 1800708.
159. C. Liu, D. Wang, S. Zhang, Y. Cheng, F. Yang, Y. Xing, T. Xu, H. Dong and X. Zhang, ACS nano, 2019, Biodegradable biomimic copper/manganese silicate nanospheres for chemodynamic/photodynamic synergistic therapy with simultaneous glutathione depletion and hypoxia relief, 13, 4267-4277.
160. K. K. Pohaku Mitchell, A. Liberman, A. C. Kummel and W. C. Trogler, J. Am. Chem. Soc., 2012, Iron (III)-doped, silica nanoshells: a biodegradable form of silica, 134, 13997-14003.
161. P. Huang, X. Qian, Y. Chen, L. Yu, H. Lin, L. Wang, Y. Zhu and J. Shi, J. Am. Chem. Soc., 2017, Metalloporphyrin-encapsulated biodegradable nanosystems for highly efficient magnetic resonance imaging-guided sonodynamic cancer therapy, 139, 1275-1284.
162. Y. Chen and J. Shi, Adv. Mater., 2016, Chemistry of mesoporous organosilica in nanotechnology: molecularly organic–inorganic hybridization into frameworks, 28, 3235-3272.
163. K. Möller and T. Bein, Chem. Mater., 2019, Degradable drug carriers: Vanishing mesoporous silica nanoparticles, 31, 4364-4378.
164. L. Maggini, I. Cabrera, A. Ruiz-Carretero, E. A. Prasetyanto, E. Robinet and L. De Cola, Nanoscale, 2016, Breakable mesoporous silica nanoparticles for targeted drug delivery, 8, 7240-7247.
165. Y. Yang, J. Wan, Y. Niu, Z. Gu, J. Zhang, M. Yu and C. Yu, Chem. Mater., 2016, Structure-dependent and glutathione-responsive biodegradable dendritic mesoporous organosilica nanoparticles for safe protein delivery, 28, 9008-9016.
166. M. Porgham Daryasari, M. Dusti Telgerd, M. Hossein Karami, A. Zandi-Karimi, H. Akbarijavar, M. Khoobi, E. Seyedjafari, G. Birhanu, P. Khosravian and F. SadatMahdavi, Artif. Cells Nanomed. Biotechnol., 2019, Poly-l-lactic acid scaffold incorporated chitosan-coated mesoporous silica nanoparticles as pH-sensitive composite for enhanced osteogenic differentiation of human adipose tissue stem cells by dexamethasone delivery, 47, 4020-4029.
167. A. Neumann, A. Christel, C. Kasper and P. Behrens, RSC Adv., 2013, BMP2-loaded nanoporous silica nanoparticles promote osteogenic differentiation of human mesenchymal stem cells, 3, 24222-24230.

168. X. Zhou, W. Feng, K. Qiu, L. Chen, W. Wang, W. Nie, X. Mo and C. He, ACS Appl. Mater. Interfaces, 2015, BMP-2 derived peptide and dexamethasone incorporated mesoporous silica nanoparticles for enhanced osteogenic differentiation of bone mesenchymal stem cells, 7, 15777-15789.

169. Q. Gan, J. Zhu, Y. Yuan, H. Liu, J. Qian, Y. Li and C. Liu, J. Mater. Chem. B, 2015, A dual-delivery system of pH-responsive chitosan-functionalized mesoporous silica nanoparticles bearing BMP-2 and dexamethasone for enhanced bone regeneration, 3, 2056-2066.

170. P. Sun, Q. Zhang, W. Nie, X. Zhou, L. Chen, H. Du, S. Yang, Z. You, J. He and C. He, ACS Biomater. Sci. Eng., 2019, Biodegradable mesoporous silica nanocarrier bearing angiogenic QK peptide and dexamethasone for accelerating angiogenesis in bone regeneration, 5, 6766-6778.

171. Y. Zhou, G. Quan, Q. Wu, X. Zhang, B. Niu, B. Wu, Y. Huang, X. Pan and C. Wu, Acta Pharm. Sin. B., 2018, Mesoporous silica nanoparticles for drug and gene delivery, 8, 165-177.

172. W. Cha, R. Fan, Y. Miao, Y. Zhou, C. Qin, X. Shan, X. Wan and J. Li, Molecules, 2017, Mesoporous silica nanoparticles as carriers for intracellular delivery of nucleic acids and subsequent therapeutic applications, 22, 782.

173. P. Mora-Raimundo, D. Lozano, M. Manzano and M. Vallet-Regí, ACS Nano, 2019, Nanoparticles to knockdown osteoporosis-related gene and promote osteogenic marker expression for osteoporosis treatment, 13, 5451-5464.

174. X. Liu, Y. Sun, J. Shen, H. S. Min, J. Xu and Y. Chai, Nanomed. Nanotechnol. Biol. Med., 2022, Strontium doped mesoporous silica nanoparticles accelerate osteogenesis and angiogenesis in distraction osteogenesis by activation of Wnt pathway, 41, 102496.

175. X. Bai, C. Lin, Y. Wang, J. Ma, X. Wang, X. Yao and B. Tang, Dent. Mater., 2020, Preparation of Zn doped mesoporous silica nanoparticles (Zn-MSNs) for the improvement of mechanical and antibacterial properties of dental resin composites, 36, 794-807.

176. X. Huang, X. Guo, L. Qu, Z. Wu, T. Yu, Y. Jiao and C. Zhou, Appl. Mater. Today, 2021, Gradient regulation of osteo-immune microenvironment by chitooligosaccharide-containing ion-doped mesoporous silica nanoparticles to accelerate osteogenesis, 23, 101067.

177. P. Sutthavas, Z. Tahmasebi Birgani, P. Habibovic and S. van Rijt, Adv. Healthc. Mater., 2021, Calcium Phosphate-Coated and Strontium-Incorporated Mesoporous Silica Nanoparticles can Effectively Induce Osteogenic Stem Cell Differentiation, 2101588.

178. H. P. Rim, K. H. Min, H. J. Lee, S. Y. Jeong and S. C. Lee, Angew. Chem., Int. Ed., 2011, pH-tunable calcium phosphate covered mesoporous silica nanocontainers for intracellular controlled release of guest drugs, 50, 8853-8857.

Chapter 3

The shape-effect of calcium phosphate nanoparticle based films on their osteogenic properties

Published in Biomaterials Science, 2021, doi: 10.1039/D0BM01494J

The shape-effect of calcium phosphate nanoparticle based films on their osteogenic properties.

Pichaporn Sutthavas[a], Pamela Habibovic[a], Sabine H. van Rijt[a]

[a] Department of Instructive Biomaterials Engineering, MERLN Institute for Technology-Inspired Regenerative Medicine, Maastricht University, P.O. Box 616, 6200 MD Maastricht, the Netherlands

Abstract

Calcium phosphates (CaPs) in the form of hydroxyapatite (HA) have been extensively studied in the context of bone regeneration due to their chemical similarity to natural bone mineral. While HA is known to promote osteogenic differentiation, the structural properties of the ceramic have been shown to affect the extent of this effect; several studies have suggested that nanostructured HA can improve the bioactivity. However, the role shape plays in the osteogenic potential is more elusive. Here we studied the effect of HA nanoparticle shape on the ability to induce osteogenesis in human mesenchymal stromal cells (hMSCs) by developing nanoparticle films using needle-, rice- and spherical-shaped HA. We showed that the HA films made from all three shapes of nanoparticles induced increased levels of osteogenic markers (i.e. runt-related transcription factor 2 (RUNX2), bone morphogenetic protein 2 (BMP2), alkaline phosphatase (ALP), osteopontin (OPN), osteocalcin (OCN) on protein and gene level in comparison to hMSCs cultured on cover glass slides. Furthermore, their expression levels and profiles differed significantly as a function of nanoparticle shape. We also showed that nanoparticle films were more efficient in inducing osteogenic gene expression in hMSCs compared to adding nanoparticles to hMSCs in culture media. Finally, we demonstrated that hMSCs morphology upon adhesion to the HA nanoparticle films is dependent on nanoparticle shape, with hMSCs exhibiting a more spread morphology on needle-shaped nanoparticle films compared to hMSCs seeded on rice- and spherical-shaped nanoparticle films. Our data suggests

that HA nanoparticle films are efficient in inducing hMSC osteogenesis in basic cell culture conditions and that nanoparticle shape plays a vital role in cell adhesion and morphology and extent of induction of osteogenic differentiation.

1. Introduction

Calcium phosphate (CaP) ceramics are extensively used materials in the field of bone regeneration due to their inherent ability to stimulate and facilitate bone formation *in vivo* [1-6]. CaP ceramics are chemically similar to the inorganic component of human bone, which is composed of nano-sized CaP crystals in the form of hydroxyapatite (HA). To circumvent the drawbacks associated with autologous bone grafts, which include limited availability and donor site complications, researchers have focused on developing synthetic HA-based bone graft substitutes. Synthetic HA ceramics have demonstrated excellent biocompatibility and bioactivity in terms of osteoconductivity and bone-bonding potential [7-15]. Amongst other applications, HA ceramics have gained interest for use as coatings on (metallic) implants to improve cell adhesion and increase bone-to-implant contact *in vivo* [16-19]. While HA is generally accepted as a bioactive material in a bony environment, the chemical and structural characteristics of the HA surface highly affect the extent and the type of interactions between the material and the local (cellular) environment. For example, the chemical composition influences cellular interactions with the surface and can be employed to tune protein adsorption on a material, a pre-requisite for cell attachment [20, 21]. Additionally, the ceramic itself can affect the dynamics of calcium and phosphate ions exchange with the microenvironment, which in turn may favour the deposition of new bone matrix [22-24]. The HA surface structure, the so-called surface topography, can also modulate cellular behaviour where it has been shown that especially structural features at nanoscale can positively influence cell adhesion and subsequent hMSC proliferation and differentiation [25-28].

A popular way to create nanostructured HA coatings is by depositing nano-sized HA particles on implant surfaces [29-31]. Driven by the popularity and potential of HA nanoparticles (nHA) in the field of bone regeneration but also in the field of drug delivery [32, 33], many methods have been reported to chemically synthesize nHA including various wet and dry synthesis method [30, 33-37]. However, obtaining nHA with homogeneous shape and size remains challenging. This is especially true for wet chemical precipitation methods as calcium and phosphate ions can spontaneously precipitate and crystallize above pH 7. As a result, the effect of nHA shape on the ability to induce osteogenic differentiation in hMSCs is much less studied, although several studies hint that nHA shape plays an important role in their osteogenic effect. For example, Xu et al showed that osteoblasts cultured with needle-shaped nHA increased cell proliferation and upregulated alkaline phosphatase (ALP) and osteocalcin (OCN) expression after 4 days, compared to osteoblasts exposed to spherical nHA [38]. Another study reported that HA nanospheres triggered a stronger osteogenic effect in hMSCs compared to HA nanorods [39]. In contrast, Liu et al. reported a relatively limited effect of spherical nHA on its ability to promote osteogenic differentiation in hMSCs under standard culture conditions [40]. Importantly, these studies were performed under conditions where HA nanoparticles were directly added to the cell culture media of hMSCs adhered to the surface, and their osteogenic effect was related to hMSCs cellular uptake of nHA. The effect of different nanoparticle shapes on their osteogenic potential when deposited in the form of stable coatings has, to our knowledge, not yet been studied.

Here we synthesized needle-, rice- and spherical-shaped nHA and used these to deposit homogeneous films on glass slides. We investigated the effect of nanoparticle shape on the expression profiles of different stage osteogenic markers in primary hMSCs. Specifically, we investigated the effect of nanoparticle shape on bone morphogenetic protein 2 (BMP2), and runt-related transcription factor 2 (RUNX2) which are important markers in the first stage of bone formation where mesenchymal precursors commit to osteoblast differentiation lineage. In addition, we investigated the effect of nHA shape on ALP, osteopontin (OPN), and OCN, which are good indicators of middle to later stage bone formation where there is an increase of metabolic activity and bone cells deposit and mineralize matrix [41]. In addition, the morphology and adhesion of hMSCs on the different nanoparticle films were analysed. Finally, the ability of nanoparticles to induce osteogenic differentiation when added as single particles to the cell culture medium and nanoparticle conditioned media was compared to osteogenic marker expression of hMSCs cultured on the nHA films.

2. Experimental Methods

2.1. Materials

Tetraethyl orthosilicate (TEOS),3-mercaptopropyl triethylsilane (MPTES), triethanolamine (TEA), 3-aminopropyl triethoxysilane (APTES), cetyltrimethylammonium chloride (CTAC), cetyltrimethylammonium bromide (CTAB), ammonium fluoride, hydrochloric acid (37%), ammonium nitrate, N,N-dimethylformamide (DMF), phosphate-buffered saline (PBS), foetal bovine serum, ascorbic acid, bis[N,N-bis(carboxymethyl)aminomethyl] were purchased from Sigma Aldrich GmbH (Germany). Absolute ethanol, paraformaldehyde (PFA), Triton X-100, bovine serum albumin (BSA), Tween-20 and Alizarin Red S (sodium alizarin sulphonate) were purchased from VWR (US). Minimum essential medium alpha (αMEM), L-glutamine, and trypsin were purchased from Fisher Scientific (The Netherlands). Penicillin and streptomycin were purchased from Gibco Life Technologies (US).

2.2. Synthesis of needle-shaped HA nanoparticles

To produce needle-shaped nanoparticles, 0.6 mM calcium nitrate and 0.4 mM potassium phosphate salt solutions in milliQ water (40 ml) were prepared. Both salt solutions were slowly added drop wise via a syringe pump at 2 ml per min into a reactor containing 100 ml milliQ water under rigorous stirring. The reaction was kept at pH 10 by adding ammonium nitrate. After 20 minutes, 1 ml of a 6 µM calcium nitrate solution was added to the mixture. To stop crystal growth, 1 ml 4 µM phosphate– polyethylene glycol (phosphate-PEG) solution was added to the reactor immediately after addition of calcium nitrate solution. Afterwards the mixture was washed three times with absolute ethanol using centrifugation. The slurry was then dried overnight before sintering at 800 °C for 12 hours to remove PEG-chain from the surface.

2.3. Synthesis of rice-shaped HA nanoparticles

In order to achieve rice shape HA nanoparticles, CTAB was used as a template. 0.6 mM calcium nitrate and 0.4 mM potassium phosphate solutions were slowly added drop wise via a syringe pump at 2 ml per min into 1 mM of CTAB in milliQ water under the rigorous stirring. After washing with absolute ethanol three times, the CTAB template was removed via ion exchange reactions under basic conditions: nanoparticles were resuspended in 100 ml absolute ethanol with 100 mg of NH_4NO_3 for 45 minutes at 90 °C under reflux conditions. The rice nanoparticles were then washed again with absolute ethanol before further use.

2.4. Synthesis of spherical nanoparticles

Mesoporous silica nanoparticles (MSN) were used as hard templates for calcium and phosphate ion deposition. MSN with amine surface functionalization were synthesized via modified co-condensation methods as reported previously [42]. The amine groups on the MSN' surface were further modified to obtain carboxylic acid groups, which allowed positive ion deposition. Carboxyl-functionalized MSN nanoparticles (MSN-COOH) were obtained as follows: 3 g of succinic anhydride was added in 20 ml DMF, and allowed to fully dissolve for 30 minutes at room temperature (solution 1).

Subsequently, 0.2 g of MSN were dispersed in 30 ml DMF, and the suspension was added into solution 1 under magnetic stirring. The reaction was kept at 60 ^{o}C for 48 h. Afterwards, the suspension was collected by centrifugation and extensively washed with absolute ethanol. MSN-COOHs were resuspended in milliQ water adjusted to pH 10 by NH_4NO_3. Afterwards, 200 µl 6 µM calcium nitrate solution was added to the mixture and allowed to react for 30 mins. The mixture was then washed with milliQ water once before adding 200 µl 4 µM of $(NH_4)_3PO_4$ solution, and subsequently washed with absolute ethanol. The process of calcium ions and phosphate ions addition was repeated two more times.

2.5. Characterization of the nanoparticles

Zeta potential and polydispersity index (pdi) of all nanoparticles were measured on a Malvern Zetasizer Nano (Malvern Panalytical, UK). For the analysis, nanoparticles were suspended in ethanol at a concentration of 0.3 µg/ml. Morphology of all nanoparticles was further visualized by scanning electron microscopy (SEM; Teneo, FEI, US). For SEM-analysis, dry nanoparticle powder was suspended in absolute ethanol, a drop was placed on an aluminium SEM stub and allowed to dry overnight. The samples were sputtered with a 2-nm layer of iridium before imaging. X-ray diffractograms (XRD) of all HA nanoparticles were collected using a Bruker D2 Phaser diffractometer (Bruker) using Cu Kα radiation ($\lambda = 1.542$ Å) in the range of $6 \leq 2\Theta \leq 60°$ in increments of 0.02° and an integration time of 0.5 s.

2.6 Thin film formation and characterization

Prior to spinning, cover slips were surface-activated with O_2 plasma treatment (Plasma Cleaner, Diener Electronics Femto PCCE) at 0.4 bar, 5 sscm O_2, 70 W, 1.5 min. All nanoparticles were collected by centrifugation (14000 rpm, 20°C, 10 min) and dispersed in absolute ethanol at a concentration of 50 µg/ml. A volume of 20 µl of the suspension was pipetted centrally on a cover slip and spun at 2000 rpm for 20 sec and then at 7000 rpm for 30 sec on a tabletop spin coater. The obtained films were stored dry at room temperature in the dark. To characterize the films, three-dimensional laser scanning microscopy (Keyence VR-200 3D Profilometer, Keyence, Japan) was used to estimate film thickness and surface roughness.

2.7 Thin film stability

To investigate the stability of nanoparticles thin films in aqueous environment and cell culture medium, nHA films were immersed in either 2 ml PBS at pH 7.4 or cell culture medium (αMEM with 10% v/v 100x penicillin and streptomycin) and incubated at room temperature. 20 µl of solution were taken for analysis at 1, 3, 6, 24, 72 and 144 hours upon nHA film immersion. The concentration of calcium and phosphorus was quantitatively studied by inductively coupled plasma mass spectroscopy (ICP-MS, iCaP Q, Thermo Scientific). To this end, aliquots were diluted 1:200 in aqueous 1% HNO_3 containing 20 ppb Sc as internal standard and analysed using He as collision gas in standard mode. Element quantification was based on calibrations with element standards of calcium and phosphorus.

2.8 *In vitro* cell culture

hMSCs of one donor, obtained with written consent, were expanded in αMEM with addition of 10% FBS, 2 mM L-glutamine, 0.2 mM ascorbic acid, 100 U/ml penicillin and 100 mg/ml streptomycin at 37 °C, 5% CO2 in a humidified atmosphere. Cells of passage 4 were used for experiments. The cells were seeded at a density of cells/cm^2. For cell seeding, 250 µl of cell suspension was carefully pipetted on the all nanoparticle films, or uncoated glass cover slips, and cells were left to adhere for 6-8 h before addition of 2 ml medium.

2.9 Quantitative polymerase chain reaction (qPCR)

The effect of nanoparticle shape on osteogenic differentiation of hMSCs was evaluated by measuring expression of osteogenic markers (RUNX2, BMP2, ALP, OPN, OCN) after 7, 14 and 21 of culture, respectively. hMSCs expanded in basic medium were detached at a confluence of 70–80% and seeded on nanoparticles films. Cells grown on uncoated, O_2 plasma surface-activated cover slips were used as control. hMSCs basic medium were refreshed every 3 days.

Total RNA was isolated from hMSCs cultured on thin films via the Trizol method. RNA was further purified using RNA isolation kit (Bioline

ISOLATE II RNA Mini Kit) and the total concentration was measured using the nanodrop method (Thermo Scientific NanoDrop). The cDNA was then prepared using an iScript kit (Bio-Rad) according to the manufacturer's protocol and kept in RNAse free water to be used for qPCR (Bio-Rad) using Syber Green I master mix (Invitrogen). The primer sequences (Sigma) are listed in Table 1. Expression of osteogenic marker genes were normalized to GAPDH levels and basic fold indications were calculated by using ΔΔCT method. hMSCs cultured on plasma cleaned cover slides in basic medium for 7 days were used as calibrator. Two independent experiments with n = 3 for each condition were performed for the qPCR analysis and the results of one representative experiment are presented here.

Table 1: Primer sequence of the osteogenic genes investigated

Gene	Primer sequences
Glyceraldehyde3-phosphate dehydrogenase (GAPDH ,housekeeping gene)	5'-CCATGGTGTCTGAGCGATGT 5'-CGCTCTCTGCTCCTCCTGTT
Runt-related transcription factor 2 (RUNX 2)	5'-GGAGTGGACGAGGCAAGAGTTT 5'-AGCTTCTGTCTGTGCCTTCTGG
Bone morphogenetic protein 2 (BMP2)	5'-GCATCTGTTCTCGGAAAACCT 5'-ACTACCAGAAACGAGTGGGAA
Alkaline phosphatase (ALP)	5'-TTCAGCTCGTACTGCATGTC 5'-ACAAGCACTCCCACTTCATC
Osteopontin (OPN)	5'-CCAAGTAAGTCCAACGAAAG 5'-GGTGATGTCCTCGTCTGTA
Osteocalcin (OCN)	5'-CGCCTGGGTCTCTTCACTAC 5'-TGAGAGCCCTCACACTCCTC

2.10 Nanoparticle suspension experiments

The osteogenic effect of the nHA applied as film, as suspensions in the cell culture medium, and nanoparticle-conditioned medium (containing ions released from nanoparticles) was determined. For this, 3 osteogenic markers; ALP, OPN and OCN were quantified using qPCR analysis after 21 days of culture. Two types of nanoparticles, needle and spherical nHA were chosen for this comparison. hMSCs were detached at a confluence of 70–80% and seeded on nanoparticles films. Cells grown on uncoated, O_2 plasma surface-activated cover slips were used for the other two groups. The same amount of nHA in weight that was used to coat the films was added to the cell culture medium (32 ug/ml for needle nanoparticles and 43 ug/ml for spherical nanoparticles) to create suspension medium and divided over the duration of the experiment. To create the conditioned medium, the cell culture medium was incubated with spherical or needle shaped nanoparticles overnight. This was then centrifuged at 3000 rcf and the supernatant was used in the cell culture experiments. For all conditions, the medium was refreshed every 3 days for the duration of the experiment. qPCR analysis was performed as described in 2.9.

2.11 Western blot

Proteins were isolated from cells cultured on films in RIPA buffer (Sigma-Aldrich), supplemented with cOmplete™, Mini, EDTA-free Protease Inhibitor Cocktail (Sigma-Aldrich). To obtain sufficient protein amounts, cells from two films were mixed into 400 µl lysis buffer for a single protein isolation. Experiments were repeated three times for biological triplicates. Film surfaces were scraped with cell scrapers and samples were centrifuged. Protein quantification was done using the Pierce BCA protein assay kit (Thermo Fisher Scientific). Twenty micrograms of protein was incubated with laemmli loading buffer (Bio-Rad) and 10% 2-mercaptoethanol (Sigma-Aldrich) for 5 min at 95 °C and loaded into a 4–15% polyacrylamide gel (Bio-Rad). Proteins were transferred to a 0.45 µm PVDF membrane (Bio-Rad) using the semi-dry transfer method. Membranes were blocked for 1 h with 5% fat free milk powder (Bio-Rad) in TBS + 0.05% tween-20 (Sigma-Aldrich). OPN and GAPDH antibody incubations were performed overnight at 4 °C in blocking buffer. All antibodies were ordered from Abcam and diluted 1/1000, except for RUNX2 which was diluted 1/500. Blots were subsequently incubated with 0.33 µg/ml goat-anti-rabbit or mouse horseradish peroxidase (Bio-Rad) in blocking buffer for 1 h at room temperature. Protein bands were then visualized using Clarity Western ECL (Bio-Rad).

2.12 Cell morphology analysis

To conserve cells for morphological analysis, hMSCs were fixed using 4% PFA in PBS, 3 days after cell seeding. Samples were stored in PBS at 4 °C until staining. After fixation, hMSCs were permeabilized with 0.2% Triton X-100 in PBS solution for 1 h. Cells were washed with PBS and subsequently stained with phalloidin Alexa Flour 647 antibody (Invitrogen) at room temperature in the dark for 2 h. After incubation, cells were washed with

PBS twice and stained with DAPI antibody (Sigma-Aldrich/Fluka) for 15 minutes. The cells were then washed with PBS and imagined using a Nikon Eclipse Ti-E microscope (Nikon Instruments Europe BV, the Netherlands) at 40× magnification. Images were acquired with a Zyla sCMOS (Andor Technology Ltd, UK) and a Nikon DS-Ri2 camera (Nikon Instruments Europe BV, the Netherlands). Cells stained with phalloidin and DAPI were used for quantitative analysis of cell morphology. The data was analysed in CellProfiler software. Cell morphology was quantified in terms of cell area (measured by the number of pixels occupied) and cell perimeter (total number of pixels (2D) around the boundary of each object in the image), eccentricity (morphological elongation expressed as the deviation from a circle with values between 0 and 1, where 0 is a circle and 1 is a line segment), and compactness (mean squared distance of the object pixels from the centroid divided by the area. A filled circle will have a compactness of 1, with irregular objects or objects with holes having a value greater than 1). A schematic of this data analysis process is shown in supplementary Figure S5.

2.13 Cell adhesion experiments

Cellular adhesion on nanoparticle films was analyzed by immunohistochemical staining of the focal adhesion protein vinculin. hMSCs were seeded on at a density of 3000 cells/cm^2. After 3-day culture, cells were fixed with 4% PFA. Prior to staining, cells were washed once with PBS and permeabilized with Triton X-100 (0.01% (vol/vol) in PBS) for 10 min at room temperature followed by washing three times with PBS. Samples were then incubated for 60 min in blocking buffer (4% BSA and 0.05% (vol/vol) Tween-20 in PBS) at room temperature. Mouse monoclonal IgG1 anti-vinculin antibody (SPM227, 1:500; Abcam) was used as the primary antibody and incubated with the cells overnight at 4 °C in the dark. The samples were then washed with washing buffer (blocking buffer diluted 1:5 in PBS) and incubated overnight at 4 °C with the secondary antibody, biotin-conjugated, rabbit anti-mouse IgG1 (1:1000; Sigma Aldrich). After washing, samples were incubated for 1 h with streptavidin Alexa FluorTM 647 conjugate (1:200; Fisher Scientific), followed by washing 3 times with washing buffer. All antibody dilutions were prepared with washing buffer (blocking buffer diluted 1:5 in PBS). To visualize actin bundles, cells were stained with Alexa FluorTM 488 phalloidin (1:200 in PBS; Thermo Fisher Scientific) for 30 min at room temperature, followed by washing three times with PBS. To visualize cell nuclei, samples were incubated for 6 min with 4’,6-Diamidin-2-phenylindol (DAPI, 1:70 in PBS; Sigma Aldrich) at room temperature, washed three times with PBS and mounted with Dako® (Sigma Aldrich). Cells were imaged with a Nikon Eclipse Ti-E microscope (Nikon Instruments Europe BV, the Netherlands) using an oil objective. Images were further processed and merged using ImageJ.

2.14 Statistical analysis

Statistical comparisons were performed using one-way analysis of variance (ANOVA) followed by a Turkey’s multiple comparison post-hoc test.

Error bars indicate one standard deviation. For all figures the following p-values apply: $^{*}p < 0.01$; $^{**}p < 0.01$; $^{***}p < 0.001$.

3. Results and discussion

3.1. Needle-, rice- and spherical-shaped nHA synthesis and characterization

Three types of nHA (needle-, rice- and spherical-shaped) were successfully synthesized (Figure 1a). To develop the needle-shaped nHA (Figure 1a, left panel), calcium and phosphate ions were precipitated while maintaining the pH at 10 using an ammonium solution. To synthesize the rice-shaped nanoparticles, structure-directing agent CTAB was used to form micelles which restricted the crystal growth by surrounding the particles. This closure caused thickening of the particles in comparison to needle-shaped nHA, resulting in formation of rice-shaped nanoparticles (Figure1a, middle panel). After nanoparticle synthesis, CTAB was removed using ion exchange in a basic environment. To develop spherical CaP nanoparticles, MSN were used as a template for calcium and phosphate ion deposition. MSN with amine surface functionalization were synthesized via modified co-condensation methods as reported previously [42, 43]. The amine groups on the MSN surface were further modified to obtain carboxylic acid groups to allow positive ion deposition. Calcium and phosphate sources were added alternately to create a CaP layer on the MSN surface (Figure 1a, right panel). The hydrodynamic size of the nHA and their pdi in an ethanol solution were measured using dynamic light scattering (DLS). All three nanoparticle types were similar in size, with hydrodynamic sizes of 240±40 nm, 230±20nm and 250± 10 for needle-, rice- and spherical-shaped nanoparticles, respectively (Figure 1b). The nanoparticles were monodispersed with pdi indices of 0.31 (needle-shaped), 0.26 (rice-shaped) and 0.30 (sphere-shaped). Thus, all three methods enabled the formation of nanoparticles that were homogenous in both size and shape. X-ray diffraction analysis showed that the three types of nanoparticles showed patterns typical of HA (Figure 1c). All particles, and in particular needle shaped nHA showed a low crystallinity.

The HA nanoparticle shape strongly depends on the synthesis method and the parameters of the synthesis process. In general, HA crystals found in natural tissues such as bone and teeth, and HA microparticles precipitated using conventional methods [44, 45], have the shape of needles, rods, fibers, or thin plates because of the preferred orientation for growth along the c-axis of HA crystals [46]. Needle-shaped HA particles are the most commonly reported and can be achieved via different approaches such as hydrothermal processing [47], microwave-assisted deposition [48] and wet chemical precipitation [49-54]. The latter method is the most widely used due to low cost, simple setup and low temperature required for the synthesis. However, by using the wet chemical precipitation, it remains challenging to obtain nanoparticles with homogenous size and shape, because calcium and phosphate ions can spontaneously precipitate and crystallize above pH 7. To overcome this problem, in the current study, a combination of slow addition of calcium and phosphate ion precursors and phosphate-PEG, an inhibitor of crystal growth, were used to create needle-shaped nHA with homogenous size and shape.

Wet chemical precipitation also allows the addition of surfactants to the reaction mixture that act as directing agents to develop nanoparticles with different shapes, including rice-shaped and spherical HA particles. Here we used CTAB as a surfactant to yield rice-shaped nanoparticles [55]. Finally, to synthesize spherical-shaped nanoparticles, we used MSN as a template. MSN are commonly used as delivery vehicles because of their mesoporous structure and, in addition, can be easily surface modified for e.g., controlled drug delivery [56]. In particular, deposition of a CaP layer on the MSN surface has been reported for pH-responsive gating of the pores for controlled drug delivery [57, 58]. In our study, MSN were first surface modified to contain carboxylic acid groups (MSN-COOH) and subsequently calcium and phosphate ions were alternately deposited on the MSN-COOH leading to homogeneous-size spherically shaped nanoparticles. Importantly, the MSN-COOH provided a preferred surface for ion deposition, preventing unspecific precipitation of CaP in solution.

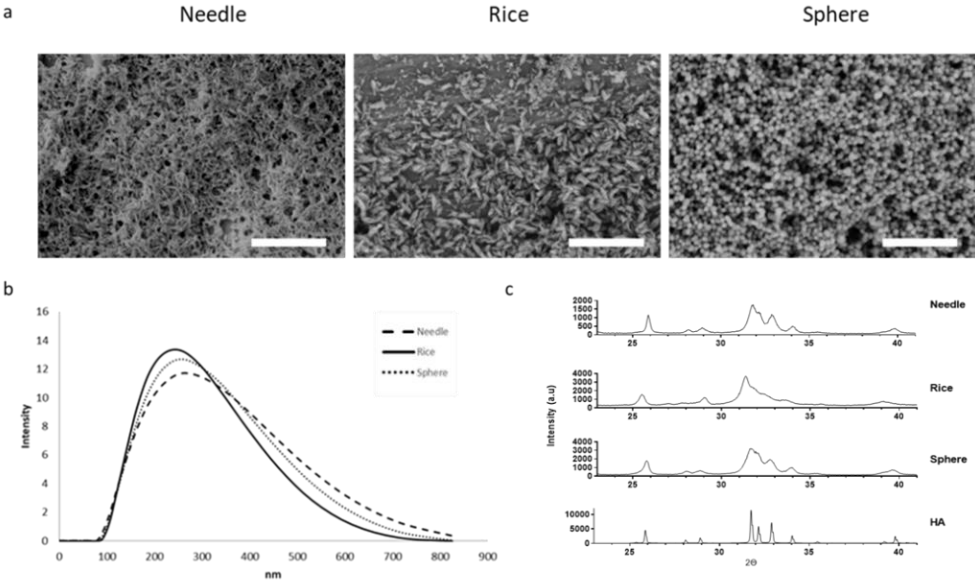

Figure 1: Needle-, rice- and spherical-shaped nHA were characterized for their morphology, size and crystallinity. a) SEM images show distinct needle-, rice- and spherical-shaped nHA particles. Scale bar for SEM images is 1 µm. b) Size of the nHA in ethanol measured by DLS. c) Crystallinity of nHA: X-ray diffraction patterns of needle, rice and spherical shaped nHA in comparison to commercially bought sintered HA powder. nHA showed diffraction patterns typical of poorly crystalline HA.

3.2 nHA film synthesis and characterization

To construct the films, nHA were deposited onto surface-activated glass cover slips by spin-coating of nanoparticle suspensions in ethanol, as reported previously [43]. SEM imaging revealed the deposition of continuous layers of nanoparticles with a homogeneous surface structure, independent of the nanoparticle shape used (Figure 2a). The overall roughness and arithmetic average roughness (Ra) were measured using a profilomete.

Needle nHA films had the highest Ra value (79 ± 4), followed by rice nHA films (69 ± 3), and spherical nHA films (38 ± 2). An example of this Ra calculation process is shown in supplementary data (Figure S1).

Next, nHA film stability by immersion in PBS (pH 7.4) and cell culture medium was followed over a period of 6 days, and calcium and phosphorus concentrations were measured using ICP-MS (Figure 2b and c). In PBS, phosphate depletion from the PBS was observed for all nHA films, with no significant difference observed as a function of nHA shape. Furthermore, the same phosphate depletion from the PBS was observed for the plasma treated control glass slides. In contrast, some calcium release from the films was observed in PBS for all three nHA films. This release was immediate, and remained stable over the 6-day period (Figure 2c). Needle-shaped nHA films showed higher calcium release, followed by rice- and spherical-shaped nHA films. However, the overall amount of calcium release was limited compared to total amount present on the films (less than 1% for each film). In contrast, when the nHA films were immersed in cell culture medium, calcium and phosphate depletion from the cell culture media was observed for all three nHA films as well as for the plasma treated glass slide (Figure 2d). The calcium depletion from the medium was nHA shape dependent after 24 hours, with needle nHA films showing least calcium depletion, followed by spherical- and rice-shaped nHA films. However, at later time-points calcium depletion was similar for all nHA films as well as for plasma treated glass slides. We also investigated the long-term stability of the needle, sphere, and rice nanoparticle based films over 21 days in media that was exchanged every 3 days to simulate our cell culture conditions. A continuous reduction of calcium and phosphorous from the cell culture media could be observed indicating calcium and phosphate deposition on the films (Figure S2). Indeed, calcium and phosphate deposition on the films in the form of brushite crystals could be observed on the nanoparticle films as well as on the glass control slides after 6 days of incubation using SEM imaging (Figure 2d). Calcium and phosphate ion deposition on the glass slides may be due to its negative charge inferred by the plasma treatment, triggering calcium and phosphate deposition.

The dissolution of HA coatings in non-cellular environments depends on the coating characteristics (including roughness, crystallinity, porosity) and on the buffer conditions (e.g. pH, ion concentrations) [59, 60]. In addition, next to the dissolution of HA there is another competing process; re-precipitation of HA. The precipitation mechanism is mainly dominated by the concentration of calcium and phosphate ions as well as the overall ionic strength of the solution [59, 61, 62]. The observed differences for calcium between the two conditions may thus be explained by the presence (cell culture medium) and absence (PBS) of calcium in the buffers.

Next, the spherical nanoparticles were labelled with a fluorescent dye in their core (without affecting the surface chemistry of the nanoparticles) and nanoparticle release in media was followed over 7, 14 and 21 days to further investigate nanoparticle film stability. No significant nanoparticle release could be observed (Figure S3), further proving the stability of the films.

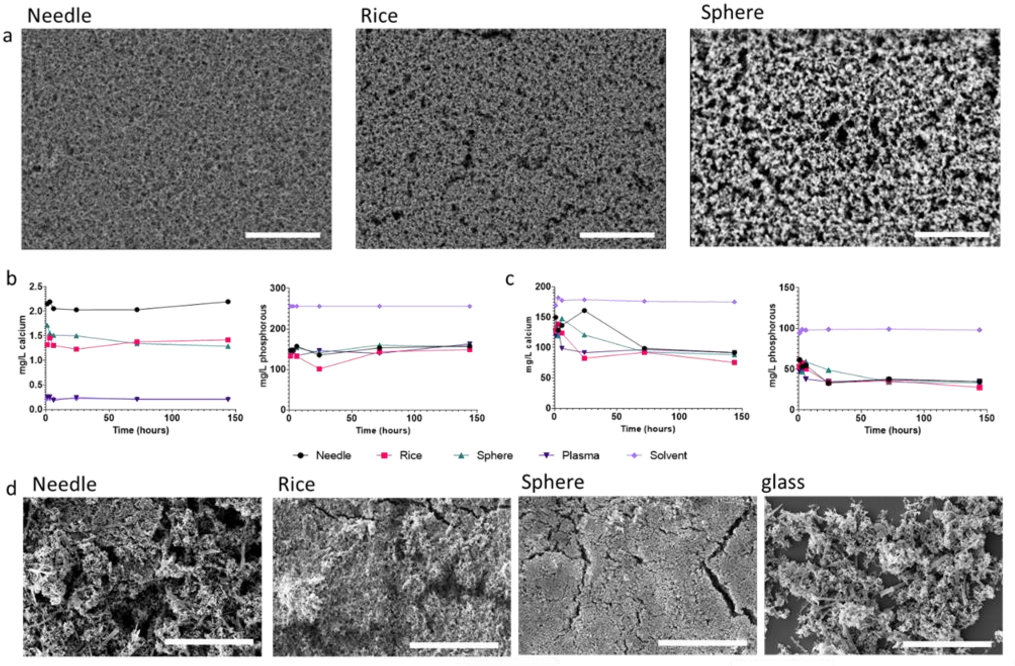

Figure 2: Characterization of nHA films. (a) Scanning electron microscopy (SEM) images of films deposited using needle-, rice- and spherical-nHA. Scale bars are 5 µm. Calcium and phosphorus concentration profiles after immersion of the nHA films in (c) PBS and (d) cell culture medium. (d) SEM images of needle-, rice- , spherical-nHA film and plasma treated control glass slides after incubated in cell culture media for 6 days. Scale bar is 10 µm.

3.3 Effect of nHA shape on hMSCs osteogenic gene and protein expression

To study the effect of nHA shape on the osteogenic differentiation, hMSCs were cultured on films deposited using nHA of different shape and the expression of osteogenic markers RUNX2, BMP2, ALP, OPN, OCN was quantified using qPCR analysis after 7, 14 and 21 days of culture in basic cell culture medium, thus without stimulators of osteogenic differentiation (Figure 3). Cells cultured on glass slides without nanoparticle coating served as a control. hMSCs cultured on films of needle- and rice-shaped nHA could significantly induce RUNX2, an early-stage marker of osteoblast differentiation [63], after 14 days of culture. After 21 days, a significantly upregulated expression of RUNX2 was observed for hMSCs cultured on rice- and spherical-shaped nHA films compared to the control (Figure 3a).

Rice-shaped nHA-based films also induced early expression (day 7) of BMP2, which plays an important role in MSC differentiation [64]. BMP2 expression remained high even after 21 days of culture. In contrast, needle nHA films only induced significant BMP2 expression after 14 days, which decreased after 21 days, whereas spherical nHA films did not induce any significant BMP2 expression at any of the time-points (Figure 3b).

ALP is an enzyme which acts as a mineralization promoter, and is usually expressed after 14 and 21 days of culture [65]. On all three films, ALP expression was upregulated only after 21 days of culture, with the highest expression observed on needle nHA films, followed by rice- and spherical nHA films, respectively (Figure 3c). Needle- and rice nHA films also induced late osteogenic marker OPN [41] in hMSCs after 14 days, whereas hMSCs cultured on spherical nHA films only showed a significant upregulation of this marker after 21 days of culture. Interestingly, where needle- and rice nHA films induced similar OPN expression after 14 days, after 21 days, needle nHA films showed a significantly higher OPN expression (Figure 3d).

The expression of osteocalcin (OCN), a calcium binding protein involved in bone mineralization [66, 67], of hMSCs cultured on needle- and rice nHA films was significantly expressed after 14 and 21 days, whereas spherical nHA films only significantly induced OCN after 21 days of culture (Figure 3e). To confirm that the observed effect on the gene level was also translated to protein level, the effect of nanoparticle shape on hMSCs osteogenic protein expression was investigated for RUNX2 and OPN using Western blot analysis (Figure 3f). RUNX2 protein expression followed a similar trend as was observed for gene expression. This was also the case for OPN protein expression, with needle-shaped and rice-shaped nanoparticle films showing similar OPN levels after 14 days (Figure S4), whereas after 21 days, the OPN expression levels followed the trend needle> rice> sphere (Figure 3f). Taken together, overall, all three nHA coated films could induce the expression of osteogenic markers in basic culture conditions. Even though all nHA films showed the ability to induce osteogenic differentiation in hMSCs, we observed that the expression profile and the expression extent was dependent on the shape of the HA nanoparticles used to deposit the films. Regarding differences amongst the three shapes, overall, needle nHA films were most effective in inducing osteogenic gene expression and spherical nHA films least effective. However, for RUNX2, BMP2 and OCN at certain time-points rice nHA films showed higher gene induction compared to spherical and needle nHA films. In addition, needle nHA films showed a different expression pattern for the early markers (RUNX2, BMP2) which were significantly induced after 14 days of hMSCs culture and reduced after 21 days of culture. In contrast, no significant induction of BMP2 was observed in hMSCs cultured on spherical nHA films, and hMSCs cultured on rice nHA films resulted in the prolonged expression of RUNX2 and BMP2 even after 21 days of hMSCs culture. It has been shown that RUNX2 protein levels are maximal in preosteoblasts and early mature osteoblasts, following a gradual increase during the process of commitment. RUNX2 levels are then decreased significantly in mature osteoblasts and osteocytes, which is in line with our observations of hMSCs osteogenic marker expression on needle shaped nHA films. In addition, all three nHA films induced high expression of middle to late osteogenic markers (ALP, OPN and OCN) after 14 and 21 days of hMSCs culture which followed the order needle> rice> sphere nHA films.

The presence of brushite precipitation shown in Fig.2d would contribute to osteogenic behaviour of hMSCs. However, precipitation occurred in all the films and control group under cell culture condition as evidence in calcium depletion from media (Figure 2c), change in all the osteogenic markers were measured in the relative to the control, therefore the increase in relative expression of markers then would have resulted primary from the different shape of the nanoparticles presented on the nanoparticles film. Furthermore, hMSCs cells would have grew to cover most of the surface after culturing for 7 days. Cells coverage of the surface could prevent further precipitation of these brushite phase on to the surface and minimize brushite contribution to osteogenic potential of the film.

Previous studies have shown that stem cells can sense nanotopographies leading to increased osteogenic marker levels [68-71]. Furthermore, it has been shown that nHA, when added directly to the cell culture medium, can induce osteogenesis in hMSCs [38-40, 67]. However, there are only a limited amount of studies investigating the effect of HA nanoparticle shape on their ability to induce hMSCs osteogenesis [38-40]. One of these studies reported increased upregulation of OCN and ALP markers in hMSCs when exposed to nHA needles compared to spherical nHA. In a similar study it was shown that 50 nm sized HA spheres and nanorods were both osteogenic, however higher upregulation of late osteogenic markers OCN and OPN was observed in hMSCs when exposed to spherical nHA [39]. Although these results highlight that nHA shape is an important factor in their osteogenic capabilities, these studies were performed by adding nHA directly to the medium and not as coated films as studied here.

In summary, all three nanoparticle films studied here induced increased levels of a selection of early, middle and late osteogenic markers at basic culture conditions. However, their expression levels and profiles over time differed significantly as a function of nanoparticle shape, with needle-shaped nanoparticles-based films generally showing highest expression of all tested osteogenic markers.

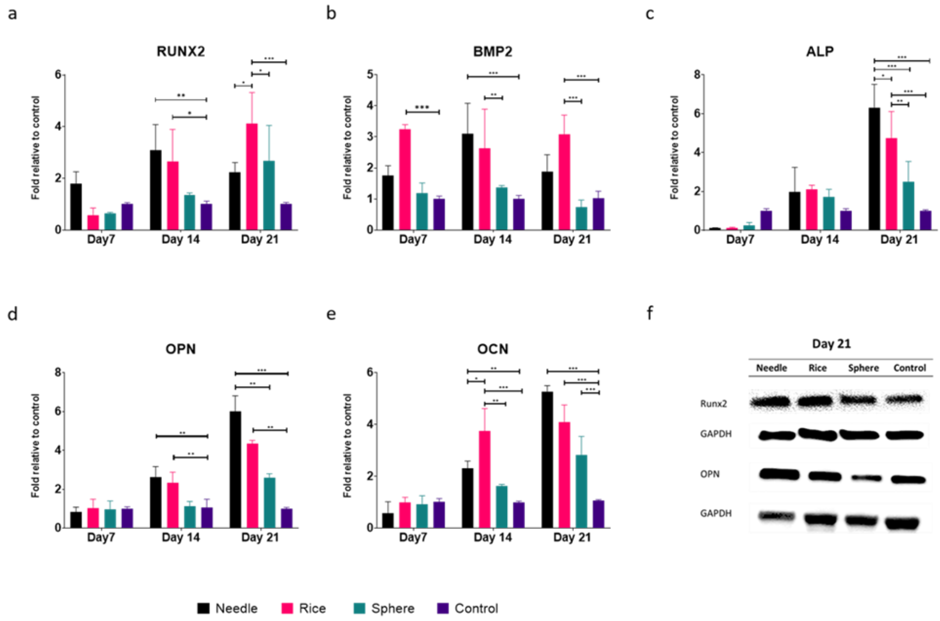

Figure 3: mRNA expression of (a) RUNX2, (b) BMP2, (c) ALP, (d) OPN, (e) OCN of hMSCs cultured on needle- (black), rice- (pink), spherical-shaped (green) nHA films. The results were normalized to GAPDH as housekeeping gene and calibrated to to gene expression of hMSCs cultured on plasma cleaned glass slides (controls, purple). All samples were cultured in basic medium for 7, 14 and 21 days. The significant differences were indicated as follows: *$p < 0.01$; **$p < 0.01$; ***$p < 0.001$. (f) western blot analysis of RUNX2 and OPN protein expression after 21 days of hMSC culture on needle-, rice-, spherical-shaped nHA films or control glass slides.

3.4 nHA coated films versus nHA added directly to the cell culture medium

To further investigate the osteogenic effect of the nHA, a new set of experiments was run. Suspension and conditioned medium were compared to the osteogenic capabilities of the nHA films (film) in basic conditions. The needle- and spherical-shaped nanoparticles were added directly to the cell culture medium (32 ug/ml for needle nanoparticles and 43 ug/ml for spherical nanoparticle) to create the suspension medium. Conditioned media was created by incubating cell culture media with the nanoparticles overnight, and removing the nanoparticle using centrifugation before addition of the media to the hMSCs. Cells cultured on glass slides again served as a control and basic cell culture medium was used for all groups. Intermediate- and late osteogenic markers expression (ALP, OPN and OCN) were quantified using qPCR analysis after 21 days of culture (Figure 4).

In accordance to the first set of experiments, hMSCs cultured on both needle- and spherical-shaped nanoparticle films induced significantly higher expression of ALP, OPN and OCN compared to the control. Interestingly, when needle and spherical nHA were added to the cell culture medium as a suspension, no upregulation of ALP and OCN expression was observed. The OPN expression was upregulated, although to a lower extent compared to hMSCs seeded on the nHA films. Cell culture medium conditioned with nHA did not show significant ALP, OPN and OCN expression compared to the control. Thus, nHA films had a higher capacity to induce osteogenic differentiation in hMSCs compared to nHA added as suspension or the nHA conditioned medium.

To our knowledge, a direct comparison of the osteogenic marker expression in hMSCs between surface-immobilized and ‘free” nHA has not been done previously. Several studies have reported the osteogenic effect of supplementation of cell culture medium with CaP nanoparticles or with calcium and/or phosphate ions [41, 72-78]. While adding nHA as a suspension resulted in a significant increase of OPN compared to the control, this was much lower compared to nHA coated films. Interestingly, also in suspension conditions, needle nHA resulted in higher OPN expression in hMSCs compared to spherical nanoparticles. It should be noted that the concentration of the nanoparticles in suspension used here was 32 - 43 µg /ml in basic media, whereas in an earlier study, the amount ranged from 10 µg/ml - 3 mg/ml in osteogenic media [79]. The chosen concentration in this study was calculated such that the total amount of nHA the hMSCs were exposed to, remained constant across the film and suspension groups. Conditioned media did not lead to any significant upregulation of osteogenic markers, likely because studies that looked into the effect of calcium and phosphate ions on cell behaviour used relatively high ion concentrations in the range of 1.8 - 50 mM to induce osteogenesis [73-76].

The osteogenic effects of nHA added to cell culture medium involves their internalization by hMSCs, where cell internalization rate and concentration is highly dependent on shape and size of the nHA [39, 79]. In our study, the films were stable under cell culture conditions, and no ions were released from the coatings under cell culture conditions (Figure 2d), indicating that osteogenic induction of hMSCs via nHA coatings occurs via different pathways compared to adding nHA directly to the medium. In addition, although we kept the total amount of nHA the same across both conditions, in the case of the nanoparticle-based films; the MSCs experience the contribution of the nHA already from day one. These considerations makes it difficult to do direct comparisons between the two administration routes. Our results do suggest that adding nHA at relatively low concentrations does not effectively induce osteogenic differentiation of hMSCs in basic conditions, where immobilizing an equal amount of nanoparticles on a surface in the form of a film resulted in significant osteogenic gene expression of hMSCs for both needle- and spherical-shaped nHA (Figure 4).

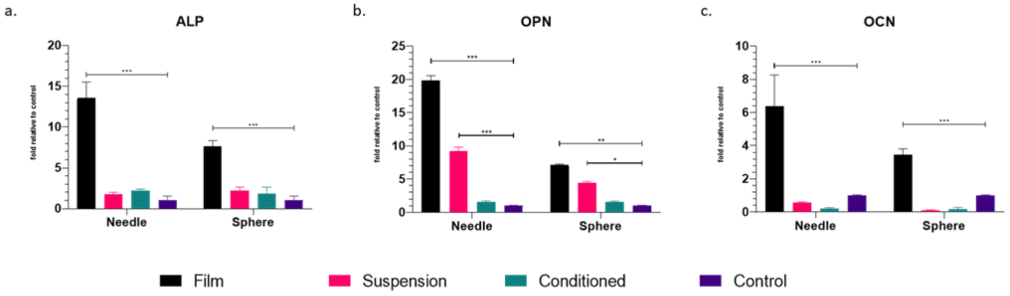

Figure 4: hMSCs mRNA expression of (a)ALP, (b) OPN and (c) OCN after 21 days of culture in basic cell culture medium on nHA films (black), exposed to medium containing nanoparticles (pink), exposed to medium conditioned with nanoparticles (green). The results were normalized for GAPDHmRNA level (housekeeping gene) and calibrated to the mRNA levels of hMSCs cultured on plasma cleaned glass slides (control; blue). The statistically significant differences are indicated as follows: *$p < 0.01$; **$p < 0.01$; ***$p < 0.001$.

3.5 Cell morphology on nanoparticle-based films

To investigate the effect of the nHA shape on cell attachment and morphology, hMSCs were cultured for 3 days on needle, rice and spherical nHA films. Following immunofluorescence staining of cell nuclei, cytoskeleton and focal adhesions, their morphology was characterized in terms of cell area, perimeter, and compactness of cell (irregularity of shape) (see Figure S5 for image analysis workflow). HMSCs grown on needle nHA films exhibited a significantly larger cell area than the cells cultured on the other two films. The cell area of hMSCs cultured on needle nHA films was 175% and 59 % larger compared to hMSCs cultured on rice and spherical nHA films, respectively (Figure 5a). Also the cell perimeter of hMSCs on needle nHA films was 120% and 76% larger in comparison to hMSCs grown on rice and spherical nHA films, respectively (Figure 5b). hMSCs cultured on spherical nHA films were overall more irregularly shaped as indicated by a compactness that was 11% and 13.7% higher compared to needle and rice nHA films, respectively (Figure 5c).

Stem cell attachment mainly occurs through bundling of focal adhesion proteins such as vinculin [80, 81]. Therefore, the formation of focal adhesions of hMSCs on the nanoparticle films was observed using fluorescence microscopy imaging of vinculin staining. A typical hMSCs morphology with extended filopodia could be observed for hMSCs grown on needle nHA films (Figure 5d) that was very similar to hMSCs grown on glass slides exposed to osteogenic media (Figure S6b). In comparison, hMSCs grown on rice and spherical nHA films showed less extended filopodia.

Especially in the case of spherical-shaped nanoparticle films, hMSCs showed elongation in one or two directions (Figure 5d) which showed similar morphology to hMSCs grown on glass slides in basic conditions (Figure S6a).

In summary, we observed a larger cell area and perimeter of hMSCs cultured on needle-shaped nHA films, indicating a more pronounced spreading compared to hMSCs cultured on rice and spherical nHA films. hMSCs spreading has been correlated to enhanced osteogenic differentiation of hMSCs [82-85], mediated by intracellular tension and mechanical changes in the cytoskeleton sending signals via contractile forces to the nucleus [86, 87]. Here, hMSCs cultured on needle-shaped nanoparticle films showed increased cell spreading which correlated with the upregulation of markers of osteogenic differentiation. However, even though hMSCs cultured on rice nHA showed less cell spreading, rice nHA films were effective in inducing osteogenic differentiation.

Higher compactness and elongation was observed for hMSCs seeded on spherical nHA films in comparison to needle and rice nHA films. Higher hMSC compactness suggests a less pronounced formation of filopodia in hMSCs seeded on spherical nHA films. Similar to our findings, Zhao *et al* [88] showed that osteoblast cultured on spherical nHA exhibited an elongated morphology, while osteoblasts cultured on rod shaped nHA showed an increased number of filopodia.

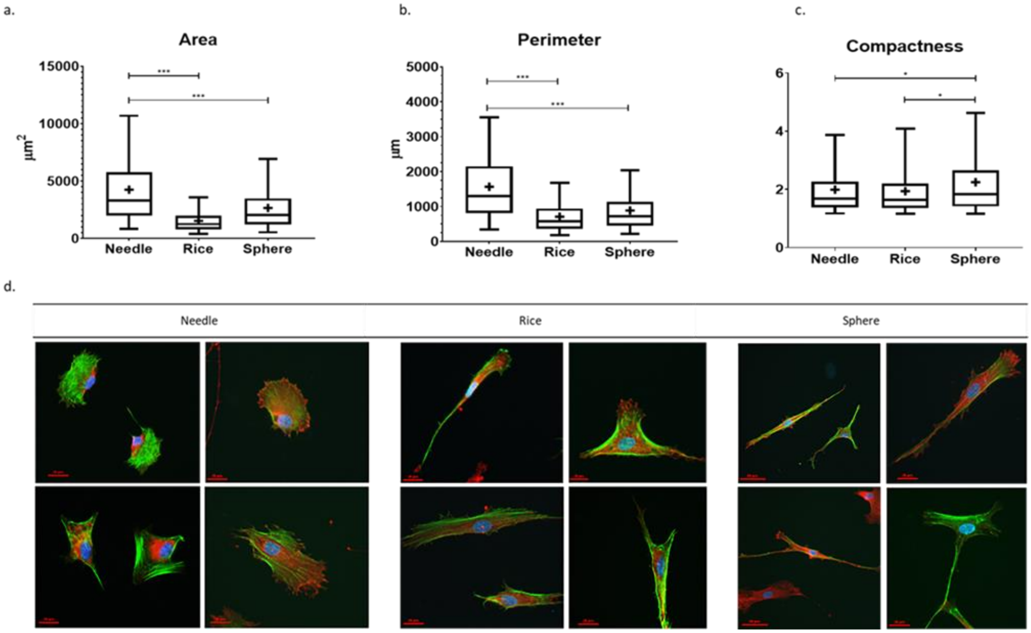

Figure 5: Box plots showing the (a) area, (b) perimeter and (c) compactness of hMSCs grown on needle-, rice- and spherical-shaped nHA films for 3 days. The statistically significant differences are indicated as follows: *p < 0.01; **p < 0.01; ***p < 0.001. Upper border and lower border of the boxes are third quartile and first quartile respectively. + indicates the mean of each data group. (d) Fluorescence microscopy images of focal adhesions of hMSCs cultured on HA nanoparticle films of different shape at day 3 of culture ; green represents actin (phalloidin), red represents focal adhesions (vinculin) and blue represents nuclei (DAPI) staining.

4. Conclusions

Here we showed that hMSCs cultured on needle, rice and spherical nHA films could efficiently induce the expression of osteogenic markers in the absence of other osteogenic stimulators. Although all three nHA films had a stimulatory effect, differences in their potential to promote osteogenesis *in vitro* was observed. In particular, needle nHA films induced the expression of early osteogenic markers RUNX2 and BMP2 after 14 days, whereas rice nHA induced late induction of BMP2 and RUNX2 in hMSCs. In addition, needle nHA films showed a higher induction of late markers (ALP, OCN and OPN) compared to spherical and rice-shaped nanoparticle films. Spherical nHA films were least efficient in inducing osteogenesis in hMSCs *in vitro*.

Previously it has been shown that nHA can induce osteogenesis in hMSCs when added directly to cell culture media in high concentrations. Here we showed that nHA in the form of stable films can efficiently promote osteogenic marker expression in hMSCs. The pronounced positive effect of nHA films on osteogenic differentiation of hMSCs, particularly the needle nHA films, is plausibly related to the initial adhesion and spreading of the hMSCs on these films. We observed that hMSCs seeded on needle nHA films showed a typical hMSC morphology with extended filopodia.

The results of this study suggest that the coatings based on homogeneously synthesized needle-shaped nHA may be a promising strategy for improving bioactivity of biomedical implants, like the biocompatible but bioinert metallic implants used in orthopedics and maxillofacial surgery. Indeed, nHA have been used as coatings to promote bone ingrowth and enhance osteointegration [89, 90]. Additional understanding of how (nano)particle shape influences the bioactivity of these coatings will enhance their efficiency and potentially expand their applicability.

Conflicts of interest

The authors have declared that no competing interest exists.

Acknowledgements

We thank Denis van Beurden for technical assistance with SEM imaging and Dr. Eva Gubbins for technical assistance with ICP-MS. This research was financially supported by the Gravitation Program “Materials Driven Regeneration”, funded by the Netherlands Organization for Scientific Research (024.003.013) and Royal Thai Government Scholarship Program (offered by OCSC).

Supplementary data

Synthesis of MSN

To synthesise MSN with amines on the surface a mixture of 1.63 g TEOS (7.82 mmol) and 14.3 g TEA (95.6 mmol) was heated to 90 °C under static conditions (Solution 1). Solution 2 included 100 mg ammonium fluoride (2.70 mmol) dissolved in a solution of 2.41 ml CTAC (1.83 mmol, 25% (wt) in H2O) and 21.7 ml bi-distilled water (1.21 mmol) by heating to 60 °C. Solution 2 was rapidly added to solution 1, and the mixture was stirred vigorously at 700 rpm for 20 min while left to cool. Then, 138.2 mg TEOS (0.922 mmol) was added in four equal increments (34.55 mg each) every 3 min, and the mixture was stirred for another 30 min. Thereafter, 19.3 mg TEOS (92.5 µmol) and 20.5 mg APTES (92.5 µmol) were added, and the solution was stirred overnight at room temperature. The next day, particles were collected by centrifugation at 7800 rpm for 20 min and washed once with ethanol. Template extraction was performed by dispersion into an ammonium nitrate in ethanol solution (2 g NH4NO3 in100 ml ethanol) and refluxed for 45 min at 90 °C. MSN were collected by centrifugation and washed with ethanol before further template extraction in 100 ml of a 3.7% hydrochloric acid solution in ethanol for 45 min at 90 °C. MSN were collected by centrifugation, washed twice with ethanol and stored in suspension at -20 °C.

Spherical nHA films stability using particle labelling.

To investigate whether nanoparticles could dislodge from film upon immersion to cell culture media, spherical nanoparticles were labelled with a fluorescent dye (ATTO 647) in their core and spin coated on plasma cover glass slide to create nanoparticles film. Core-labelled nHA films were immersed in cell culture medium (αMEM with 10% v/v 100x penicillin and streptomycin) and incubated at 37 °C, 5% CO2 in a humidified atmosphere in the dark. Supernatantsolution were taken for analysis at 7, 14, 21 days upon nHA film immersion. Media without nanoparticles and media containing same amount of labelled nanoparticles as film were keep in the same condition and used as negative and positive control respectively.

Long-term nHA Films stability using ICP-MS.

To investigate the stability of nanoparticles thin films under cell culture condition, nHA films were immersed in cell culture medium (αMEM with 10% v/v 100x penicillin and streptomycin) and incubated at 37 °C, 5% CO2 in a humidified atmosphere. Media were taken for analysis every 3 days after nHA film immersion. New cell culture media were then refreshed. The concentration of calcium and phosphorus was quantitatively studied by inductively coupled plasma mass spectroscopy (ICP-MS, iCaP Q, Thermo Scientific). To this end, aliquots were diluted 1:200 in aqueous 1% HNO3 containing 20 ppb Sc as internal standard and analysed using He as collision gas in standard mode. Element quantification was based on calibrations with element standards of calcium and phosphorus.

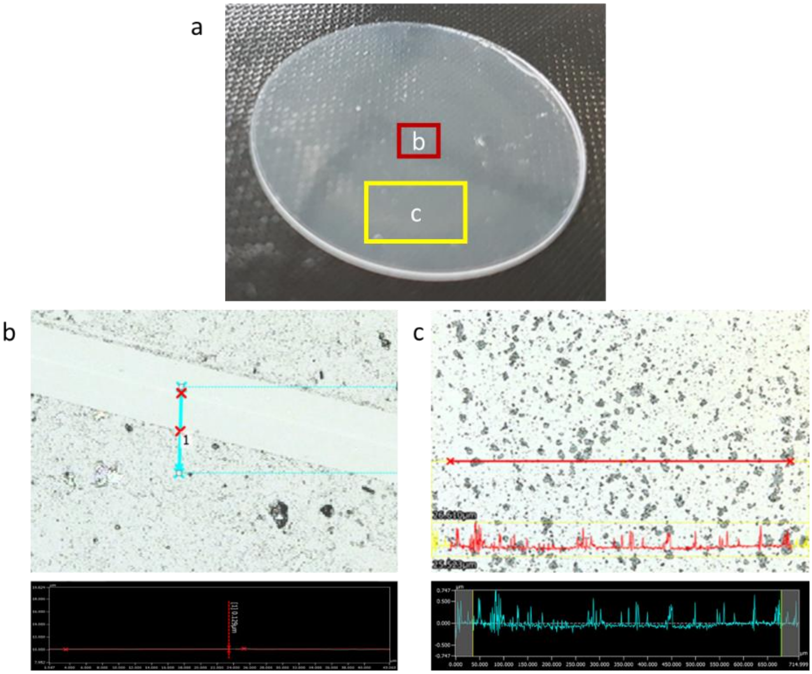

Figure S1: Film thickness and roughness profile. (a) Example of nHA film (b) Film thickness measured at centre of the cover slip by 3D laser scanning microscopy. A scratch was made and the minimal point of scratched area was used as a reference. The difference in height shown in this example is 0.129 µm. c) Arithmetic average roughness (Ra) of each nanoparticles films was calculated using the Multiprofiler program from 3D laser scanning microscopy images. Ra is the squared root of the mean squared distance between peak and valley within the measuring length.

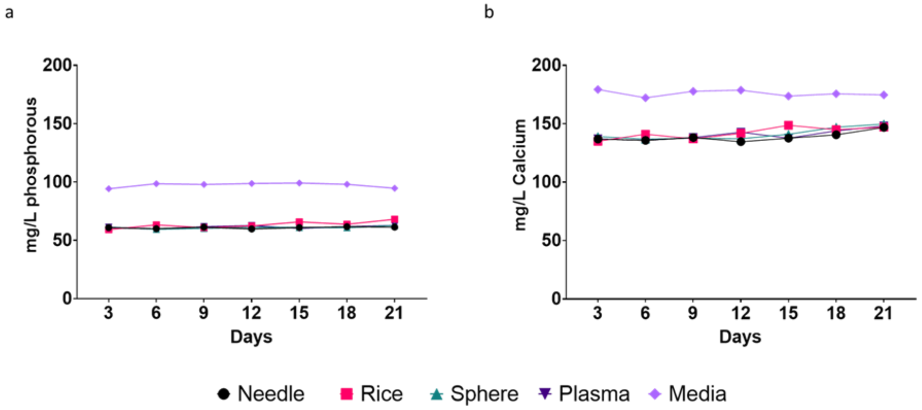

Figure S2: (a) Calcium and (b) phosphorus concentration profiles in cell culture media after immersion of the nHA films at 37 degrees celsius. Cell culture media were exchanged every 3 days and the amount of calcium and phosphorous within the incubated cell culture media was quantified using ICP-MS analysis.

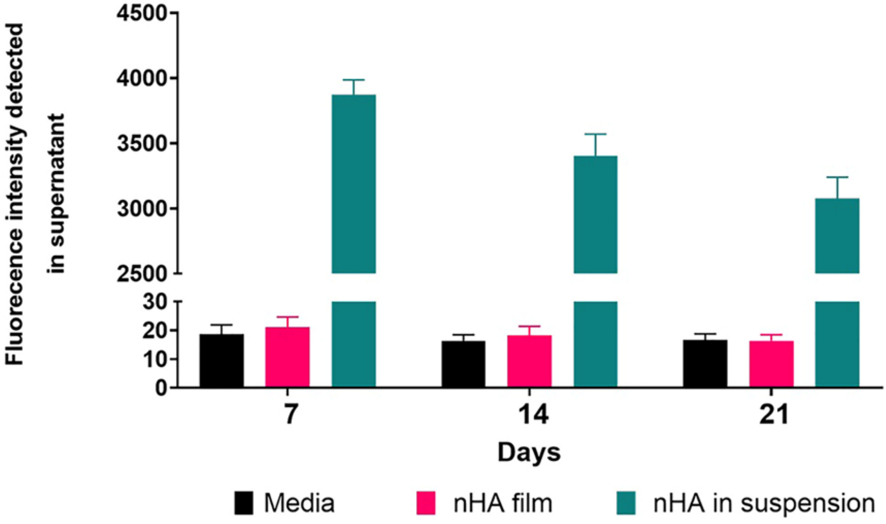

Figure S3: Spherical nHA films stability using particle labelling. Spherical nanoparticles were labelled with a fluorescent dye (ATTO 647) in their core and spin coated on plasma cover glass slide to create nanoparticles film. Nanoparticle release in media was followed over 7, 14 and 21 days. Low fluorescence signal in supernatant in comparison to negative control (media without nanoparticles) and positive control (media with labelled nanoparticles) indicated no major dislocation of labelled nanoparticles from film.

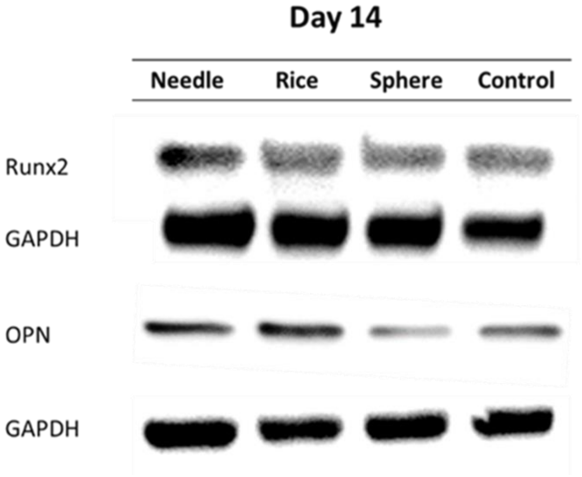

Figure S4: The protein expression of Runx2 protein and OPN protein of hMSCs cultured on needle-, rice-, sphere-shaped nanoparticles films and control group after 14 days of culturing in basic medium.

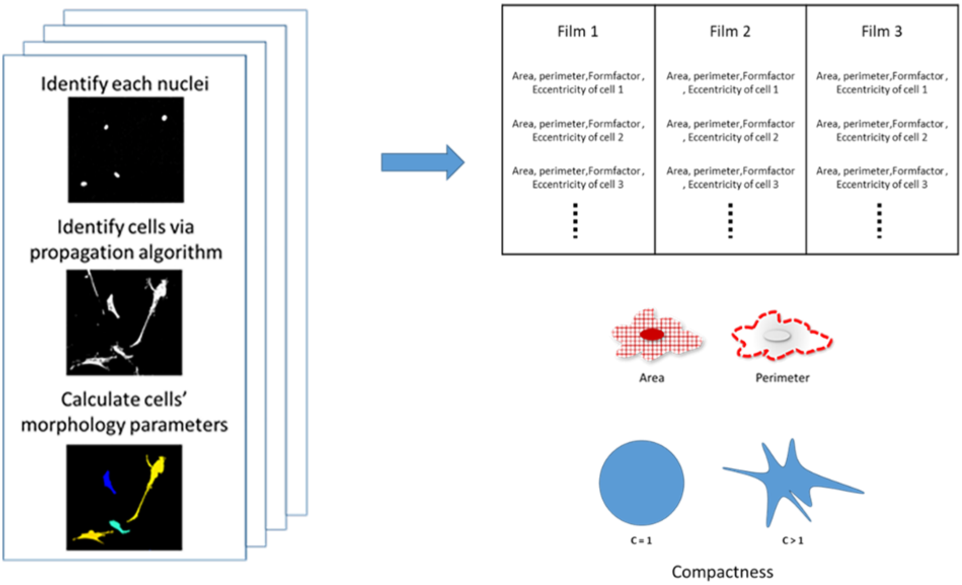

Figure S5: Image analysis workflow including: segmentation (identification of objects, measurements and tracking) in multiple frames; assembly of data in tables; and final merge of the data into groups representing cell morphology measurements as a function cell area, cell perimeter and compactness.

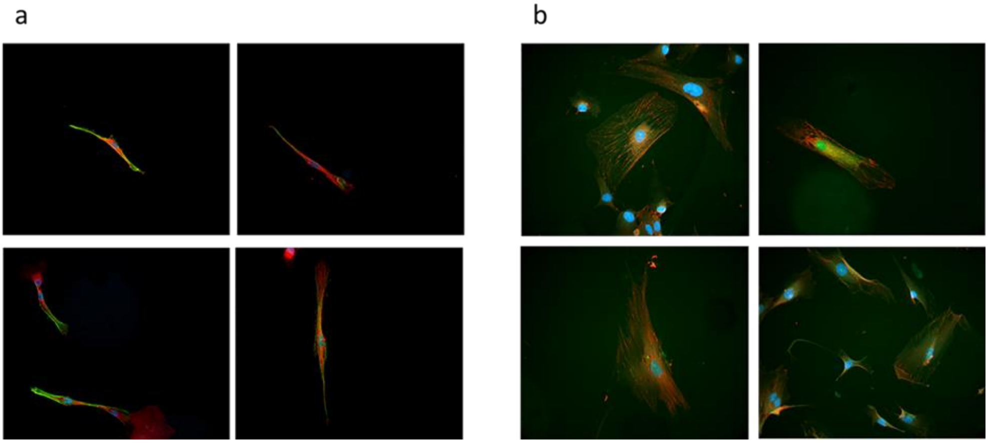

Figure S6: Fluorescence microscopy images of hMSCs cultured on plasma treated control slides after 3days of culture with (a) basic media and (b) osteogenic media; green represents actin (phalloidin), red represents focal adhesions (vinculin) and blue represents nuclei (DAPI) staining.

References

1. M. Nagano, T. Nakamura, T. Kokubo, M. Tanahashi and M. Ogawa, Biomaterials, 1996, Differences of bone bonding ability and degradation behaviour *in vivo* between amorphous calcium phosphate and highly crystalline hydroxyapatite coating, 17, 1771-1777.
2. D. Apelt, F. Theiss, A. El-Warrak, K. Zlinszky, R. Bettschart-Wolfisberger, M. Bohner, S. Matter, J. A. Auer and B. von Rechenberg, Biomaterials, 2004, *In vivo* behavior of three different injectable hydraulic calcium phosphate cements, 25, 1439-1451.
3. S. K. Ghosh, S. K. Nandi, B. Kundu, S. Datta, D. K. De, S. K. Roy and D. Basu, J. Biomed. Mater. Res. Part B Appl. Biomate., 2008, *In vivo* response of porous hydroxyapatite and β-tricalcium phosphate prepared by aqueous solution combustion method and comparison with bioglass scaffolds, 86, 217-227.
4. R. Z. LeGeros, Chem. Rev., 2008, Calcium phosphate-based osteoinductive materials, 108, 4742-4753.
5. F. Barrère, C. A. van Blitterswijk and K. de Groot, Int. J. Nanomed., 2006, Bone regeneration: molecular and cellular interactions with calcium phosphate ceramics, 1, 317.
6. S. Utara and J. Klinkaewnarong, Ceram. Int., 2015, Sonochemical synthesis of nano-hydroxyapatite using natural rubber latex as a templating agent, 41, 14860-14867.
7. Y. Su, S. Komasa, P. Li, M. Nishizaki, L. Chen, C. Terada, S. Yoshimine, H. Nishizaki and J. Okazaki, Int. J. Nanomed., 2017, Synergistic effect of nanotopography and bioactive ions on peri-implant bone response, 12, 925.
8. D.-X. Wang, Y. He, L. Bi, Z.-H. Qu, J.-W. Zou, Z. Pan, J.-J. Fan, L. Chen, X. Dong and X.-N. Liu, Int. J. Nanomed., 2013, Enhancing the bioactivity of Poly (lactic-co-glycolic acid) scaffold with a nano-hydroxyapatite coating for the treatment of segmental bone defect in a rabbit model, 8, 1855.
9. W. Wang, S. Itoh, Y. Tanaka, A. Nagai and K. Yamashita, Acta Biomater., 2009, Comparison of enhancement of bone ingrowth into hydroxyapatite ceramics with highly and poorly interconnected pores by electrical polarization, 5, 3132-3140.
10. P. Habibovic, T. M. Sees, M. A. van den Doel, C. A. van Blitterswijk and K. de Groot, J Biomed Mater Res A, 2006, Osteoinduction by biomaterials—physicochemical and structural influences, 77, 747-762.
11. A. Hofmann, L. Konrad, L. Gotzen, H. Printz, A. Ramaswamy and C. Hofmann, J Biomed Mater Res A, 2003, Bioengineered human bone tissue using autogenous osteoblasts cultured on different biomatrices, 67, 191-199.
12. K. Ogata, S. Imazato, A. Ehara, S. Ebisu, Y. Kinomoto, T. Nakano and Y. Umakoshi, J Biomed Mater Res A, 2005, Comparison of osteoblast responses to hydroxyapatite and hydroxyapatite/soluble calcium phosphate composites, 72, 127-135.
13. D. Richard, N. Dumelié, H. Benhayoune, S. Bouthors, C. Guillaume, N. Lalun, G. Balossier and D. Laurent-Maquin, J. Biomed. Mater. Res. B Appl. Biomate., 2006, Behavior of human osteoblast-like cells in contact with electrodeposited calcium phosphate coatings, 79, 108-115.
14. L. W. Lin, K. L. Chow and Y. Leng, 2008.

15. R. Shu, R. McMullen, M. Baumann and L. McCabe, Biomed Mater Res A, 2003, Hydroxyapatite accelerates differentiation and suppresses growth of MC3T3-E1 osteoblasts, 67, 1196-1204.
16. F. Barrere, C. Van Der Valk, G. Meijer, R. Dalmeijer, K. De Groot and P. Layrolle, J. Biomed. Mater. Res. B, 2003, Osteointegration of biomimetic apatite coating applied onto dense and porous metal implants in femurs of goats, 67, 655-665.
17. R. Jimbo, P. G. Coelho, S. Vandeweghe, H. O. Schwartz-Filho, M. Hayashi, D. Ono, M. Andersson and A. Wennerberg, Acta Biomater., 2011, Histological and three-dimensional evaluation of osseointegration to nanostructured calcium phosphate-coated implants, 7, 4229-4234.
18. J. W. Durham III, S. A. Montelongo, J. L. Ong, T. Guda, M. J. Allen and A. Rabiei, Mater. Sci. Eng., C, 2016, Hydroxyapatite coating on PEEK implants: Biomechanical and histological study in a rabbit model, 68, 723-731.
19. C. Chen, H. Li, C. Guo and S. Chen, Exp. Ther. Med., 2016, Preparation and *in vitro* evaluation of a biomimetic nanoscale calcium phosphate coating on a polyethylene terephthalate artificial ligament, 12, 302-306.
20. Z. Othman, B. Cillero Pastor, S. van Rijt and P. Habibovic, Biomaterials, 2018, Understanding interactions between biomaterials and biological systems using proteomics, 167, 191-204.
21. Z. Othman, R. J. Mohren, B. Cillero-Pastor, Z. Shen, Y. S. Lacroix, A. P. Guttenplan, Z. T. Birgani, L. Eijssen, T. M. Luider and S. van Rijt, Mater. Today Bio, 2020, Comparative proteomic analysis of hMSC behaviour on calcium phosphate ceramics with different osteoinductive potential, 100066.
22. R. Jimbo, P. G. Coelho, M. Bryington, M. Baldassarri, N. Tovar, F. Currie, M. Hayashi, M. N. Janal, M. Andersson and D. Ono, J. Dent. Res., 2012, Nano hydroxyapatite-coated implants improve bone nanomechanical properties, 91, 1172-1177.
23. S. R. Paital and N. B. Dahotre, Mater. Sci. Eng., R: Reports, 2009, Calcium phosphate coatings for bio-implant applications: Materials, performance factors, and methodologies, 66, 1-70.
24. C. Danoux, L. Sun, G. Koçer, Z. T. Birgani, D. Barata, J. Barralet, C. van Blitterswijk, R. Truckenmüller and P. Habibovic, Adv. Mater., 2016, Development of highly functional biomaterials by decoupling and recombining material properties, 28, 1803-1808.
25. G. Thakral, R. Thakral, N. Sharma, J. Seth and P. Vashisht, J. Clin. Diagnostic Res., 2014, Nanosurface–the future of implants, 8, ZE07.
26. T. J. Webster, C. Ergun, R. H. Doremus, R. W. Siegel and R. Bizios, Biomaterials, 2000, Enhanced functions of osteoblasts on nanophase ceramics, 21, 1803-1810.
27. L. G. Gutwein and T. J. Webster, Biomaterials, 2004, Increased viable osteoblast density in the presence of nanophase compared to conventional alumina and titania particles, 25, 4175-4183.
28. H. V. Unadkat, M. Hulsman, K. Cornelissen, B. J. Papenburg, R. K. Truckenmüller, A. E. Carpenter, M. Wessling, G. F. Post, M. Uetz and M. J. Reinders, Proc. Natl. Acad. Sci., 2011, An algorithm-based topographical biomaterials library to instruct cell fate, 108, 16565-16570.
29. H. S. Alghamdi, R. Bosco, S. K. Both, M. Iafisco, S. C. Leeuwenburgh, J. A. Jansen and J. J. van den Beucken, Biomaterials, 2014, Synergistic effects of bisphosphonate and calcium

phosphate nanoparticles on peri-implant bone responses in osteoporotic rats, 35, 5482-5490.

30. D. Alves Cardoso, J. Jansen and S. G. Leeuwenburgh, J. Biomed. Mater. Res. B, 2012, Synthesis and application of nanostructured calcium phosphate ceramics for bone regeneration, 100, 2316-2326.

31. H. Urch, C. Geismann, M. Ulbricht and M. Epple, Materialwissenschaft und Werkstofftechnik: Entwicklung, Fertigung, Prüfung, Eigenschaften und Anwendungen technischer Werkstoffe, 2006, Deposition of functionalized calcium phosphate nanoparticles on functionalized polymer surfaces, 37, 422-425.

32. M. Epple, K. Ganesan, R. Heumann, J. Klesing, A. Kovtun, S. Neumann and V. Sokolova, J. Mater. Chem., 2010, Application of calcium phosphate nanoparticles in biomedicine, 20, 18-23.

33. T. J. Levingstone, S. Herbaj and N. J. Dunne, Nanomaterials, 2019, Calcium phosphate nanoparticles for therapeutic applications in bone regeneration, 9, 1570.

34. N. Kantharia, S. Naik, S. Apte, M. Kheur, S. Kheur and B. Kale, Bone, 2014,Nano-hydroxyapatite and its contemporary applications, 34, 1.71.

35. S. Koutsopoulos, J. Biomed. Mater. res., 2002, Synthesis and characterization of hydroxyapatite crystals: a review study on the analytical methods, 62, 600-612.

36. Q. Lv, L. Nair and C. T. Laurencin, Biomed Mater Res A, 2009, Fabrication, characterization, and *in vitro* evaluation of poly (lactic acid glycolic acid)/nano-hydroxyapatite composite microsphere-based scaffolds for bone tissue engineering in rotating bioreactors, 91, 679-691.

37. G. E. Poinern, R. K. Brundavanam, N. Mondinos and Z.-T. Jiang, Ultrason Sonochem, 2009, Synthesis and characterisation of nanohydroxyapatite using an ultrasound assisted method, 16, 469-474.

38. J. Xu, K. A. Khor, J. Sui, J. Zhang and W. N. Chen, Biomaterials, 2009, Protein expression profiles in osteoblasts in response to differentially shaped hydroxyapatite nanoparticles, 30, 5385-5391.

39. J. Wang, G. Yang, Y. Wang, Y. Du, H. Liu, Y. Zhu, C. Mao and S. Zhang, Biomacromolecules, 2015, Chimeric protein template-induced shape control of bone mineral nanoparticles and its impact on mesenchymal stem cell fate, 16, 1987-1996.

40. Y. Liu, G. Wang, Y. Cai, H. Ji, G. Zhou, X. Zhao, R. Tang and M. Zhang, Biomed Mater Res A, 2009, *In vitro* effects of nanophase hydroxyapatite particles on proliferation and osteogenic differentiation of bone marrow-derived mesenchymal stem cells, 90, 1083-1091.

41. E. D. Jensen, R. Gopalakrishnan and J. J. Westendorf, Biofactors, 2010, Regulation of gene expression in osteoblasts, 36, 25-32.

42. R. Rosenbrand, D. Barata, P. Sutthavas, R. Mohren, B. Cillero-Pastor, P. Habibovic and S. van Rijt, Int. J. Nanomed., 2018, Lipid surface modifications increase mesoporous silica nanoparticle labeling properties in mesenchymal stem cells, 13, 7711.

43. L. Andrée, D. Barata, P. Sutthavas, P. Habibovic and S. van Rijt, Acta Biomater., 2019, Guiding mesenchymal stem cell differentiation using mesoporous silica nanoparticle-based films, 96, 557-567.

44. H. Zhou and J. Lee, Acta Biomater., 2011, Nanoscale hydroxyapatite particles for bone tissue engineering, 7, 2769-2781.

45. A. Haider, S. Haider, S. S. Han and I.-K. Kang, RSC Adv., 2017, Recent advances in the synthesis, functionalization and biomedical applications of hydroxyapatite: a review, 7, 7442-7458.

46. M. Aizawa, T. Matsuura and Z. Zhuang, Biol. Pharm. Bull., 2013, Syntheses of single-crystal apatite particles with preferred orientation to the a-and c-axes as models of hard tissue and their applications, 36, 1654-1661.

47. R. Zhu, R. Yu, J. Yao, D. Wang and J. Ke, J. Alloys Compd., 2008, Morphology control of hydroxyapatite through hydrothermal process, 457, 555-559.

48. A. Siddharthan, S. Seshadri and T. S. Kumar, Trends Biomater Artif Organs., 2005, Rapid synthesis of calcium deficient hydroxyapatite nanoparticles by microwave irradiation, 18, 110-113.

49. P. Wang, C. Li, H. Gong, X. Jiang, H. Wang and K. Li, Powder Technol., 2010, Effects of synthesis conditions on the morphology of hydroxyapatite nanoparticles produced by wet chemical process, 203, 315-321.

50. W. Wijesinghe, M. Mantilaka, E. Premalal, H. Herath, S. Mahalingam, M. Edirisinghe, R. Rajapakse and R. Rajapakse, Mater. Sci. Eng., C, 2014, Facile synthesis of both needle-like and spherical hydroxyapatite nanoparticles: Effect of synthetic temperature and calcination on morphology, crystallite size and crystallinity, 42, 83-90.

51. A. Paz, D. Guadarrama, M. López, J. E González, N. Brizuela and J. Aragón, Química Nova, 2012, A comparative study of hydroxyapatite nanoparticles synthesized by different routes, 35, 1724-1727.

52. S. C. Cox, P. Jamshidi, L. M. Grover and K. K. Mallick, J. Mater. Sci.: Mater. Med., 2014, Low temperature aqueous precipitation of needle-like nanophase hydroxyapatite, 25, 37-46.

53. H. Eslami, H. M. Soulati and M. Tahriri, 2008, Synthesis and characterization of hydroxyapatite nanocrystals via chemical precipitation technique.

54. S. Sagadevan and A. Dakshnamoorthy, Int. j. phys. sci., 2013, Synthesis and characterization of nano-hydroxyapatite (n-HAP) using the wet chemical technique, 8, 1639-1645.

55. K. Shiba, S. Motozuka, T. Yamaguchi, N. Ogawa, Y. Otsuka, K. Ohnuma, T. Kataoka and M. Tagaya, Cryst. Growth Des., 2016, Effect of cationic surfactant micelles on hydroxyapatite nanocrystal formation: An investigation into the inorganic–organic interfacial interactions, 16, 1463-1471.

56. E. Aznar, M. Oroval, L. Pascual, J. R. Murguía, R. Martinez-Manez and F. Sancenon, Chem. Rev., 2016, Gated materials for on-command release of guest molecules, 116, 561-718.

57. C. Yang, W. Guo, L. Cui, D. Xiang, K. Cai, H. Lin and F. Qu, Mater. Sci. Eng., C, 2014, pH-responsive controlled-release system based on mesoporous bioglass materials capped with mineralized hydroxyapatite, 36, 237-243.

58. C.-X. Zhao, L. Yu and A. P. Middelberg, J. Mater. Chem. B, 2013, Magnetic mesoporous silica nanoparticles end-capped with hydroxyapatite for pH-responsive drug release, 1, 4828-4833.

59. A. Afshar, M. Ghorbani and M. Saeri, J. Ceram. Soc. JAPAN, 2004, Adsorption/desorption phenomena of plasma sprayed hydroxyapatite coating surface during immersion in the Ca-free SBF, 112, 77-81.

60. Z. Mohammadi, A. Ziaei-Moayyed and A. S.-M. Mesgar, Biomed Mater., 2008, *In vitro* dissolution of plasma-sprayed hydroxyapatite coatings with different characteristics: experimental study and modeling, 3, 015006.

61. S. Vahabzadeh, M. Roy, A. Bandyopadhyay and S. Bose, Acta Biomater., 2015, Phase stability and biological property evaluation of plasma sprayed hydroxyapatite coatings for orthopedic and dental applications, 17, 47-55.

62. F. Fazan and P. M. Marquis, J. Mater. Sci.: Mater. Med., 2000, Dissolution behavior of plasma-sprayed hydroxyapatite coatings, 11, 787-792.

63. T. Komori, In Osteoimmunology, Springer, 2009, pp. 43-49.

64. T. Matsubara, K. Kida, A. Yamaguchi, K. Hata, F. Ichida, H. Meguro, H. Aburatani, R. Nishimura and T. Yoneda, J. Biol. Chem., 2008, BMP2 regulates Osterix through Msx2 and Runx2 during osteoblast differentiation, 283, 29119-29125.

65. E. E. Golub and K. Boesze-Battaglia, Curr Opin Orthop., 2007, The role of alkaline phosphatase in mineralization, 18, 444-448.

66. J. B. Lian and C. M. Gundberg, Clin. Orthop. Relat. Res., 1988, Osteocalcin: biochemical considerations and clinical applications, 226, 267-291.

67. M. L. Zoch, T. L. Clemens and R. C. Riddle, Bone, 2016, New insights into the biology of osteocalcin, 82, 42-49.

68. F. F. Hulshof, Y. Zhao, A. Vasilevich, N. R. Beijer, M. de Boer, B. J. Papenburg, C. van Blitterswijk, D. Stamatialis and J. de Boer, Acta Biomater., 2017, NanoTopoChip: High-throughput nanotopographical cell instruction, 62, 188-198.

69. M. Hulsman, F. Hulshof, H. Unadkat, B. J. Papenburg, D. F. Stamatialis, R. Truckenmüller, C. Van Blitterswijk, J. De Boer and M. J. Reinders, Acta Biomater., 2015, Analysis of high-throughput screening reveals the effect of surface topographies on cellular morphology, 15, 29-38.

70. S. Vermeulen and J. de Boer, Methods, 2020, Screening as a strategy to drive regenerative medicine research.

71. S. Kumari, S. Vermeulen, B. Van Der Veer, A. Carlier, J. De Boer and D. Subramanyam, Tissue Eng. Part B Rev., 2018, Shaping cell fate: influence of topographical substratum properties on embryonic stem cells, 24, 255-266.

72. M. Zayzafoon, J. Cell. Biochem., 2006, Calcium/calmodulin signaling controls osteoblast growth and differentiation, 97, 56-70.

73. L. M. Schäck, S. Noack, R. Winkler, G. Wißmann, P. Behrens, M. Wellmann, M. Jagodzinski, C. Krettek and A. Hoffmann, PLoS One, 2013, The phosphate source influences gene expression and quality of mineralization during *in vitro* osteogenic differentiation of human mesenchymal stem cells, 8, e65943.

74. C. B. Danoux, D. C. Bassett, Z. Othman, A. I. Rodrigues, R. L. Reis, J. E. Barralet, C. A. van Blitterswijk and P. Habibovic, Acta Biomater., 2015, Elucidating the individual effects of calcium and phosphate ions on hMSCs by using composite materials, 17, 1-15.

75. A. M. Barradas, H. A. Fernandes, N. Groen, Y. C. Chai, J. Schrooten, J. van de Peppel, J. P. van Leeuwen, C. A. van Blitterswijk and J. de Boer, Biomaterials, 2012, A calcium-induced signaling cascade leading to osteogenic differentiation of human bone marrow-derived mesenchymal stromal cells, 33, 3205-3215.

76. S. Nakamura, T. Matsumoto, J.-I. Sasaki, H. Egusa, K. Y. Lee, T. Nakano, T. Sohmura and A. Nakahira, Tissue Eng. Part A, 2010, Effect of calcium ion concentrations on osteogenic

differentiation and hematopoietic stem cell niche-related protein expression in osteoblasts, 16, 2467-2473.

77. G. R. Beck Jr, J. Cell. Biochem., 2003, Inorganic phosphate as a signaling molecule in osteoblast differentiation, 90, 234-243.

78. Y. C. Chai, S. J. Roberts, J. Schrooten and F. P. Luyten, Tissue Eng. Part A, 2011, Probing the osteoinductive effect of calcium phosphate by using an *in vitro* biomimetic model, 17, 1083-1097.

79. X. Yang, Y. Li, X. Liu, R. Zhang and Q. Feng, Stem Cells Int., 2018, *In vitro* uptake of hydroxyapatite nanoparticles and their effect on osteogenic differentiation of human mesenchymal stem cells, 2018.

80. A. Carisey and C. Ballestrem, Eur. J. Cell Biol., 2011, Vinculin, an adapter protein in control of cell adhesion signalling, 90, 157-163.

81. K. Collins, E. Gates, C. Gilchrist and B. Hoffman, in Bio-Instructive Scaffolds for Musculoskeletal Tissue Engineering and Regenerative Medicine, Elsevier, 2017, pp. 3-35.

82. M. J. Biggs, R. G. Richards, N. Gadegaard, C. D. Wilkinson, R. O. Oreffo and M. J. Dalby, Biomaterials, 2009, The use of nanoscale topography to modulate the dynamics of adhesion formation in primary osteoblasts and ERK/MAPK signalling in STRO-1+ enriched skeletal stem cells, 30, 5094-5103.

83. M. D. Treiser, E. H. Yang, S. Gordonov, D. M. Cohen, I. P. Androulakis, J. Kohn, C. S. Chen and P. V. Moghe, Proc. Natl. Acad. Sci., 2010, Cytoskeleton-based forecasting of stem cell lineage fates, 107, 610-615.

84. C. Seiler, A. Gazdhar, M. Reyes, L. M. Benneker, T. Geiser, K. A. Siebenrock and B. Gantenbein-Ritter, J. Tissue Eng. Regener. Med., 2014, Time-lapse microscopy and classification of 2D human mesenchymal stem cells based on cell shape picks up myogenic from osteogenic and adipogenic differentiation, 8, 737-746.

85. F. Matsuoka, I. Takeuchi, H. Agata, H. Kagami, H. Shiono, Y. Kiyota, H. Honda and R. Kato, PloS one, 2013, Morphology-based prediction of osteogenic differentiation potential of human mesenchymal stem cells, 8, e55082.

86. N. Wang, J. D. Tytell and D. E. Ingber, Nat. Rev. Mol. Cell Biol., 2009, Mechanotransduction at a distance: mechanically coupling the extracellular matrix with the nucleus, 10, 75-82.

87. A. Elosegui-Artola, I. Andreu, A. E. Beedle, A. Lezamiz, M. Uroz, A. J. Kosmalska, R. Oria, J. Z. Kechagia, P. Rico-Lastres and A.-L. Le Roux, Cell, 2017, Force triggers YAP nuclear entry by regulating transport across nuclear pores, 171, 1397-1410. e1314.

88. Y. Zhao, Y. Zhang, F. Ning, D. Guo and Z. Xu, J. Biomed. Mater. Res. Part B Appl. Biomater., 2007, Synthesis and cellular biocompatibility of two kinds of HAP with different nanocrystal morphology, 83, 121-126.

89. J. Wang, M. Wang, F. Chen, Y. Wei, X. Chen, Y. Zhou, X. Yang, X. Zhu, C. Tu and X. Zhang, Int. J. Nanomed., 2019, Nano-hydroxyapatite coating promotes porous calcium phosphate ceramic-induced osteogenesis via BMP/Smad signaling pathway, 14, 7987.

90. S.-I. Roohani-Esfahani, S. Nouri-Khorasani, Z. Lu, R. Appleyard and H. Zreiqat, Biomaterials, 2010, The influence hydroxyapatite nanoparticle shape and size on the properties of biphasic calcium phosphate scaffolds coated with hydroxyapatite–PCL composites, 31, 5498-5509.

Chapter 4

Calcium phosphate coated and strontium incorporated mesoporous silica nanoparticles can effectively induce osteogenic stem cell differentiation

Published in, Advanced Healthcare Materials, 2021, doi: 10.1002/adhm.202101588

Calcium phosphate coated and strontium incorporated mesoporous silica nanoparticles can effectively induce osteogenic stem cell differentiation

Pichaporn Sutthavas[1], Zeinab Tahmasebi Birgani[1], Pamela Habibovic[1], Sabine van Rijt[1*]

[1]Department of Instructive Biomaterials Engineering, MERLN Institute for Technology-Inspired Regenerative Medicine, Maastricht University, P.O. Box 616, 6200 MD Maastricht, the Netherlands

Abstract

Ceramic (nano) materials are promising materials for bone regeneration applications. The addition of bioinorganics such as strontium and zinc is a popular approach to further improve their biological performance. However, control over ion delivery is important to prevent off-target effects. Mesoporous silica nanoparticles (MSN) are popular nanomaterials that can be designed to incorporate and controllably deliver multiple ions to steer specific regenerative processes. In this work, we developed MSN loaded with strontium (MSN_{Sr}) and surface coated with a pH sensitive calcium phosphate (MSN_{Sr}-CaP) or calcium phosphate zinc layer (MSN_{Sr}-CaZnP). The ability of the MSN to promote osteogenesis in hMSCs under basic cell culture conditions was explored and compared to ion administration directly to the cell culture media. Here we show that MSN-CaPs can effectively induce ALP levels and osteogenic gene expression in the absence of other osteogenic stimulants, where an improved effect was observed for MSN surface coated with multiple ions. Moreover, comparatively lower ion doses were needed when using MSN as delivery vehicles compared to direct ion administration in the medium, likely due to their different uptake mechanisms. In summary, the MSN developed here represent promising vehicles to deliver (multiple) bioinorganics and promote hMSC osteogenesis in basic conditions.

1. Introduction

There is a high demand for bone substitutes due to traumatic injury, bone disease, and an increasingly ageing population. The gold standard treatment is the use of patients own bone (i.e., autografts). However, drawbacks associated with autografts including limited availability have led to the development of synthetic bone substitutes. Inorganic materials prepared from calcium (Ca), phosphate (P), and silica (Si), such as ceramics and bioactive glasses, are considered promising candidates for bone regeneration applications due to their inherent bioactivity and chemical similarity to natural bone [1-3]. The biological performance of ceramic materials can be further improved by using additives such as growth factors, small molecules, and bioinorganic ions [4-8]. Especially, bioinorganic ions are considered interesting candidates as they are known to play important roles in bone formation processes [9, 10].

For example, strontium (Sr), chemically and physically similar to Ca, is known to promote the activity of osteoblastic cells, while inhibiting osteoclast activity [11-13]. Another example of a popular additive is zinc (Zn), which is an essential trace element important in many cellular processes, including bone remodelling by supporting both pre-osteoblast differentiation and suppressing osteoclast differentiation [14-16]. The therapeutic use of bioinorganics such as Sr and Zn is promising as they are biocompatible, non-immunogenic, and are easily taken up by cells via ion channels and membrane diffusion. However, this capability to be rapidly processed by cells can also lead to nonspecific adverse effects if distributed systemically without dosage control. For example, in a study by Yu et al. it was demonstrated that Zn can have a double-edged effect; Zn doses between 2 and 5 μg mL^{-1} stimulated mesenchymal stromal cell (MSC) adhesion and proliferation, however, higher Zn doses of 15 μg mL^{-1} led to inhibition of osteogenic differentiation and induced MSCs apoptosis [17]. As such, the route of administration and dosage scheme are important parameters to be taken into account when considering the therapeutic use of bioinorganics. Ion substitution within the main network of ceramics is a popular method to incorporate and release bioinorganic ions and resulted in scaffolds with improved bone regenerative performance [18-20]. Although the effect of combining ions in a single construct has only limitedly been explored, several studies have shown that incorporating multiple ions into calcium phosphate scaffolds improves their bone formation capabilities compared to scaffolds without additional ions [21-23]. However, ion substitution within ceramics can alter the mechanical properties and degradation rates, which compromises their structure and in addition makes it difficult to precisely control ion release.

Mesoporous silica nanoparticles (MSN) are popular carriers for biomolecule delivery, and have emerged as promising materials for use in bone regeneration applications [24, 25]. MSN unique characteristics such as high drug-loading capacity, large surface area, and high pore volume as well as tuneable pore and particle size make them flexible tools to optimize cargo delivery. Many approaches have been reported where MSN have been used for the effective delivery of growth factors, ions, genetic material, and antibiotics [26]. MSN surface chemistry can, in addition, be easily modified with capping agents to allow controlled cargo delivery, e.g., in response to pH, temperature, or light [27]. MSN represent a particularly interesting alternative strategy for bioinorganic ion delivery because multiple therapeutic ions can be integrated in one nanoparticle construct, e.g., within the silica matrix, mesopores, or grafted onto the surface, resulting in unique ion release profiles. Moreover, MSN can easily be incorporated in other biomaterials and scaffolds [28-30], and as such are a promising strategy to improve ion delivery without impairing material characteristics. Finally, MSN are processed differently by cells compared to inorganic ions; where ions are taken up via ion channels present on the cell membrane, MSN are internalized via endocytotic pathways [31, 32]. We hypothesize that ion delivery using MSN is more efficient compared to direct bioinorganic ion administration in cell culture media.

In this work, we developed MSN loaded with Sr and coated with CaP or CaZnP layer as efficient and versatile carrier systems for multiple bioinorganic ion delivery to human mesenchymal stromal cells (hMSCs). Here, Zn and Sr were chosen due to their known positive effects on the osteogenic differentiation of hMSCs, however the design allows facile encapsulation of other ions. CaP surface functionalization was chosen as both a pH-sensitive gating system and to simultaneously deliver Ca and P to hMSCs, which play important roles in stimulating bone formation [1-3]. Cell internalization and the ability of the synthesized MSN to promote osteogenesis in hMSCs under basic cell culture conditions was explored and compared to ion administration directly to the cell culture media.

Here, we show that MSN incorporating Sr, and coated with Ca, P, and Zn can effectively induce osteogenic marker expression in the absence of other osteogenic stimulants, where an improved effect was observed for MSN functionalized with multiple ions. Moreover, comparatively lower ion doses were needed when using MSN as delivery vehicles compared to direct ion administration in the cell culture media. In summary, the MSN developed here represent promising vehicles to efficiently and locally deliver bioinorganics and promote hMSCs osteogenesis in basic conditions.

2. Experimental Methods

2.1 Materials

Tetraethyl orthosilicate (TEOS), 3-merCaPi topropyl triethylsilane (MPTES), triethanolamine (TEA), 3-aminopropyl triethoxysilane (APTES), cetyltrimethylammonium chloride (CTAC), ammonium fluoride, hydrochloric acid (37 V/V%), ammonium nitrate, N,N-dimethylformamide (DMF), phosphate-buffered saline (PBS), foetal bovine serum (FBS), ascorbic acid, bis[N,N-bis(carboxymethyl)aminomethyl] were purchased from Sigma Aldrich GmbH (Germany). Absolute ethanol, paraformaldehyde (PFA), Triton X-100, bovine serum albumin (BSA), Tween-20 and Alizarin Red S (sodium alizarin sulphonate) Minimum essential medium alpha (αMEM), L-glutamine and trypsin were purchased from Fisher Scientific (The Netherlands). Penicillin and streptomycin were purchased from Gibco Life Technologies (US). Concentrated Nitric acid 60 V/V% (HNO3), hydrochrolic acid 37 V/V% (HCL) element standards of Ca, Si, P, Sr, Zn and scandium (Sc) for ICP-MS were also purchased from VWR (US).

2.2 Synthesis of Mesoporous silica nanoparticles (MSN)

Synthesis of MSN with thiol functional groups in the particles' core and functional amine groups at the particles' surface was based on the co-condensation method as previously reported [33, 34]. Further details on MSN synthesis and characterization can be found in the supporting information (S1). The amine groups in the MSN pores and surface were further modified to obtain carboxylic acid groups, which allowed positive ion deposition. Carboxyl-functionalized MSN nanoparticles (MSN-COOH) were obtained as follows; 3 g of succinic anhydride was added in 20 mL DMF, and allowed to fully dissolve for 30 minutes at room temperature. Subsequently, 0.2 g of MSN were dispersed in 30 mL DMF, and the suspension was added into the above solution under magnetic stirring. The reaction was kept at 60 ^{o}C. After stirring for 48 hours, the suspension was collected by centrifugation and extensively washed with absolute ethanol. MSN were stored at -20 °C until further use.

2.3 Strontium ion loading and calcium, phosphate, zinc composite layer formation

To create MSN containing Sr ions (MSN_{Sr}), MSN-COOHs were suspended in 10 µM $SrNO_3$ in milliQ water overnight. The suspension was collected by centrifugation and washed once with milliQ water. To synthesize calcium phosphate coated MSN (MSN_{Sr}-CaP) and calcium phosphate, zinc coated MSN (MSN_{Sr}-CaZnP), 100 mg of MSN_{Sr} were re-suspended in 100 ml milliQ water adjusted to pH 10 by NH_4NO_3. 200 µl of 4 µM $(NH_4)_3PO_4$ were added to the mixture and allowed to react for 30 minutes. After 30 minutes, 200 µl of 6 µM calcium nitrate for MSN_{Sr}-CaP or 6 µM calcium nitrate and zinc (10:1 molar ratio) solution for MSN_{Sr}-CaZnP was added and allowed to react for 30 minutes. Calcium and phosphate ion addition was repeated two more times to achieve nanoparticle sizes of roughly 100 nm. The nanoparticles were then collected by centrifugation and washed with absolute ethanol. MSN_{Sr}-CaP and MSN_{Sr}-CaZnP were stored at -20 °C until further use.

2.4 Characterization of the MSN

The MSN were characterized for their morphology and size using transmission electron microscopy (TEM FEI Tennai G2 Spirit BioTWIN iCorr (G0.201)). For this, 5 µL of 0.3 µg/mL MSN suspended in ethanol were dropped onto the gold TEM grids and dried overnight before imaging.

The total ion composition in the composite nanoparticles were determined by inductively coupled plasma mass spectrometry (ICP-MS, iCaP Q, Thermo Scientific). For this, MSN_{Sr}, MSN_{Sr}-CaP and MSN_{Sr}-CaZnP were digested with aqua regia (nitric acid: hydrochloric acid in a molar ratio of 1:3) until completely dissolved. Digested MSN were diluted 1:10 in aqueous 1% HNO3 containing 20 ppb Sc as internal standard and analyzed using He as collision gas in normal mode. Element quantification was based on calibration with element standards of Ca, Si, P, Sr and Zn. Results are expressed as percentage of the total element presented for each type of nanoparticle. X-ray diffraction (XRD) of all synthesized MSN were collected using a Bruker D2 Phaser diffractometer (Bruker) using Cu Kα radiation (λ = 1.5406 Å) in the range of $6^0 \leq 2\Theta \leq 50^0$ in increments of 0.02^0 and an integration time of 0.5 s.

2.5 Degradation study

The degradation of MSN_{Sr}, MSN_{Sr}-CaP, MSN_{Sr}-CaZnP was studied for up to 6 days at pH 5 and pH 7.4 at a concentration of 1 mg/ml in cacodylate buffer. After 1, 3, 6, 24, 72 and 144 hours, leftover solid and supernatants were separated by centrifugation and stored at -20 °C for subsequent elemental analysis. The content of Ca, P and Si of was assessed by ICP-MS (Thermo Scientific). None-degraded solid were digested with aqua regia until completely dissolved. Both digested and supernatant were diluted 1:10 in aqueous 1% HNO_3 containing 20 ppb Sc as internal standard and analyzed using He as collision gas in normal mode. Element quantification was based on calibration with element standards of Ca, Si, P, Sr and Zn. Results are expressed as percentage of the total element presented in each type of nanoparticles.

2.6 *In vitro* cell culture

Human mesenchymal stromal cells (hMSCs, PromoCell) of passage 3 were expanded in αMEM with addition of 10% FBS, 2 mM L-glutamine, 0.2 mM ascorbic acid, and 100 U/mL penicillin and 100 mg/mL streptomycin at 37 ° C, 5% CO2 in a humidified atmosphere. Cells of passage 4 were used for the experiments. 1 ml of cells suspended in medium (5000 cells per cm^2) were seeded in each well of 12-well cell culture plates. Cells were left to adhere for 24 hours before change of media.

2.7 Cell uptake of nanoparticles

Flow cytometry was performed to quantitatively assess the uptake of the MSN by hMSCs. For short-term flow cytometry uptake study, hMSCs were seeded in 12-well plates at 5000 cells per cm^2 density. ATTO633-maleimide labeled MSN (labeling procedure can be found in SI) were suspended in cell culture media at a concentration of 70 µg/mL and exposed to the hMSCs when they had reached 80-90% confluence. Flow cytometry was performed after 6 and 24 hours of MSN exposure. To prepare the samples, cells were washed with PBS, trypsinized, and re-dispersed in culture medium. Cell suspensions were then centrifuged and re-dispersed in 300 µL PBS and kept on ice for flow cytometry analysis (BD Accuri C6). A total of 10000 cells (gated) were collected for each measurement. FlowJo version 10 was used for data analysis.

Cellular uptake of MSN was also analyzed by immunohistochemical staining. hMSCs were seeded at a density of 3000 cells/cm^2 on a plasma treated cover slide. At 80-90% confluency, hMSCs were exposed to ATTO647-maleimide labeled MSN for 6 and 24 hours. After exposure, cells were fixed with 4% paraformaldehyde (PFA). Prior to staining, cells were washed once with PBS and permeabilized with Triton X-100 (0.01% (vol/vol) in PBS) for 10 minutes at room temperature followed by washing three times with PBS. Samples were then incubated for 60 minutes in blocking buffer (4% BSA and 0.05% (vol/vol) Tween-20 in PBS) at room temperature. To visualize actin bundles, cells were stained with Alexa FluorTM 488 phalloidin (1:200 in PBS; Thermo Fisher Scientific) for 30 minutes at room temperature, followed by washing three times with PBS. To visualize cell nuclei, samples were incubated for 6 minutes with 4’,6-Diamidin-2-phenylindol (DAPI, 1:70 in PBS; Sigma Aldrich) at room temperature, washed three times with PBS and mounted with Dako® (Sigma Aldrich). Cells were imaged with a Nikon Eclipse Ti-E microscope (Nikon Instruments Europe BV, the Netherlands) using an oil objective. To further visualize internalization of MSN without membrane permeabilization, cellular uptake of MSN was analysed by laser scanning confocal microscope. hMSCs were seeded at a density of 2000 cells/cm^2 on a 6 cm^2 glass bottom cell culture well. At 80-90% confluency, hMSCs were exposed to ATTO488-maleimide labeled MSN for 6 hours. Cells were stained with CellMask™ Deep Red Plasma membrane Stain (1:800 in PBS; Thermo Fisher Scientific) and 4’,6-Diamidin-2-phenylindol (DAPI, 1:100 in PBS; Sigma Aldrich. Images were captured by Nikon A1R+ laser scanning confocal microscope (Nikon, Japan). Z-stack scan were used to end sure internalization of MSN. Images were further processed and merged using ImageJ.

For long-term flow cytometry uptake study, hMSCs were cultured and exposed to MSN similar to short-term experiments. However, 140 µg/mL of labelled MSN in media were used and media were refreshed every 3 days. MSN were freshly added into the media just before the media change. At 1, 3, 7, 14 and 21 days of culturing, samples were collected for flow cytometry analysis.

2.8 Cytotoxicity

The cytotoxicity of MSN$_{Sr}$, MSN$_{Sr}$-CaP, MSN$_{Sr}$-CaZnP at concentrations ranging from 70-1000 µg/mL, was determined using the MTT

(3-(4,5-dimethylthiazol-2-yl)-2,5-diphenyl tetrazolium bromide) assay according to manufacturer’s protocol (Sigma-Aldrich). hMSCs were seeded in 12-well plates at 5000 cells per cm^2 density. As hMSCs reached 80-90% confluence, they were exposed toMSN at concentrations ranging from 35 to 1000 µg/mL. Cytotoxicity was assessed after 24 and 72 hours of exposure. Amount of dissolved formazan was determined immediately using a microplate reader (BIO-RAD microplate reader-550) at absorbance wavelength of 570 nm. Wells with complete medium, MSN and MTT reagent, without cells were used as blanks.

2.9 Alkaline phosphatase assay

Osteogenic differentiation was evaluated by measuring alkaline phosphatase (ALP) levels at days 14 and 21 of culture. CyQuant® Cell Proliferation Assay Kit (Thermo Fisher Scientific) was used to measure DNA content for normalization of ALP levels. To measure ALP levels and DNA content, cells were lysed with cell-lysis buffer (provided with the kit, 1:20 in PBS) containing 0.1% (vol/vol) RNAse A (Thermo Fisher Scientific) and three cycles of freezing-thawing at -80 °C. First, medium was discarded, and cell layers were washed once with PBS. After freezing-thawing for 30 minutes, RNAse lysis buffer was added to each well, and samples were frozen-thawed for two cycles of 30 minutes each. Once thawed, more RNAse lysis buffer was added, and samples were sonicated for 5 minutes. To assure complete lysis of the cells, samples were then incubated for 60 min at room temperature.

ALP activity was quantified using CDP-star solution (ready-to-use, Sigma Aldrich). Cell lysate was incubated 1:5 with the reagent for 30 min in the dark at room temperature in a white-bottom, 96-well plate. Using a microplate reader (BIO-RAD microplate reader-550) ALP values were normalized with total DNA content per sample and expressed as an x-fold increase compared to hMSCs cultured on plastic with non-osteogenic medium. For the quantification of total DNA content, cell lysate was mixed with GR-dye solution (provided in the CyQuant kit, 1:200 in lysis buffer) according to the supplier’s instructions. After 15 min, the fluorescent signal was measured with a spectrophotometer at 520 nm. Absolute DNA amounts were calculated using the standard curve prepared following the supplier’s instructions.

2.10 RNA extraction and gene expression (qPCR) assay

Total RNA was isolated from hMSCs via the Trizol method. RNA was further purified using RNA isolation kit (Bioline ISOLATE II RNA Mini Kit). RNA was collected in RNAse–free water and the total concentration was measured using nano-drop (Thermo Scientific NanoDrop). The cDNA of the cultures were then prepared using an iScript kit (Bio-Rad) according to the manufacturer’s protocol and kept in RNAse-free water to be used for quantitative real time PCR (qPCR). The qPCR measurement (Bio-Rad equipment) was performed using Syber Green I master mix (Invitrogen) using primer sequences (Sigma) as listed in Table 1. Expression of osteogenic marker genes were normalized to GAPDH levels as housekeeping gene and basic fold indications were calculated by using ΔΔCT method. hMSCs not exposed to nanoparticles were used as controls. All the conditions were done with biological triplicate (n = 3).

Table 1: Primer sequence of the osteogenic genes investigated

Gene	Primer sequences
GAPDH (housekeeping gene)	5’-CCATGGTGTCTGAGCGATGT 5’-CGCTCTCTGCTCCTCCTGTT
RUNX 2	5’-GGAGTGGACGAGGCAAGAGTTT 5’-AGCTTCTGTCTGTGCCTTCTGG
Bone morphogenetic protein 2 (BMP2)	5’-GCATCTGTTCTCGGAAAACCT 5’-ACTACCAGAAACGAGTGGGAA
Osteopontin (OPN)	5’-CCAAGTAAGTCCAACGAAAG 5’-GGTGATGTCCTCGTCTGTA
Osteocalcin (OCN)	5’-CGCCTGGGTCTCTTCACTAC 5’-TGAGAGCCCTCACACTCCTC
Collagen I (COL I)	5’-GATTCCCTGGACCTAAAGGTGC 5’-AGCCTCTCCATCTTTGCCAGCA
Podoplanin (E11)	5’-GTGTAACAGGCATTCGCATCG 5’-TGTGGCGCTTGGACTTTGT

2.11 Mineralization assay

Calcium deposition of hMSCs was assessed by Alizarin Red S (sodium alizarin sulphonate) staining to visualize mineralization. After 28 days of culture, cells were fixed with 4% PFA, and calcium deposits were made visible by Alizarin Red S staining. Alizarin Red S was dissolved in bi-distilled water at a concentration of 22 mg/ml. Once the solid was completely dissolved, pH was adjusted to 4.2 with ammonium hydroxide. Prior to staining, cells were rinsed once with PBS followed by washing twice with bi-distilled water. Alizarin Red solution were added to samples were incubated for 15 minutes at room temperature followed by washing thrice with bi-distilled water. Staining was assessed by visual inspection.

A quantification method was carried out using a de-staining method with 10 % (w/v) cetylpyridinium chloride (CPC) (Sigma) in 10 mM sodium phosphate (pH 7.0), adding 1 ml of CPC solution/well. After incubating for 15 minutes at room temperature under constant shaking, 10 µl from the extracted stain were transferred to a 96-well plate and diluted 10 folds with CPC solution. The violet colored supernatant was read with a microplate reader (CLARIOstar Multimode Microplate Reader) at 555 nm.

2.12 Statistical analysis

For statistical comparisons for biocompatibility and ALP activity analyses, a two-way analysis of variance (2-way ANOVA) were used followed by Turkey's multiple comparison. For gene expression analysis, a 2-way ANOVA was performed followed by Dunnett's multiple comparison post-hoc test. For all figures, error bars indicate one standard deviation and for the p-values, the following applies: *$p < 0.033$; **$p < 0.02$; ***$p < 0.001$.

3. Results

3.1 Synthesis and characterization of Sr loaded and Ca, P, Zn surface coated MSN

MSN functionalized with thiols in the core structure, were synthesized via hydrolysis and condensation of silica precursors in the presence of a micelle template, as we have reported previously [33, 34]. The presence of the thiol groups was confirmed by labelling with a thiol reactive fluorescent dye (ATTO-647-Maleimide; Figure S1). The surface and mesopores of the MSN were then further modified with amine groups using APTES post grafting to create MSN-NH_2. Spherical, evenly shaped MSN with a mesoporous structure were obtained (Figure S2a). In addition, the surface zeta potential changed from negative (-20.6±0.1 for MSN) to a positive zeta potential (19.6±0.3 for MSN-NH_2), after amine surface grafting (Table S1). The surface grafted amines could then be modified by reaction with succinic anhydride to carboxylic acid groups (MSN-COOH), to allow Ca and P deposition on the surface of MSN, as we reported previously [35]. The surface modification resulted in another surface potential change to -17.7±0.2, indicating that the modification from positively charged amine groups to negatively charged carboxylic acid groups was successful (Table S1). The carboxylic acid group modification was further confirmed by FTIR with an observable peak of around 1627 1/cm (COOH stretch, Figure S2c). Two types of MSN-COOH particles were created; one with COOH groups only on the nanoparticle surface and one where COOH groups were incorporated on the surface and in the mesopores. The COOH modified MSN were then soaked in a Sr solution to create MSN_{r}. The MSN containing COOH in the mesopores showed increased uptake of Sr ions compared to the MSN which only had COOH groups on the surface (Figure S1), and were used for the remainder of the study. Sr incorporation did not alter the morphology of the MSN (Figure 1a).

To graft the CaP layer on the surface of the MSN (MSN_{Sr}-CaP), Ca and P precursors in solution were added alternately on MSN_{Sr} until a thin layer of CaP was obtained (Figure 1b). Zn were added to the CaP layer, Zn precursors were added along with Ca precursors during layer formation at 10% molar equivalent, to create MSN with a thin layer of Zn doped CaP (MSN_{Sr}-CaZnP, Figure 1c). The X-ray diffraction (XRD) pattern of MSN grafted with calcium and phosphate in the absence of Sr and Zn ions (MSN-CaP) showed only broad peaks, suggesting the formation of a rather amorphous CaP layer using this method. Similarly, the XRD analysis indicated that the CaP layer on MSN_{Sr}-CaP was amorphous and that MSN_{Sr}-CaZnP had a low of crystallinity (Figure S3). ICP-MS analysis of the dissolved nanoparticles confirmed the presence of Ca, P, Sr and Zn in the MSN (Table 2). Furthermore, MSN_{Sr}, MSN_{Sr}-CaP and MSN_{Sr}-CaZnP were similar in size, with hydrodynamic sizes of 203±5 nm, 218±14 nm and 223±10 nm, respectively (Table 3). The nanoparticles were monodisperse with polydispersity indexes (Pdi) of 0.1 (MSN_{Sr}), 0.33 (MSN_{Sr} -CaP) and 0.27 (MSN_{Sr}-CaZnP) and had a negative surface potential (Table 3). In summary, our layer-by-layer method enabled the formation of MSN incorporating Sr and coated with Ca, P, and Zn, which were homogenous in both size and shape.

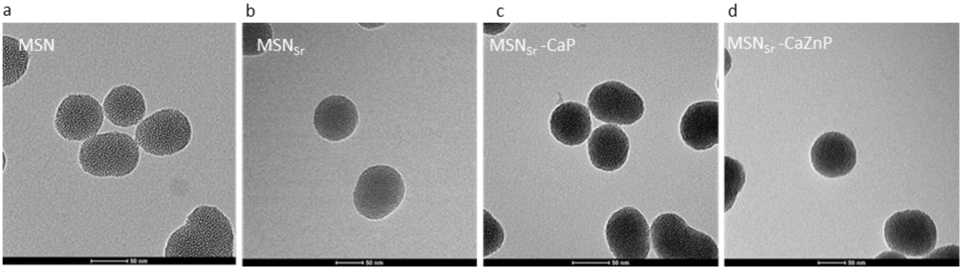

Figure 1: Characterization of a) MSN, b)MSN$_{Sr}$, c) MSN$_{Sr}$-CaP and d) MSN$_{Sr}$-CaZnP by TEM. Scale bar is 50 nm.

Table 2: Ion composition of MSN$_{Sr}$, MSN$_{Sr}$-CaP and MSN$_{Sr}$-CaZnP (in 100 mg) using ICP-MS analysis.

Sample	Si (mg)	Ca (mg)	P (mg)	Zn (mg)	Sr (mg)
MSN$_{Sr}$	99.97613	-	-	-	0.03856
MSN$_{Sr}$-CaP	95.57849	2.759965	1.652674	-	0.04526
MSN$_{Sr}$-CaZnP	95.41935	2.700724	1.626942	0.248765	0.04222

Table 3: hydrodynamic size, Pdi and surface zeta potential of MSN$_{Sr}$, MSN$_{Sr}$-CaP and MSN$_{Sr}$-CaZnP in ethanol measured by DLS.

Sample	Hydrodynamic size in ethanol (nm)	Pdi	Zeta potential
MSN$_{Sr}$	203±5	0.1	-5.34
MSN$_{Sr}$-CaP	218±14	0.33	-20.43
MSN$_{Sr}$-CaZnP	223±10	0.27	-20.56

3.2 ion release from MSN at neutral and acidic pH

To assess ion release at different pH found in extracellular (pH 7.4) and intracellular (endosomes; pH 5) environments, MSN_{Sr}, MSN_{Sr}-CaP and MSN_{Sr}-CaZnP were incubated in cacodylate buffer (does not contain Ca, P, Zn, Sr or Si), at pH 5 and 7.4 for 0, 1, 3, 6, 24, 72 and 144 hours, and ion release was quantified using ICP-MS (Figure 2).

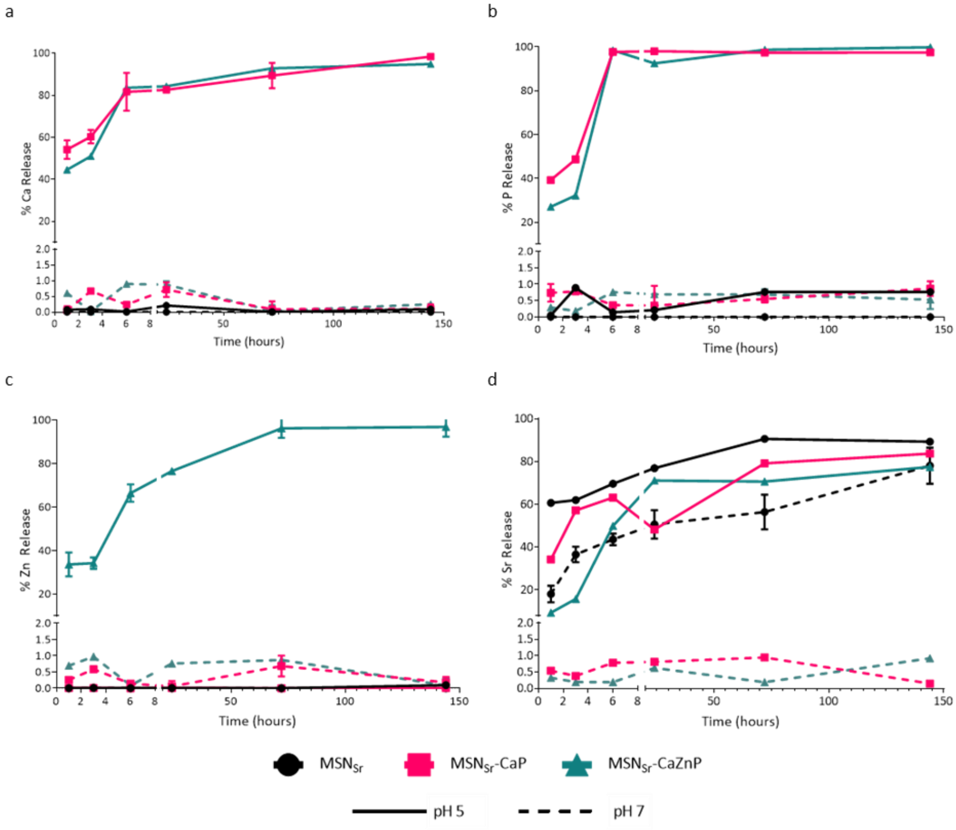

Figure 2: MSN ion release in neutral and acidic pH. Ion release profiles of a) Ca, b) P, c) Zn and d) Sr from MSN_{Sr} (black), MSN_{Sr}-CaP (red) and MSN_{Sr}-CaZnP (blue) in cacodylate buffer

pH 5 (solid lines) and pH 7.4 (dashed lines) analysed by ICP-MS. The percentage of each element present in the supernatant compared to total amount is shown.

MSN_{Sr}-CaP and MSN_{Sr}-CaZnP were stable at neutral pH as no significant Si, Ca, P or Zn release could be observed after 6 days of incubation (Figure 2). Also no Sr release was observed from MSN_{Sr}-CaP or MSN_{Sr}-CaZnP at pH 7.4. In contrast, Sr diffused out rapidly from non-gated nanoparticles (MSN_{Sr}) with 43.6% release after 6 hours in neutral pH.

At pH 5, rapid dissolution of the CaP layer was observed. Specifically, the calcium phosphate layer of MSN_{Sr}-CaP and MSN_{Sr}-CaZnP showed total dissolution of P within 6 hours (Figure 2a, b). Interestingly, Ca and Zn release was slower than that of P (Figure 2c). Since P readily dissolved within 24 hours, the slower release of the Ca and Zn might be due to ion adsorption on to the MSN. Sr release at pH 5 was similar for all three nanoparticles, and slower compared to Zn and Ca degradation, this may be due to increased affinity of Sr towards carboxylic acid groups present in the MSN mesopores (Figure 2a, c). The MSN matrix remained stable for all nanoparticles at both pH 7.4 and pH 5 (Figure S4).

In summary, here we showed that the CaP surface coating on MSN prevented release of encapsulated and surface coated ions when in neutral (extracellular) pH. The CaP and CaZnP surface coatings could rapidly degrade at acidic pH values like those found in endosomes/lysosomes, triggering ion release of the surface coated and encapsulated ions, where the mesoporous silica matrix remained intact.

3.3 Biocompatibility and cell internalization

Next, the biocompatibility of MSN_{Sr}, MSN_{Sr}-CaP and MSN_{Sr}-CaZnP at concentrations ranging from 35 to 1000 µg/mL was assessed in hMSCs using the MTT assay. Only relatively high nanoparticle concentrations of 500 and 1000 µg/mL MSN_{Sr}, MSN_{Sr}-CaP and MSN_{Sr}-CaZnP led to a significant decrease in hMSCs cell metabolism after 24 hours of exposure compared to control cells cultured in the absence of MSN (Figure 3a). After 3 days of exposure, also the lower concentration of 280 µg/mL resulted in a significant decrease in cell metabolism for all three tested MSN (Figure 3b). There was no statistical difference between the MSN groups after 24 hours, however, after 72 hours; MSN_{Sr} was significantly more toxic than MSN_{Sr}-CaP and MSN_{Sr}-CaZnP at the higher concentration range (280-1000 µg/mL). In conclusion, MSN concentrations lower or equal to 140 µg/mL did not affect hMSCs viability for any of the MSN tested. Based on these results, 70 and 140 µg/mL were selected for further studies.

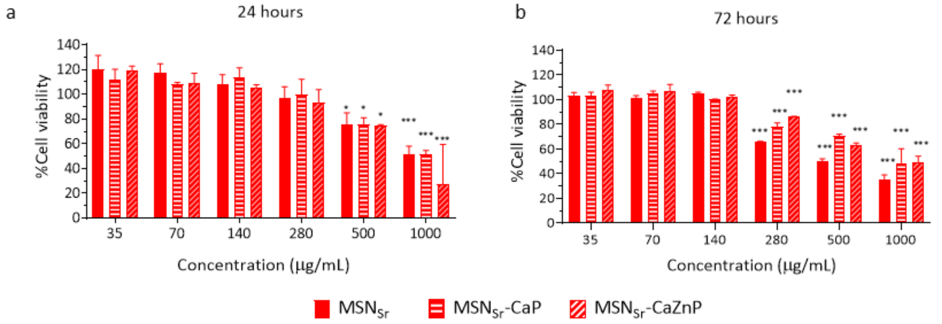

Figure 3: hMSCs metabolic activity of MSN_{Sr}, MSN_{Sr}-CaP and MSN_{Sr}-CaZnP at concentrations ranging from 35-1000 µg/mL after a) 24 and b) 72 hours of exposure using the MTT assay.

Cell viability is shown as % compared to control cells (not incubated with MSN). Significant differences between sample groups and control groups are shown by * representing p-values as follows; *$p < 0.033$; **$p < 0.02$; ***$p < 0.001$.

Next, hMSCs internalization of fluorescently core labeled MSN_{Sr}, MSN_{Sr}-CaP and MSN_{Sr}-CaZnP was visualized using fluorescent and confocal microscopy (Figure 4a, Figure S5). Nanoparticles could be observed within hMSCs, where hMSC morphology remained intact (Figure 4a). Moreover, orthogonal sectioning using confocal microscopy revealed that the nanoparticles spread throughout the hMSCs and were internalized (Figure S5). hMSCs uptake of MSN_{Sr}, MSN_{Sr}-CaP and MSN_{Sr}-CaZnP after 6 and 24 hours were further quantitatively analyzed using flow cytometry. All three types of MSN were internalized relatively fast after 6 hours of exposure; over 95 % of hMSCs were positive for nanoparticle uptake (Figure 4b, left panel). Furthermore, MSN_{Sr}-CaP and MSN_{Sr}-CaZnP showed higher uptake compared to MSN_{Sr}, indicating that the CaP coating positively affected nanoparticle cell uptake. After 24 hours, 83.6% (MSN_{Sr}), 89% (MSN_{Sr}-CaP) and 79.5% (MSN_{Sr}-CaZnP) of hMSCs had internalized nanoparticles (Figure 4b, right panel).

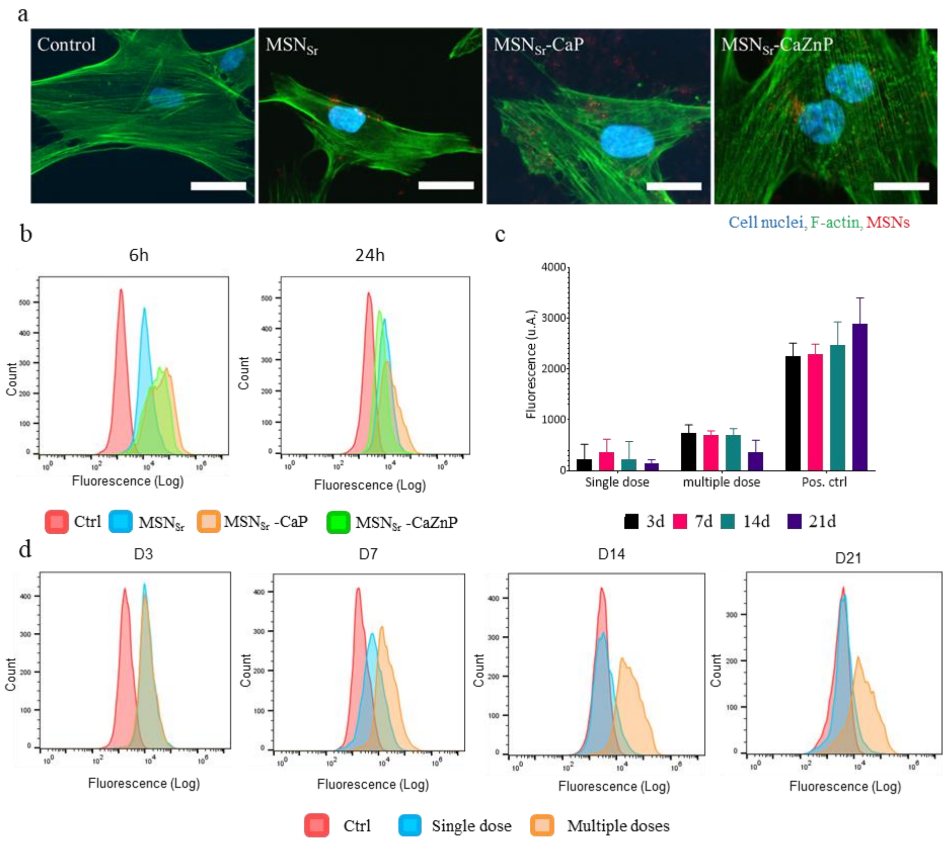

Figure 4: MSN internalization in hMSCs. a) Fluorescence microscopy images of hMSCs exposed to MSN_{Sr}, MSN_{Sr}-CaP and MSN_{Sr}-CaZnP at 140 µg/ml for 6 h. Cells stained for nuclei (dapi; blue) and actin (phalloidin 488; green). MSN are shown in red. Scale bars are 50 µm. b) flow cytometry histograms of hMSCs exposed to MSN_{Sr}, MSN_{Sr}-CaP and MSN_{Sr}-CaZnP at140 µg/ml for 6 and 24 h. c) Fluorescence intensity of labelled MSN_{Sr}-CaZnP in supernatant after 3, 7, 14 and 21 days of culture measured by a microplate reader. Positive control (Pos. ctrl) is cell culture media with 140 µg/mL labelled MSN_{Sr}-CaZnP. d) Flow cytometry histograms of MSN_{Sr}-CaZnP uptake, by hMSCs exposed to single dose and multiple doses after 3, 7, 14 and 21 days of cell culture.

Next, we set out to investigate how long-term nanoparticle exposure, matching our hMSC osteogenic differentiation protocols of 21 days, affected hMSCs nanoparticle uptake. Since similar uptake for all three nanoparticle types was observed, MSN_{Sr}-CaZnP were chosen for this experiment. The effect of single and multiple doses (media change every 3 days) of 140 µg/ml MSN_{Sr}-CaZnP (termed MSN_{Sr}-CaZnP(s) and MSN_{Sr}-CaZnP (m), respectively) on their uptake efficiency in hMSCs was investigated using flow cytometry. The amount of MSN_{Sr}-CaZnP present in the cell culture media was also measured, and remained steady over-time even after multiple dose exposures (Figure 4c). This indicates that the cells did not excrete the nanoparticles.

After 3 days of exposure, no significant difference in nanoparticle uptake after single or multiple dose administration could be observed (86.6% for MSN_{Sr}-CaZnP(s), and 91.5% for MSN_{Sr}-CaZnP (m)). However, after 7 days, single dose exposure resulted in a lower signal and after 14 days no significant signal could be detected using flow cytometry (Figure 4d). In contrast, hMSCs exposed to MSN_{Sr}-CaZnP every three days maintained a similar nanoparticle uptake signal over time (Figure 4d).

In summary, here we showed that MSNs and CaP coated MSN are efficiently and rapidly taken up by hMSCs and that exposure every 3 days could maintain the nanoparticle uptake levels as observed by flow cytometry.

3.4 Alkaline Phosphatase (ALP) activity

Next, we assessed the ability of MSN_{Sr}, MSN_{Sr}-CaP and MSN_{Sr}-CaZnP to induce enzymatic ALP activity. ALP plays a critical role in hard tissue formation by facilitating mineralization and reducing pyrophosphate concentrations, a mineralization inhibitor [36]. hMSCs were exposed to single and multiple doses (70 and 140 µg/mL) of the three nanoparticles in basic media (no osteogenic stimulants) and ALP activity was measured after 14 and 21 days (Figure 5). In addition, hMSCs cultured in osteogenic media (OS) were included as positive control. The data was normalized for DNA content and expressed relative to ALP activity of hMSCs in basic medium.

After 14 days, a significant change in ALP activity was observed in hMSCs exposed to multiple doses of 140 µg/mL of MSN_{Sr}-CaP and MSN_{Sr}-CaZnP. In contrast, multiple dose administrations of MSN_{Sr} only led to a 1.59 fold upregulation of ALP activity (Fig 5a).

After 21 days, hMSCs exposure to multiple doses of 140 µg/mL of all three MSN led to a significant increase in ALP activity, (3.5, 3.4, and 3.5 fold for MSN_{Sr}, MSN_{Sr}-CaP and MSN_{Sr}-CaZnP, respectively). Although no significant increase in ALP activity could be observed for single administrations for the three tested MSN after 14 days, a single dose of MSN_{Sr}-CaZnP was sufficient to significantly increase ALP levels (2.58-fold) after 21 days of exposure. In addition, multiple doses at a lower concentration (70 µg/mL) of MSN_{Sr}-CaZnP also resulted in significant increased ALP activity after 21 days (2.66-fold; Figure 5b). Overall, all three MSN were able to induce ALP enzyme expression in hMSCs, where MSN_{Sr}-CaZnP were most effective also when applied at single and multiple lower doses.

Next, we assessed the ability of multiple doses of Ca, P, Zn and Sr ions dissolved directly in the cell culture media to induce ALP activity in hMSCs, in order to compare its effectiveness to the nanoparticles. Similar to MSN multiple dose exposure experiments, the media was refreshed every 3 days. Three different concentrations were chosen based on our experimental settings and values found in literature. Specifically, ion concentration set [1] consisted of bioinorganics present in the same concentrations as found in 140 µg/mL of MSN. Concentration set [2] and [3] corresponded to ion concentrations found in literature that are known to increase ALP activity in hMSCs (Table 4) [6, 16, 37-42].

Addition of Sr or Ca and P at the highest tested concentration [3] resulted in increased ALP activity after 7, 14 and 21 days (Figure 5). Interestingly, when Sr, Ca, P or Sr, Ca, P and Zn were presented together in cell medium, significant ALP induction was also observed at lower concentrations [1] and [2], albeit significantly lower (below 2-fold) than what was observed after exposure to the nanoparticles.

No significant ALP induction was observed when hMSCs were exposed to the concentrations as found in the MSN (concentration [1]) (Figure 5). This indicates that the concentration of ions required to increase ALP activity in hMSCs are much lower when administered via MSN constructs compared to dissolving ions directly in the medium (Table. 4). In fact, the effective concentrations required for direct ion supplementation were significantly higher compared to administration using MSN (specifically; 276 times for Sr, 207 times for Ca, 66 times for P, and 1073 times for Zn). Thus, multiple ions administered via MSN appear to be more effective in inducing ALP expression than multiple administration of the same ions dissolved within medium.

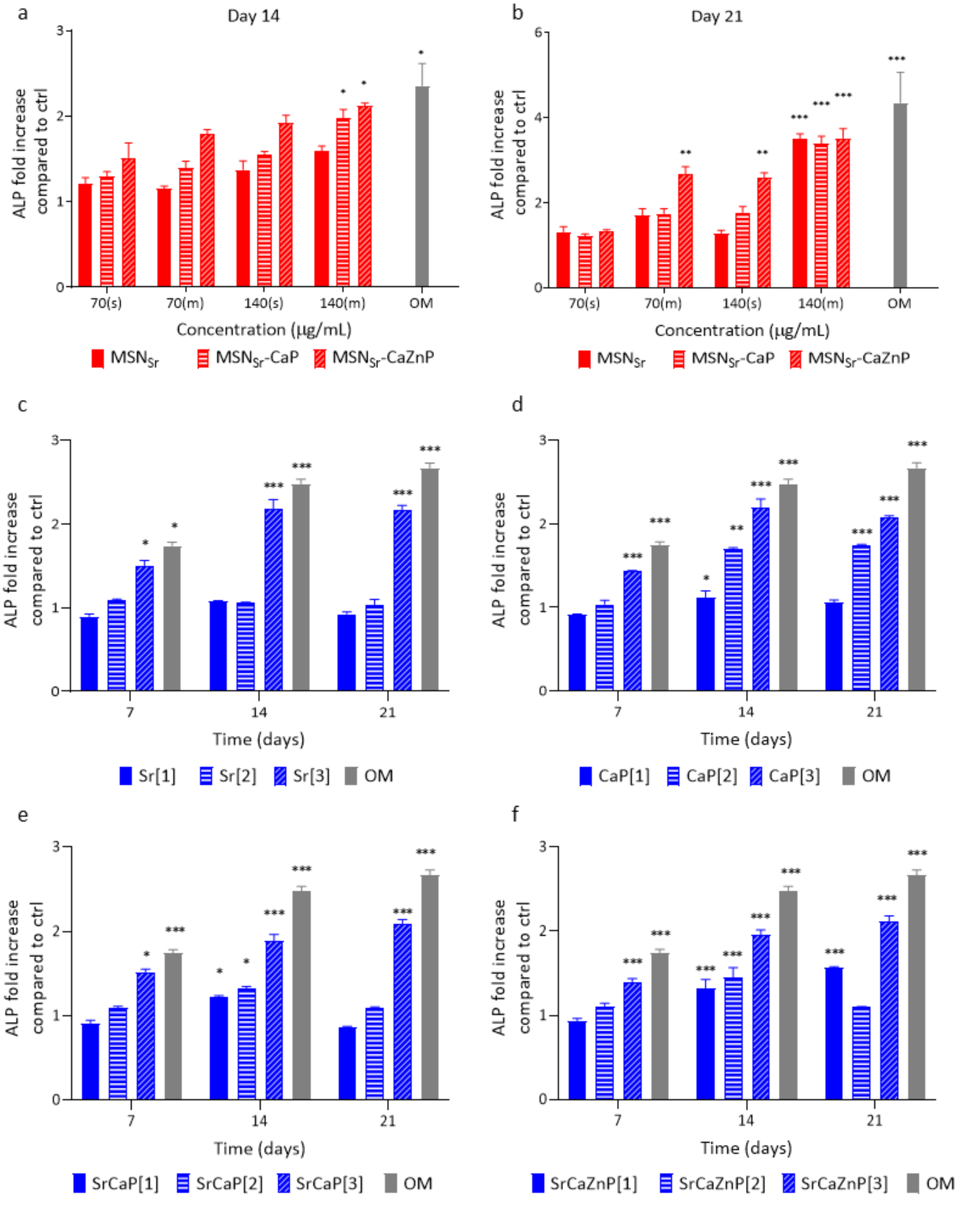

Figure 5: Relative ALP activity in hMSCs after exposure to MSN (a, b) or ions directly dissolved in media (c-f). hMSCs were exposed to a single dose (s) or multiple doses (m) of

70 µg/mL or 140 µg/mL of MSN_{Sr}, MSN_{Sr}-CaP and MSN_{Sr}-CaZnP and ALP activity assayed after (a) 14 and (b) 21 days. hMSCs were further exposed to three concentrations sets of (c) Sr, (d) Ca and P, (e) Sr, Ca and P and (f) Sr, Ca, Zn and P dissolved in cell culture media. Concentration set [1] consisted of ion concentration as present in multiple doses 140 µg/mL of MSN_{Sr}, MSN_{Sr}-CaP or MSN_{Sr}-CaZnP, while concentration sets [2] and [3] corresponded to ion concentrations found in literature that are known to induce osteogenic markers expression in hMSCs. The data was normalized to hMSC DNA content. For all figures, error bars indicate one standard deviation among the triplicate. Significant difference compared to the controls are shown by * representing p-values as follows; *p < 0.033; **p < 0.02; ***p < 0.001.

Table 4: Sr, Ca, P and Zn ions concentrations dissolved in cell culture medium

Sample code	Concentration [1]	Concentration [2]	Concentration [3]
Sr	0.723 µM	25 µM	200 µM
CaP	Ca 96.25 µM P 74.637µM	1.8 mM 0.09 mM	20 mM 5 mM
SrCaP	Sr 0.723 µM Ca 96.25 µM P 74.637 µM	25 µM 1.8 mM 0.09 mM	200 µM 20 mM 5 mM
SrCaZnP	Sr 0.723 µM Ca 96.25 µM P 74.637 µM Zn 9.31478 µM	25 µM 1.8 mM 0.09 mM	200 µM 20 mM 5 mM 10 mM

3.5 Osteogenic gene expression and mineralization

Next, the effect of the MSN on known early, middle and late osteogenic markers were tested using qPCR and compared to ions directly dissolved in the medium. Specifically, early osteogenic marker expression

(BMP2 and RUNX2) were quantified after 7 and 14 days. RUNX2 is effective in the first stage of bone formation where mesenchymal precursors commit to the osteoblast differentiation lineage, and BMP2 is related to regulating the bone marrow matrix microenvironment and promoting osteogenic differentiation of hMSCs [43]. Intermediate osteogenic marker (OPN), which participates in bone remodelling via promoting osteoclastogenesis and osteoclast activity [44], was quantified after 14 days. Finally, late osteogenic and mineralization marker (OCN) [45], and matrix production (Col1) [46] marker expression were quantified after 21 days. Similar to the ALP assay, hMSCs were exposed to 140 µg/ml MSN, where a media change took place every 3 days (labelled as MSN_{Sr} (m), MSN_{Sr}-CaP (m) and MSN_{Sr}-CaZnP (m)). A single dose of 140 µg/ml MSN_{Sr}-CaZnP was also included (labelled as MSN_{Sr}-CaZnP(s)), and cells in OS medium were included as positive control. Based on our previous results, we selected Sr, SrCaP and SrCaZnP ions dissolved in the medium at the highest concentration [3] for these experiments. Importantly, basic media (without addition of osteogenic molecules) was used for all of our sample conditions.

PCR analysis showed that all tested MSN, and their respective ions dissolved in medium at concentration [3] (Table 4) could significantly induce the expression of several osteogenic markers in hMSCs relative to the controls (Figure 6a-h). Interestingly, an increased effect on osteogenic gene expression could be observed when ions were used in combination, independent of how the ions were administered.

Specifically, after 7 and 14 days, hMSCs exposed to MSN_{Sr}-CaP (m) and MSN_{Sr}-CaZnP (m) showed significantly increased RUNX2 expression

(Figure 6a,b). Ion concentrations Sr[3], SrCaP[3] and SrCaZnP[3] resulted in significantly increased RUNX2 expression only after 14 days of exposure.

After 7 days of exposure, BMP2 expression was significantly upregulated for hMSCs exposed to MSN$_{Sr}$-CaP and MSN$_{Sr}$-CaZnP. After 14 days, all MSN significantly induced BMP2 expression. Similarly, the addition for individual ions resulted in increased BMP2 expression after 14 days, except for Sr[3] (Figure 6c,d).

After 14 days of exposure, MSN$_{Sr}$-CaP (m) and MSN$_{Sr}$-CaZnP (m) also significantly induced OPN expression. While hMSCs exposed to MSN$_{Sr}$ (m) also showed an increase in OPN expression, the upregulation was relatively low compared to the other groups (1.86 fold). After 21 days, all MSN conditions significantly increased OPN expression, where MSN$_{Sr}$-CaP (m) and MSN$_{Sr}$-CaZnP (m) resulted in the highest induction. Similarly, medium containing combinations of ions (i.e. SrCaP[3] and SrCaZnP[3]) resulted in increased OPN expression already after 14 days (Figure 6e), and all ion conditions led to upregulated OPN after 21 days of exposure (Figure 6f).

After 21 days of exposure, OCN was significantly expressed after exposure to MSN with the exception of single administration of MSN$_{Sr}$-CaZnP(s). Also with this marker, increased levels were observed when a CaP layer on the MSN was present (Fig 6g). Similarly, all conditions using ions dissolved in media led to increased OCN expression after 21 days exposure.

Finally, all MSN conditions, except for single administration of MSN$_{Sr}$-CaZnP, led to increased expression of Col1 (Figure 6h). Significantly, increased Col1 gene expression was also observed for conditions when multiple ions were used.

To assess whether our nanoparticles could also induce the transition from osteoblast to osteocyte, gene expression of osteocyte marker podoplanin (E11) was evaluated. Podoplanin is a known marker that is upregulated during the embedding of osteocytes in a mineralized matrix [47-50]. We compared podoplanin induction to RUNX2 expression after 14 and 21 days (Figure 7). Significantly increased podoplanin expression could be observed after 21 days of exposure to MSN_{Sr}-CaP (m), MSN_{Sr}-CaZnP(m) and SrCaZnP[3]. Conversely, a trend towards a lower expression of Runx2 was observed after 21 days of culture, although not significant. This data indicates that the overall population is transitioning to osteocytes in conditions when multiple ions are present and after longer exposure times.

Next, we investigated the effect of the nanoparticles and dissolved ions on hMSCs mineralization using Alizarin red staining. hMSCs cultured in basic and mineralization media were used as negative and positive controls, respectively. hMSCs cultured in basic media did not show any signs of mineralization (Figure 8a). In contrast, hMSCs exposed to multiple doses of the three types of MSN showed high mineralization (Figure 8b-i). All three ion conditions also resulted in significant mineralization. Exposure to a single dose of MSN_{Sr}-CaZnP was not sufficient to promote significant mineralization in hMSCs (Figure 8e, j).

Furthermore, the amount of calcium deposited by hMSCs exposed to MSN_{Sr}(m) and MSN_{Sr}-CaP(m) was similar (0.445 mM and 0.467 mM respectively), while hMSCs cultured with MSN_{Sr}-CaZnP(m) showed highest amount of calcium deposition (0.823 mM; Figure 8j). In contrast, single administration of MSN_{Sr}-CaZnP resulted in only 0.0388 mM of calcium deposition. Thus, multiple exposures to MSN_{Sr}, MSN_{Sr}-CaP and MSN_{Sr}-CaZnP promoted the mineralization process during osteogenesis of hMSCs, where MSNs with a CaP and CaZnP layer showed the highest effect. This was also observed for the hMSCs exposed to ions dissolved in medium, where high mineral deposition was observed for SrCaP[3] and SrCaZnP[3] (0.722 mM and 0.869 mM, respectively) and relatively low mineral deposition for hMSCs exposed to Sr[3] (0.237 mM).

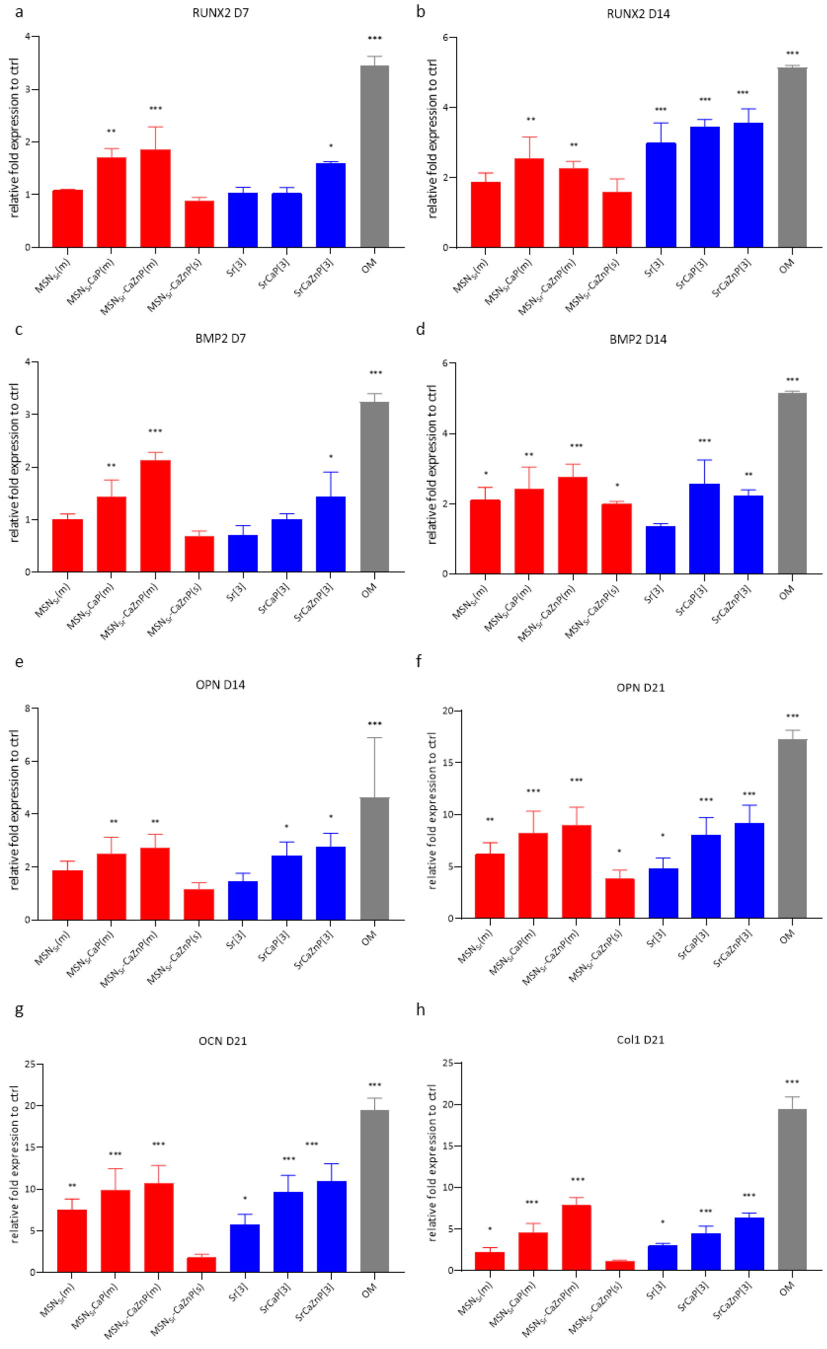

Figure 6: hMSCs mRNA expression of RUNX2 at (a) 7 and 14 (b) days; BMP2 at 7 (c) and 14 (d) days; OPN at (e) 14 and (f) 21 days, OCN at (g) 21 days, and Col I at (h) 21 days after exposure to MSN (MSN$_{Sr}$(m), MSN$_{Sr}$-CaP(m) MSN$_{Sr}$-CaZnP(m), and MSN$_{Sr}$-CaZnP(s)) and

medium dissolved ions (Sr[3], SrCaP[3] and SrCaZnP[3]) in basic conditions. The results were normalized to GAPDH as housekeeping gene and calibrated to mRNA level of the respective markers in hMSCs cultured with basic media as the control. hMSCs cultured with osteogenic medium (OM) were used as positive control. Significant difference between sample and basic control groups are shown by * representing p-values as follows; $^*p < 0.033$; $^{**}p < 0.02$; $^{***}p < 0.001$.

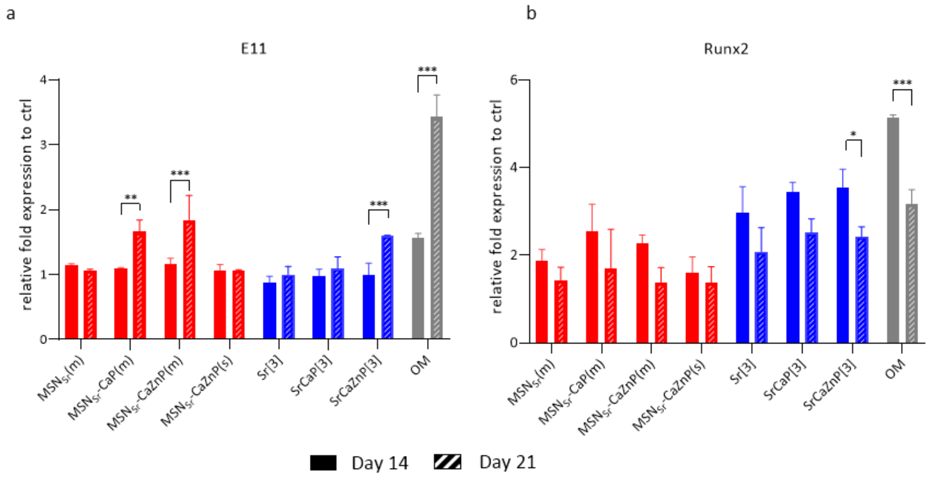

Figure 7: hMSCs mRNA expression of (a) Runx2 and (b) E11 at 14 and 21 days after exposure to nanoparticles composites (red) and ions (blue). All condition were cultured in basic cell culture media. The results were normalized to GAPDH as housekeeping gene and calibrated to mRNA level of the respective markers in hMSCs cultured with basic media as the control. hMSCs cultured with osteogenic medium (OM) were used as positive control (grey). Significant difference between day 14 and day 21 samples are shown by * representing p-values as follows; $^*p < 0.033$; $^{**}p < 0.02$; $^{***}p < 0.001$.

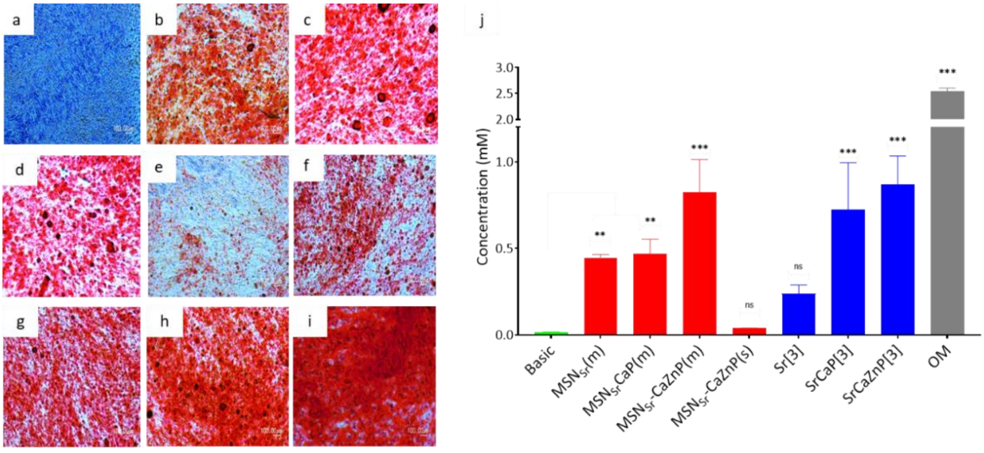

Figure 8: Light microscopy images of mineral formation by hMSCs (n=3) when cultured in (a) basic medium, (b) medium containing MSN_{Sr}(m), (c) MSN_{Sr}-CaP(m), (d) MSN_{Sr}-CaZnP(m), (e) MSN_{Sr}-CaZnP(s), (f) Sr[3], (g) SrCaP[3], and (h) SrCaZnP[3] compared to (i) osteogenic medium (OM). Calcium minerals were stained with Alizarin Red S. (j) Quantification of calcium content at day 28 was performed using a de-staining method. Significant difference between samples and control groups are shown by * representing p-values as follows; $*p < 0.033$; $**p < 0.02$; $***p < 0.001$, ns means non-significant.

4. Discussion

In this work we developed MSN incorporating Sr and coated with a pH sensitive CaP or CaZnP layer. Doping ceramic nanoparticles and scaffolds with different bioactive ions is a popular strategy in the field to further improve their bone regenerative capabilities. Many examples are known especially in the bioactive glass field where doping with strontium, zinc, copper amongst others has resulted in nanoparticles with improved bone regenerative capabilities [4-6]. While there are several studies using MSN to deliver known osteogenic stimulants such as dexamethasone and BMP-2 [51], the use of MSN for ion delivery is still limited explored. There are only several reports where MSN were used to deliver therapeutic ions for bone regeneration purposes [52-54]. In these studies the ions are doped within the silica matrix, where particle degradation is needed to allow ion release. There are no studies looking into using MSN as stable carriers for multiple ion delivery as we have presented here. To facilitate their delivery, we surface grafted CaP onto MSN to act both as pH sensitive gating system to prevent Sr release and to facilitate delivery of CaP ions upon nanoparticle uptake in hMSCs. Previously it has been reported that MSN are actively taken up by MSCs via endocytosis [31, 32], which involves the formation of acidic endosomal vesicles containing an average pH of 5. CaP solubility is dependent on its crystallinity and pH and CaP solubility dramatically increases below pH 6.0 [55]. Several other examples exist where CaP surface modified MSN have been used for pH responsive drug delivery of anticancer drugs [56-58]. Our method used direct CaP precipitation on carboxylic acid surface modified MSN, similar to a previously published method [56-58]. We modified the procedure to also create carboxyl group within the mesopores to increase Sr ion loading capacity of the MSN. In addition, we modified the protocol to also introduce Zn on the CaP surface coating, as zinc is a popular additive to promote bone regeneration in dentistry and orthopedic applications [59].

The developed MSN were efficiently taken up by hMSCs. Our results further showed that CaP coating of MSN increases their uptake. This is in line with other studies showing that various nanoparticle structural features including size, shape, and surface chemistry and charge effect nanoparticle cell internalization [60]. Several studies suggest that the majority of MSN uptake by hMSCs goes via clathrin-mediated endocytosis but also involves unknown pathways [31, 32]. The MSC uptake mechanism of CaP nanoparticles seems to involve not only clathrin-mediated endocytosis but also ATP-dependent endocytosis [61].

After single dose exposure, the nanoparticle signal disappeared within 7 days, however, there was no increase in fluorescence in the cell culture media indicating that the cells did not excrete the nanoparticles. Although there are only a few studies that have looked into the long-term uptake of MSN in MSCs, our data is in line with what others and we have previously reported. Huang et al. demonstrated that FITC-labelled MSN could still be observed by confocal microscope 21 days after single exposure to hMSCs. However the percentage of positively labelled hMSCs could only be detected up to 7 days via flow cytometry indicating that the particle number per cell reduced over-time due to the cell proliferation [62]. In our previous study, we observed that the MSN signal was halved after every cell passage, resulting in the loss of signal in flow cytometry after about 15 days [33, 34]. Here we showed that when we expose the hMSCs to multiple doses in 3 day intervals, the level of nanoparticle uptake can be maintained over 21 days when observed using FACS analysis. Moreover, although we did not test this condition, our data indicates that administration every 7 days would also be sufficient to maintain nanoparticle levels.

Taken together, our ALP activity, gene expression and mineralization data demonstrated that MSN incorporating Sr and coated with CaZnP layer (MSN_{Sr}-CaZnP) were most osteogenic. MSN_{Sr}-CaZnP could significantly induce early, middle and late osteogenic markers in hMSCs at all tested time points and led to pronounced mineralization. MSN containing only Sr ions (MSN_{Sr}) were least effective, indicating that there is an additive effect when using multiple ions within a single nanoparticle construct. This additive effect was also observed in the conditions where ions were added directly to the cell culture media; also here Sr[3] was the least effective condition, whereas SrCaZnP[3] showed the strongest osteogenic gene induction and most pronounced mineralization. The effects of combining bioinorganic ions have only limitedly been explored. Several studies have shown that incorporating Sr, Si or Zn ions into CaP scaffolds improves bone formation capabilities compared to scaffolds without additional ions [21-23]. Mao et al. compared the effect of Sr and Si media extract from β-TCP to Sr and Si ions alone in similar concentrations on osteoblast cells. It was found that Sr and Si ions possessed synergistic effects by upregulating the expression of osteogenic gene OCN and angiogenic gene VEGF in rBMSCs-OVX cells [21]. Jia et. al. has previously shown that ALP, OCN and Col I were upregulated when mouse osteoblasts were exposed to a combination of Zn and Sr released from Zn-Sr alloy submerged in media compared to pure Zn [22]. To our knowledge, our study is the first to use a single nanoparticle construct to deliver a combination of SrCaP and SrCaZnP ions to hMSCs, and to demonstrate that this has positive effects on osteogenic marker expression.

Although the ions dissolved in the medium had a similar effect on the osteogenic gene expression in hMSCs as the ion incoprorated MSN, the concentrations required to obtain this effect by directly dissolving ions in the medium was significantly higher. Indeed, the cumulative ion concentration present in the nanoparticles was 134 (P), 208 (Ca), 277 (Sr) and 538 (Zn) times lower compared to respective ions when dissolved in the cell culture medium (Table 4). When exposing hMSCs to the same effective ion dose in the cell culture medium as was present in the ions-functionalized MSN, no significant ALP activity was observed (Figure 5). This difference may be due to different uptake routes: where nanoparticle internalization in hMSCs is known to involve endocytosis, ions are generally taken up via ion channels. By surface-coating the particles with a CaP coating that is degradable only at lower pH, the ion dissolution only takes place at low pH values such as those found in endosomes, while they remain stable at pH 7. This pH responsive mechanism likely decreased their effective dose by preventing unwanted release of ions when not internalized. Importantly, our MSN could induce osteogenesis in hMSCs without the presence of any other osteogenic stimulants in the media (e.g. under basic conditions). Another advantage of using our MSN composites is that the administration dose and frequency can potentially be reduced. Even though we did not test other conditions, our flow cytometry data suggests that administering the nanoparticles every 7 days should also be effective. This advantage combined with lower effective doses, make our developed MSN-CaP promising constructs for use in bone regeneration applications.

5. Conclusions

Bioinorganic ions are promising additives in bone regenerative biomaterial based strategies to stimulate bone and blood vessel formation. However, local ion release and dosage control are critical to prevent adverse side effects. In this study, we demonstrated that silica based nanoparticles (MSN) incorporating Sr ions and coated with CaP or CaZnP layers are promising ion carriers for bone regenerative strategies. The CaP or CaZnP coat acted as a pH-sensitive gating system with rapid ion release when in acidic conditions.

Our developed MSN could efficiently induce the expression of early, middle and late osteogenic markers in the absence of other stimulators of osteogenic differentiation. While all the MSN tested here had a stimulatory effect, MSN containing CaZnP surface coating were most osteogenic while MSN without CaP coat (MSN_{Sr}) were least effective, indicating an additive effect when delivering multiple bioinorganic ions using MSN. To our knowledge, our study is the first to use a single nanoparticle construct to deliver a combination of Sr, Ca, Zn, P ions, and to demonstrate that this has positive effects on osteogenic marker expression in hMSCs. Furthermore, our MSN promoted osteogenic marker expression in hMSCs at a much lower dose compared to adding the same ions but directly dissolved in the cell culture media, likely due to different cell internalisation uptake routes. As such, the developed MSN represent a promising strategy to decrease ion dosage and effectively induce hMSCs osteogenesis. A further in-depth understanding of how ion dosing and possible synergy influences not only osteogenesis but also other regenerative processes such as angiogenesis could potentially maximize their use in bone regeneration approaches.

The type of MSN developed here could be easily applied in injectable biomaterials and printable scaffolds used for bone regeneration purposes without impairing their mechanical properties. Additional advantages of using MSN is that they allow ion release and dosage control, and they can be surface modified to target cells. Considering these advantages combined with lower effective and less required administration doses, the MSN developed here represent promising constructs for use in bone regeneration applications.

Acknowledgements

The authors thank Dr. Eva Gubbins for technical assistance with ICP-MS and Maria José Eischen-Loges with primers design. The authors thank Timo Rademakers for help with confocal microscopy imaging. This research was financially supported by the Gravitation Program “Materials Driven Regeneration,” funded by the Netherlands Organization for Scientific Research (024.003.013) and Royal Thai Government Scholarship Program (offered by OCSC). Z.T.B. gratefully acknowledges the NWO Incentive Grant for Women in STEM (Project “Biotetris”; grant no. 18748).

Conflict of Interest

The authors declare no conflict of interest.

Supplementary data

S.1 Synthesis of core-labelled MSN

To synthesize MSN with amines on the surface, a mixture of 1.63 g TEOS (7.82 mmol), MPTES (112 mg, 0.48 mmol) and 14.3 g TEA (95.6 mmol) was heated to 90 °C under static conditions (Solution 1). Solution 2 included 100 mg ammonium fluoride (2.70 mmol) dissolved in a solution of 2.41 ml CTAC (1.83 mmol, 25% (wt) in H_2O) and 21.7 ml bi-distilled water (1.21 mmol) by heating to 60 °C. Solution 2 was rapidly added to solution 1, and the mixture was stirred vigorously at 700 rpm for 20 min while left to cool. Then, 138.2 mg TEOS (0.922 mmol) was added in four equal increments (34.55 mg each) every 3 minutes. The solution was then left stirred overnight at room temperature. The particles were then collected by centrifugation at 7800 rpm for 20 min and washed once with ethanol. Template extraction was performed by dispersion into an ammonium nitrate in ethanol solution (2 g NH4NO3 in 100 ml ethanol) and refluxed for 45 minutes at 90 °C. MSN were collected by centrifugation and washed with ethanol before further template extraction in 100 ml of a 3.7% hydrochloric acid solution in ethanol for 45 minutes at 90 °C. MSN were collected by centrifugation, washed twice with ethanol and stored in suspension at -20 °C. The thiol groups functionalized core of the MSN were labelled with ATTO-647-Maleimide to create fluorescent core labeled MSN.

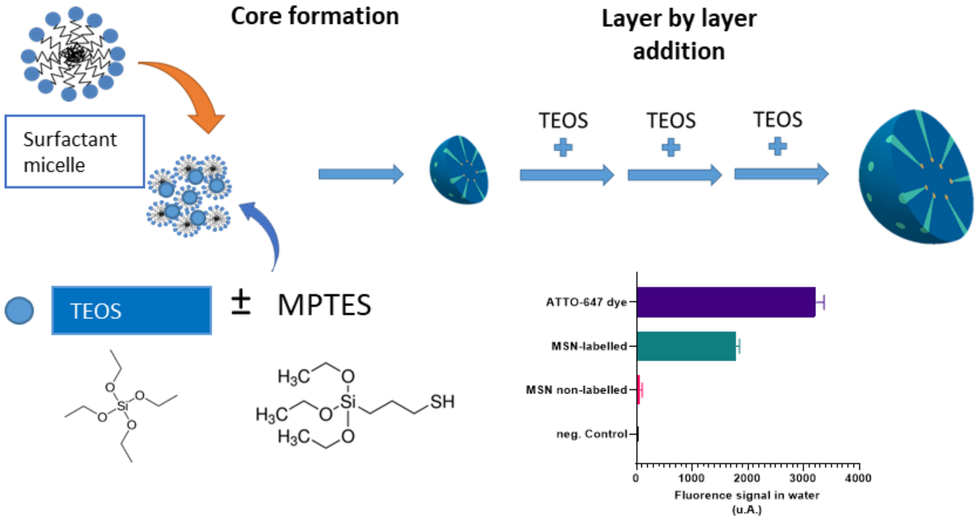

Figure S1: Synthesis scheme of core-labelled MSN. Thiol groups core functionalization MSN were further confirmed by labelled with ATTO-647-Maleimide and measured in a microplate reader (BIO-RAD) at 647 nm.

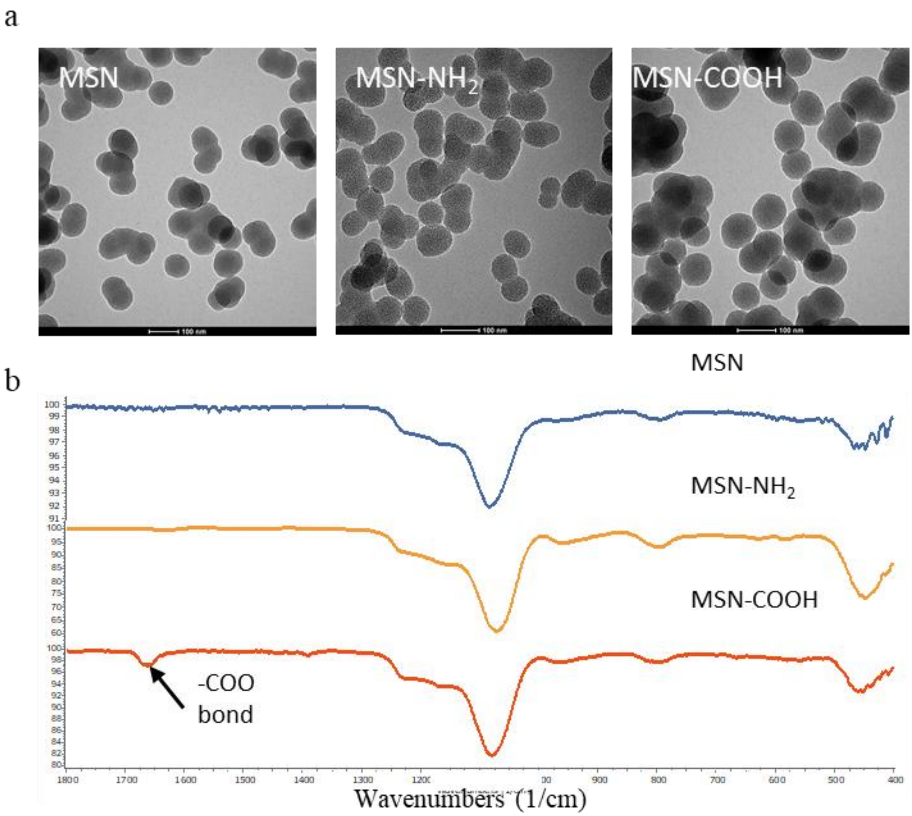

Figure S2: Characterization of MSN, MSN-NH2 and MSN-COOH. a) TEM images show spherical-shaped porous structure for all nanoparticles. b) FTIR spectra of MSN, MSN-NH$_2$ and MSN-COOH.

Table S1: Hydrodynamic size, polydispersity index (Pdi) and zeta potential of MSN, MSN-NH_2 and MSN-COOH in ethanol measured by DLS.

Sample	Hydrodynamic size in ethanol (nm)	Pdi	Zeta potential
MSN-OH	188±1.47	0.107	-20.6±0.13
MSN-NH_2	195.8±0.56	0.09	+19.6±0.31
MSN-COOH	203±2.1	0.27	-17.7±0.2

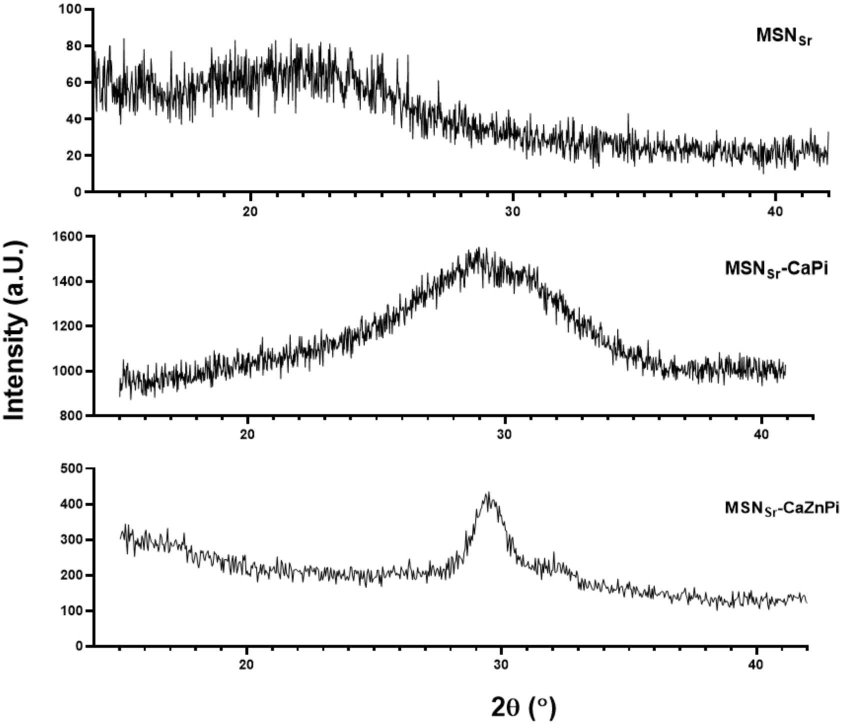

Figure S3: XRD patterns of MSN$_{Sr}$, MSN$_{Sr}$-CaP and MSN$_{Sr}$-CaZnP displayed amorphous non-crystallization of all nanoparticles.

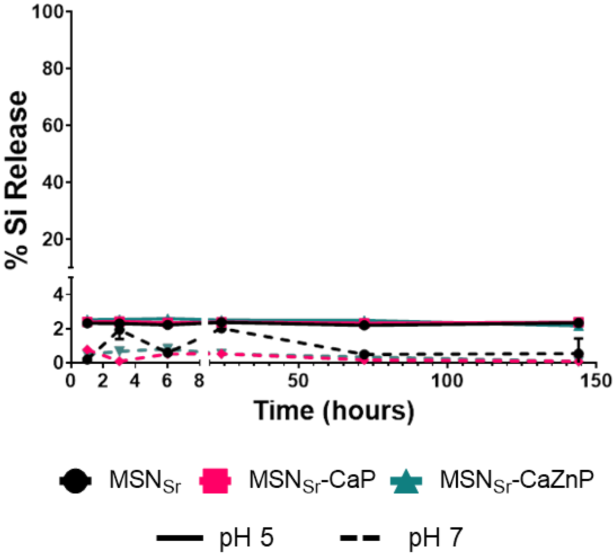

Figure S4: Silica ions release profiles of MSN$_{Sr}$ (black), MSN$_{Sr}$-CaP (blue) and MSN$_{Sr}$-CaZnP (red) in cacodylate buffer with pH 5 (solid lines) and 7.4 (dashed lines) analysed by ICP-MS.

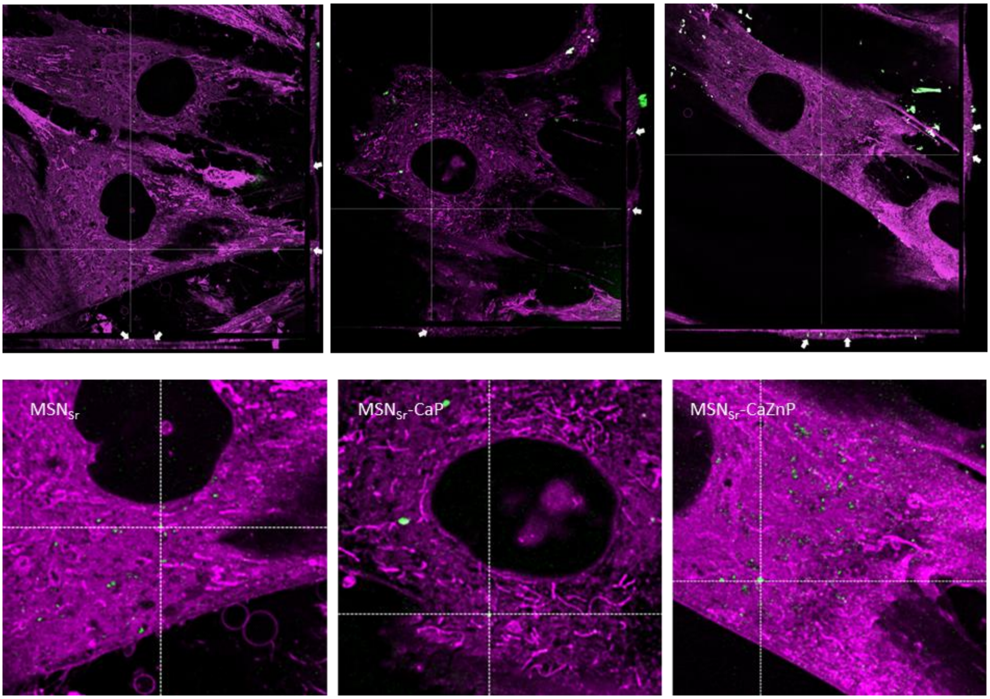

Figure S5: Confocal microscopy images of hMSCs exposed to 140 µg/ml (a) MSN$_{Sr}$, (b) MSN$_{Sr}$-CaP and (c) MSN$_{Sr}$-CaZnP for 6 hours. Cells were washed with PBS 3 times to remove non-internalized MSNs. Cell bodies were labelled with CellMask (in purple). Core labelled MSN are shown in green. Arrows in orthogonal sections indicate the MSN located within the cell body and not on the surface of cell membrane. Lower panel illustrates a magnification of the cells showing nanoparticle distribution in the cells.

References

1. S. Pina, R. Rebelo, V. M. Correlo, J. M. Oliveira and R. L. Reis, Osteochondral Tissue Eng., 2018, Bioceramics for osteochondral tissue engineering and regeneration, 53-75.
2. J. R. Jones, D. S. Brauer, L. Hupa and D. C. Greenspan, Int. J. Appl. Glass Sci., 2016,Bioglass and bioactive glasses and their impact on healthcare, 7, 423-434.
3. W. Wang and K. W. Yeung, Bioact. Mater., 2017, Bone grafts and biomaterials substitutes for bone defect repair: A review, 2, 224-247.
4. H. Zhu, K. Zheng and A. R. Boccaccini, Acta Biomater., 2021, Multi-Functional Silica-based mesoporous materials for simultaneous delivery of biologically active ions and therapeutic biomolecules.
5. S. An, Q. Gong and Y. Huang, Biol. Trace Elem. Res., 2017, Promotive effect of zinc ions on the vitality, migration, and osteogenic differentiation of human dental pulp cells, 175, 112-121.
6. S. Nakamura, T. Matsumoto, J.-I. Sasaki, H. Egusa, K. Y. Lee, T. Nakano, T. Sohmura and A. Nakahira, Tissue Eng. Part A, 2010, Effect of calcium ion concentrations on osteogenic differentiation and hematopoietic stem cell niche-related protein expression in osteoblasts, 16, 2467-2473.
7. V. Rosen, Cytokine Growth Factor Rev., 2009, BMP2 signaling in bone development and repair, 20, 475-480.
8. S. Bose and S. Tarafder, Acta Biomater., 2012, Calcium phosphate ceramic systems in growth factor and drug delivery for bone tissue engineering: a review, 8, 1401-1421.
9. E. Bosch-Rué, L. Diez-Tercero, B. Giordano-Kelhoffer, L. M. Delgado, B. M. Bosch, M. Hoyos-Nogués, M. A. Mateos-Timoneda, P. A. Tran, F. J. Gil and R. A. Perez, Front. Cell Dev. Biol. , 2021,Biological roles and delivery strategies for ions to promote osteogenic induction, 8, 1809.
10. E. O’Neill, G. Awale, L. Daneshmandi, O. Umerah and K. W.-H. Lo, Drug Discov. Today., 2018, The roles of ions on bone regeneration, 23, 879-890.
11. F. Yang, D. Yang, J. Tu, Q. Zheng, L. Cai and L. Wang, Stem Cells, 2011, Strontium enhances osteogenic differentiation of mesenchymal stem cells and *in vivo* bone formation by activating Wnt/catenin signaling, 29, 981-991.
12. L. Zhao, H. Wang, K. Huo, X. Zhang, W. Wang, Y. Zhang, Z. Wu and P. K. Chu, Biomaterials, 2013, The osteogenic activity of strontium loaded titania nanotube arrays on titanium substrates, 34, 19-29.
13. E. Gentleman, Y. C. Fredholm, G. Jell, N. Lotfibakhshaiesh, M. D. O'Donnell, R. G. Hill and M. M. Stevens, Biomaterials, 2010, The effects of strontium-substituted bioactive glasses on osteoblasts and osteoclasts *in vitro*, 31, 3949-3956.
14. B. S. Moonga and D. W. Dempster, J. Bone Miner. Res., 1995, Zinc is a potent inhibitor of osteoclastic bone resorption *in vitro*, 10, 453-457.
15. D. S. Brauer, E. Gentleman, D. F. Farrar, M. M. Stevens and R. G. Hill, Biomed. Mater., 2011, Benefits and drawbacks of zinc in glass ionomer bone cements, 6, 045007.
16. G. Jin, H. Cao, Y. Qiao, F. Meng, H. Zhu and X. Liu, Colloids Surf. B, 2014, Osteogenic activity and antibacterial effect of zinc ion implanted titanium, 117, 158-165.

17. Y. Yu, K. Liu, Z. Wen, W. Liu, L. Zhang and J. Su, RSC Adv., 2020, Double-edged effects and mechanisms of Zn 2+ microenvironments on osteogenic activity of BMSCs: Osteogenic differentiation or apoptosis, 10, 14915-14927.

18. J. Barralet, U. Gbureck, P. Habibovic, E. Vorndran, C. Gerard and C. J. Doillon, Tissue Eng. Part A, 2009, Angiogenesis in calcium phosphate scaffolds by inorganic copper ion release, 15, 1601-1609.

19. Z. T. Birgani, E. Fennema, M. J. Gijbels, J. De Boer, C. A. Van Blitterswijk and P. Habibovic, Acta Biomater., 2016, Stimulatory effect of cobalt ions incorporated into calcium phosphate coatings on neovascularization in an *in vivo* intramuscular model in goats, 36, 267-276.

20. A. M. Brokesh and A. K. Gaharwar, ACS Appl. Mater. Interfaces, 2020, Inorganic biomaterials for regenerative medicine, 12, 5319-5344.

21. L. Mao, L. Xia, J. Chang, J. Liu, L. Jiang, C. Wu and B. Fang, Acta Biomater., 2017, The synergistic effects of Sr and Si bioactive ions on osteogenesis, osteoclastogenesis and angiogenesis for osteoporotic bone regeneration, 61, 217-232.

22. B. Jia, H. Yang, Z. Zhang, X. Qu, X. Jia, Q. Wu, Y. Han, Y. Zheng and K. Dai, Bioact. Mater., 2021, Biodegradable Zn–Sr alloy for bone regeneration in rat femoral condyle defect model: *In vitro* and *in vivo* studies, 6, 1588-1604.

23. S. Bose, S. Tarafder, S. S. Banerjee, N. M. Davies and A. Bandyopadhyay, Bone, 2011, Understanding *in vivo* response and mechanical property variation in MgO, SrO and SiO2 doped β-TCP, 48, 1282-1290.

24. M. Gisbert-Garzarán, M. Manzano and M. Vallet-Regí, Pharm., 2020, Mesoporous silica nanoparticles for the treatment of complex bone diseases: Bone cancer, bone infection and osteoporosis, 12, 83.

25. S. van Rijt and P. Habibovic, J R Soc Interface, 2017, Enhancing regenerative approaches with nanoparticles, 14, 20170093.

26. Z. Li, Y. Zhang and N. Feng, Expert Opin. Drug Delivery, 2019, Mesoporous silica nanoparticles: synthesis, classification, drug loading, pharmacokinetics, biocompatibility, and application in drug delivery, 16, 219-237.

27. E. Aznar, M. Oroval, L. Pascual, J. R. Murguía, R. Martinez-Manez and F. Sancenon, Chem. Rev., 2016, Gated materials for on-command release of guest molecules, 116, 561-718.

28. N. Wang, M. Ma, Y. Luo, T. Liu, P. Zhou, S. Qi, Y. Xu and H. Chen, Chem. Nano. Mat., 2018, Mesoporous silica nanoparticles-reinforced hydrogel scaffold together with pinacidil loading to improve stem cell adhesion, 4, 631-641.

29. S. Shruti, A. J. Salinas, G. Lusvardi, G. Malavasi, L. Menabue and M. Vallet-Regi, Acta Biomater., 2013, Mesoporous bioactive scaffolds prepared with cerium-, gallium-and zinc-containing glasses, 9, 4836-4844.

30. Q. Yao, Y. Liu, B. Selvaratnam, R. T. Koodali and H. Sun, J Control Release, 2018, Mesoporous silicate nanoparticles/3D nanofibrous scaffold-mediated dual-drug delivery for bone tissue engineering, 279, 69-78.

31. Z. Li, J. C. Barnes, A. Bosoy, J. F. Stoddart and J. I. Zink, Chem. Soc. Rev, 2012, Mesoporous silica nanoparticles in biomedical applications, 41, 2590-2605.

32. J. L. Vivero-Escoto, I. I. Slowing, B. G. Trewyn and V. S. Y. Lin, Small, 2010, Mesoporous silica nanoparticles for intracellular controlled drug delivery, 6, 1952-1967.

33. R. Rosenbrand, D. Barata, P. Sutthavas, R. Mohren, B. Cillero-Pastor, P. Habibovic and S. van Rijt, Int. J. Nanomed., 2018, Lipid surface modifications increase mesoporous silica nanoparticle labeling properties in mesenchymal stem cells, 13, 7711.
34. L. Andrée, D. Barata, P. Sutthavas, P. Habibovic and S. van Rijt, Acta Biomater., 2019, Guiding mesenchymal stem cell differentiation using mesoporous silica nanoparticle-based films, 96, 557-567.
35. P. Sutthavas, P. Habibovic and S. H. van Rijt, Biomater. Sci., 2021, The shape-effect of calcium phosphate nanoparticle based films on their osteogenic properties, 9, 1754-1766.
36. S. Vimalraj, Gene, 2020, Alkaline phosphatase: Structure, expression and its function in bone mineralization, 754, 144855.
37. A. Aimaiti, A. Maimaitiyiming, X. Boyong, K. Aji, C. Li and L. Cui, Stem Cell Res. Ther., 2017, Low-dose strontium stimulates osteogenesis but high-dose doses cause apoptosis in human adipose-derived stem cells via regulation of the ERK1/2 signaling pathway, 8, 1-12.
38. Y.-Z. Huang, C.-G. Wu, H.-Q. Xie, Z.-Y. Li, A. Silini, O. Parolini, Y. Wu, L. Deng and Y.-C. Huang, Stem Cells Int., 2019, Strontium Promotes the Proliferation and Osteogenic Differentiation of Human Placental Decidual Basalis-and Bone Marrow-Derived MSCs in a Dose-Dependent Manner, 2019.
39. S. Current opinion in dentistryBose and S. Tarafder, Acta Biomater., 2012, Calcium phosphate ceramic systems in growth factor and drug delivery for bone tissue engineering: a review, 8, 1401-1421.
40. Q. Wang, S. Zhong, J. Ouyang, L. Jiang, Z. Zhang, Y. Xie and S. Luo, Clin. Orthop. Relat. Res., 1998, Osteogenesis of electrically stimulated bone cells mediated in part by calcium ions, 259-268.
41. S. An, Q. Gong and Y. Huang, Biol. Trace Elem. Res., 2017, Promotive effect of zinc ions on the vitality, migration, and osteogenic differentiation of human dental pulp cells, 175, 112-121.
42. X. Yang, Y. Li, X. Liu, Q. Huang, W. He, R. Zhang, Q. Feng and D. Benayahu, Biomed. Mater., 2016, The stimulatory effect of silica nanoparticles on osteogenic differentiation of human mesenchymal stem cells, 12, 015001.
43. H. Cai, J. Zou, W. Wang and A. Yang, Mol. Med. Report., 2021, BMP2 induces hMSC osteogenesis and matrix remodeling, 23, 1-1.
44. A. Singh, G. Gill, H. Kaur, M. Amhmed and H. Jakhu, Prog. Orthod, 2018, Role of osteopontin in bone remodeling and orthodontic tooth movement: a review, 19, 1-8.
45. P. Ducy, Diabetologia, 2011, The role of osteocalcin in the endocrine cross-talk between bone remodelling and energy metabolism, 54, 1291-1297.
46. K. Gelse, E. Pöschl and T. Aigner, Adv. Drug Delivery Rev., 2003, C ollagens—structure, function, and biosynthesis, 55, 1531-1546.
47. T. A. Franz-Odendaal, B. K. Hall and P. E. Witten, Dev. Dyn. DEV DYNAM, 2006, Buried alive: how osteoblasts become osteocytes, 235, 176-190.
48. W. Yang, M. A. Harris, J. G. Heinrich, D. Guo, L. F. Bonewald and S. E. Harris, Bone, 2009, Gene expression signatures of a fibroblastoid preosteoblast and cuboidal osteoblast cell model compared to the MLO-Y4 osteocyte cell model, 44, 32-45.
49. F. Paic, J. C. Igwe, R. Nori, M. S. Kronenberg, T. Franceschetti, P. Harrington, L. Kuo, D.-G. Shin, D. W. Rowe and S. E. Harris, Bone, 2009, Identification of differentially expressed genes between osteoblasts and osteocytes, 45, 682-692.

50. L. F. Bonewald, J. Bone Miner. Res., 2011, The amazing osteocyte, 26, 229-238.
51. M. Shi, Y. Zhou, J. Shao, Z. Chen, B. Song, J. Chang, C. Wu and Y. Xiao, Acta Biomater., 2015, Stimulation of osteogenesis and angiogenesis of hBMSCs by delivering Si ions and functional drug from mesoporous silica nanospheres, 21, 178-189.
52. X. Guo, H. Shi, W. Zhong, H. Xiao, X. Liu, T. Yu and C. Zhou, Ceram. Int., 2020, Tuning biodegradability and biocompatibility of mesoporous silica nanoparticles by doping strontium, 46, 11762-11769.
53. X. Bai, C. Lin, Y. Wang, J. Ma, X. Wang, X. Yao and B. Tang, Dent. Mater., 2020, Preparation of Zn doped mesoporous silica nanoparticles (Zn-MSNs) for the improvement of mechanical and antibacterial properties of dental resin composites, 36, 794-807.
54. J. Zhang, L. Cai, L. Tang, X. Zhang, L. Yang, K. Zheng, A. He, A. R. Boccaccini, J. Wei and J. Zhao, Colloids Surf. B, 2018, Highly dispersed lithium doped mesoporous silica nanospheres regulating adhesion, proliferation, morphology, ALP activity and osteogenesis related gene expressions of BMSCs, 170, 563-571.
55. L. Wang and G. H. Nancollas, Chem. Rev., 2008, Calcium orthophosphates: crystallization and dissolution, 108, 4628-4669.
56. H. P. Rim, K. H. Min, H. J. Lee, S. Y. Jeong and S. C. Lee, Angew. Chem., Int. Ed., 2011, pH-tunable calcium phosphate covered mesoporous silica nanocontainers for intracellular controlled release of guest drugs, 50, 8853-8857.
57. C.-X. Zhao, L. Yu and A. P. Middelberg, J. Mater. Chem. B, 2013, Magnetic mesoporous silica nanoparticles end-capped with hydroxyapatite for pH-responsive drug release, 1, 4828-4833.
58. Z. Chen, Z. Li, Y. Lin, M. Yin, J. Ren and X. Qu, Biomaterials, 2013, Biomineralization inspired surface engineering of nanocarriers for pH-responsive, targeted drug delivery, 34, 1364-1371.
59. J. P. O'Connor, D. Kanjilal, M. Teitelbaum, S. S. Lin and J. A. Cottrell, Materials, 2020, Zinc as a therapeutic agent in bone regeneration, 13, 2211.
60. S. E. Gratton, P. A. Ropp, P. D. Pohlhaus, J. C. Luft, V. J. Madden, M. E. Napier and J. M. DeSimone, Proc. Natl. Acad. Sci., 2008, The effect of particle design on cellular internalization pathways, 105, 11613-11618.
61. T. J. Levingstone, S. Herbaj, J. Redmond, H. O. McCarthy and N. J. Dunne, Nanomaterials, 2020, Calcium phosphate nanoparticles-based systems for RNAi delivery: Applications in bone tissue regeneration, 10, 146.
62. D. M. Huang, Y. Hung, B. S. Ko, S. C. Hsu, W. H. Chen, C. L. Chien, C. P. Tsai, C. T. Kuo, J. C. Kang and C. S. Yang, FASEB J., 2005, Highly efficient cellular 153xplosion of mesoporous nanoparticles in human mesenchymal stem cells: implication for stem cell tracking, 19, 2014-2016.

Chapter 5

Zn loaded and Calcium phosphate coated degradable silica nanoparticles can effectively promote osteogenesis in human mesenchymal stromal cells

Published in Nanomaterials, 2022, doi: 10.3390/nano12172918

Zn loaded and Calcium phosphate coated degradable silica nanoparticles can effectively promote osteogenesis in human mesenchymal stromal cells

Pichaporn Sutthavas[1], Matthias Schumacher[1], Kai Zheng[2], Pamela Habibovic[1], Aldo R. Boccaccini[3], and Sabine van Rijt[1*]

[1] Department of Instructive Biomaterials Engineering, MERLN Institute for Technology-Inspired Regenerative Medicine, Maastricht University, P.O. Box 616, 6200 MD Maastricht, the Netherlands

[2] Jiangsu Province Engineering Research Center of Stomatological Translational Medicine, Nanjing Medical University, Nanjing 210029, China

[3] Institute of Biomaterials, University of Erlangen-Nuremberg, 91058 Erlangen, Germany

Abstract

Nanoparticles such as mesoporous bioactive glasses (MBG) and mesoporous silica nanoparticles (MSN) are promising for use in bone regeneration applications due to their inherent bioactivity. Doping silica nanoparticles with bioinorganic ions could further enhance their biological performance. For example, zinc (Zn) is often used as an additive because it plays an important role in bone formation and development. Local delivery and dose control are important aspects of its therapeutic application. In this work, we investigated how Zn incorporation in MSN and MBG nanoparticles impacts their ability to promote human mesenchymal stem cell (hMSCs) osteogenesis and mineralization *in vitro*. Zn ions were incorporated in three different ways; within the matrix, on the surface or in the mesopores. The nanoparticles were further coated with a calcium phosphate (CaP) layer to allow pH-responsive delivery of the ions. We demonstrate that the Zn incorporation amount and ion release profile affect the nanoparticle's ability to stimulate osteogenesis in hMSCs. Specifically, we show that the nanoparticles that contain rapid Zn release profiles and a degradable silica matrix were most effective in inducing hMSCs differentiation. Moreover, cells cultured in the presence of nanoparticle-containing media resulted in the highest induction of alkaline phosphate (ALP) activity, followed by culturing hMSCs on nanoparticles immobilized on the surface as films. Exposure to nanoparticle-conditioned media did not increase ALP activity in hMSCs. In summary, Zn incorporation mode and nanoparticle application play an important role in determining the bioactivity of ion-doped silica nanoparticles.

1. Introduction

Bone defects caused by trauma, tumour removal and infections are a tremendous burden on western healthcare systems. While autografts remain the gold standard for the treatment of bone defects in patients, issues such as limited availability and complications at the harvest site gave rise to the development of synthetic alternatives [1]. Biomaterials such as calcium phosphate ceramics and bioactive glasses are considered promising biomaterials for bone regeneration since they are inherently bioactive and are cost efficient to produce [2-4]. Nevertheless, the regenerative capabilities of synthetic biomaterials are considered inferior to natural bone. Doping ceramic biomaterials with bioinorganic ions is an attractive approach to further improve their biological performance since ions are cheap, stable and play vital roles in bone regeneration processes [5, 6]. One such example is zinc (Zn), which is an essential trace element found in bones where it plays an important role in bone development, formation and maintenance [7, 8]. Lack of Zn is associated with devastating diseases such as osteoporosis, dwarfism and inhibited bone development [9]. *In vitro* studies have shown that the stimulatory effect of Zn is highly dose dependent. Specifically, Zn Ions applied in the range of 2-5 μg mL^{-1} can stimulate hMSCs' adhesion and proliferation, whereas higher Zn doses of 15 μg mL^{-1} negatively affect osteogenic differentiation and can lead to cell apoptosis [10]. While ion delivery and dose control is an important aspect in the therapeutic application of Zn, the same is true for other ions as well. To date, several methods have been explored to allow controlled and localised ion delivery to guide bone regenerative processes while limiting harmful side effects, including the use of nano and microparticles [11, 12]. In this regard, mesoporous silica (MSN) and mesoporous bioactive glass (MBG) nanoparticles gained interest for use in bone applications as they are inherently bioactive [13]. For example, MBG are known to promote calcium phosphate mineralization when in the presence of high calcium and phosphate containing buffers. Moreover, their ordered mesoporous structure makes these nanoparticles promising tools for drug delivery purposes in various biomedical fields [14, 15].

Bioinorganic ion delivery using MBG is well established in the field [16], and there are also several examples regarding the use of MSN for ion delivery. MSN and MBG are both synthesized using sol-gel processes where micelles act as structure directing agents (templates) creating the mesoporous structure. While the MSN network consists solely of Si-O bonds, MBG contain network modifiers such as CaO, creating an open glass structure [17, 18]. Generally, in biological fluids, MSN are relatively stable towards biodegradation when no other network modifiers are present [19], whereas MBG are biodegradable in physiological conditions due to their open glass structure. MSN and MBG can be modified to carry multiple bioinorganic ions via incorporation within the silica network or loading in the 2-6 nm wide mesopores. Moreover, ions can be deposited on the nanoparticle surface [20, 21].

Considering the dependency of Zn dose on its biological efficacy, we set out to investigate how different ion incorporation methods influence MSN and MBG ability to promote hMSCs osteogenic differentiation. Recently, we have shown that MSN coated with a CaP layer can be used to efficiently deliver multiple ions to hMSCs and that multiple ion delivery is beneficial in stimulating *in vitro* osteogenesis [21]. In these systems, the CaP layer can act as a pH sensitive coat, triggering fast ion release at acidic pH (~pH 5) like those found in endocytic vesicles, while remaining stable at neutral pH.

In this work, we hypothesize that the ion incorporation mode within the mesoporous nanoparticles and nanoparticle degradability affects their ability to promote osteogenesis *in vitro*. To investigate this, four nanoparticle groups were created containing a CaP surface layer and incorporating Zn ions either in the mesopores, on the surface or within the matrix. Specifically, Zn was incorporated within the mesopores of the MSN and coated with a CaP surface layer to create MSN_{Zn}-CaP nanoparticles. The second group also contained Zn in the mesopores, and in addition contained an impurity within the silica network resulting in degradable MSN in neutral aqueous conditions ($DMSN_{Zn}$-CaP). In the third group, the Zn was deposited together with CaP on the surface to create MSN-CaZnP. The fourth group consisted of MBG containing Zn within the silica network and surface modified with a CaP layer to create MBGZn-CaP. Using these four nanoparticle constructs, we aimed to investigate how Zn incorporation amount and release from MSN-CaP and MBG-CaP nanoparticles impacts their ability to promote ALP activity as a marker for hMSCs osteogenesis and mineralization to assess matrix deposition. We tested three nanoparticle administration routes; exposure of cultured hMSCs to nanoparticle-containing media, hMSCs cultured on top of nanoparticle films or hMSCs exposed to nanoparticle-conditioned media.

2. Experimental Methods

2.1. Materials

Cetyltrimethylammonium chloride (CTAC), triethanolamine (TEA), tetraethyl orthosilicate (TEOS), (3-Mercaptopropyl) trimethoxysilane (MPTES), 3-aminopropyl triethoxysilane (APTES), ammonium fluoride, phosphate-buffered saline (PBS), foetal bovine serum (FBS), ammonium nitrate (NH_4NO_3), N,N-dimethylformamide (DMF), ascorbic acid, MTT (3-(4,5-dimethylthiazol-2-yl)-2,5-diphenyl tetrazolium bromide), anhydrous toluene and N,N-bis(carboxymethyl)aminomethyl were purchased from Sigma Aldrich GmbH (Germany). Sodium alizarin sulphonate (Alizarin Red S), Triton X-100, paraformaldehyde (PFA), Tween-20, Bovine serum albumin (BSA), L-glutamine, Trypsin and minimum essential medium alpha (αMEM) were purchased from Fisher Scientific (The Netherlands). Penicillin and streptomycin were purchased from Gibco Life Technologies (US). Absolute, ethanol, ICP-MS graded 60 V/V% Nitric acid (HNO_3) and ICP-MS graded 37 V/V% hydrochloric acid (HCl), were purchased from VWR (US).

2.2. Synthesis of MSN DMSN and MBGZn

Thiol core-functionalized MSN were synthesized based on a co-condensation method (Figure S1) similar to what was reported previously [22]. Degradable MSN were synthesized by incorporating a network impurity within the silica network similar to what was reported by Muller and Bein [23]. Zn doped mesoporous bioactive glass nanoparticles (MBGZn) were synthesized by using a sol-gel with microemulsion-assisted approach [24]. Further details of synthesis and characterization for MSN, DMSN and MBGZn can be found in the supporting information (SI).

2.3. Synthesis of COOH modified MSN and MBGZn (MSN-COOH and MBG-COOH, respectively)

MSN and MBG were first surface modified by post grafting with amine groups; 100 mg of each nanoparticle was added into 200 mL anhydrous toluene and the mixture was heated to 110 ℃. Under reflux conditions, 1 mL of APTES was introduced under vigorous stirring and left stirring for 24 hours. The nanoparticles were collected via centrifugation and washed with absolute ethanol three times. The amine groups were modified to carboxylic acid groups using our previously reported method [25]. In short, 3 grams of succinic anhydride was dissolved in 20 mL DMF and left stirring for 30 minutes at room temperature to allow complete dissolution of succinic anhydride. 0.2 g of MSN re-suspended in 30 mL DMF and was added to the succinic anhydride solution and mixed under vigorous stirring at 60 ^{o}C for 48 hours. The nanoparticles were collected via centrifugation and washed three times with absolute ethanol. The nanoparticles were stored at -20 °C in absolute ethanol for future use.

2.4. Zn ion loading in mesopores and calcium phosphate layer coating w/o zinc on MSN and MBG

To create MSN containing Zn ions (MSN_{Zn}), 100 mg of MSN-COOHs were immersed in 10 mM Zn $(NO_3)_2$ in milliQ water for 12 hours. The nanoparticles were collected via centrifugation and the pellets were washed with milliQ water. To create calcium phosphate coating, 100 mg of Zn loaded MSN were re-suspended in 100 ml milliQ water at pH 9 (adjusted by $NH_4NO)_3$. Then, 200 µl of 4 µM $(NH_4)_3PO_4$ were immediately added into the solution and allowed to react for 30 minutes. Next, 200 µl of a 10:1 molar ratio 6 µM $CaNO_3$ to $ZnNO_3$ solution were added to the mixture and stirred for another 30 minutes. Alternating phosphate and calcium ion addition was repeated for two more times. The nanoparticles were collected by centrifugation and washed with absolute ethanol three times. Both MSN_{Zn}-CaP and MSN-CaZnP were stored in ethanol at -20 °C.

2.5. Characterization of the inorganic nanoparticles

Nanoparticle size and zeta potential were measured at a concentration of 0.3 µg/ml in ethanol using a Zetasizer Nano (Malvern Panalytical, UK). Their morphology and size were further confirmed using transmission electron microscopy (TEM, FEI Tennai G2 Spirit BioTWIN iCorr (G0.201)). To prepare the samples for TEM analysis, 5 µL of 0.3 µg/mL nanoparticles in absolute ethanol were pipetted onto gold TEM grids and left to dry at room temperature for at least 6 hours before imaging. The total element composition of the nanoparticles was measured using inductively coupled plasma mass spectrometry (ICP-MS, iCaP Q, Thermo Scientific). All inorganic nanoparticles were completely dissolved by aqua regia (nitric acid and hydrochloric acid mixture in a molar ratio of 1:3) overnight. Standard matrix for ICP-MS analysis consisted of aqueous 1% HNO_3 containing 20 ppb Sc as internal standard. Digested MSN and MBG were diluted 1:10 in standard matrix and analyzed in normal mode using He as collision gas. Element amount presented in each analysis was based on calculation in comparison to known concentration curve of standard Si, Zn, Ca and P ions solution in standard matrix.

2.6. Creating and characterization nanoparticles thin film formation

Spin-coating was used to create thin nanoparticle based films. Glass cover slides were first surface-activated with O_2 plasma treatment at 0.4 bar at 70 W for 1.5 min (Plasma Cleaner, Diener Electronics Femto PCCE). Then, 20 µl of a nanoparticle suspension (50 µg/ml in absolute ethanol) was pipetted onto central area of the coverslip and immediately spun at 2000 rpm for 20 sec followed by 7000 rpm for 30 sec forming a thin film on the glass slide. Nanoparticle based films were dried and stored in the dark at room temperature.

2.7. Degradation of nanoparticles in cacodylate buffer and cell culture media

MSN and MBG degradation in aqueous solutions with pH 5 or pH 7.4 was studied over 6 day period. 1 mg nanoparticles were incubated in 1 ml cacodylate buffer (4.3 g sodium cacodylate (Na $(CH_3)_2AsO_2$) in MilliQ water; adjusted for pH with 0.2 M HCl). The degradation of MSN and MBG in basic medium under the cell culture environment (5% CO_2 in a humidified atmosphere at 37 °C) was also studied after 1, 3, 6, 24, 72 and 144 hours. The amount of Si, Zn, Ca and P released from nanoparticles was determined using ICP-MS analysis.

2.8. *In vitro* cell culture

hMSCs (PromoCell) were expanded in basic cell culture media (αMEM supplemented with 0.2 mM ascorbic acid, 2 mM L-glutamine, 100 U/ml penicillin, 100 mg/ml streptomycin and 10% FBS) and the cultures kept at 5% CO_2 in a humidified atmosphere at 37 °C. hMSCs at passage 4 were seeded in 12-well cell culture plates at 5000 cells per cm^2. For experiments on nanoparticles films, hMSCs were seeded at the same seeding density in non-treated 6 well culture plate. hMSCs were allowed to adhere for 24 hours. Human osteoblast cell (FOB) were purchased from ATCC (hFOB 1.19). Frozen cells were thawed and expanded in specific media consisting of 1:1 mixture of Ha''s F12 Medium Dulbecc''s Modified Eagl''s Medium and 2.5 mM L-glutamine along with 10% of G418 fetal bovine serum (ATCC) and the cultures kept at 5% CO_2 in a humidified atmosphere at 37 °C. Human umbilical vein endothelial cells (HUVEC) purchased from Bio-connect were expanded in endothelial cell growth medium 211-500 (Sigma-Aldrich) and the cultures kept at 5% CO2 in a humidified atmosphere at 37 °C. FOB at passage 4 and HUVEC at passage 6 were seeded in 96 well plate at 5000 cells per cm^2. Both FOB and HUVEC were allowed to adhere for 24 hours before toxicity experiment.

2.9. Cytotoxicity

The cytotoxicity of MSN-CaZnP, MSN$_{Zn}$-CaP, DMSN$_{Zn}$-CaP and MBGZn-CaP in concentrations ranging from 70 to 500 µg/mL, was tested using the MTT assay according to manufacturer's protocol. In short; at 80-90% cells' confluency, freshly prepared media with MSN at different concentrations was added to the cells. Cytotoxicity after 24 and 72 hours exposure to MSN was analysed. At each time point, 10 µL MTT reagent was added to each well and incubated for 4 hours. Formed formazan crystals were dissolved by adding 150 µL of acidified isopropanol (Triton-X 100 with isopropanol in the ratio 1:9). Dissolved crystals were quantified immediately by a microplate reader (BIO-RAD microplate reader-550) at absorbance wavelength of 570 nm. A standard curve of known formazan concentration was used to calculated average formazan concentration in each condition.

2.10. Alkaline phosphatase (ALP) assay

To evaluate ALP activity in hMSCs cells, nanoparticles were added at a concentration of 70 µg/mL in basic medium (no osteogenic stimulants added). Cell culture medium was refreshed every 3 days. To prepare the conditioned media, nanoparticles were immersed in basic culture medium at 70 µg/ml for 3 days. Centrifugation of the media was then performed to separate nanoparticles from the media and the conditioned media was added to hMSCs and refreshed every 3 days. The ALP activity was measured after 7, 14 and 21 days for all conditions. hMSCs cultured with osteogenic media were included as positive control for all samples. Osteogenic differentiation was evaluated by measuring alkaline phosphatase (ALP) levels at days 7, 14 and 21 of culture. ALP activity was quantified using the CyQuant® Cell Proliferation Assay Kit (Thermo Fisher Scientific) and normalized to DNA similar to what we reported previously [21]. Cells were lysed using cell-lysis buffer (provided with the kit, 1:20 in PBS) containing 0.1% (vol/vol) RNAse A (Thermo Fisher Scientific), and then freeze-thawing cycles. ALP activity was measured by incubating cell lysates at a 1:5 ratio (volume) with the CDP-star solution (Sigma Aldrich) in a white-bottom 96-well plate for 30 min in the dark at room temperature. Relative absorbance was determined by microplate reader (BIO-RAD microplate reader-550). Partial cell lysates were used for the quantifying total DNA content via GR-dye solution according to the supplier's instructions. The fluorescent signal was measured with a spectrophotometer at 520 nm. DNA concentration was calculated using a standard curve according to the manufacturers protocol. ALP values were normalized to total DNA content per sample. For evaluating ALP activity of hMSCs cells seeded on top nanoparticles films a similar protocol was performed with only alteration in the initial volume RNAse lysis buffer that was used was increased to 1000 µL to ensure full submersion the films and complete lysis of the cells.

2.11. Mineralization

Calcium deposition of hMSCs was assessed using Alizarin Red S (sodium alizarin sulphonate) stainin. After 28 days of culture, cells were fixed with 4% PFA. Alizarin Red S was dissolved in bi-distilled water at a concentration of 22 mg/ml and pH adjusted to 4.2 with ammonium hydroxide. Prior to staining, cells were rinsed once with PBS followed by washing twice with bi-distilled water. Alizarin Red solution was added to the samples and incubated for 15 minutes at room temperature, followed by washing thrice with bi-distilled water. Quantification was carried out by using a destaining method by adding 1 ml of 10 % (w/v) cetylpyridinium chloride (CPC) (Sigma) in 10 mM sodium phosphate (pH 7.0) solution to each well. After 15 minutes incubation at room temperature, 10 µl from the extracted stain was transferred to a 96-well plate and diluted 10 folds with CPC solution. The violet colored supernatant was recorded with a microplate reader (CLARIOstar Multimode Microplate Reader) at 555 nm.

2.12 Statistical analysis

Statistical analysis was conducted using one- or two-way analysis of variance (2 way ANOVA) followed by Turkey’s multiple comparison. For all figures, error bars indicate one standard deviation with p-values: $^{*}p < 0.033$; $^{**}p < 0.02$; $^{***}p < 0.001$ unless stated otherwise.

3. Results

3.1. Synthesis and characterization of Zn incorporated MSN and MBG

In this study, non-degradable MSN surface coated with a CaPZn surface layer, nondegradable MSN containing Zn ions in the mesopores and a CaP surface layer, biodegradable MSN containing Zn ions in the mesopores and a CaP surface layer, and MBG containing Zn in the silica matrix and surface coated with a CaP layer were developed (Scheme 1). DMSN were synthesized by creating an imperfection within the silica network using an adopted co-condensation method, which was first reported by Moller and Bein [23]. Our synthesized DMSN degraded up to 80% of its total mass in an aqueous solution with neutral pH within 6 days (Figure S2). MBGZn synthesis was performed as reported previously [26]. To allow Ca, P and Zn ion deposition on the surface and within mesopores, the MSN, DMSN and MBGZn were first aminated by postgrafting using APTES. The surface grafted amines were subsequently modified to carboxylic acid groups by reaction with succinic anhydride, which we reported recently [25]. Zn ions were then incorporated into the mesopores of modified MSN and DMSN by physical diffusion to create Zn loaded MSN and Zn loaded DMSN (MSN_{Zn} and $DMSN_{Zn}$, respectively). The CaP layer was created immediately afterwards to encapsulate the ions within the structure to yield MSN_{Zn}-CaP and $DMSN_{Zn}$-CaP by adding Ca and P precursors alternately until a thin layer of CaP was obtained, as we reported previously [21]. In similar fashion, Zn doped CaP surface coated was created by adding Zn precursors to Ca precursors at a 10% molar ratio during layer formation.

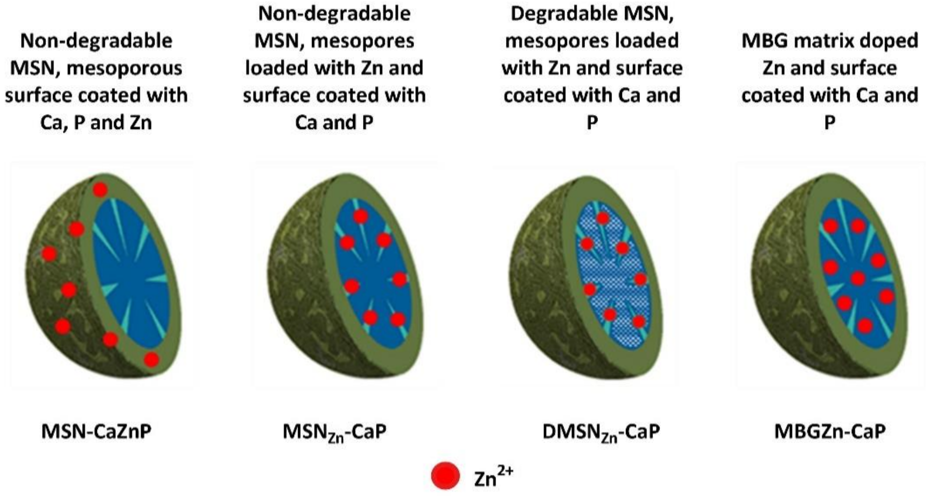

Scheme 1: Schematic representation of synthesized nanoparticles and location of Si, Ca, P and Zn ions within the nanoparticles; blue represents Si network, green represents calcium phosphate layer and red represents Zn ions.

Spherical nanoparticles with ordered mesoporous structure were obtained (Figure 1). CaP modification resulted in less visible mesoporous structure compared to MSN and MBG before CaP coating (Figure S3). Dynamic light scattering (DLS) analysis showed that MSN-CaZnP, MSN$_{Zn}$-CaP and DMSN$_{Zn}$-CaP were similar in hydrodynamic size while MBGZn-CaP were slightly larger than their original size (Table 1). Polydispersity indexes (Pdi) lesser than 0.3 indicted that all synthesised nanoparticles were monodisperse. All nanoparticles had similar surface potential charge as shown in Table 1. Crystallinity analysis (XRD) indicated that calcium phosphate layer on MSN$_{Zn}$-CaP, DMSN$_{Zn}$-CaP and MBGZn-CaP were amorphous and that MSN-CaZnP had a certain level of crystallinity (Figure S4), albeit it lower than what is normally observed for crystallized CaP layers[27]. ICP-MS analysis of the digested nanoparticles confirmed the presence of Ca, P, and Zn in all nanoparticles, however their dose varied (Table 2). In particular, MBGZn had the highest Zn content per mg of nanoparticle, while Zn inside the CaP surface coating was relatively low. Moreover, CaP deposition was much higher on MBG nanoparticles compared to the MSN, explaining their increased size. In summary, Zn incorporation and CaP layer surface formation were successful, creating four unique nanoparticle constructs.

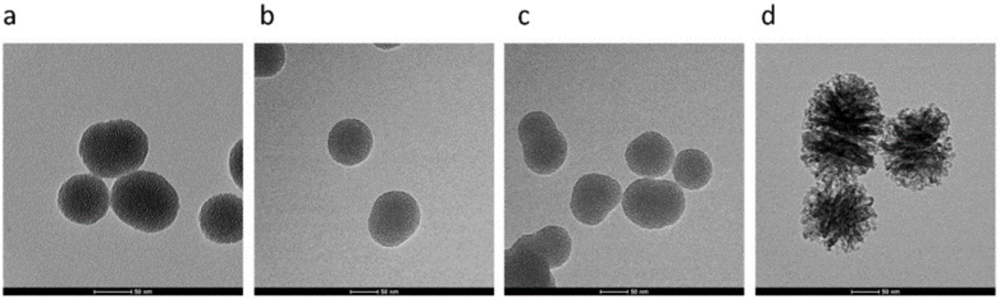

Figure 1: TEM images showing mesoporous structure and nanoparticle size of a) MSN-CaZnP, b) MSN$_{Zn}$-CaP, c) DMSN$_{Zn}$-CaP and d) MBGZn-CaP.

Table 1: Hydrodynamic size, Pdi and surface potential of MSN-CaZnP, MSN_{Zn}-CaP, $DMSN_{Zn}$-CaP and MBGZn-CaP measured by dynamic light scatting. All nanoparticles were measured in distillled water.

Sample	Size (nm)	Pdi	Zeta potential [mV]
MSN-CaZnP	195±15	0.219±0.09	-28±7
MSN_{Zn}-CaP	215±9	0.259±0.10	-22±9
$DMSN_{Zn}$-CaP	225±23	0.251±0.13	-26±4
MBGZn-CaP	270±12	0.31±0.11	-19±7

Table 2: Ion composition of 100 mg/L of MSN-CaZnP, MSN_{Zn}-CaP, $DMSN_{Zn}$-CaP and MBGZn-CaP using ICP-MS analysis.

Sample	Si (mg/L)	Ca (mg/L)	P (mg/L)	Zn (mg/L)
MSN-CaZnP	25.412	0.217	0.143	0.022
MSN_{Zn}-CaP	24.704	0.203	0.138	3.833
$DMSN_{Zn}$-CaP	22.976	0.186	0.120	3.230
MBGZn-CaP	23.111	2.317	1.389	9.655

3.2. Ca, P, Zn and Si release profiles at neutral and acidic pH

To determine the stability and ion release capacity of the developed MSN and MBG nanoparticles, their ion release profile over-time was investigated using ICP-MS analysis in neutral environment (pH 7.4) and acidic environment similar to endosomal vesicles (pH 5). Cacodylate buffer was used for these studies as it does not contain Ca or P. At pH 7.4, Si, Ca, P and Zn ion release was minimal for all four nanoparticles tested (less than 1%, Figure 2 dashed line), showing that the nanoparticles are stable for at least 6 days in buffer at neutral pH. In contrast, at pH 5 rapid dissolution of the CaP coating layer was observed for all nanoparticles. Specifically, total dissolution of phosphate occurred within 24 h of incubation for all four nanoparticles (Figure 2a). Similar rates of calcium ion release could be detected for the MSN-CaZnP, MSN_{Zn}-CaP and $DMSN_{Zn}$-CaP (Figure 2b). This was not the case for the MBG nanoparticles, where a rapid release of about 60% of total calcium was observed within the first 4 hours, followed by a more sustained release over the 6 days period. This can be explained by rapid calcium release from the CaP surface layer, followed by slower release of network-incorporated calcium. This is in line with the observed sustained silica matrix dissolution over the 6-day period (Figure 2c). Also $DMSN_{Zn}$-CaP showed dissolution of its silica matrix, which was significantly more rapid compared to MBGZn-CaP particles. No silica degradation was observed for the MSN-CaZnP and MSN_{Zn}-CaP particles, similar to what we have reported recently[21]. Further information for non-linear best fit curves and half-release time calculation can be found in section S.3 in supplementary information.

Zn ion release profiles at acidic pH followed the trend; DMSN$_{Zn}$-CaP > MSN-CaZnP > MSN$_{Zn}$-CaP > MBGZn-CaP (Figure 2d), which may be related to the different modes of Zn incorporation. Specifically, the slower release of Zn in MBG nanoparticles can be explained by its dependency on silica matrix degradation. In contrast, in MSN$_{Zn}$-CaP, the Zn is physically entrapped in the mesopores, which are capped by the CaP composite layer. Dissolution of the CaP is needed to facilitate Zn release in these particles. In addition, Zn ions are absorbed via electrostatic interactions with the negatively charged mesopores, which may further slow Zn release. While the Zn was incorporated in a similar manner in DMSN$_{Zn}$-CaP, Zn release from DMSN$_{Zn}$-CaP was significantly faster (Figure 2d). This is likely due to the simultaneous dissolution of the silica network accelerating Zn release. Similar fast release of Zn was observed for MSN-CaZnP, which can be explained by the Zn deposition on the surface rather than in the mesopores or silica matrix. Thus, the resulting dissolution rates of the CaZnP layer are similar to CaP layer dissolution.

In summary, here we show that the synthesized nanoparticles are stable at neutral pH and dissolve at acidic pH values. Furthermore, the Zn ion release profiles depended on the mode of ion incorporation. Specifically, CaP and CaZnP surface coatings dissolved rapidly at acidic pH, while matrix or mesoporous incorporated ions released more slowly.

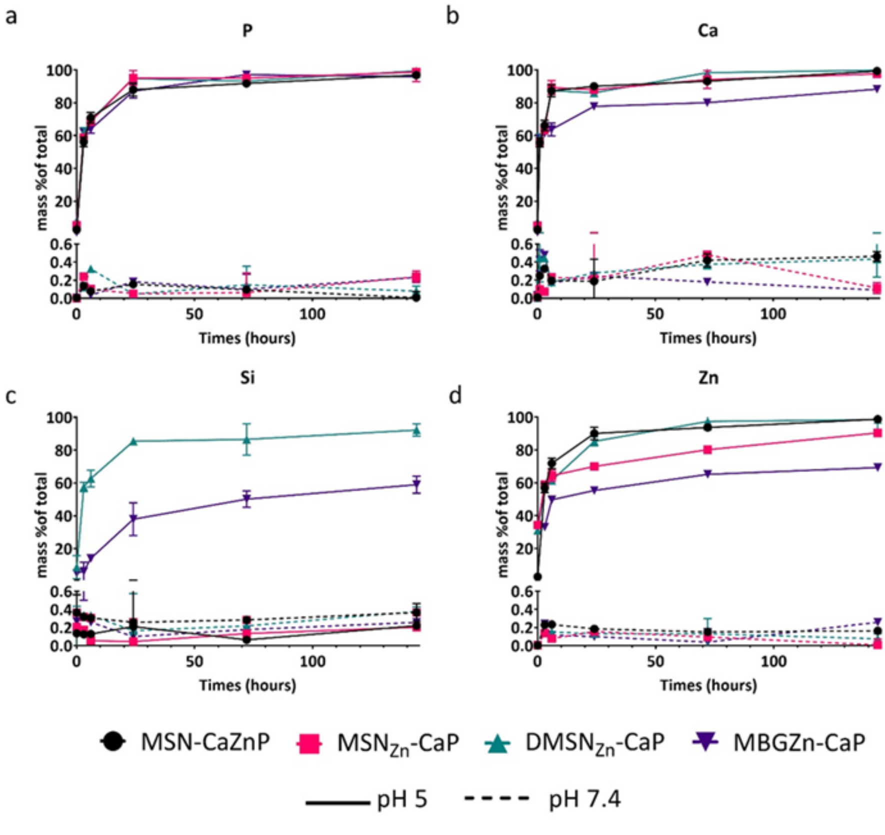

Figure 2: Ion release from nanoparticles analysed by ICP-MS ; a) P, b) Ca, c) Si and d) Zn from MSN-CaZnP (black), MSN$_{Zn}$-CaP (red), DMSN$_{Zn}$-CaP (green) and MBGZn-CaP (purple) in cacodylate buffer pH 5 and pH 7.4.

3.3. Stability of the nanoparticles and nanoparticles thin films in cell culture media

To assess nanoparticle stability in cell culture medium, ion release from the nanoparticles was investigated after 21 days. Less than 1% of total mass of Si, Ca, P and Zn ions were released from MSN-CaZnP, MSN$_{Zn}$-CaP and

MBGZn-CaP after the 21-day incubation period. This is in line with our previously obtained results in cacodylate buffer at neutral conditions (Figure 2, dot line). In contrast, slow ion release that increased over time was observed from $\mathrm{DMSN_{Zn}}$-CaP (Figure 3a, green line). Specifically, Si ion release from $\mathrm{DMSN_{Zn}}$-CaP became apparent after 6 days of incubation in cell culture medium and increased until day 9 before levelling off. The release profile of Ca, P and Zn ions followed a similar trend (Figure 3b, c and d). The dissolution of DMSN in cell culture medium was however slow; the amount of released Si ions amounted only to about 2.58 % of the total Si amount in DMSN after 10 days in cell culture medium. DMSN contain a network impurity making the silica network more prone to hydrolysis.

We also assessed ion release in cell culture medium from the four nanoparticles when deposited as thin films on glass slides. To create these thin films, the nanoparticles were spin coated on glass slides as we have reported recently.[21] Also in these conditions, no ion release was observed from MSN-CaZnP, $\mathrm{MSN_{Zn}}$-CaP and MBGZn-CaP particles over the 21 days (Figure S5). In contrast to our results obtained with $\mathrm{DMSN_{Zn}}$-CaP in suspension (Figure 3, green line), $\mathrm{DMSN_{Zn}}$-CaP films were also stable as no significant ion release could be observed over the 21 day period (Figure S5, green line).

In summary, MSN-CaZnP, $\mathrm{MSN_{Zn}}$-CaP and MBGZn-CaP were stable in cell culture medium over 21 days in both tested conditions. $\mathrm{DMSN_{Zn}}$-CaP showed slow release and relatively limited release of all incorporated ions when in suspension in cell culture medium. All nanoparticles were stable over the 21 day time period when deposited as films.

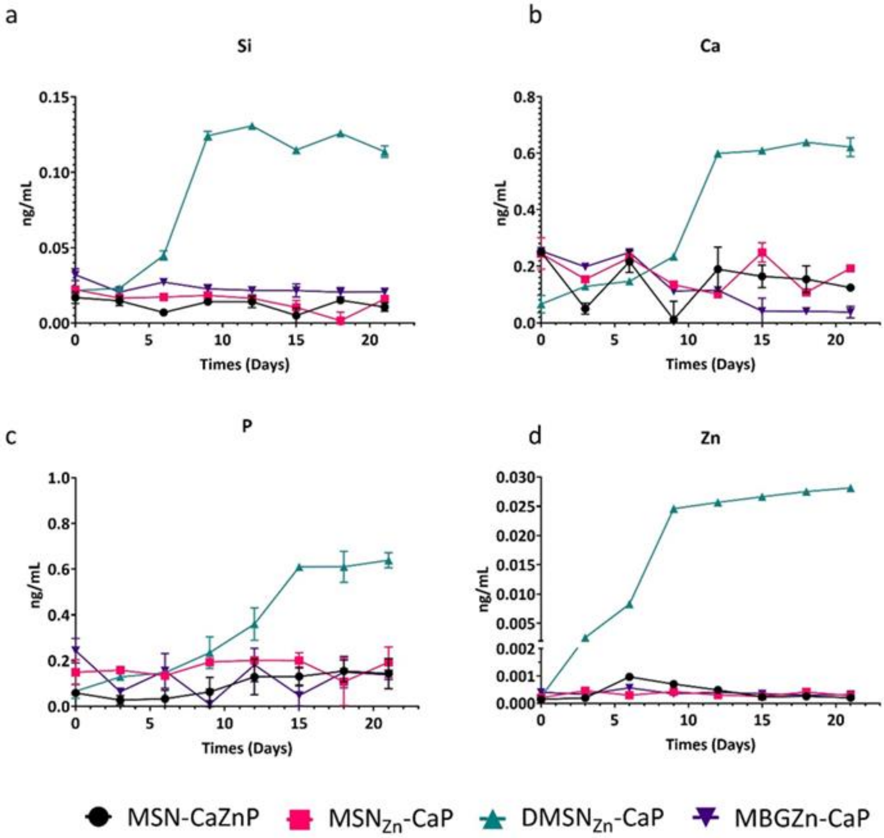

Figure 3: Ion release profiles analysed using ICP-MS of a) Si, b) Ca, c) P and d) Zn from MSN-CaZnP (black), MSN$_{Zn}$-CaP (red), DMSN$_{Zn}$-CaP (green) and MBGZn-CaP (purple) in cell culture media while kept at 37 °C, 5% CO_2 in a humidified atmosphere.

3.4. Nanoparticle biocompatibility

Next, the biocompatibility of MSN-CaZnP, MSN$_{Zn}$-CaP, DMSN$_{Zn}$-CaP and MBGZn-CaP to hMSCs at concentrations ranging from 70 to 500 µg/mL was tested using the MTT assay. At concentrations of 500 µg/mL for MSN-CaZnP, MSN$_{Zn}$-CaP and MBGZn-CaP, hMSCs cell metabolism showed significant reduction compared to control cells cultured in the absence of nanoparticles after 24 hours of exposure (Figure 4a). $DMSN_{Zn}$-CaP nanoparticle concentrations above 140 µg/mL led to a significant decrease in hMSCs cell metabolism after 24 hour exposure. After 3 days of exposure, the lower concentration of 280 µg/mL also led to a significant decrease in hMSCs metabolism after exposure to MSN-CaZnP, MSN_{Zn}-CaP and MBGZn-CaP. $DMSN_{Zn}$-CaP significantly affected cell metabolism already at 140 µg/mL (Figure 4b). In conclusion, hMSCs viability were not affected by nanoparticle concentrations up to 280 µg/mL when exposed to MSN-CaZnP, MSN_{Zn}-CaP or MBGZn-CaP. However, $DMSN_{Zn}$ -CaP concentrations of 140 µg/mL and higher affected hMSCs viability. Therefore, the concentration of 70 µg nanoparticles per mL was selected for further studies.

Furthermore, the non-specific cytotoxicity of MSN-CaZnP, MSN_{Zn}-CaP, $DMSN_{Zn}$-CaP and MBGZn-CaP were test in FOB and HUVEC cells. After 24 and 72 hours exposure to MSN-CaZnP, MSNZn-CaP, and MBGZn-CaP, FOB cells and HUVEC cells did not shown any decrease in their metabolism in comparison to control cells for all the concentration tested. FOB cells exposed to 500 µg/mL MSN-CaZnP showed slightly decrease in their metabolism (96.11% after 24 hours and 91.3 % after 72 hours) but not significant, while HUVEC exposed to MSN-CaZnP did not decrease their metabolism. When exposed to DMSNZn-CaP at concentration 280 and 500 µg/mL, FOB showed the reduction in metabolism in comparison control cells (88.12% for 280 µg/mL and 78.33% for 500 µg/mL) after 24 hours. Further decrease in metabolism also observed for the same concentration after 72 hours of exposure (83.15% for 280 µg/mL and 73.82% for 500 µg/mL). In HUVEC cells, metabolism also significantly decrease when cells exposed to concentration higher than 140 µg/mL (after24 hours; 92.29 % for 280 µg/mL and 92.34% for 500 µg/mL, after 72 hours; 89.07% for 280 µg/mL and 85.81% for 500 µg/mL). All the nanoparticles tested did not cause the reduction in metabolism at concentration 140 µg/mL and below for both FOB and HUVEC cells. Therefore, we could be assured that all of the nanoparticles tested have no non-specific toxicity at the concentration below140 µg/mL.

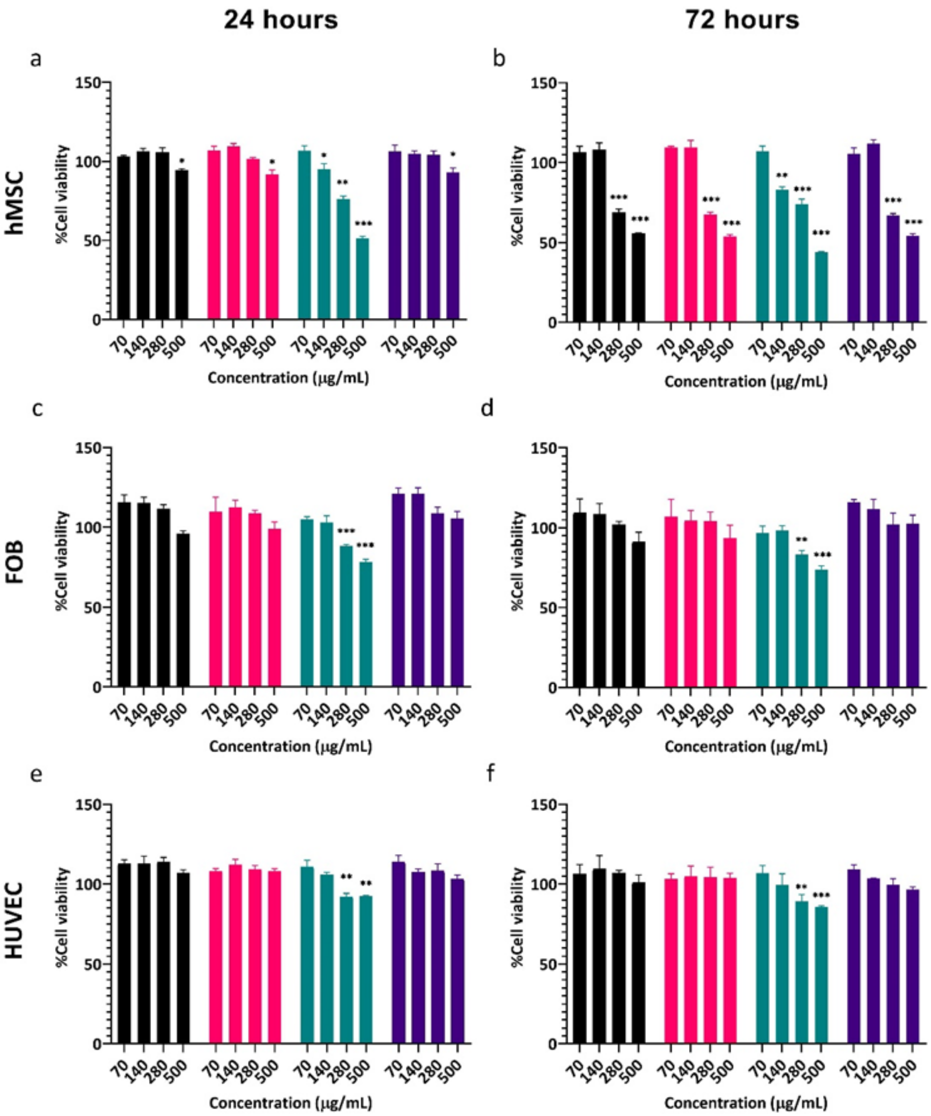

Figure 4: Metabolic activity of hMSCs (a,b), FOB (c,d) and HUVEC (e,f) measured using the MTT assay after 24 and 72 hours exposure to MSN-CaZnP, MSN$_{Zn}$-CaP, DMSN$_{Zn}$-CaP and MBGZn-CaP to concentrations ranging between 70 and 500 µg/mL. Cell viability is shown as % compared to control cells (not incubated with nanoparticles). Significant difference between samples and control groups are Significant differences between samples and control groups were calculated by two- way ANOVA followed by Turkey's multiple comparison, * representing p-values as follows; *$p < 0.033$; **$p < 0.02$; ***$p < 0.001$.

3.5. Effect of Zn-functionalized nanoparticles on osteogenic differentiation

Next, the ability of the nanoparticles to induce osteogenic differentiation, by means of measured ALP enzymatic activity, was assessed. The osteogenic capabilities of our nanoparticles were tested in basic cell culture conditions (absence of osteogenic stimulators) using three different application methods. In the first application method, the nanoparticles were applied as a suspension in the cell culture medium at a concentration of 70 µg/mL. In the second application method, nanoparticle-conditioned medium was used in order to assess the effect of ionic degradation products and ion exchange. In the third application method, the nanoparticles were first deposited as thin films on the bottom of cell culture plates and hMSCs were then cultured on top of these films. hMSCs cultured in osteogenic medium (OM, containing 100 nM of dexamethasone) and in basic medium in the absence of nanoparticles were used as positive and negative control, respectively.

Application of the nanoparticles to hMSCs as a suspension in cell culture medium resulted in a significant increase in ALP production after 14 and 21 days for all four nanoparticles. However, the induced ALP levels differed significantly between the tested nanoparticles. Specifically, after 14 days, DMSN_{Zn}-CaP and MBGZn-CaP exposure led to significantly higher ALP levels compared to MSN_{Zn}-CaP and MSN-CaZnP (Figure 5a). A similar trend was observed after 21 days of exposure, except that DMSN_{Zn}-CaP showed similar ALP induction compared to hMSCs cultured in OM and was significantly more effective compared to MBGZn-CaP ($p = 0.007$).

ALP activity of hMSCs cultured on nanoparticle films only increased after 21 days of exposure (Figure 5b). Similar ALP levels were observed regardless of the nanoparticle type (2.45 fold for MSN-CaZnP, 2.94 fold for MSN$_{Zn}$-CaP, 3.15 folds for DMSN$_{Zn}$-CaP and 2.64 folds for MBGZn-CaP increase in ALP level compared to negative controls, respectively). The ALP levels were significantly lower compared to those observed after addition of nanoparticles in suspension. Moreover, hMSCs exposed to conditioned media resulted in no significant increase in ALP activity (Figure S7).

Overall, hMSCs exposed to nanoparticles in a 70ug/mL suspension led to high ALP production for all four nanoparticles where DMSN$_{Zn}$-CaP were most efficient. Deposition of the nanoparticles as films only led to significantly increased ALP production after 21 days of exposure, albeit at lower levels compared to suspension conditions.

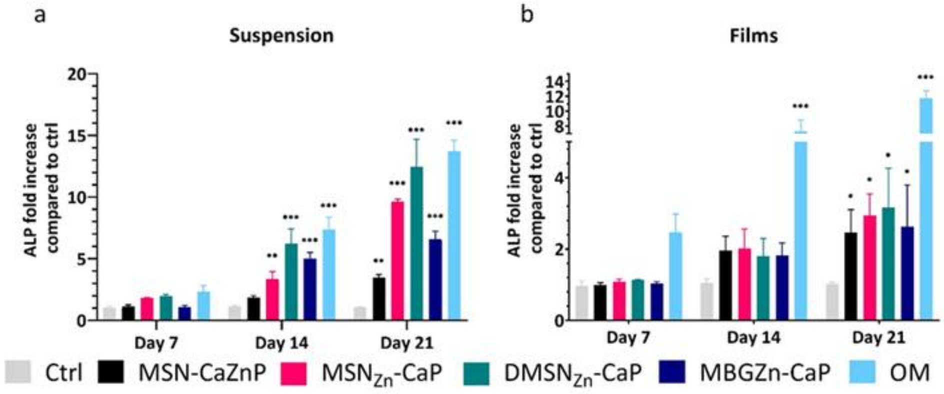

Figure 5: ALP activity in hMSCs normalized to DNA content after exposure to nanoparticles as a) 70 ug/mL suspension, b) or cultured on thin nanoparticle films. Data is shown relative to control (cells not exposed to nanoparticles). The experiments were done in triplicate. Significant differences between samples and control groups are calculated by one-way

ANOVA followed by Turkey's multiple comparison, * representing p-values as follows; *$p < 0.033$; **$p < 0.02$; ***$p < 0.001$.

3.6 Mineralization

Next, we investigated whether nanoparticle exposure could promote the ability of hMSCs to mineralize their extracellular matrix. The mineralization of differentiated hMSCs after 28 days in culture was determined using Alizarin Red S Staining. hMSCs cultured in basic and osteogenic media in the absence of nanoparticles were used as negative and positive controls, respectively. Two application methods were considered for these experiments; application of the nanoparticles as suspension and nanoparticle conditioned media. Limited mineralization could be observed for nanoparticle conditioned media with $DMSN_{Zn}$-CaP particles (Figure 6d) and no mineralization was observed for the other nanoparticles (Figure 6b, c and e). In contrast, hMSCs exposed to the nanoparticles in suspension resulted in high mineralization for all conditions compared to the negative control (Figure 6a).

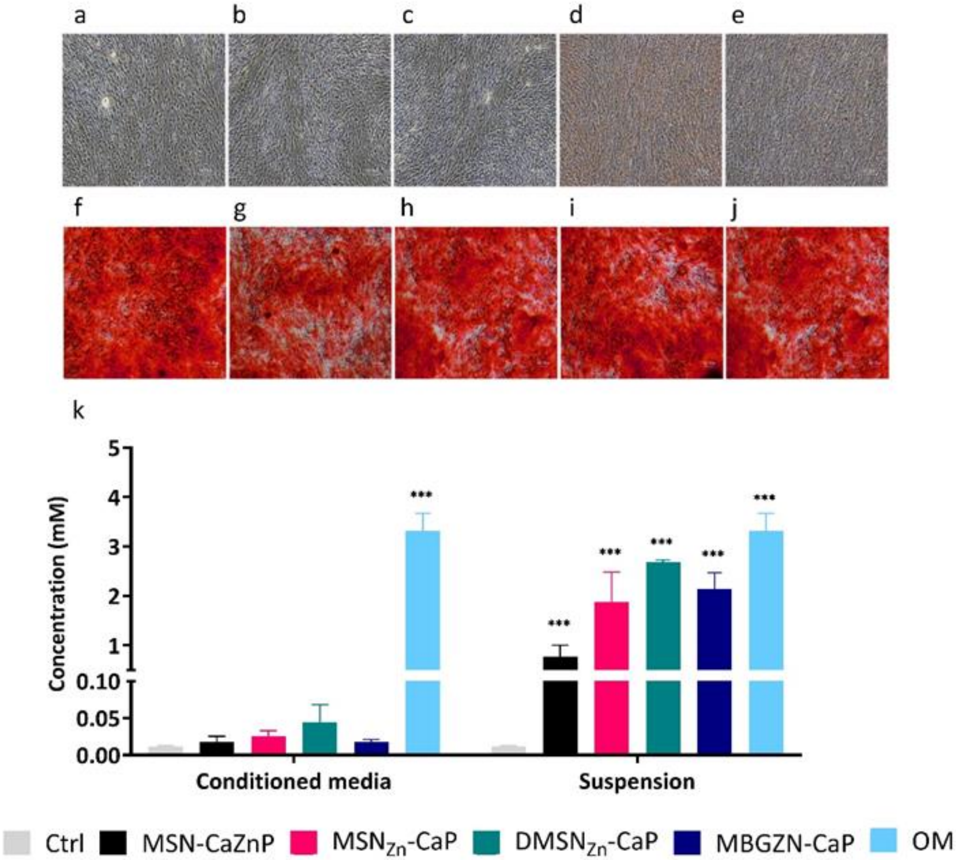

Figure 6: Calcium deposition by hMSCs at day 28 determined by Alizarin Red staining (n=3) when cultured in; a) basic medium (Ctrl); conditioned medium of b) MSN-CaZnP c) MSN$_{Zn}$-CaP d) DMSN$_{Zn}$-CaP and e) MBGZn-CaP; f) osteogenic medium (OM), g) MSN-CaZnP, h)MSN$_{Zn}$-CaP, i)DMSN$_{Zn}$-CaP, j) MBGZn-CaP. k) Quantification of calcium content at day 28. Significant differences between samples and control groups are calculated by one-way ANOVA followed by Turkey's multiple comparison, * representing p-values as follows; $*p < 0.033$; $**p < 0.02$; $***p < 0.001$.

4. Discussion

In this work, we developed four unique mesoporous ceramic nanoparticles based on MSN and MBG containing Zn ions and with CaP coated surface. Zn ions were incorporated in three locations in the nanoparticles; in the CaP layer, inside the mesopores or inside the silica matrix. The CaP layer dissolves quickly in acidic conditions like those found in endosomal vesicles (pH~5) [28], and can be used as pH sensitive gating system for controlled release of therapeutic drugs[29]. For our nanoparticles, CaP surface coating prevented nanoparticle dissolution in neutral buffer conditions as well as in cell culture medium. In contrast, MBG nanoparticles without CaP layer but with similar Zn composition commonly dissolve in neutral aqueous conditions within one week of incubation.[26] Moreover, we showed that DMSN without CaP layers also dissolved in neutral conditions within 6 days similar to what was observed by others[23]. Thus, surface grafting of CaP layers onto DMSN and MBG nanoparticles can confer stability towards dissolution in aqueous neutral conditions. Conversely, rapid ion release was observed in acidic conditions for all four nanoparticles.

Among the nanoparticles tested, $DMSN_{Zn}$-CaP applied at 140 μg/mL led to reduced hMSCs viability after 72 h incubation. The other nanoparticles only showed a decrease in cell viability upon 72 h incubation when applied at concentrations of 280 ug/mL and higher. This may be due to the relatively high amount of Si ions released from DMSN in contrast to MSN-CaZnP, MSN_{Zn}-CaP or MBGZn-CaP, which contain a more stable silica network. Previously it has been reported that the silicate exposure after 24 h incubation at 50 μg/mL or higher is cytotoxic for osteoblast cells [30].

In this study, two methods (ALP activity assay and Alizarin Red S Staining) were used to determine the ability of the developed MSN and MBG to stimulate osteogenic differentiation in hMSCs. Increased ALP activity in hMSCs is a known marker for osteogenic differentiation due to its role in supporting mineralization of cellular matrix during osteogenesis. Moreover, ALP is also involved in the hydrolysis of phosphate esters which provide the phosphate groups required for hydroxyapatite formation [31]. When the nanoparticles were applied as particle suspensions in cell culture medium, high ALP levels in hMSCs were observed. After 14 days, $DMSN_{Zn}$-CaP induced similar ALP activity as our positive control (media supplemented with dexamethasone), followed by MBGZn-CaP nanoparticles. The higher effectiveness of $DMSN_{Zn}$-CaP may be due to the co-delivery of Si ions. Although Si release was also observed from MBGZn-CaP particles, in these nanoparticles the silica release was much slower compared to $DMSN_{Zn}$-CaP particles. Indeed, both Si and Zn are known to support the growth of bone cells in a dose-dependent manner. Moreover, both soluble Si and SiO_2 nanoparticles have been shown to induce osteogenic activity in hMSCs at low concentrations. For example, one study reported that solid SiO_2 nanoparticles could increase ALP activity levels in hMSCs already at a concentration of 10 µg/ml [32]. Although MSN_{Zn}-CaP did not have a degradable Si matrix, this nanoparticle also led to significantly increased ALP production in hMSCs, whereas MSN-CaZnP were effective to a much lower extend. This difference can be explained by its low Zn content compared to the other three nanoparticles.

After 21 days of incubation, $DMSN_{Zn}$-CaP exposure led to highest ALP activity followed by MSN_{Zn}-CaP and MBGZn-CaP nanoparticles. The improved effectiveness of MSN_{Zn}-CaP over MBGZn-CaP after longer incubation periods may be related to the faster Ca and Zn release profiles for MSN_{Zn}-CaP particles compared to MBGZn-CaP. This data indicates that Zn incorporation mode and release profile are important factors in determining the biological activity and ability to promote osteogenesis of Zn doped ceramic nanoparticles. All four nanoparticles could also significantly promote mineralization where MSN_{Zn}-CaP, $DMSN_{Zn}$-CaP and MBGZn-CaP were most and equally effective. The lower effectiveness of MSN-CaZnP in promoting both ALP activity and mineralization is likely related to its lower Zn ion content compared to the other 3 nanoparticles.

No increase in ALP activity nor mineralization was observed in hMSCs exposed to nanoparticle-conditioned media. This is in line with the observation that all four nanoparticles were stable in cell culture media at neutral conditions, shielded from ion dissolution by the CaP layer. Previously we have shown that MSN-CaP nanoparticles are efficiently internalized by hMSCs, promoting high ion uptake [21]. Taken together, our data indicate MSN-CaP and MBG-CaP cell internalization via endocytosis followed by pH-responsive intracellular ion release as a likely mechanism leading to the induction of hMSCs osteogenesis.

hMSCs cultured on stable films prepared from the four nanoparticles also resulted in increased ALP activity albeit significantly lower compared to nanoparticle suspension conditions, and only after 21 days of culture. Moreover, no difference in ALP induction was observed between the nanoparticles. Considering that the films were stable and no ion release was observed in cell culture media in neutral conditions, this may be explained by the similarity between surface crystallinity and nanoscale surface topography. While the exact mechanism of how CaP surfaces influence osteogenesis process remains unclear, it has been suggested that the crystallinity, chemical composition and nanoscale topography of CaP surfaces are important factors in inducing osteogenesis in bone cells.

5. Conclusions

In this study, we developed four nanoparticles incorporating Zn in the CaP layer, inside the mesopores or inside the silica matrix of MSN or MBG particles. The particles were further surface coated with CaP layers as a pH sensitive gating system. We demonstrated that CaP surface coating can be used to infer stability to degradable MSN and MBG at neutral conditions and stimulate ion release at acidic conditions. The Zn incorporating MSN and MBG enabled significant induction of ALP activity and mineralization of hMSCs in the absence of other stimulators. Degradable MSN with Zn incorporated in the mesopores were equally effective as osteogenic medium, followed by MBG containing Zn in the silica matrix. The difference in bioactivity between the four nanoparticles is likely related to Zn incorporation amount and release profile, in association with Si ion release. Comparison between the modes of nanoparticle application revealed that Zn incorporated silica nanoparticles were more effective in inducing ALP activity when applied as a suspension compared to stable thin films of the same materials or nanoparticle-conditioned media. Moreover, our data show that Zn ion incorporation mode and release rate are important factors in the bioactivity of MSN and MBG when applied as nanoparticle suspensions and should be considered in the design of ion doped ceramic nanoparticles to improve their therapeutic use.

Funding: This research was financially supported by the Gravitation Program “Materials Driven Regeneration”, funded by the Netherlands Organization for Scientific Research (024.003.013) and the Royal Thai Government Scholarship Program (offered by OCSC).

Acknowledgments: We thank Dr Eva Gubbins for technical assistance with ICP-MS.

Conflicts of Interest: The authors declare no conflict of interest

Supplementary data

S.1 Synthesis of core-labelled MSN

To synthesize MSN, a mixture of 1.63 g TEOS (7.82 mmol), MPTES (112 mg, 0.48 mmol) and 14.3 g TEA (95.6 mmol) was heated to 90 °C under static conditions (Solution 1). Solution 2 included 100 mg ammonium fluoride (2.70 mmol) dissolved in a solution of 2.41 ml CTAC (1.83 mmol, 25% (wt) in H_2O) and 21.7 ml bi-distilled water (1.21 mmol) by heating to 60 °C. Solution 2 was rapidly added to solution 1, and the mixture was stirred vigorously at 700 rpm for 20 min while left to cool. Then, 138.2 mg TEOS (0.922 mmol) was added in four equal increments (34.55 mg each) every 3 minutes. The solution was then left stirred overnight at room temperature. The particles were then collected by centrifugation at 7800 rpm for 20 min and washed once with ethanol. Template extraction was performed by dispersion into an ammonium nitrate in ethanol solution (2 g NH_4NO_3 in 100 ml ethanol) and refluxed for 45 minutes at 90 °C. MSN were collected by centrifugation and washed with ethanol before further template extraction in 100 ml of a 3.7% hydrochloric acid solution in ethanol for 45 minutes at 90 °C. MSN were collected by centrifugation, washed twice with ethanol and stored in suspension at -20 °C. The thiol groups functionalized core of the MSN were labelled with ATTO-647-Maleimide to create fluorescent core labeled MSN.

S.2 Synthesis of MBGZn

Zn-containing mesoporous bioactive glass nanoparticles (MBGZn) were synthesized by using a microemulsion-assisted sol-gel approach[24]. Briefly, 2.24 g hexadecyltrimethylammonium bromide (CTAB) was dissolved in 104 mL of deionized water under continuous stirring at 30 °C for 30 min. Then, 32 mL of ethyl acetate was slowly poured into the solution under continuous stirring for 30 min. Subsequently, ammonium hydroxide (28%) was used to maintain pH at 10.5. After 15 min 23.04 mL of tetraethyl orthosilicate (TEOS) was added to the mixture and stirred for 30 min. Afterwards 4.34 g of $Ca(NO_3)$2.4H2O was dissolved into the mixture. After 30 min, 1.09 g $Zn(NO_3)$2.6H2O was introduced into the solution. The nominal composition of Zn-MBGNs was 70SiO2–25CaO–5ZnO (mol%). The mixture was stirred further for 4 h and then the suspension was centrifuged at a rate 9000 rpm (Centrifuge 5430R, Eppendorf, Germany) for 10 min to separate particles from the mixture. The precipitate was then washed twice with water and once with ethanol. Subsequently, the precipitate was dried in an oven at 60 °C for 24 h, followed by calcination at 700 °C for 2 h at a heating rate of 2 °C min−1.All the used chemicals were purchased from Sigma-Aldrich (Darmstadt, Germany) without further purification.

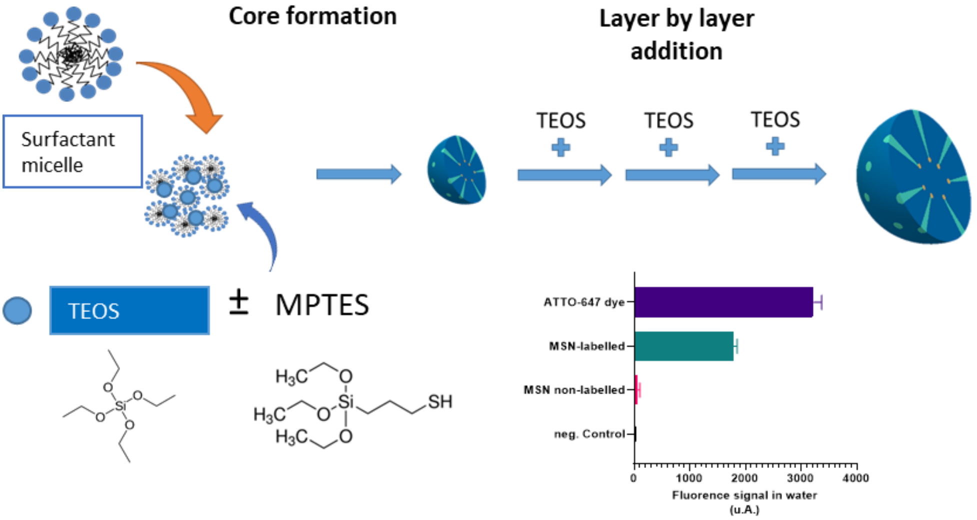

Figure S1: Synthesis scheme of core-labelled MSN. Thiol groups core functionalization MSN were further confirmed by labelled with ATTO-647-Maleimide and measured in a microplate reader (BIO-RAD) at 647 nm.

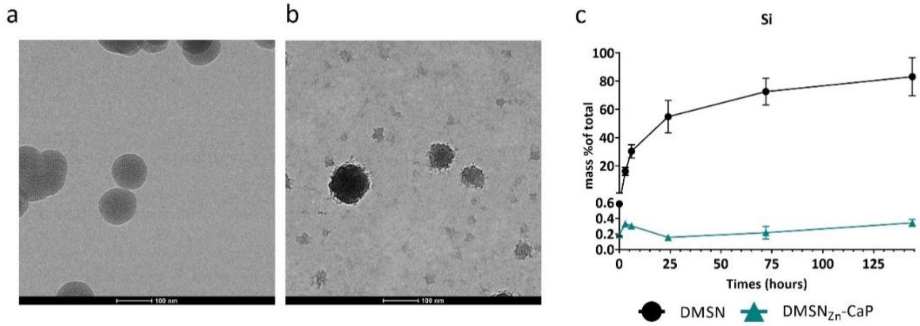

Figure S2: TEM images showing morphology of a) $DMSN_{Zn}$-CaP and b) DMSN after incubation in milliQ water of pH 7.4 for 144 hours. c) Ion release profiles of Si from DMSN and $DMSN_{Zn}$-CaP

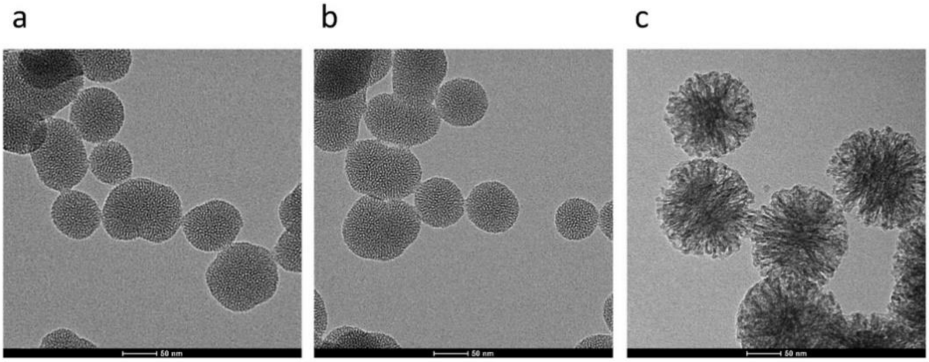

Figure S3: TEM images showing morphology of a) MSN, b) DMSN and c) MBGZn Scale bar is 50 nm.

Table S1 : Hydrodynamic size, Pdi and surface potential of MSN-CaZnP, MSNZn-CaP, DMSNZn-CaP and MBGZn-CaP measured by dynamic light scatting. All nanoparticles were measured in absolute ethanol.

Sample	Size (nm)	Pdi	Zeta potential [mV]
MSN-CaZnP	190±15	0.214±0.03	-19±5
MSN$_{Zn}$-CaP	198±9	0.247±0.05	-21±3
DMSN$_{Zn}$-CaP	201±22	0.250±0.10	-22±6
MBGZn-CaP	247±12	0.292±0.04	-18±10

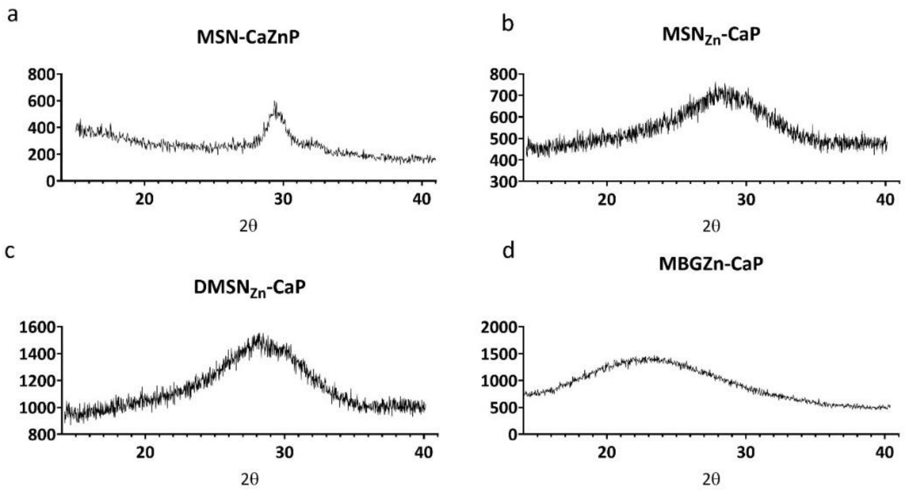

Figure S4 : XRD patterns of displayed amorphous non- crystallization of ; a) MSN-CaZnP, b) MSNZn-CaP, c) DMSNZn-CaP and d) MBGZn-CaP displayed amorphous non- crystallization of all nanoparticles.

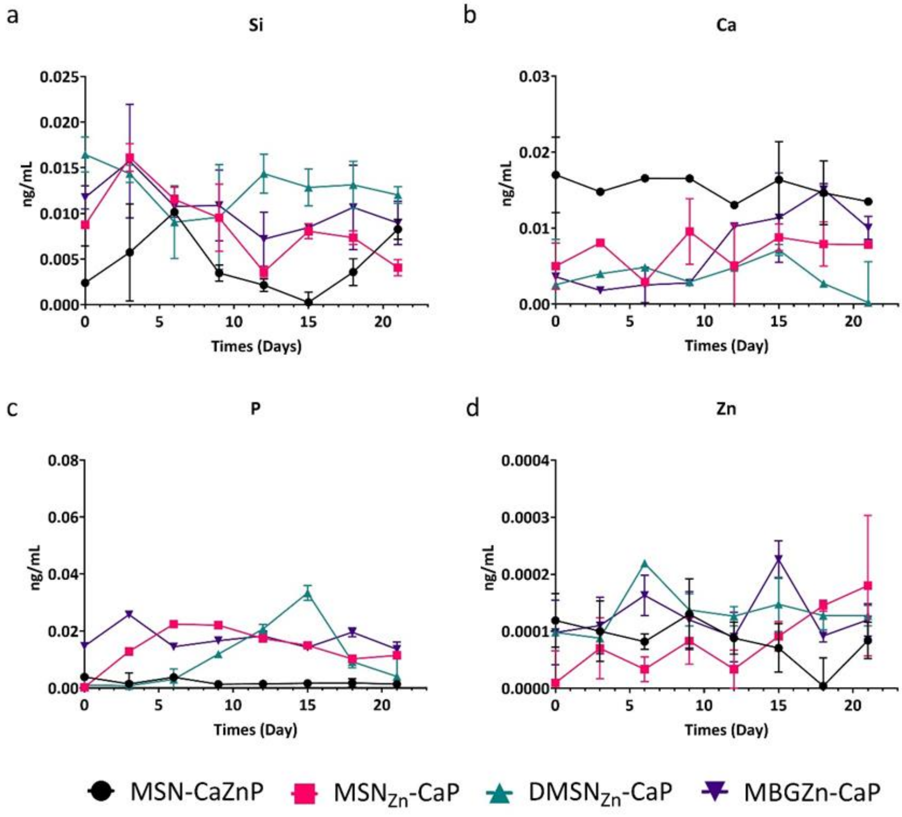

Figure S5: Ion release profiles using ICP-MS of a) Si, b) Ca, c) P and d) Zn of MSN-CaZnP (black), MSN$_{Zn}$-CaP (red), DMSN$_{Zn}$-CaP (green) and MBGZn-CaP (purple) thin nanoparticles film in cell culture media kept at 37 °C, 5% CO_2 in a humidified atmosphere.

S.3 Half-release time calculation

The half-release time required for silica, calcium, phosphate and zinc ions was calculated by fitting the data as displayed in Figure 2 to a non-linear fitting curve. The mathematical equation is shown below. Individual variables for each data sets can be found in Table R2.

$$M\% = YM * \frac{Y0}{(YM - Y0) * exp(-k * t) + Y0}$$

Equation 1

Where M% is % of total amount of ions present and t is time (hours).

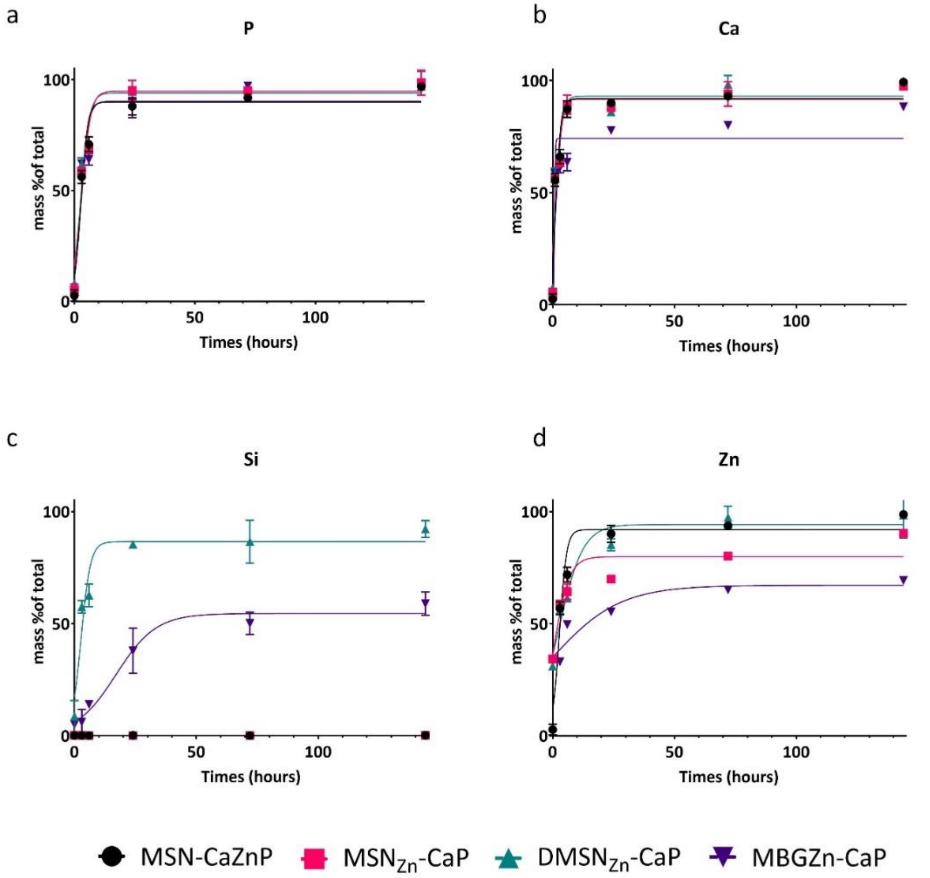

Figure S6: non-linear fitting curves based on equation 1 applied to a) P, b) Ca, c) Si, and d) Zn ion released from MSN-CaZnP, MSN$_{Zn}$-CaP, DMSN$_{Zn}$-CaP and MBGZn-CaP.

Table S2: calculated variables from non-linear logarithmic growth model

Si		MSN-CaZnP	MSN$_{Zn}$-CaP	DMSN~~$_{Zn}$~~-CaP	MBG$_{Zn}$-CaP
	YM	N.A.	N.A.	86.51	54.52
	Y0	N.A.	N.A.	17.23	6.052
	k	N.A.	N.A.	0.514	0.122
Ca					
	YM	91.77	92	93.13	74.2

	Y0	19.83	21.67	23.99	1.025
	k	0.9356	0.8144	0.7455	5.551
P					
	YM	89.88	94.79	94.01	90.27
	Y0	11	15.76	17.2	13.57
	k	0.7171	0.5355	0.5528	0.6361
Zn					
	YM	91.92	79.87	94.24	67.12
	Y0	11.64	36.23	35.76	34.95
	k	0.6877	0.318	0.2009	0.07062

The time required for 50% of each ion to be release from the nanoparticles was calculated by solving t in Equation 1 and can be found in Table R3

Table S3: The time required for 50 % of Si , Ca, P and Zn ions to be released from MSN-CaZnP, MSN$_{Zn}$-CaP, DMSN$_{Zn}$-CaP and MBGZn-CaP. N.A. = non applicable with equation 1

	MSN-CaZnP	MSN$_{Zn}$-CaP	DMSN$_{Zn}$-CaP	MBG$_{Zn}$-CaP
Ions	Half release time (hours)			
Si	N.A.	N.A	3.68	38.04
Ca	1.55	1.66	1.60	0.90
P	3.06	3.22	2.93	3.07
Zn	3.08	2.22	3.19	13.90

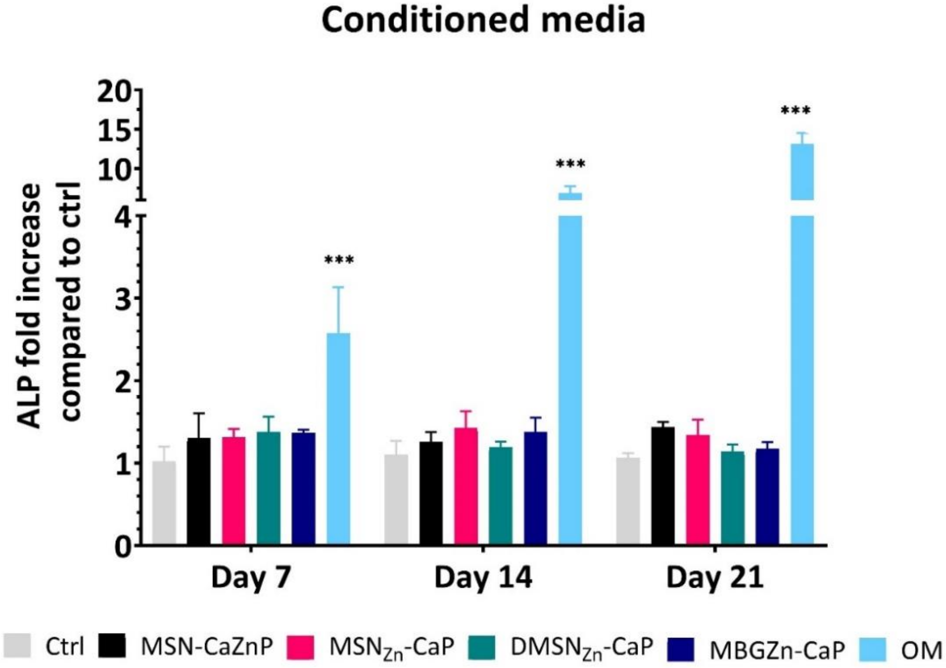

Figure S7: Relative ALP activity in hMSCs after exposure to nanoparticles in the form of conditioned media normalized to DNA content. The experiments were done in triplicate. Significant difference compared to the controls are shown by * representing p-values as follows; *p < 0.033; **p < 0.02; ***p < 0.001.

References

1. E. M. Younger and M. W. Chapman, J. Orthop. Trauma, 1989, Morbidity at bone graft donor sites, 3, 192-195.
2. S. Pina, R. Rebelo, V. M. Correlo, J. M. Oliveira and R. L. Reis, Osteochondral Tissue Eng., 2018, Bioceramics for osteochondral tissue engineering and regeneration, 53-75.
3. J. R. Jones, D. S. Brauer, L. Hupa and D. C. Greenspan, Int. J. Appl. Glass Sci., 2016,Bioglass and bioactive glasses and their impact on healthcare, 7, 423-434.
4. W. Wang and K. W. Yeung, Bioact. Mater., 2017, Bone grafts and biomaterials substitutes for bone defect repair: A review, 2, 224-247.
5. E. Bosch-Rué, L. Diez-Tercero, B. Giordano-Kelhoffer, L. M. Delgado, B. M. Bosch, M. Hoyos-Nogués, M. A. Mateos-Timoneda, P. A. Tran, F. J. Gil and R. A. Perez, Front. Cell Dev. Biol. , 2021, Biological roles and delivery strategies for ions to promote osteogenic induction, 8, 1809.
6. E. O'Neill, G. Awale, L. Daneshmandi, O. Umerah and K. W.-H. Lo, Drug Discov. Today., 2018,The roles of ions on bone regeneration, 23, 879-890.
7. M. Yamaguchi, J. trace elem. exp. med., 1998, Role of zinc in bone formation and bone resorption, 11, 119-135.
8. B. S. Moonga and D. W. Dempster, J. Bone Miner. Res., 1995, Zinc is a potent inhibitor of osteoclastic bone resorption *in vitro*, 10, 453-457.
9. A. S. Prasad, Adv. Nutr., 2013, Discovery of human zinc deficiency: its impact on human health and disease, 4, 176-190.
10. Y. Yu, K. Liu, Z. Wen, W. Liu, L. Zhang and J. Su, RSC Adv., 2020, Double-edged effects and mechanisms of Zn 2+ microenvironments on osteogenic activity of BMSCs: osteogenic differentiation or apoptosis, 10, 14915-14927.
11. C. Wu and J. Chang, J Control Release, 2014, Multifunctional mesoporous bioactive glasses for effective delivery of therapeutic ions and drug/growth factors, 193, 282-295.
12. K. Dashnyam, G.-Z. Jin, J.-H. Kim, R. Perez, J.-H. Jang and H.-W. Kim, Biomaterials, 2017, Promoting angiogenesis with mesoporous microcarriers through a synergistic action of delivered silicon ion and VEGF, 116, 145-157.
13. S. van Rijt, K. de Groot and S. C. Leeuwenburgh, Tissue Eng., 2022, Calcium phosphate and silicate-based nanoparticles: history and emerging trends, 28, 461-477.
14. Y. Wang, Q. Zhao, N. Han, L. Bai, J. Li, J. Liu, E. Che, L. Hu, Q. Zhang and T. Jiang, Nanomed. Nanotechnol. Biol. Med., 2015, Mesoporous silica nanoparticles in drug delivery and biomedical applications, 11, 313-327.
15. V. Lalzawmliana, A. Anand, M. Roy, B. Kundu and S. K. Nandi, Mater. Sci. Eng., C, 2020, Mesoporous bioactive glasses for bone healing and biomolecules delivery, 106, 110180.
16. H. Zhu, K. Zheng and A. R. Boccaccini, Acta Biomater., 2021, Multi-Functional Silica-based mesoporous materials for simultaneous delivery of biologically active ions and therapeutic biomolecules.
17. G. M. Luz and J. F. Mano, Nanotechnology, 2011, Preparation and characterization of bioactive glass nanoparticles prepared by sol–gel for biomedical applications, 22, 494014.
18. C. Vichery and J.-M. Nedelec, Materials, 2016, Bioactive glass nanoparticles: from synthesis to materials design for biomedical applications, 9, 288.

19. Y.-S. Lin, N. Abadeer and C. L. Haynes, Chem. Commun., 2011, Stability of small mesoporous silica nanoparticles in biological media, 47, 532-534.

20. W. J. Znidarsic, I.-W. Chen and V. P. Shastri, J. Mater. Chem., 2012, Influence of surface charge and protein intermediary layer on the formation of biomimetic calcium phosphate on silica nanoparticles, 22, 19562-19569.

21. P. Sutthavas, Z. Tahmasebi Birgani, P. Habibovic and S. van Rijt, Adv. Healthcare Mater., 2021, Calcium Phosphate-Coated and Strontium-Incorporated Mesoporous Silica Nanoparticles can Effectively Induce Osteogenic Stem Cell Differentiation, 2101588.

22. R. Rosenbrand, D. Barata, P. Sutthavas, R. Mohren, B. Cillero-Pastor, P. Habibovic and S. van Rijt, Int. J. Nanomed., 2018, Lipid surface modifications increase mesoporous silica nanoparticle labeling properties in mesenchymal stem cells, 13, 7711.

23. K. Möller and T. Bein, Chem. Mater., 2019, Degradable drug carriers: Vanishing mesoporous silica nanoparticles, 31, 4364-4378.

24. Q. Liang, Q. Hu, G. Miao, B. Yuan and X. Chen, Mater. Lett., 2015, A facile synthesis of novel mesoporous bioactive glass nanoparticles with various morphologies and tunable mesostructure by sacrificial liquid template method, 148, 45-49.

25. P. Sutthavas, P. Habibovic and S. H. van Rijt, Biomater. Sci., 2021, The shape-effect of calcium phosphate nanoparticle based films on their osteogenic properties, 9, 1754-1766.

26. Z. Neščáková, K. Zheng, L. Liverani, Q. Nawaz, D. Galusková, H. Kaňková, M. Michálek, D. Galusek and A. R. Boccaccini, Bioact. Mater., 2019, Multifunctional zinc ion doped sol–gel derived mesoporous bioactive glass nanoparticles for biomedical applications, 4, 312-321.

27. M. Prokopowicz, A. Szewczyk, A. Skwira, R. Sądej and G. Walker, Drug Deliv. Transl. Res., 2020, Biphasic composite of calcium phosphate-based mesoporous silica as a novel bone drug delivery system, 10, 455-470.

28. L. Wang and G. H. Nancollas, Chem. Rev., 2008, Calcium orthophosphates: crystallization and dissolution, 108, 4628-4669.

29. H. P. Rim, K. H. Min, H. J. Lee, S. Y. Jeong and S. C. Lee, Angew. Chem. Int. Ed., 2011, pH-tunable calcium phosphate covered mesoporous silica nanocontainers for intracellular controlled release of guest drugs, 50, 8853-8857.

30. S. P. H. Moghaddam, R. Mohammadpour and H. Ghandehari, J Control Release, 2019, *In vitro* and *in vivo* evaluation of degradation, toxicity, biodistribution, and clearance of silica nanoparticles as a function of size, porosity, density, and composition, 311, 1-15.

31. E. E. Golub and K. Boesze-Battaglia, Curr Opin Orthop., 2007, The role of alkaline phosphatase in mineralization, 18, 444-448.

32. X. Yang, Y. Li, X. Liu, Q. Huang, W. He, R. Zhang, Q. Feng and D. Benayahu, Biomed. Mater., 2016, The stimulatory effect of silica nanoparticles on osteogenic differentiation of human mesenchymal stem cells, 12, 015001.

Chapter 6

Laser-based ion doping is a suitable alternative to dope biologically active ions into colloidal bioglass nanoparticles

Laser-based ion doping is a suitable alternative to dope biologically active ions into colloidal bioglass nanoparticles

Pichaporn Sutthavas[1], Matthias Schumacher[1], Martyna Nikody[1,2], Vaijayanthi Ramesh[4], Jurij Jakobi[4], Elizabeth R. Balmayor[1,3], Pamela Habibovic[1], Christoph Rehbock[4], Stephan Barcikowski[4*] and Sabine van Rijt[1*]

[1]Department of Instructive Biomaterials Engineering, MERLN Institute for Technology-Inspired Regenerative Medicine, Maastricht University, P.O. Box 616, 6200 MD Maastricht, the Netherlands

[2]Department of Complex Tissue Regeneration, MERLN Institute for Technology-Inspired Regenerative Medicine, Maastricht University, P.O. Box 616, 6200 MD Maastricht, the Netherlands

[3]Experimental Orthopaedics and Trauma Surgery, Department of Orthopaedic, Trauma, and Reconstructive Surgery, RWTH Aachen University Hospital, Aachen, Germany.

[4]Technical Chemistry I and Center for Nanointegration Duisburg-Essen (CENIDE), University of Duisburg Essen, Universitaetsstr.2, 45141 Essen, Germany

Abstract

Bioactive glass nanoparticles (nBGs) have demonstrated promising properties for bone regeneration due to their bone-binding ability. Incorporating multiple ions into nBGs can improve their bioactivity and provide them with additional functionalities aiding bone repair. However, incorporating multiple ions into nBGs combining different functionalities is still challenging as the additional ions often interfere with the nanoparticle properties. To overcome these challenges, here we report the use of pulsed laser doping and co-doping techniques as an alternative method for ion incorporation into colloidal nBGs. We demonstrate the simultaneous laser-induced incorporation of (Fe), strontium (Sr), and/or copper (Cu) ions into nBGs from simple salt solutions without altering the particles´ morphology or structure. Furthermore, laser-doped nBGs were biocompatible and could significantly increase alkaline phosphatase (ALP) production in human mesenchymal stromal cells (hMSCs). Moreover, laser-co-doped nBGs containing Fe and Sr ions significantly increased vessel formation by human umbilical vein endothelial cells (HUVEC). Therefore, pulsed laser doping in liquids was shown to be a versatile technique to incorporate multiple ions into nBGs and allow systematic studies on cooperative effects of dopants in active biomaterials.

1. Introduction

Bioactive glass nanoparticles (nBGs) are extensively researched in the bone regenerative medicine field due to their inherent bioactivity and bone-bonding capabilities [1]. nBGs consist of a silica network containing calcium and phosphate ions, creating an open glass structure. The extent of calcium and phosphate present in the glass plays an important role in their biodegradation rate and bioactivity. Specifically, the dissolution of the particles and subsequent silica, calcium, and phosphate ion release can promote osteogenic processes (stem cell differentiation towards mature osteoblasts). Moreover, silica ions are known to promote angiogenesis (*de novo* formation of blood vessels) [2]. Due to their small size, ranging from 20 to 800 nm, nBGs have been used as components in scaffolds, coatings, and drug delivery vehicles [3].

The incorporation of additional ions into nBGs (i.e. ion doping) such as copper (Cu), strontium (Sr), and zinc (Zn) can be used to further improve their bioactivity or add new functionalities [2,4]. For example, the incorporation of metallic dopants such as silver and gold could infer antibacterial properties to the nBGs particles [5,6]. Furthermore, Cu doping improved nBGs angiogenic properties, whereas Sr and Zn doping has been used to improve nBGs osteogenic activity [7-9]. Wet synthesis methods are generally used to dope nBGs with ions by mixing the ionic salts with the silica precursors. However, the selection of ions, doping ratio, and synthesis protocol highly influence nBGs formation and can (negatively) influence their morphology, homogeneity, and biodegradation rate [10]. Moreover, ion doping via sol-gel wet synthesis is limited in the number and amounts of ions that can be doped before nBGs are negatively influenced, and discrepancies between the intended and actual doping amounts frequently occur [11]. Finally, with current methods, it is difficult to dope multiple ions simultaneously in single nBGs particles and ion distribution inside the nBGs matrix may be impaired.

Reactive laser processing of colloids has emerged as an alternative method in the last few years and was recently reviewed by the Tibbets group [12]. Process variants are irradiation of precursor solutions in liquids (reductive laser synthesis in liquids), ablation of a bulk target in the presence of an ionic precursor solution (reactive laser ablation in liquids), or irradiation of a nanoparticle or microparticle suspension in the presence of ionic precursors. Here, two processes are involved: I) Formation, size reduction, or excitation of a nanoparticle or microparticle base material, and II) Reduction of the ionic precursor to form small nanoparticles. The result is usually a composite material forming base materials supporting nanoparticles or different types of alloy ultra-structures [12]. One sub-field of reactive laser synthesis in liquids is laser doping, where not nanoparticles but single atoms from a liquid are incorporated into the base material, a process usually favored by low precursor concentrations. For example, the laser ablation of a Gd_2O^3 target in a Eu^{3+} solution yielded doped material with a characteristic visible fluorescence [13]. Other studies describe the incorporation of single atoms of gold and nickel into metallic Ru [14,15] or silver into Ir [16]. Recently Zerebecki *et al.* reported laser-induced doping of Fe ions into Co_3O_4 by applying low fluence laser heating and precisely controlling the number of laser pulsed per colloid volume. They observed an accumulation of small $FeO(OH)_x$ clusters on the surface, followed by diffusion-based distribution of Fe atoms in the Co_3O_4 matrix under retention of particle size [17]. Laser-based doping of bioactive glass (BG) on the other hand is only limitedly explored. In one study Li and Ramesh *et al.* examined the reactive laser fragmentation of micrometer-sized 45S5 BG in the presence of Cu (EDTA) and Fe (EDTA) complex solutions and found two effects I) Incorporation of Fe and Cu into the BG network and II) partial reduction of particles size. The authors further examined the ion release from these materials and found Fe to be more strongly incorporated into the BG network while Cu was more active [18]. Major advantages of the pulsed laser doping method include the facile control of doping levels by ion concentrations as well as the possibility for homogeneous ion incorporation. However, the previously published laser-doping experimental designs either only achieved very low dopant concentrations (surface doping) while keeping the host particle size constant or caused significant downsizing /fragmentation) of the host particles while doping. Achieving higher doping levels at constant particle size and morphology during pulsed laser doping has not been achieved yet. Thereto, in this work we chose a two-step approach, generating nBGs by established sol-gel chemistry and consecutively irradiating the nBGs suspension by a nanosecond-pulsed, kilohertz-repetition-rate UV laser in salt solutions, while keeping the nBGs particle size constant. Furthermore, we extended the range of ions utilizing Sr^{2+} due to its known osteogenic activity and Cu^{+} and Fe^{2+} as they support angiogenesis [19-22]. The ability of doped nBGs to stimulate angiogenesis was investigated using a tubular formation assay. Moreover, we investigated whether ion doped nBGs showed improved osteogenic bioactivity by assessing ALP levels and ability to promote matrix production in hMSCs.

2. Experimental Methods

2.1 Reagents

25% aqueous ammonia was purchased from Carl Roth (Germany). Absolute ethanol (EtOH) and phosphate-buffered saline (tablets, PBS) were purchased from VWR (Germany). Methanol, tetraethyl orthosilicate (TEOS, ≥99.0%), triethyl phosphate (TEP, ≥99.8%), calcium nitrate tetrahydrate (CNT, ≥ 98%) and MTT (3-(4,5-dimethylthiazol-2-yl)-2,5-diphenyl tetrazolium bromide) kit were obtained from Sigma Aldrich (Germany). Human vascular endothelial growth factor (VEGF165) was purchased from Miltenyi Biotec (Germany). Streptomycin and penicillin were purchased from Gibco, Life Technologies (USA). Alizarin Red S (sodium alizarin sulphonate), endothelial growth medium BulletKit was purchased from Lonza (Germany). Bovine serum albumin (BSA), trypsin, L-glutamine, tween-20, triton X-100, NHS-Fluorescein (5/6-carboxyfluorescein succinimidyl ester), minimum essential medium alpha (αMEM) and paraformaldehyde (PFA) were purchased from Thermo Fisher (The Netherlands).

2.2 Synthesis of nano-sized bioactive glass (nBGs) particles

nBGs particles were synthesized by a base-catalyzed sol-gel process[23]. Unless stated otherwise, all synthesis steps were performed at room temperature (RT) while vigorously stirring. First 2.77 g TEOS and 0.25 mL TEP were dissolved in 2.8 mL methanol. After 30 minutes, a mixture of 12.6 mL ddH_2O, 29 mL ethanol, and 2.56 mL 25% ammonia was added. After another 60 minutes, 1.57 g CNT were added. After 12 hours, nBGs particles were collected by centrifugation at 1500 g for 5 minutes and washed in a mixture of methanol and ethanol. The collected particles were vacuum-dried, calcinated at 600°C for 3 hours with a heating rate of 2 K /minutes (Nabertherm, Germany), and re-suspended in ethanol at a concentration of 10 mg/ mL for subsequent processing.

2.3 Laser in situ doping of nBGs particles

Laser-doping was carried out in a liquid-jet flow through a reactor introduced by Lau *et al*. [24] following a procedure described in detail in our previous work [18]. In short, a 20 wt% suspension of nBGs was initially washed three times with deionized water and then dispersed in mixed Fe-EDTA, Cu-EDTA, and $Sr(NO_3)_2$ solutions (178 mM stock solutions) and laser irradiated for 30 passages with a mean volume flow-rate of 0.54 mL/s using a nanosecond-pulsed laser (Avia 355-14, Coherent, Inc., USA) at a wavelength of λ=355 nm, a repetition rate of 40 kHz and a laser fluency of 60 mJ/cm^2. The irradiated samples had initial Fe:Cu:Sr molar ratios of A) 1:1.5:1.5, B) 1:3:0, C) 1:0:3. Furthermore, a control immersed in a 1:1.5:1.5 solution was processed similarly in the passage reactor, just without laser irradiation. The processed samples were washed twice in deionized water, twice in ethanol, and finally dispersed in fresh ethanol.

2.4 Nanoparticle characterization

Crystallinity of synthesized nBGs were determined by X-ray diffractograms (XRD) using a Bruker D2 Phaser diffractometer (USA) with Cu Kα radiation ($\lambda = 1.5406$ Å) in the range of $6 \leq 2\Theta \leq 60°$ in 0.02° increments and with an integration time of 0.75 s. ATR-FTIR (Nicolet iS50, Thermo Scientific, USA) was used to assess functional groups, running 32 scans between 400 and 4000 per cm with a resolution of 0.5 per cm. Spectra were analyzed with Spectragryph (F. Menges, Version 12, 2018, http://www.effemm2.de/spectragryph/). nBGs' morphology were visualized and assessed using transmission electron microscopy (TEM, FEI Tecnai G2 Spirit BioTWIN iCorr (G0.201), USA). The particle size was determined from TEM images using ImageJ analysis (ImageJ 1.52n). The surface charge of synthesized and modified particles suspended in PBS (0.5 mg/mL) was evaluated with zeta potential analysis (Malvern Zetasizer Nano, Panalytical, UK). Further characterization of the nBGs samples after doping was done with scanning electron microscopy (SEM, Thermo Fisher Scientific, Apreo LoVac, USA), and global composition was determined using energy-dispersive X-ray spectroscopy (EDX). Further EDX (Thermo Fisher Scientific, Apreo LoVac, USA) measurements of the laser-doped nBGs composition on a single particle level were performed using Cs-corrected transmission electron microscope Jeol 2200FS (Japan) operating at 200 kV acceleration voltage. The samples were prepared by evaporation of a droplet of nBGs solution on a carbon film-supported gold grid.

2.5 *In vitro* cell culture

hMSCs (PromoCell, Germany) at passage 3 were expanded in αMEM supplemented with 10% FBS, 2 mM L-glutamine, 0.2 mM ascorbic acid, 100 U/mL penicillin and 100 mg/mL streptomycin, and the cultures kept in a humidified atmosphere with 5% CO_2 at 37 °C. 5000 cells/cm2 density and 1 mL in volume of cells at passage 4 suspending in cell culture media, were seeded in each well of 12-well cell culture plates. For proper adhesion, cell culture media were exchanged after 24 hours incubation time. Tube formation assay was performed using HUVEC pooled from different donors (Lonza, Germany). Prior to the experiment, the cells were cultured in endothelial growth medium (EGM, Lonza, Germany) without VEGF supplementation at 37°C and 5% CO_2.

2.6 Cytotoxicity

The cytotoxicity of nBGs, iron and copper ion laser-doped nBGs with (FeCu) and iron, copper, and strontium ions laser-doped nBGs (FeCuSr) at concentrations ranging from 25 to 100 µg/mL was determined by the MTT assay according to kit's instruction. hMSCs were seeded at 5000 cells/cm^2 density in 96-well plates. As the confluence reached 80-90%, hMSCs were exposed to freshly prepared media with nBGs at different concentrations. Cytotoxicity was assessed 72 hours after exposure of the cells to nBGs. At each time point, 10 µL of MTT reagent was added to each well, followed by 4 hours of incubation at 37 ˚C, 5% CO_2. Crystalized formazan were dissolved in 150 µL of isopropanol with 10 % by volume Triton-X 100. Amount of dissolved formazan was immediately determined by absorption at 570 nm using a microplate reader (BIO-RAD microplate reader-550, USA). Wells without cells but with complete medium, nBGs, and MTT reagent were used as blank baseline. The average formazan concentration for each condition was used to calculate based on standard curve of known formazan concentration.

2.7 Alkaline phosphatase assay

To evaluate the osteogenic capabilities in suspension, nanoparticles were suspended in basic media (no osteogenic stimulants) at a concentration of 100 µg/mL. Cell culture medium was refreshed every 3 days. After 7, 14, and 21 days of culturing, the ALP activity was measured for all conditions. 100 nM dexamethasone was added into basic media to make osteogenic media (OM). hMSCs cultured in osteogenic medium (OM; 100 nM dexamethasone) were included as a positive control for all samples. Alkaline phosphatase (ALP) production of hMSCs were used to evaluate their osteogenic differentiation at days 7, 14, and 21 of culture. ALP levels were normalized with DNA content measured by CyQuant Cell Proliferation assay kit (Thermo Fisher Scientific, Germany). Cell lysis buffer were made by diluted provided with the kit concentrated lyse buffer at ration of 1:20 in PBS and RNAse A (Thermo Fisher Scientific, Germany) were added to achieved 0.1% volume/volume. After discarding cell culture media, the cell layers were washed once with PBS. Samples in 100 µL of PBS were then undergo 6 times of 5 minutes each freezing-thawing cycle. 200 µL of cell lysis buffer was then introduced to each well and the samples undergo two more times of 30 minutes freeze-thawing cycles. After thawing, each sample were transferred into Eppendorf tube. All the samples' volume were then equalized by adding more cell lysis buffer. To ensure complete lysis of the cells, samples were sonicated for 5 minutes and incubated for 60 minutes at RT. DNA content were then quantified by mixing 100 µL of cell lysate with 100 µL CyQuant GR dye in 96 well plate. After 15 minutes incubation, fluorescence signals of samples and standard DNA concentrations were measured using microplate reader (BIO-RAD microplate reader-550, USA). CDP-star solution (ready-to-use, Sigma Aldrich, Germany) was used to quantify ALP activity. 40 µL of each sample cell lysate was incubated with 200 µL of CDP-star solution in a white-bottom 96-well plate at RT for 30 minutes in the dark. After incubation, chemical luminescence signal were measured at 466 nm using a microplate reader (BIO-RAD microplate reader-550, USA). The ALP values of each sample, normalized to their total DNA content, were expressed as an x-fold increase compared to hMSCs cultured with non-osteogenic medium.

2.8 Mineralization assay

Mineralization by hMSCs was measured via calcium deposition after 28 days of culturing using Alizarin Red S (sodium alizarin sulphonate) staining. After cell media were removed, 4% PFA was used to fixed cells to the cell culture plate. Alizarin Red S were then added to stained calcium present within each well. Red S solution was prepared by dissolving 2 g of solid dye powder in 100 mL of bi-distilled water. Once the solid was completely dissolved, pH of solution was then adjusted to 4.2 by 0.1mM ammonium hydroxide in bi-distilled water. Prior to staining, cells were first washed once with PBS, then twice with bi-distilled water. 200 µL Alizarin Red solution was added to each well and incubated for 15 minutes at RT. Sample were then washed thrice with bi-distilled water to remove excess dye. Staining was visualized and image were recorded under a microscope (Nikon SMZ-25, Nikon, Japan) with 10X magnification.

A quantification method was carried out by performing extraction of the dye by 10 % (w/v) cetylpyridinium chloride (CPC) (Sigma Aldrich, Germany) in 10 mM sodium phosphate (pH 7.0). Alizarin Red dye were dissolved from the samples by adding 1 mL of CPC solution per well and incubated for 15 minutes at RT under constant shaking. Exact dye solution were then removed from the cell culturing plate. To quantified amount of dye exacted, 10 µL of the extracted dye was further diluted 10 folds with CPC solution and transferred to a 96-well plate and. The absorbance at 555 nm of violet-coloured supernatant was analysed with a microplate reader (CLARIOstar Multimode Microplate Reader, BMG Labtech, Germany). Concentration were then calculated based on standard curve of known calcium concentration solution.

2.9 *In vitro* tube formation assay

HUVECs pooled from different donors were cultured in endothelial growth medium (EGMTM, Lonza, Germany) without VEGF supplementation at 37°C and 5% CO_2. An *in vitro* tube formation assay was performed in 48 well tissue culture plates (NUNC, Thermo Fisher Scientific, Germany). Wells were coated with 50 µL per well Geltrex™ (Thermo Fisher Scientific, Germany) according to the manufacturer's instructions. The laser-doped nBGs particles were suspended in Geltrex at 0.25 mg/mL. Pure Geltrex and Geltrex with the addition of 100 ng/mL of VEGF served as controls. HUVECs at passage 3 were seeded at a density of 40 000 cells/cm^2 in EGM. After 12 hours of incubation, cells were washed twice with PBS and fixed with 4% PFA for 20 minutes. Then, cells were washed twice and stored at 4^{o}C for subsequent analysis.

2.10 Fluorescent staining and microscopy

Fixed cells were permeabilized with 0.1% TritonX-100 in PBS (200 µL /well) for 10 minutes and washed twice with PBS. Then, F-actin staining was performed by incubation with 50 µL/well of 1:200 PBS-diluted Alexa Fluor™ 488 phalloidin (Thermo Fisher Scientific) for 20 minutes in the dark, followed by two washing steps in PBS. Cell nuclei were stained by immersion in 50 µL per well of DAPI (Thermo Fisher Scientific, Germany) at a concentration of 0.5 µg/mL in PBS for 5 minutes, followed by a last washing step. Imaging was performed using an inverted Nikon TI-E microscope (Nikon Instruments Europe BV, the Netherlands). Images were processed and analyzed using Nikon NIS-Elements Viewer 4.50, and quantitative analysis of *in vitro* tubule formation was performed using the AngioTool software[25].

2.11 Statistical analysis

Statistical analysis of ALP activity and mineralization experiments were performed using triplicates (n=3), and data is presented as mean ±

standard deviation. To analyze the data regarding the osteogenic differentiation, statistical evaluation was performed using GraphPad Prism 9.1 using one-way ANOVA followed by Turkey’s multiple comparisons and mean differences were considered statistically significant when $p<0.033$. Statistical analysis of the tube-formation assay was performed using ordinary one-way ANOVA followed by Tukey’s multiple comparison test. The level of significance was set to $p<0.05$.

3. Results and discussion

3.1 nBGs synthesis and metal ion doping

nBGs particles with glass composition of $SiO_2/CaO/P_2O_5$ = 80/15/5 mol-% were synthesized using a base-catalyzed sol-gel process, and subsequently calcined at 600°C, similar to what we reported previously [23]. Uniform round-shaped nanosized nBGs particles were obtained as shown by TEM (Figure 1a). Fourier transform-infrared (FTIR) spectrum of the nBGs particles displayed a peak at ~400 and ~1000 cm^{-1} characteristic for the Si-O bond (Figure 1b). Moreover, XRD analysis showed that nBGs particles were amorphous (Figure 1c).

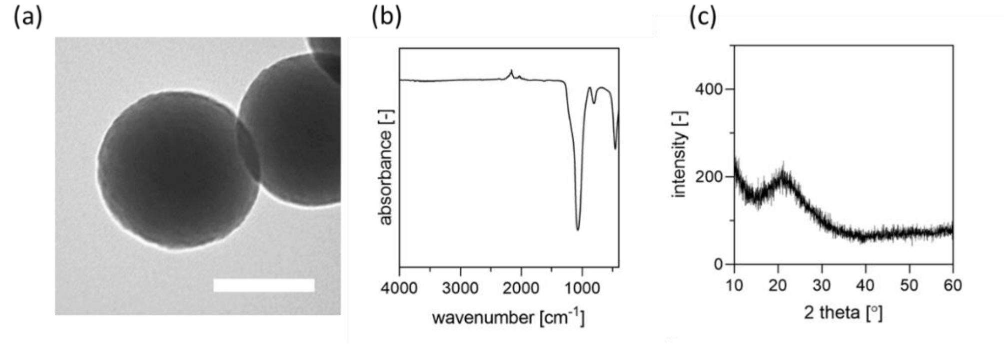

Figure 1: Characterization of nBGs; (a) Morphology of synthesized nBGs by TEM. Scale bar represents 100nm (b) FTIR spectra of the nBGs (c) X-ray diffraction patterns of nBGs.

Laser doping was conducted using the nanosecond UV laser irradiating the free liquid jet of the passage reactor (30 passages for each sample). The 20 wt% nBG suspensions were exposed to initial Fe: Cu: Sr molar ratios of A) 1:1.5:1.5, B) 1:3:0, C) 1:0:3. Furthermore, a control immersed in a 1:1.5:1.5 solution was processed. Fe-EDTA solutions with a pronounced UV extinction at 355 nm (laser wavelength) were used to ensure an efficient absorbance of the laser energy by the sample. After laser processing, nBGs samples were analyzed with SEM. Figure 2 shows exemplary SEM images of the raw and doped samples. Number-weighted particle size distributions obtained from these images indicate a mean value of 124.7 ± 11.3 nm before and 127.5 ± 13.6 nm after laser processing, which indicates that particle size was not significantly affected by the laser processing. In contrast to our previous work using micrometer-sized BG particles [18], no fragmentation process (size reduction) was observed, which allows us to evaluate doping effects independently from particle size effects. Moreover, our method also presents an advantage over conventional co-precipitation methods for nBGs ion doping which are known to negatively impact nBGs formation, structure, and morphology depending on ion concentration and synthesis conditions [11]. Especially incorporation of Fe in BG has resulted in the formation of particle agglomerates and can negatively impact nanoparticle structure [26, 27].

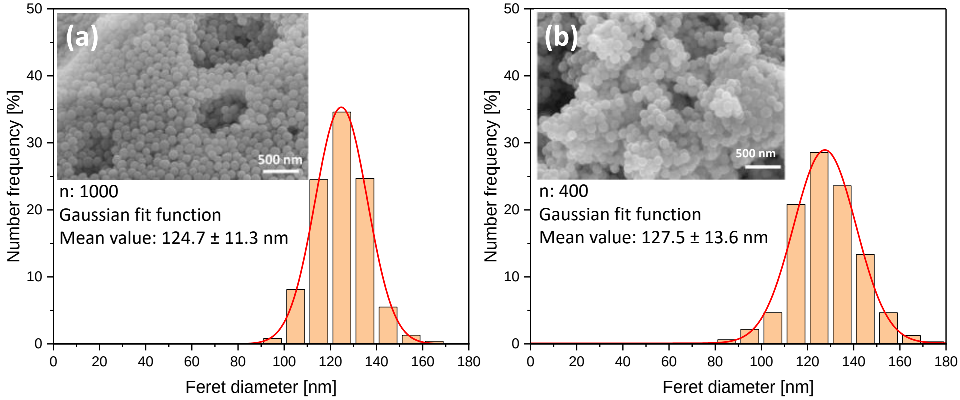

Figure 2: Number-weighted particle size distributions and exemplary SEM images of a) raw nBGs and b) nBGs laser-doped with Fe:Cu:Sr distributions.

Next, we analyzed the elemental composition of the doped nBGs. The Si content as the major network-forming element was unaffected by the doping (Figure 3a), which is to be expected as minor changes in the composition of the dominant element may not have been detectable with sufficient accuracy. For the major network modifier Ca, a reduction of about 50% for all doped and immersed samples was found. This may be due to the presence of EDTA in the samples, which could have initiated Ca leaching by complexation, as documented e.g. for hard tissue decalcification [28]. Moreover, we observed that Fe, Cu, and Sr were present in the doped nBGs particles showing that the laser treatment was effective. In contrast, no ion concentrations could be detected in immersed nBGs, likely because of unsuccessful or too low ion incorporation in the absence of a laser beam. Examination of the doping levels of the corresponding elements revealed that in Fe:Cu doped nBGs, higher levels of Cu were embedded compared to Fe, which was to be expected as the Fe:Cu ratio in the experiment was 1:3. However, this contradicts our previous findings on micro-sized BG educt particles [18], where 1) the overall doping levels were 50 times higher and 2) the embedding of Fe was much more pronounced than Cu. This seems to indicate that under comparable process conditions, doping in conjunction with a laser fragmentation process (particle size reduction) is more efficient than laser doping without size reduction which was done in this work. Higher doping levels in our previous study were probably caused by the in-situ size reduction process occurring simultaneously to the doping, which created a highly active and larger surface area, favoring ion adsorption. Even at similar incident laser fluence, the far higher optical cross-section of micro-BG compared to nBGs would cause higher effective laser fluence and trigger photomechanical effects. Recently, laser fragmentation mechanism has been studied for single microparticles, pointing at a photomechanical contribution to the fragmentation [29] not to be expected for smaller particles (such as nBGs) as those are unlikely to fulfill the stress confinement criteria for nanosecond pulses. Hence, nanosecond-pulsed UV laser excitation of nanoparticles in the low fluence regime applied here is most likely linked to a particle-surface-heating process, causing pulsed-laser-induced diffusion enhancement [17].

Furthermore, ion uptake specificity (higher affinity of Fe than Cu as found in [18]) seems to be less pronounced (not dominant) at lower doping levels or in case no size reduction occurs. Upon co-doping with Sr, the Fe doping levels drastically increased by a factor of 9, so the presence of Sr seemed to promote Fe doping. This may be attributed to the overall larger ionic radius of Sr^{2+} in comparison to Ca^{2+} [30,31]. This may have widened the BG network and promoted the uptake of other ions such as Fe. In the case of the Cu:Fe:Sr co-doping we found a higher doping level of Fe in comparison to Cu, which is in accordance with our previous findings [18]. Finally, we probed for the presence of Fe, Cu, and Sr in nBGs on a single particle level using TEM-EDX (Figure 3c and d) and found a moderate accumulation of the corresponding ions in the particles, though total doping levels were low. The distribution of the elements as determined by TEM-EDX mapping of the particles in Figure 3 was homogeneous. This is in contrast with previous experiments where the laser-induced embedding of Fe atoms into Co_3O_4 led to an enrichment of Fe in the near surface regions [17], though such a surface enrichment phenomenon may not have been detectable due to the overall low signals of the corresponding elements. Overall, the nanosecond UV laser excitation of nBGs dispersed in metal salts or metal salt mixtures results in homogeneous doping or co-doping of the metals into the nBGs volume, without changing the host particle size.

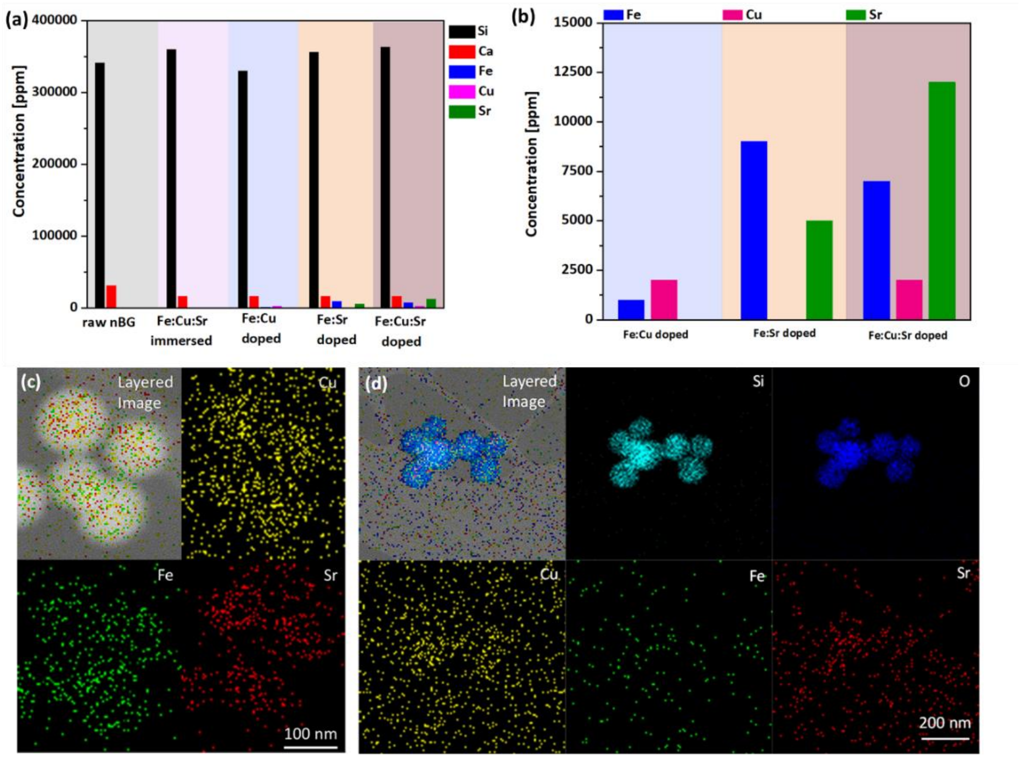

Figure 3: Particle composition: SEM-EDX ensemble measurements of a) all elements and b) Fe, Cu, and Sr present in laser-doped samples. TEM-EDX elemental mapping of c) Fe, Cu, Sr doped and d) Fe, Cu, Sr immersed samples.

3.2 Biocompatibility and induction of ALP levels

The biocompatibility of immersed nBGs, FeCu, and FeCuSr laser-doped nBGs was assessed in hMSCs after 72 hours of exposure to concentrations ranging from 25 to 100 μg/mL using the MTT assay (Figure 4a). None of the conditions tested resulted in a significant change in hMSCs metabolic activity compared to control cells. These results indicate that both, immersed and laser-doped nBGs were biocompatible with hMSCs at the concentrations tested.

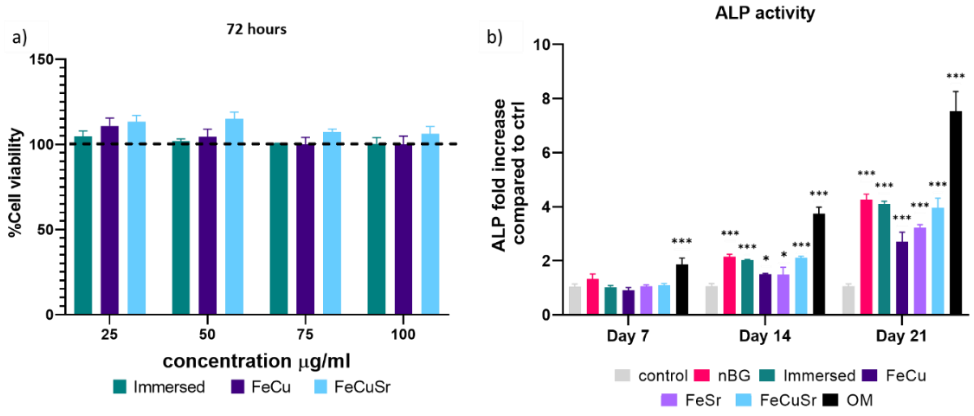

Figure 4: Metabolic activity and ALP production in hMSCs. a) Metabolic activity of hMSCs measured using the MTT assay after 72 hours exposure to 25, 50, 75, and 100 µg/mL immersed nBGs, FeCu, and FeCuSr laser doped nBGs (depicted as immersed, FeCu and FeCuSr, respectively). The metabolic activity is shown as % compared to control cells. b) hMSCs ALP activity after exposure to 100 µg/mL of nBGs, immersed nBGs, and FeCu, FeSr, FeCuSr laser doped nBGs. ALP activity was normalized to DNA content. Negative control group was cells cultured in basic media and the positive control is cells cultured in OM media. All conditions were performed in triplicate. Significant differences between samples and negative controls were indicated by *, as * representing p-values as follows; *$p < 0.033$; **$p < 0.02$; ***$p < 0.001$.

Next, the ability of the nBGs and laser-doped nBGs nanoparticles to induce ALP activity, a known marker for hMSCs osteogenic differentiation, was assessed.

After 7 days of incubation, no significant ALP activity was measured in any of the sample conditions. Significant ALP production was observed after 14 and 21 days of exposure for all samples tested although lower compared to the positive control (OM). The ALP activity in hMSCs exposed to nBGs, immersed nBGs, and FeCuSr laser doped nBGs after 14 days was similar; 2.14 fold (in comparison to control) for nBGs, 2.02 fold for immersed nBGs, and 2.12 fold for FeCuSr laser doped nBGs. hMSCs exposed to FeCu and FeSr laser-doped nBGs also led to increased ALP production albeit significantly lower compared to the other sample conditions (1.49 fold for FeCu and 1.48 fold for FeSr). After 21 days, overall ALP levels were higher than after 14 days and showed a similar trend; exposure to immersed nBGs, and FeCuSr laser-doped nBGs resulted in similar ALP production (4.16 fold for nBGs, 4.1 fold for immersed nBGs, and 3.94 fold for FeCuSr nBGs) and significant albeit lower ALP production for FeCu and FeSr laser doped nBGs was observed (2.69 fold for FeCu and 3.22 fold for FeSr laser doped nBGs).

Next, we investigated whether nBGs, immersed and laser-doped nBGs nanoparticle exposure could promote the ability of hMSCs to mineralize their extracellular matrix, an important step in *de novo* bone formation. Calcium deposition by differentiated hMSCs was determined after 28 days using Alizarin Red S Staining (Figure 5). hMSCs cultured in basic and mineralization media (MM) in the absence of nanoparticles were used as negative and positive controls, respectively. nBGs, immersed and laser-doped nBGs exposure to hMSCs led to significant calcium deposition, however, significantly less compared to the positive control (Figure 5). Further quantification of the staining revealed that similar mineralization production was observed for hMSCs exposed to nBGs, immersed nBGs, FeSr, and FeCuSr laser-doped nBGs (Figure 5b). In contrast, hMSCs exposed to FeCu laser-doped nBGs resulted in the lowest calcium deposition (0.48 mM).

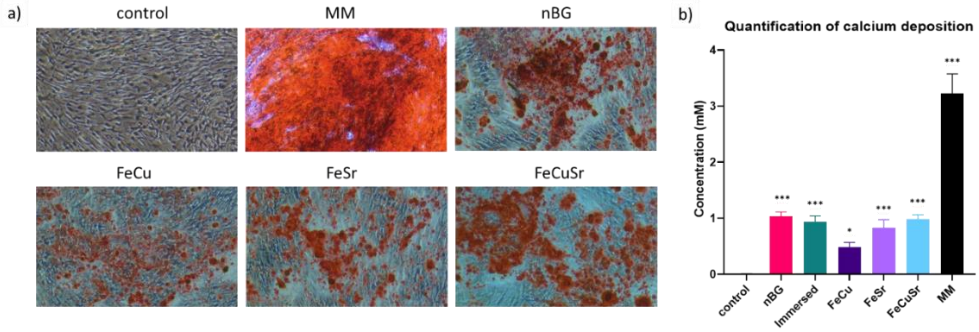

Figure 5: a) Calcium deposition by hMSCs at day 28 determined by Alizarin Red staining (n=3); exposed to basic medium, MM medium, nBGs, and laser-doped FeCu, FeSr, and FeCuSr. b) Quantification of calcium deposition via dye extraction of Alizarin Red. Significant differences between samples and negative controls were indicated by *, as * representing p-values as follows; $*p < 0.033$; $**p < 0.02$; $***p < 0.001$.

In conclusion, laser metal doped nBGs were biocompatible, and did not significantly enhance the osteogenic activity of nBGs particles nor their ability to promote hMSCs mineralization. Specifically, non-doped nBGs, immersed nBGs, and nBGs laser-doped with FeCuSr resulted in the induction of similar hMSCs ALP activity levels, and lower ALP levels were observed for FeSr and FeCu-doped nBGs. Similar observations were made for their ability to promote mineralization. The lower ALP and mineralization levels observed after exposure to FeSr and FeCu doped nBGs are likely related to the known effect of Fe on reducing ALP activity in bone cells [32-34]. For example, osteoblasts exposed to 50-200 µM ferric ammonium citrate led to a concentration-dependent decrease of ALP activity and negatively impacted mineralization [32]. Another study showed that high intracellular Fe levels in primary rat bone marrow stem cells led to downregulation of several osteogenic markers such as Runx2, osterix, osteopontin, and osteocalcin, but enhanced proliferation of pre-osteoblasts [33]. Although Sr is known to induce osteogenesis and ALP production in the absence of other osteogenic supplements [8, 35, 36], the Fe may negatively influence ALP production, lowering the overall bioactivity of FeSr-doped nBGs. Although Cu is also known to reduce ALP activity of hMSCs and suppress mineralization [37], FeCuSr doped nBGs showed similar ALP levels compared to undoped nBGs. The differential osteogenic activity of FeSr doped nBGs particles compared to FeCuSr nBGs is likely related to the relatively higher Sr concentration in the latter nanoparticles; Sr doping in the FeCuSr nBGs was more than double compared to FeSr nBGs.

3.3 *In vitro* tube formation

To investigate the influence of laser doping of nBGs on their angiogenic properties, HUVECs were cultured with the nBGs incorporated into Geltrex for 12 hours (Figure 6). Tube-like structure formation was observed in all tested conditions. In comparison with the Geltrex control, the addition of VEGF as well as all tested nBGs resulted in more pronounced tubule formation. Furthermore, cells cultured in the presence of FeSr laser-doped nBGs formed smaller loops compared to the other conditions. Quantitative analysis of the network parameters showed a significant increase in the number of junctions and vessel area in the positive control (VEGF exposure) and for HUVECs exposed to FeSr doped nBGs (Figure 6b).

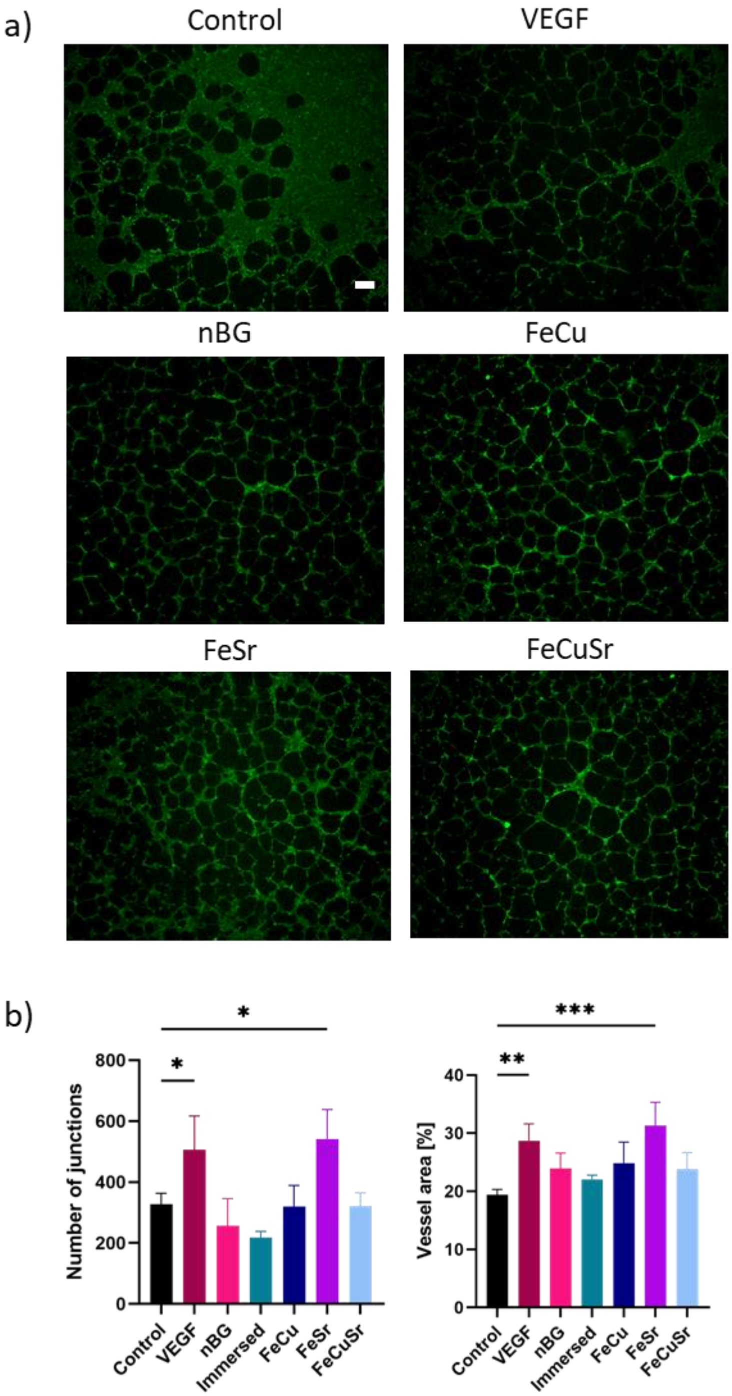
a)
Control
VEGF
nBG
FeCu
FeSr
FeCuSr
b)
*
*
Number of junctions
800
600
400
200
0
Control
VEGF
nBG
Immersed
FeCu
FeSr
FeCuSr
***
**
Vessel area [%]
40
30
20
10
0
Control
VEGF
nBG
Immersed
FeCu
FeSr
FeCuSr

Figure 6: Tube formation assay. a) HUVECs cultured on Geltrex in control and experimental conditions stained with phalloidin (green). Scale bar = 0.25 mm. b) Quantitative analysis of the number of junctions and vessel area performed AngioTube software.

Differential activity was observed in the *in vitro* tubular experiments; nBGs doped with FeSr led to significantly increased vessel area and number of junctions compared to the control. Indeed, Fe is known to be able to stimulate angiogenesis and tube formation. For example, one study showed that Fe released from calcium phosphate scaffold enhanced the proliferation of HUVECs, and upregulated VEGF and endothelial nitric oxide synthase (eNOS) [38]. Fe-doped octacalcium phosphate nanoparticles also have been shown to promote HUVEC proliferation and upregulate the expression of several angiogenic genes [22]. Moreover, in addition to Sr's well-known ability to induce osteogenesis, Sr can also have a beneficial effect on angiogenesis. In one study, Sr-doped BG sub-microparticles upregulated mRNA expression of angiogenesis-related genes (Angiogenin, FGF-2, and SDF) in HUVECs and increased vascularization within a gelatin scaffold *in vivo* [39]. Although Cu is known to promote angiogenesis, we observed no significant effect of Cu-doped nBGs on *in vitro* sprouting of HUVECs. This is likely due to the low Cu content in our laser-doped nBGs.

4. Conclusions

In this work, we show that nBGs could be successfully doped with Fe, Sr, and/or Cu using nanosecond-pulsed laser excitation in liquids. Furthermore, laser ion doping did not alter the morphology or size of the nBGs. This is critical as a size reduction could also alter the cellular response due to changes in overall BG surface area and solubility. nBGs and laser-doped nBGs were biocompatible up to 100 µg/mL and could significantly increase ALP production in hMSCs cells compared to non-exposed hMSCs cells. Non-doped nBGs and nBGs laser-doped with Fe, Cu, and Sr were most effective in inducing ALP activity. However, a reduction in ALP induction and mineralization was observed in FeCu-doped nBGs, likely due to the presence of Fe. Differential activity was observed in the *in vitro* tubular experiments; nBGs doped with FeSr led to significantly increased vessel area and number of junctions. This data shows that pulsed laser doping is a promising technique to dope multiple ions in nBGs without negatively impacting their structure or size and that laser doping of FeSr into nBGs can improve the angiogenic properties of nBGs.

References

1. K. Zheng and A. R. Boccaccini, Adv. Colloid Interface Sci., 2017, Sol-gel processing of bioactive glass nanoparticles: A review, 249, 363-373.

2. A. Hoppe, N. S. Güldal and A. R. Boccaccini, Biomaterials, 2011, A review of the biological response to ionic dissolution products from bioactive glasses and glass-ceramics, 32, 2757-2774.

3. C. H. Kong, C. Steffi, Z. Shi and W. Wang, J. Biomed. Mater. Res. B, 2018, Development of mesoporous bioactive glass nanoparticles and its use in bone tissue engineering, 106, 2878-2887.

4. I. Cacciotti, J. Mater. Sci., 2017, Bivalent cationic ions doped bioactive glasses: The influence of magnesium, zinc, strontium and copper on the physical and biological properties, 52, 8812-8831.

5. A. M. El-Kady, A. F. Ali, R. A. Rizk and M. M. Ahmed, Ceram. Int., 2012, Synthesis, characterization and microbiological response of silver doped bioactive glass nanoparticles, 38, 177-188.

6. M. Catauro, F. Papale, P. Caputo and G. Donnarumma, Int. J. Appl. Ceram, 2017, Chemical, biological, and antibacterial characterization of silica glass containing silver and gold nanoparticles, 14, 108-116.

7. A. Bari, N. Bloise, S. Fiorilli, G. Novajra, M. Vallet-Regí, G. Bruni, A. Torres-Pardo, J. M. González-Calbet, L. Visai and C. Vitale-Brovarone, Acta Biomater, 2017, Copper-containing mesoporous bioactive glass nanoparticles as multifunctional agent for bone regeneration, 55, 493-504.

8. P. Naruphontjirakul, A. E. Porter and J. R. Jones, Acta Biomater, 2018, In vitro osteogenesis by intracellular uptake of strontium containing bioactive glass nanoparticles, 66, 67-80.

9. P. Sutthavas, M. Schumacher, K. Zheng, P. Habibović, A. R. Boccaccini and S. van Rijt, Nanomaterials, 2022, Zn-loaded and calcium phosphate-coated degradable silica nanoparticles can effectively promote osteogenesis in human mesenchymal stem cells, 12, 2918.

10. S. van Rijt, K. de Groot and S. C. Leeuwenburgh, Tissue Eng., 2022, Calcium phosphate and silicate-based nanoparticles: history and emerging trends, 28, 461-477.

11. N. Pajares-Chamorro and X. Chatzistavrou, ACS Omega, 2020, Bioactive glass nanoparticles for tissue regeneration, 5, 12716-12726.

12. L. M. Frias Batista, A. Nag, V. K. Meader and K. M. Tibbetts, Sci. China Phys., Mech. Astron., 2022, Generation of nanomaterials by reactive laser-synthesis in liquid, 65, 1-45.

13. A. Chemin, J. Lam, G. Laurens, F. Trichard, V. Motto-Ros, G. Ledoux, V. Jarý, V. Laguta, M. Nikl and C. Dujardin, Nanoscale Adv., 2019, Doping nanoparticles using pulsed laser ablation in a liquid containing the doping agent, 1, 3963-3972.

14. C. H. Chen, D. Wu, Z. Li, R. Zhang, C. G. Kuai, X. R. Zhao, C. K. Dong, S. Z. Qiao, H. Liu and X. W. Du, Adv. Energy Mater., 2019, Ruthenium-based single-atom alloy with high electrocatalytic activity for hydrogen evolution, 9, 1803913.

15. L. Shang, J. Q. Wang, C. Q. Cheng, Y. Zhang, F. F. Zhang, Y. M. Xie, J. D. Lu, J. Mao, Q. J. Guo and C. K. Dong, J. Alloys Compd., 2021, Oxidized single nickel atoms embedded in Ru matrix for highly efficient hydrogen evolution reaction, 874, 159909.

16. F. F. Zhang, C. Q. Cheng, J. Q. Wang, L. Shang, Y. Feng, Y. Zhang, J. Mao, Q. J. Guo, Y. M. Xie and C. K. Dong, ACS Energy Lett., 2021, Iridium oxide modified with silver single atom for boosting oxygen evolution reaction in acidic media, 6, 1588-1595.

17. S. Zerebecki, K. Schott, S. Salamon, J. Landers, E. Budiyanto, H. Wende, H. Tüysüz, S. Barcikowski and S. Reichenberger, J. Phys. Chem. C, 2022, Gradually Fe-doped Co3O4 nanoparticles in 2-propanol and water oxidation catalysis with single laser pulse resolution, 126.

18. Y. Li, V. Ramesh, F. Bider, N. Bradshaw, C. Rehbock, A. R. Boccaccini and S. Barcikowski, J. Biomed. Mater. Res. A, 2022, Co-doping of iron and copper ions in nanosized bioactive glass by reactive laser fragmentation in liquids, DOI: https://doi.org/10.1002/jbm.a.37393.

19. B. Kołodziejska, N. Stępień and J. Kolmas, Int. J. Mol. Sci., 2021, The influence of strontium on bone tissue metabolism and its application in osteoporosis treatment, 22, 6564.

20. M. Šalandová, I. A. van Hengel, I. Apachitei, A. A. Zadpoor, B. C. van der Eerden and L. E. Fratila-Apachitei, Adv. Healthc. Mater, 2021, Inorganic agents for enhanced angiogenesis of orthopedic biomaterials, 10, 2002254.

21. C. Giacomelli, M. L. Trincavelli, C. Satriano, Ö. Hansson, D. La Mendola, E. Rizzarelli and C. Martini, Int. J. Biochem. Cell Biol., 2015, Copper (II) ions modulate Angiogenin activity in human endothelial cells, 60, 185-196.

22. H. Shi, S. Yang, S. Zeng, X. Liu, J. Zhang, T. Wu, X. Ye, T. Yu, C. Zhou and J. Ye, Appl. Mater. Today, 2019, Enhanced angiogenesis of biodegradable iron-doped octacalcium phosphate/poly (lactic-co-glycolic acid) scaffold for potential cancerous bone regeneration, 15, 100-114.

23. M. Schumacher, P. Habibović and S. van Rijt, ACS Appl. Mater. Interfaces, 2022, Peptide-Modified Nano-Bioactive Glass for Targeted Immobilization of Native VEGF, 14, 4959-4968.

24. M. Lau and S. Barcikowski, Appl. Surf. Sci., 2015, Quantification of mass-specific laser energy input converted into particle properties during picosecond pulsed laser fragmentation of zinc oxide and boron carbide in liquids, 348, 22-29.

25. E. Zudaire, L. Gambardella, C. Kurcz and S. Vermeren, PloS One, 2011,A computational tool for quantitative analysis of vascular networks, 6, e27385.

26. N. Gupta, D. Santhiya, S. Murugavel, A. Kumar, A. Aditya, M. Ganguli and S. Gupta, Colloids Surf., A, 2018, Effects of transition metal ion dopants (Ag, Cu and Fe) on the structural, mechanical and antibacterial properties of bioactive glass, 538, 393-403.

27. A. El-Fiqi and H.-W. Kim, Mater. Lett, 2021, Iron ions-releasing mesoporous bioactive glass ultrasmall nanoparticles designed as ferroptosis-based bone cancer nanotherapeutics: Ultrasonic-coupled sol–gel synthesis, properties and iron ions release, 294, 129759.

28. G. Nikiforuk and L. Sreebny, J. Dent. Res., 1953, Demineralization of hard tissues by organic chelating agents at neutral pH, 32, 859-867.

29. M. Spellauge, M. Tack, R. Streubel, M. Miertz, K. S. Exner, S. Reichenberger, S. Barcikowski, H. P. Huber and A. R. Ziefuss, Small, 2023, Photomechanical Laser Fragmentation of IrO2 Microparticles for the Synthesis of Active and Redox-Sensitive Colloidal Nanoclusters, DOI: https://doi.org/10.1002/smll.202206485, e2206485.

30. S. Siekierski, Comments Inorg. Chem., 1997, Ionic radii: effect of shell radius, cation charge and lone electron pair, 19, 121-131.

31. D. W. Smith, J. Chem. Educ., 1977, Ionic hydration enthalpies, 54, 540.

32. Y. F. He, Y. Ma, C. Gao, G. y. Zhao, L. L. Zhang, G. F. Li, Y. Z. Pan, K. Li and Y. J. Xu, Biol. Trace Elem. Res., 2013, Iron overload inhibits osteoblast biological activity through oxidative stress, 152, 292-296.

33. Q. Yang, J. Jian, S. B. Abramson and X. Huang, J. Bone Miner. Res., 2011, Inhibitory effects of iron on bone morphogenetic protein 2–induced osteoblastogenesis, 26, 1188-1196.

34. E. Balogh, E. Tolnai, B. Nagy Jr, B. Nagy, G. Balla, J. Balla and V. Jeney, Biochim Biophys Acta Mol Basis Dis BBA-MOL BASIS DIS, 2016, Iron overload inhibits osteogenic commitment and differentiation of mesenchymal stem cells via the induction of ferritin, 1862, 1640-1649.

35. A. A. Gorustovich, T. Steimetz, R. L. Cabrini and J. M. Porto López, J Biomed Mater Res A, 2010, Osteoconductivity of strontium-doped bioactive glass particles: a histomorphometric study in rats, 92, 232-237.

36. E. Gentleman, Y. C. Fredholm, G. Jell, N. Lotfibakhshaiesh, M. D. O'Donnell, R. G. Hill and M. M. Stevens, Biomaterials, 2010, The effects of strontium-substituted bioactive glasses on osteoblasts and osteoclasts in vitro, 31, 3949-3956.

37. S. Li, M. Wang, X. Chen, S. Li, J. Li-Ling and H. Xie, Cell Prolif., 2014, Inhibition of osteogenic differentiation of mesenchymal stem cells by copper supplementation, 47, 81-90.

38. J. Zhang, H. Shi, J. Liu, T. Yu, Z. Shen and J. Ye, J. Mater. Chem. B, 2015, Good hydration and cell-biological performances of superparamagnetic calcium phosphate cement with concentration-dependent osteogenesis and angiogenesis induced by ferric iron, 3, 8782-8795.

39. F. Zhao, B. Lei, X. Li, Y. Mo, R. Wang, D. Chen and X. Chen, Biomaterials, 2018, Promoting in vivo early angiogenesis with sub-micrometer strontium-contained bioactive microspheres through modulating macrophage phenotypes, 178, 36-47.

Chapter 7

Discussion

1. Introduction

The application of silica and calcium phosphate (CaP) based nanomaterials in the field of tissue regeneration has expanded rapidly over the last decade [1-3]. As reviewed in **Chapter 2** of this thesis, these materials have an especially high potential for use in the bone regeneration field due to their excellent biocompatibility and intrinsic ability to promote bone growth. Spherical nanoparticles (NP) within the 20-200 nm size range have attracted particular interest in this field. There have been many advancements in synthesis techniques that offer more refined control over material and surface properties. However, the importance of certain nanomaterial properties such as size, shape, composition, and crystallinity on their ability to promote regenerative processes is still poorly understood. As discussed in **Chapter 2**, a strong focus in this field has been on the incorporation of therapeutic ions into NPs by a process known as ion doping, to improve their bioactivity or even expand it towards other clinical applications. Although many reports have shown beneficial use of various ion-doped NP, not much is known about the importance of ion choice, controlled ion release or in general, what parameters allow optimization of ion doping processes.

Moreover, inorganic NP can be applied in many different ways, e.g., as components of scaffolds and coatings, but also as injectables for the delivery of therapeutics, which in turn affect the ability of NP to guide tissue regenerative processes. It is therefore important to further investigate the optimal way of applying nanomaterials in bone regeneration.

In this thesis, we set out to investigate the effect of nanoparticle parameters and application methods on their ability to promote hMSC osteogenesis. Moreover, we focused on optimising the inherent bioactivity of the NP by exploring various methods to incorporate bioinorganic ions. This chapter discusses the results obtained in the experimental chapters in the context of optimising bioceramic NP including mesoporous silica NP (MSN), mesoporous bioactive glass NP (MBG), and calcium phosphate (CaP) NP for application in bone regeneration in terms of their morphology, administration, and ability to deliver therapeutic ions.

2. Importance of NP morphology and administration on their ability to promote bone regenerative processes

Bone has a well-defined micro and nano architecture consisting of hydroxyapatite (HA) particles in nano-meter size range embedded in a collagen matrix. HA nanocrystals in bone are needle shaped and provide bone matrix with exceptional mechanical strength and bioactivity. In recent years, there has been increased interest in mimicking the hierarchical structure of bone by using nanosized HA particles. Previous studies have shown that the size of CaP particles is indeed important; for example, it has been shown that CaP NP are superior to CaP microparticles in their ability to promote bone cells proliferation and differentiation *in vitro*, and that even differently sized NP can influence hMSCs and osteoblast proliferation rates [4-7]. For example, Cai et al. found that hMSCs exposed to 20 nm sized CaP particles led to significantly higher cell proliferation compared to 80 nm CaP NP and micron sized CaP particles [5].

However, the mechanism behind this size-dependent effect is not well understood. It is suspected that smaller-sized NP can be more readily taken up by hMSCs, thereby increasing intracellular Ca ion release, which in turn can promote several cellular processes including cell proliferation [7]. Only a few studies have investigated the influence of CaP NP shape on their ability to promote bone regeneration [8-10]. This is probably due to the lack of synthesis routes that allow fine control over both CaP NP size and shape. In **chapter 3**, we reported a wet synthesis method that allows control over CaP NP shape while maintaining a similar size and chemistry. This method made use of micellar templates, controlling NP growth in terms of both size and shape. Using this method, we studied the influence of rice-shaped, needle-shaped, and spherical CaP NP on hMSCs adhesion and differentiation when deposited as stable coatings on glass slides. The results of **chapter 3** indicate that the expression levels and patterns of osteogenic markers Runx2, BMP2, OPN, and OCN varied significantly over time depending on NP shape. Specifically, we saw that needle-shaped CaP NPs were most efficient in upregulating early-, middle- and late osteogenic genes in hMSCs [11].

The ability of surfaces with nano-sized features (or nano-topography) to promote certain stem cell behaviours is widely recognized in the field [12-14]. Cells can sense nano-topography via the formation of focal adhesions through integrin receptors, which can promote cell proliferation and differentiation [15]. hMSCs interact with material surfaces through bundling of focal adhesion proteins such as vinculin [16, 17]. A recent study suggests that nanostructures may induce cellular cytoskeletal reorganization via integrin binding, that consequently leads to osteogenic differentiation of hMSCs [18]. This is in line with our findings in **chapter 3,** where we observed a typical hMSCs morphology with extended filopodia on needle-shaped CaP NPs films. In contrast, hMSCs grown on rice-shaped and spherical CaP NP films showed more elongated morphology.

Thus, our and other studies indicate that CaP NP's size and shape play essential roles in their ability to promote hMSCs' adhesion and differentiation. To improve their clinical application, more studies are needed to improve our understanding of the role (nano) particle shape and size plays in directing these processes. Moreover, translation of the findings to relevant *in vivo* models is needed to increase our understanding of more complex biological environments.

3. NP administration

Inorganic NPs have been frequently used as fillers in polymeric scaffolds, as coatings on metallic implants and as injectables for drug delivery purposes. Depending on the application mode, the mechanism of action will differ drastically. For example, in the case of injectables and fillers, single NPs are available in the extracellular environment of cells. In contrast to micro-sized or bulk ceramics, ceramic NPs can be efficiently internalised into cells via a process known as endocytosis. During endocytosis, cells take up substances from outside the cell by forming a vesicle around and engulfing it. Several studies suggest that the majority of silica and CaP NP are taken up via clathrin-mediated endocytosis [19-22]. Efficiency of NP cell internalization is, however, highly influenced by NP size, shape, surface chemistry, and surface charge [20, 21, 23]. The internalisation of NP in hMSCs and subsequent degradation an ion release, is thought to be one of the pathways responsible for their ability to promote osteogenic differentiation [24]. A second pathway is the dissolution of the NP in extracellular space and subsequent uptake of the ions by nearby (stem cells) through ion channels [25, 26]. In **chapter 4** we investigated the effectiveness of these two pathways by comparing ion release via NPs upon cell internalization, and exposure to ions dissolved in cell culture media. To ensure that ion release could only take place upon cell internalisation, the surface of mesoporous silica NP was modified with a pH responsive CaP surface layer. We showed that this layer prevented ion release at neutral conditions and promoted ion release at low pH values like those found in endosomal vesicles. This mechanism allowed efficient delivery of NP incorporated therapeutic ions, while avoiding unwanted ion release in extracellular spaces. We showed that these NP were efficiently taken up by hMSCs, and that the CaP coating improved cell uptake efficiency. We compared uptake of bioinorganic ions dissolved in the cell culture medium to bioinorganic ion delivery using MSN and observed that ion-incorporated MSN induced hMSCs differentiation at significantly lower ion concentrations. In particular, our MSN needed 134- (P), 208- (Ca), 277- (Sr) and 538 (Zn) times lower dose compared to ions directly dissolved in media. This observation can be explained by the different uptake routes; where MSN are internalized by endocytosis, ions are generally taken up via ion channels. This indicates that NP mediated endocytosis is a more efficient method to deliver higher concentrations of therapeutic ions to hMSCs. Our research was the first to compare directly media-dissolved ions versus NP-mediated endocytosis and demonstrated the therapeutic advantage of using MSN, even for molecules that may be internalized on their own.

Bioceramic NP and CaP in particular, can also be used as coatings on (metallic) implants to increase bone-to-implant contact by improving cell adhesion. As mentioned in the previous section, hMSCs functions can be regulated through physical interaction with specific nano-topographical cues [27, 28]. These cues can determine cell attachment, integrin clustering, and cytoskeletal structure resulting in mechanotransductive signalling and further causing downstream effects including stem cell differentiation [28-30]. **Chapter 3** showed that the CaP NP could be immobilized at the surface of glass slides; no CaP NP dissolution or cellular uptake were observed. In **chapter 4** and **5,** we set out to also compare stable NP coatings with NP application in suspension, facilitating endocytosis. The expression or activity of alkaline phosphatase (ALP) is often used as an indication of hMSCs differentiation and osteogenesis, as it is highly expressed in the cells of mineralized tissue. ALP activity of hMSCs was more efficiently upregulated when exposed to NP suspensions compared to hMSCs seeded on thin NP films of the same chemical composition. This result demonstrated that NP internalisation in hMSCs has a superior efficiency in stimulating osteogenesis *in vitro*.

We were the first to investigate and compare different silica NP administration routes on their ability to promote hMSCs osteogenesis. This knowledge can aid the field by providing guidelines to select the most suitable method to administer NP. Our results showed that ion doped MSN can promote hMSCs osteogensis via two distinct pathways; through nano-topographical cues and by facilitating ion uptake via NP mediated endocytosis. Endocytosis was the most effective in terms of concentration efficiency. However, we also showed that hMSCs exposure to NP is ideally repeated every 3 days, which complicates their use over prolonged periods. As such, it is important to consider all factors when deciding on which NP administration method to choose.

4. Enhancing NP bioactivity via ion incorporation methods

4.1 Using unique structure of MSN to allow multiple ion incorporation

Several metallic ions are known to play important roles in bone formation. Trace metallic elements including strontium (Sr), Zinc (Zn), iron (Fe), and copper (Cu) are seen as viable alternatives to biologics because they are lower in costs, stable, and can promote various biological processes. For example, Sr and Zn can stimulate osteogenic differentiation, while Fe is known to aid angiogenesis [31-36]. Moreover, metallic ions can also have anti-microbial or anti-inflammatory properties [37]. For this reason, incorporation of trace metallic elements in biomaterials and tissue engineering constructs has received significant attention over the past decades [38].

Metallic ions can be easily incorporated in CaP and silica NPs via ion doping [39, 40], a process that entails the incorporation of metallic ions within the CaP or Si or CaP matrix via ion substitution. Using this method, cations such as strontium (Sr), zinc (Zn) or copper (Cu) have been successfully incorporated in CaP and silica NPs. However, there is a limit to the amount of ions that can be incorporated using this method before negatively affecting NPs formation. Specifically, ionic substitutions can cause changes in NP structure, stability, lattice parameters, particle morphology, crystallinity, and solubility [41-43]. Moreover, ions can affect pore formation of mesoporous NP. For example, Sr doping in bioactive glass can weaken the overall network leading to higher degradation rates [44-46]. The larger atomic size of Sr compared to Ca can lead to lattice expansion and increased NP solubility. In addition, Ca content of more than 20% within the MBG is difficult to achieve, even if higher Ca ion concentrations are present during synthesis process [47]. High Ca doping has led to increased NP size and lower particle homogeneity [48, 49]. While variety of ions have been successfully incorporated in bioceramic NP, multiple ion doping is rare.

In **chapter 4, 5** and **6** we investigated the use of MSN to deliver multiple ions to hMSCs. The mesoporous structure allows efficient ion incorporation, and its large surface area can be used to deposit ions. Lastly, ions can be directly incorporated into silica network during synthesis. In **chapter 4**, MSN containing Zn, CaP and Sr were synthesized. In these constructs, Zn was added to the CaP coating via ion substitution, while Sr was incorporated into mesopores of NPs. Importantly, the CaP layer acted both as ion source and as pH sensitive gatekeeper for Sr ions loaded within the mesopores. As mentioned in the previous section, the CaP coating also improved NP internalization in hMSCs. Moreover, in **chapter 5** we showed that CaP surface coating prevented degradation of MBG and degradable MSN in neutral conditions. Thus, the CaP layer provides multiple advantages. Finally, the silica network itself can be used to provide control over ion release and silica ions are also known to promote both osteogenic and angiogenic processes. To allow silica ion release from the NPs, in **chapter 5**, we synthesized degradable MSN by creating an imperfection within the silica network using 1,3,5-Triisopropylbenzene (TiPB). TiPB creates gaps within the silica network resulting in faster hydrolysis of the silica matrix. Within 6 days, our synthesized degradable MSN released over 80% of its ion content in neutral aqueous conditions. However, this high amount of Si release negatively affected hMSCs viability already after 72 h of exposure. It has been reported that high silicate concentrations can be cytotoxic to osteoblasts [50, 51]. Thus, adjusting MSN degradation is an important factor in optimizing these NP for future use.

Where in **chapter 4** and **5** we attempted to modify MSN unique structure to allow incorporation of multiple ions, in **chapter 6** we investigated the use of a modified laser fragmentation in liquids (LFL) for multiple ion doping. LFL is an established technique mainly used to fracture macro materials into micro- and NP. LFL process utilizes coloured complex solutions of metal ions, often Fe, which act as light-absorbing agents [52]. By adjusting exposure time and frequency, controllable fragmentation limited to the surface of NPs can be achieved, rather than the fragmentation of the entire structure [53]. Trace elements within the ion complex solution could successfully be deposited on to processed micro- and NP using this method [54]. In our study, a laser-doping technique was used to incorporate Fe, Sr, and Cu ions into solid bioactive glass NP without altering their overall morphology and size. Although all three ions were incorporated in the NP, the amounts were lower compared to our wet synthesis methods.

Incorporation of multiple ions in NPs remains difficult to achieve because most used ion substitution within the CaP or silica matrix can lead to altered NP properties such as crystallinity and morphology. In this thesis, we investigated coating of MSN' surface and mesoporous properties and rather than ions substitution, to allow multiple ion incorporation in single NPs. We observed that especially the use of a CaP coating on MSN is a very promising way to incorporate multiple ions but also to improve intracellular uptake, and to avoid unwanted ion release by acting as a pH responsive gatekeeper. Although LFL represented a promising alternative technique to incorporate multiple ions, the technique needs to be further optimized to allow incorporation of higher ion concentrations.

4.2 Advantages of multiple ion delivery using NPs

Multiple ion doping may be beneficial to stimulate biological processes more efficiently or to stimulate multiple biological processes simultaneously. Our data supports this; in **chapter 4** we observed that hMSCs exposure to multiple ions dissolved in media resulted in significantly higher expression of osteogenic genes compared to single ion exposure. This is in line with other studies in which multiple ions were investigated [55, 56]. In **chapter 4** and **5**, we observed clear benefits of using MSN for multiple ion delivery. Multiple ion MSN and MBG performed better than single ion incorporated MSN in terms of increased expression of osteogenic markers and enhanced mineralization *in vitro*. In addition, the use of MSN significantly decreased the required ion concentrations needed to observe an effect.

However, we also observed that both ion concentration and ion release profiles are important parameters in stimulating stem cells differentiation. Ca, P, Si, Sr and Zn are known to support the growth of bone cells in a dose-dependent manner. In **chapter 5**, we investigated three Zn incorporation modes; as part of the CaP layer, inside the mesopores, and inside the silica matrix. Each incorporation mode yielded not only different overall Zn concentration present in the final NP composition but also led to different Zn release profiles. Incorporation in CaP layer resulted in the lowest concentration of incorporated Zn, while incorporation inside the silica matrix led to longer and more sustained Zn release. Degradable MSN and MBG resulted in the highest ALP activity and mineralization, despite the presence of a lower concentration of Zn compared to similar non-degradable MSN. This is likely due to the high amount of Si release, and the positive role Si ions play in ALP production [57]. These results demonstrated that degradable MSN have an advantage; however, their degradation rates and Si ion release need to be controlled in order to avoid cytotoxicity.

Using LFL technology, ions such as Fe and Cu that are otherwise difficult to dope in ceramic NPs, can be incorporated. In **chapter 6**, we showed that LFL is a suitable alternative ion doping technique, without negative effects on NP morphology and size. Using this technique, we could dope Fe, Cu and Sr in bioglass NP. Multiple ion laser doped bioglass NP improved vessel formation by human umbilical vein endothelial cells, but did not enhance ALP activity in hMSCs. Cu and Fe are known to negatively affect ALP production, which can explain our findings. Hence, ion choice remains an important consideration when designing biomaterials for multiple ion delivery.

In summary, using MSN and MBG for multiple ion delivery has multiple advantages including lowering ion concentrations needed to observe a biological effect, possible synergistic effects, and a more precise control over ion incorporation and release profile. However, more research is needed to determine the most effective concentrations and ion combinations in order to maximize their potential for bone regeneration applications.

References

1. S. van Rijt, K. de Groot and S. C. Leeuwenburgh, Tissue Eng., 2022, Calcium phosphate and silicate-based nanoparticles: history and emerging trends, 28, 461-477.
2. S. Balasubramanian, B. Gurumurthy and A. Balasubramanian, Int J Pharm Sci Res, 2017, Biomedical applications of ceramic nanomaterials: a review, 8, 4950-4959.
3. M. J Hill, B. Qi, R. Bayaniahangar, V. Araban, Z. Bakhtiary, M. R. Doschak, B. C. Goh, M. Shokouhimehr, H. Vali and J. F. Presley, Nanomedicine, 2019, Nanomaterials for bone tissue regeneration: updates and future perspectives, 14, 2987-3006.
4. Y. Cai, Y. Liu, W. Yan, Q. Hu, J. Tao, M. Zhang, Z. Shi and R. Tang, Journal of Materials Chemistry, 2007, Role of hydroxyapatite nanoparticle size in bone cell proliferation, 17, 3780-3787.
5. Z. Shi, X. Huang, Y. Cai, R. Tang and D. Yang, Acta Biomater, 2009, Size effect of hydroxyapatite nanoparticles on proliferation and apoptosis of osteoblast-like cells, 5, 338-345.
6. N. Li, G. Wu, H. Yao, R. Tang, X. Gu and C. Tu, Dent. Mater. Journal, 2019, Size effect of nano-hydroxyapatite on proliferation of odontoblast-like MDPC-23 cells, 38, 534-539.
7. X. Yang, Y. Li, X. Liu, R. Zhang and Q. Feng, Stem Cells Int., 2018, In vitro uptake of hydroxyapatite nanoparticles and their effect on osteogenic differentiation of human mesenchymal stem cells, 2018.
8. J. Xu, K. A. Khor, J. Sui, J. Zhang and W. N. Chen, Biomaterials, 2009, Protein expression profiles in osteoblasts in response to differentially shaped hydroxyapatite nanoparticles, 30, 5385-5391.
9. J. Wang, G. Yang, Y. Wang, Y. Du, H. Liu, Y. Zhu, C. Mao and S. Zhang, Biomacromolecules, 2015, Chimeric protein template-induced shape control of bone mineral nanoparticles and its impact on mesenchymal stem cell fate, 16, 1987-1996.
10. Y. Liu, G. Wang, Y. Cai, H. Ji, G. Zhou, X. Zhao, R. Tang and M. Zhang, J. Biomed. Mater. Res. A, 2009, In vitro effects of nanophase hydroxyapatite particles on proliferation and osteogenic differentiation of bone marrow-derived mesenchymal stem cells, 90, 1083-1091.
11. P. Sutthavas, P. Habibovic and S. H. van Rijt, Biomater. Sci., 2021, The shape-effect of calcium phosphate nanoparticle based films on their osteogenic properties, 9, 1754-1766.
12. R. Ravichandran, S. Liao, C. C. Ng, C. K. Chan, M. Raghunath and S. Ramakrishna, World J. Stem Cells, 2009, Effects of nanotopography on stem cell phenotypes, 1, 55.
13. B. K. K. Teo, S. Ankam, L. Y. Chan and E. K. Yim, Methods Cell Biol., 2010, Nanotopography/mechanical induction of stem-cell differentiation, 98, 241-294.
14. S. Park and G. I. Im, J. Biomed. Mater. Res. A, 2015, Stem cell responses to nanotopography, 103, 1238-1245.
15. J. Luo, M. Walker, Y. Xiao, H. Donnelly, M. J. Dalby and M. Salmeron-Sanchez, Bioact. Mater., 2021, The influence of nanotopography on cell behaviour through interactions with the extracellular matrix–A review.
16. A. Carisey and C. Ballestrem, Eur. J. Cell Biol., 2011, Vinculin, an adapter protein in control of cell adhesion signalling, 90, 157-163.

17. K. Collins, E. Gates, C. Gilchrist and B. Hoffman, in Bio-Instructive Scaffolds for Musculoskeletal Tissue Engineering and Regenerative Medicine, Elsevier, 2017, pp. 3-35.

18. E. G. Long, M. Buluk, M. B. Gallagher, J. M. Schneider and J. L. Brown, Bioact. Mater., 2019, Human mesenchymal stem cell morphology, migration, and differentiation on micro and nano-textured titanium, 4, 249-255.

19. D. M. Huang, Y. Hung, B. S. Ko, S. C. Hsu, W. H. Chen, C. L. Chien, C. P. Tsai, C. T. Kuo, J. C. Kang and C. S. Yang, FASEB J., 2005, Highly efficient cellular labeling of mesoporous nanoparticles in human mesenchymal stem cells: implication for stem cell tracking, 19, 2014-2016.

20. I. Slowing, B. G. Trewyn and V. S.-Y. Lin, J. Am. Chem. Soc., 2006, Effect of surface functionalization of MCM-41-type mesoporous silica nanoparticles on the endocytosis by human cancer cells, 128, 14792-14793.

21. X. Huang, X. Teng, D. Chen, F. Tang and J. He, Biomaterials, 2010, The effect of the shape of mesoporous silica nanoparticles on cellular uptake and cell function, 31, 438-448.

22. M. Ekkapongpisit, A. Giovia, C. Follo, G. Caputo and C. Isidoro, Int. J. Nanomed., 2012, Biocompatibility, endocytosis, and intracellular trafficking of mesoporous silica and polystyrene nanoparticles in ovarian cancer cells: effects of size and surface charge groups, 7, 4147.

23. T.-H. Chung, S.-H. Wu, M. Yao, C.-W. Lu, Y.-S. Lin, Y. Hung, C.-Y. Mou, Y.-C. Chen and D.-M. Huang, Biomaterials, 2007, The effect of surface charge on the uptake and biological function of mesoporous silica nanoparticles in 3T3-L1 cells and human mesenchymal stem cells, 28, 2959-2966.

24. A. Tautzenberger, A. Kovtun and A. Ignatius, Int. J. Nanomed., 2012, Nanoparticles and their potential for application in bone, 7, 4545.

25. G.-Y. Jung, Y.-J. Park and J.-S. Han, J. Mater. Sci.: Mater. Med., 2010, Effects of HA released calcium ion on osteoblast differentiation, 21, 1649-1654.

26. M. Zayzafoon, K. Fulzele and J. M. McDonald, J. Biol. Chem., 2005, Calmodulin and calmodulin-dependent kinase IIα regulate osteoblast differentiation by controlling c-fos expression, 280, 7049-7059.

27. J. Kim, H. N. Kim, K.-T. Lim, Y. Kim, S. Pandey, P. Garg, Y.-H. Choung, P.-H. Choung, K.-Y. Suh and J. H. Chung, Biomaterials, 2013, Synergistic effects of nanotopography and co-culture with endothelial cells on osteogenesis of mesenchymal stem cells, 34, 7257-7268.

28. H. N. Kim, A. Jiao, N. S. Hwang, M. S. Kim, D.-H. Kim and K.-Y. Suh, Adv. Drug Delivery Rev., 2013, Nanotopography-guided tissue engineering and regenerative medicine, 65, 536-558.

29. W. L. Murphy, T. C. McDevitt and A. J. Engler, Nat. Mater., 2014, Materials as stem cell regulators, 13, 547-557.

30. F. Guilak, D. M. Cohen, B. T. Estes, J. M. Gimble, W. Liedtke and C. S. Chen, Cell stem cell, 2009, Control of stem cell fate by physical interactions with the extracellular matrix, 5, 17-26.

31. Z. Saidak and P. J. Marie, Pharmacol. Ther., 2012, Strontium signaling: molecular mechanisms and therapeutic implications in osteoporosis, 136, 216-226.

32. A. A. Gorustovich, T. Steimetz, R. L. Cabrini and J. M. Porto López, J Biomed Mater Res A, 2010, Osteoconductivity of strontium-doped bioactive glass particles: a histomorphometric study in rats, 92, 232-237.

33. E. Gentleman, Y. C. Fredholm, G. Jell, N. Lotfibakhshaiesh, M. D. O'Donnell, R. G. Hill and M. M. Stevens, Biomaterials, 2010, The effects of strontium-substituted bioactive glasses on osteoblasts and osteoclasts in vitro, 31, 3949-3956.

34. D. S. Brauer, E. Gentleman, D. F. Farrar, M. M. Stevens and R. G. Hill, Biomed. Mater., 2011, Benefits and drawbacks of zinc in glass ionomer bone cements, 6, 045007.

35. H. Shi, S. Yang, S. Zeng, X. Liu, J. Zhang, T. Wu, X. Ye, T. Yu, C. Zhou and J. Ye, Appl. Mater. Today, 2019, Enhanced angiogenesis of biodegradable iron-doped octacalcium phosphate/poly (lactic-co-glycolic acid) scaffold for potential cancerous bone regeneration, 15, 100-114.

36. M. Cannas, E. Indemini, A. Krajewski, A. Ravaglioli and S. Contoli, Biomaterials, 1990, In vitro observations of iron-doped bioactive glasses, 11, 281-285.

37. J. Han, N. Hassani Besheli, D. Deng, B. A. van Oirschot, S. C. Leeuwenburgh and F. Yang, Tissue Eng. Part C: Methods, 2022, Tailoring Copper-Doped Bioactive Glass/Chitosan Coatings with Angiogenic and Antibacterial Properties.

38. H. Safiaghdam, H. Nokhbatolfoghahaei and A. Khojasteh, Iran. J.Pharm. Res., 2019, Therapeutic metallic ions in bone tissue engineering: A systematic review of the literature, 18, 101.

39. V. M. Schatkoski, T. L. do Amaral Montanheiro, B. R. C. de Menezes, R. M. Pereira, K. F. Rodrigues, R. G. Ribas, D. M. da Silva and G. P. Thim, Ceram. Int., 2021, Current advances concerning the most cited metal ions doped bioceramics and silicate-based bioactive glasses for bone tissue engineering, 47, 2999-3012.

40. S. Bose, G. Fielding, S. Tarafder and A. Bandyopadhyay, Trends Biotechnol., 2013, Understanding of dopant-induced osteogenesis and angiogenesis in calcium phosphate ceramics, 31, 594-605.

41. Y.-K. Peng, Y.-J. Tseng, C.-L. Liu, S.-W. Chou, Y.-W. Chen, S. E. Tsang and P.-T. Chou, Nanoscale, 2015, One-step synthesis of degradable T 1-FeOOH functionalized hollow mesoporous silica nanocomposites from mesoporous silica spheres, 7, 2676-2687.

42. L. Yu, Y. Chen, H. Lin, S. Gao, H. Chen and J. Shi, Small, 2018, Magnesium-engineered silica framework for pH-accelerated biodegradation and DNAzyme-triggered chemotherapy, 14, 1800708.

43. K. K. Pohaku Mitchell, A. Liberman, A. C. Kummel and W. C. Trogler, J. Am. Chem. Soc., 2012, Iron (III)-doped, silica nanoshells: a biodegradable form of silica, 134, 13997-14003.

44. S. Watts, R. Hill, M. O'donnell and R. Law, J. Non-Cryst. Solids, 2010, Influence of magnesia on the structure and properties of bioactive glasses, 356, 517-524.

45. A. M. El-Kady and A. F. Ali, Ceram. Int., 2012, Fabrication and characterization of ZnO modified bioactive glass nanoparticles, 38, 1195-1204.

46. Y. C. Fredholm, N. Karpukhina, R. V. Law and R. G. Hill, J. Non-Cryst. Solids, 2010, Strontium containing bioactive glasses: glass structure and physical properties, 356, 2546-2551.

47. W. Xie, X. Chen, Y. Li, G. Miao, G. Wang, T. Tian, L. Zeng and X. Chen, Adv. Powder Technol., 2020, Facile synthesis and in vitro bioactivity of radial mesoporous bioactive glass with high phosphorus and calcium content, 31, 3307-3317.

48. S. L. Greasley, S. J. Page, S. Sirovica, S. Chen, R. A. Martin, A. Riveiro, J. V. Hanna, A. E. Porter and J. R. Jones, J. Colloid Interface Sci., 2016, Controlling particle size in the Stöber process and incorporation of calcium, 469, 213-223.

49. A. Lukowiak, J. Lao, J. Lacroix and J.-M. Nedelec, Chem. Commun., 2013, Bioactive glass nanoparticles obtained through sol–gel chemistry, 49, 6620-6622.

50. S. P. Hudson, R. F. Padera, R. Langer and D. S. Kohane, Biomaterials, 2008, The biocompatibility of mesoporous silicates, 29, 4045-4055.

51. A. L. Gomes-Cornelio, E. M. Rodrigues, L. B. Mestieri, T. d. O. R. S. Falcoski, C. P. Soares, J. M. Guerreiro-Tanomaru, C. Rossa Junior and M. Tanomaru Filho, Braz. Oral Res., 2016, Cytotoxicity and genotoxicity of calcium silicate-based cements on an osteoblast lineage, 30.

52. M. Lau and S. Barcikowski, Appl. Surf. Sci., 2015, Quantification of mass-specific laser energy input converted into particle properties during picosecond pulsed laser fragmentation of zinc oxide and boron carbide in liquids, 348, 22-29.

53. Y. Li, V. Ramesh, F. Bider, N. Bradshaw, C. Rehbock, A. R. Boccaccini and S. Barcikowski, J. Biomed. Mater. Res. A, 2022, Co-doping of iron and copper ions in nanosized bioactive glass by reactive laser fragmentation in liquids, 110, 1537-1550.

54. Y. Li, V. Ramesh, F. Bider, N. Bradshaw, C. Rehbock, A. R. Boccaccini and S. Barcikowski, J. Biomed. Mater. Res. A, 2022, Co-doping of iron and copper ions in nanosized bioactive glass by reactive laser fragmentation in liquids, DOI: https://doi.org/10.1002/jbm.a.37393.

55. N. Lowry, Y. Han, B. Meenan and A. Boyd, Ceram. Int., 2017, Strontium and zinc co-substituted nanophase hydroxyapatite, 43, 12070-12078.

56. S. Gomes, J.-M. Nedelec, E. Jallot, D. Sheptyakov and G. Renaudin, Chem. Mater., 2011, Unexpected mechanism of Zn2+ insertion in calcium phosphate bioceramics, 23, 3072-3085.

57. P. Han, C. Wu and Y. Xiao, Biomater. Sci., 2013, The effect of silicate ions on proliferation, osteogenic differentiation and cell signalling pathways (WNT and SHH) of bone marrow stromal cells, 1, 379-392.

Chapter 8

Statement of impact

There is an urgent need for new solutions to treat large bone defects in our ever-increasing aging western population. However, current gold standard treatment is based on using patients own bone (i.e., autograft) which has limitations in availability and is associated with complications such as donor site morbidity. Therefore, researchers have explored different types of synthetic materials, which are off the shelf available in large quantities and have similarities to native bone. Calcium phosphate ceramics and silica-based biomaterials such as bioactive glass have been heavily researched for bone regeneration applications because they display good biocompatibility and possess some ability to induce bone regeneration. However, although calcium phosphate ceramics and bioglass materials can promote bone repair processes such as differentiation of primary bone cells (osteogenesis),[1] their biological performance remains inferior to natural bone. Additives such as drugs and growth factors can be incorporated into the materials to improve their bioactivity, but increases the cost and reduces the shelf life of the materials. To circumvent this issue, bioinorganic ions such as strontium, zinc, and copper have been added to the materials to improve their bioactivity, as they play important roles in bone regeneration [2, 3]. Incorporation of these synthetic bioinorganic ions in ceramic biomaterials is usually based on ion substitution; however, this can alter both the physical and chemical properties of the materials. Furthermore, ion release is hard to control as it often relies on material degradation rates. This is important, as the ability of ions to promote bone regenerative processes is highly concentration dependent.

Nanoparticles can be used as reservoirs for ion or growth factor delivery, where ion release rates can be decoupled from biomaterial degradation rates. For bone regeneration, especially nanoparticles created from calcium phosphate and bioactive glass biomaterials are of interest, due to their inherent bioactivity and chemical similarity to inorganic component of bone. In fact, several papers have shown that nano-sized calcium phosphate and bioactive glass biomaterials have superior bioactivity compared to their micro-sized counterparts. Finally, nanoparticles can be easily (surface) modified to allow tissue targeting, stimuli responsive drug release, and can be easily incorporated into other biomaterials to improve their mechanical and biological properties [4].

Despite their extraordinary potential, how nanoparticles physical properties such as their shape, composition and morphology influences their bioactivity is not well understood. Moreover, what parameters play important roles in optimizing ion delivery from nanoparticles is not known. This thesis concerns the investigation of several silica and calcium phosphate based nanoparticles, and their structural optimization towards application in the bone regeneration field.

To identify potential knowledge gaps in the field, first a literature research of bioceramic nanoparticle synthesis methods, ion-incorporating methods and their application in the bone regeneration field was conducted. While several studies investigated the effect of nanoparticle size and crystallinity on their ability to promote bone regenerative processes, not much is known about the importance of nanoparticle shape. In **chapter 3** we showed that nanoparticles shape is an important factor determining their ability to induce cell adhesion and hMSCs osteogenic differentiation. Specifically, we showed that homogeneously synthesized needle-shaped hydroxyapapatite nanoparticles can promote hMSCs osteogenesis more efficiently compared to spherical or rice shaped nanoparticles both when applied as coatings and as nanoparticle suspensions. As such, needle shaped HA particles can be used as a promising strategy to improve the clinical performance of biomedical implants, such as the frequently used metallic implants in orthopedics and maxillofacial surgery. Moreover, our research contributed to an improved understanding of how nanoparticle shape influences their ability to promote early, middle, and late osteogenic markers, which can help scientist in the field design better performing biomaterials.

Mesoporous bioglass and silica nanoparticles have been heavily explored in the drug delivery field. Their use for the delivery of ions has expanded over the past decade. However, much is still unknown on how to optimally use them in the bone regeneration field. This is partly due to difficulties in their preparation: ion doping can negatively affect nanoparticle formation and homogeneity. This thesis attempted to bridge this knowledge gap by investigating nanoparticle design parameters that allow multiple ion incorporation and controlled ion release mechanisms.

In **chapter 4,** we demonstrated that mesoporous silica nanoparticles can be modified to deliver single or multiple ions. We demonstrated that a calcium phosphate surface layer on mesoporous nanoparticles (MSN) could be used to allow pH responsive ion release and that this significantly improved their efficacy to promote osteogenesis in hMSCs. Our developed MSN could efficiently induce the expression of early, middle and late osteogenic markers in the absence of other stimulators of osteogenic differentiation where MSN containing CaZnP surface coating were most osteogenic. Our study was the first to demonstrate that a single nanoparticle construct delivering multiple ions (i.e. Sr, Ca, Zn, P) can efficiently promote osteogenic marker expression in hMSCs at a much lower dose compared to adding the same ions but directly dissolved in the cell culture media. Thus, our MSN can be used as to effectively induce hMSCs osteogenesis at relatively low ion doses. Considering these advantages, the MSN developed here represent promising constructs for use in bone regeneration applications, for example as coatings or as components in biomaterials. Our study also contributes to a better understanding of how ion dosing and possible ion synergy influences hMSCs osteogenesis processes.

In **chapter 5**, we built on this knowledge by investigating different Zn incorporation modes in degradable MSN and mesoporous bioactive glass nanoparticles (MBG). Zn was incorporated in the CaP surface layer, inside the mesopores or inside the silica matrix of MSN or MBG particles. We demonstrated that CaP surface coating led to stable MSN and MBG at neutral conditions but stimulated ion release at acidic conditions. Moreover, degradable MSN with Zn incorporated in the mesopores were most effective in promoting ALP production in hMSCs. We demonstrated that Zn incorporation amount and release profile in association with Si ion release, were important factors in determining their bioactivity. As such, these factors should be considered in the design of therapeutically active ion doped ceramic nanoparticles.

In **Chapter 6**, we investigated an alternative synthesis method to incorporate multiple bioinorganic ions into solid bioactive glass nanoparticles (nBGs) using a laser-doping technology. We showed that laser doping can be used to incorporate multiple ions in nBGs without negatively affecting their morphology or structure, however, ion concentrations were low and their biological activity only slightly improved.

While the social impact of in- vitro studies such as those done in this thesis, are difficult to estimate, the understanding and knowledge gained in this thesis could lead to the development of synthetic nanobiomaterials that are more bioactive than current synthetic biomaterials. As such, the knowledge and developed materials may lead to new products that are more cost-effective and represent a less invasive alternative to existing autograft treatments. Better performing synthetic biomaterials could make bone defect treatments more accessible and improve patients overall quality of life. The proposed nanomaterials can also be improved in the future by incorporating other ions and biologics to fulfil additional functions such as reducing inflammation and improve angiogenesis, further optimizing their tissue healing capabilities. Furthermore, the efficient and low cost of inorganic additives delivered by these nanoparticles can reduce the cost of medical treatments and help improve overall healthcare outcomes for patients suffering from large bone defects.

In summary, this thesis contributes to an increased understanding on how bioceramic nanoparticles can be designed and optimized for bone regeneration purposes, which could lead to more affordable, effective and accessible bone regeneration treatments in the future.

References

1. S. Punj, J. Singh and K. Singh, Ceram. Int., 2021, Ceramic biomaterials: Properties, state of the art and future prospectives, 47, 28059-28074.
2. P. Habibovic and J. Barralet, Acta Biomater., 2011, Bioinorganics and biomaterials: bone repair, 7, 3013-3026.
3. I. Lodoso-Torrecilla, R. K. Gunnewiek, E.-C. Grosfeld, R. B. de Vries, P. Habibović, J. A. Jansen and J. J. van den Beucken, Biomater. Sci., 2020, Bioinorganic supplementation of calcium phosphate-based bone substitutes to improve in vivo performance: a systematic review and meta-analysis of animal studies, 8, 4792-4809.
4. S. van Rijt, K. de Groot and S. C. Leeuwenburgh, Tissue Eng., 2022, Calcium phosphate and silicate-based nanoparticles: history and emerging trends, 28, 461-477.

Summary

Although bone can heal itself, large bone defects caused by e.g. trauma or disease, often cannot be repaired naturally. Patients own bone, or autografts, remain the gold standard treatment for large bone defects. However, limitations in availability of donor material and complications associated with autograft harvest, are still major clinical challenges. Hence, there is a great need for synthetic materials for bone substitution. Current synthetic materials for bone regeneration, though, often have lower bioactivity compared to natural bone. Over the past decade, major scientific progress has been made in developing synthetic biomaterials with improved bioactivity. Advancements in nanotechnology research has resulted in the controlled synthesis of nanoparticles with similar size, shape and chemical composition as the inorganic part of bone. These mainly consist of calcium phosphate (CaP) nanoparticles but also silica-based nanoparticles such as mesoporous nanoparticles (MSN) and mesoporous bioactive glass ceramic nanoparticles (MBG) have gained interest due to their inherent bioactivity. Indeed, both MSN and MBG have been reported to reduce osteoclast activity and inhibit scar tissue formation, while stimulating the differentiation of bone cells and promoting the formation of new bone matrix. CaP, MBG and MSN also have high potential to serve as carriers for therapeutic ions. Thus, ceramic nanoparticles represent promising biomaterials for bone regeneration. Chapter 2 of this thesis reviewed the synthesis and application of CaP, MSN, and MBG nanoparticles in the bone regeneration field and provided a future perspective on their clinical use.

In Chapter 3, the importance of CaP nanoparticle shape on their ability to promote osteogenic differentiation of Human mesenchymal stem cell (hMSC) was investigated. Round, rice, and needle-shaped CaP nanoparticles with similar crystallinity and chemical composition were synthesized using a wet synthesis method. hMSCs cells' adhesion and differentiation when cultured on nanoparticle coatings was studied. The results of this study showed that the expression levels and patterns of several osteogenic markers varied significantly depending on the shape of the nanoparticles. Notably, the highest efficacy for upregulating osteogenic gene expression was seen for hMSCs cultured on needle-shaped CaP nanoparticle coatings.

Bioinorganic ions are promising additives to stimulate bone formation, but local ion release and dosage control are critical in order to prevent adverse side effects. In Chapter 4, MSN for multiple therapeutic ion delivery were developed, and their ability to stimulate osteogenesis in hMSCs was evaluated. We demonstrated that MSN coated with CaP could efficiently deliver ions intracellularly by use of the CaP coat, which acted as a pH-sensitive gating system. This led to high expression of early, middle and late osteogenic markers. We demonstrated a clear additive effect when delivering multiple bioinorganic ions using MSN. Ion-incorporated MSN induced hMSCs differentiation at significantly lower ion concentrations compared to ions dissolved in cell culture media. As such, the developed MSN represent a promising strategy to effectively induce hMSCs osteogenesis.

In Chapter 5, the importance of ion concentration and release was investigated by incorporating Zinc (Zn) ions in different ways within the

MSN. Specifically, Zn was incorporated in the matrix, the surface, and within the mesopores of degradable and non-degradable MSN. The incorporation efficiency, ion release profiles, and ALP activity of hMSCs after exposure to the MSN and MBG were studied. Also in this study, the CaP surface coating served as a pH-sensitive gatekeeper and prevented degradation of MBG and degradable MSN in neutral conditions. The results showed that ion concentration and release profile as well as nanoparticle degradation rate, highly affects their effectiveness in promoting osteogenesis, where degradable MSN were most effective.

Multiple ion incorporation in ceramic nanoparticles is complicated using current wet synthesis methods. Chapter 6 examined a new technique based on laser-doping to incorporate multiple bioinorganic ions into bioglass nanoparticles. Their capacity to induce osteogenic differentiation in hMSCs and angiogenesis in human umbilical vein endothelial cells (HUVECs) was also evaluated. Laser-doping could successfully incorporate three ions; Fe, Sr, and Cu into solid bioactive glass nanoparticles without affecting their morphology and size, albeit in low quantities. The multiple ion incorporated bioactive glass nanoparticles had significantly higher angiogenic activity compared to non-doped counterparts.

In conclusion, the research in this thesis demonstrated the importance of nanoparticle shape, administration route, and explored the potential of MSN, MBG and nBGs as effective multiple ion delivery systems to promote bone regeneration.

Samenvatting

Hoewel bot zichzelf kan genezen, kunnen grote botdefecten veroorzaakt door bijvoorbeeld trauma of ziekte, vaak niet op natuurlijke wijze worden hersteld. Gebruik van het eigen bot van de patiënt is de standaard klinische behandeling voor grote botdefecten. Beperkingen in de beschikbaarheid van donormateriaal en andere complicaties vormen echter nog steeds grote klinische uitdagingen in de behandeling van grote bot defecten. Daarom is er een grote behoefte aan synthetische materialen voor botvervanging. De huidige synthetische materialen voor botregeneratie hebben echter vaak een lagere bioactiviteit in vergelijking met natuurlijk bot. De afgelopen tien jaar is er grote wetenschappelijke vooruitgang geboekt bij de ontwikkeling van synthetische biomaterialen met verbeterde bioactiviteit. Vooruitgang in het nanotechnologie veld heeft geresulteerd in nieuwe synthese technieken van nanodeeltjes die een vergelijkbare grootte, vorm en chemische samenstelling als het anorganische deel van bot hebben. Deze bestaan voornamelijk uit calciumfosfaat (CaP) nanodeeltjes, maar ook op silica gebaseerde nanodeeltjes zoals mesoporeuze nanodeeltjes (MSN) en mesoporeuze bioactieve glaskeramische nanodeeltjes (MBG) hebben belangstelling gekregen vanwege hun inherente bioactiviteit. Van zowel MSN als MBG is bekend dat ze de osteoclastactiviteit verminderen en de vorming van littekenweefsel remmen, terwijl ze de differentiatie van botcellen stimuleren en daarnaast de vorming van nieuwe botmatrix bevorderen. CaP, MBG en MSN kunnen ook gebruikt worden voor het transporteren van therapeutische ionen. Keramische nanodeeltjes zijn dus veelbelovende biomaterialen voor botregeneratie. Hoofdstuk 2 van dit proefschrift bespreekt de synthese en toepassing van CaP-, MSN- en MBG-nanodeeltjes op het gebied van botregeneratie en biedt een toekomstperspectief op hun klinisch gebruik.

In Hoofdstuk 3 werd het belang van de vorm van CaP-nanodeeltjes op hun vermogen om osteogene differentiatie van hMSCs' te bevorderen onderzocht. Ronde, rijst- en naaldvormige CaP-nanodeeltjes met vergelijkbare kristalliniteit en chemische samenstelling werden gesynthetiseerd met behulp van een natte synthesemethode. Adhesie en differentiatie van humane mesenchymale stamcellen (hMSCs) die op coatings van nanodeeltjes waren gekweekt, werd bestudeerd. De resultaten van deze studie toonden aan dat de expressieniveaus en patronen van verschillende osteogene markers aanzienlijk varieerden, afhankelijk van de vorm van de nanodeeltjes. Met name naaldvormige CaP-nanodeeltjescoatings zorgend voor het tot expressie brengen van osteogene genen in hMSCs.

Bio-anorganische ionen zijn veelbelovende additieven om botvorming te stimuleren, maar lokale ionenafgifte en doseringscontrole zijn cruciaal om nadelige bijwerkingen te voorkomen. In Hoofdstuk 4 werden MSN's ontwikkeld voor het afleveren van meerdere therapeutische ionen tegelijkertijd, en werd hun vermogen om osteogenese in hMSCs’ te stimuleren geëvalueerd. We hebben aangetoond dat MSN's gecoat met CaP efficiënt ionen intracellulair kunnen afleveren door gebruik te maken van de CaP-coating, die fungeerde als een pH-gevoelige laag. Dit leidde tot hoge expressie van verschillende osteogene markers. We hebben een duidelijk additief effect aangetoond bij het leveren van meerdere bio-anorganische ionen met behulp van MSN's. MSN's induceerden hMSCs-differentiatie bij significant lagere ionconcentraties in vergelijking met ionen opgelost in celkweekmedia. De hierin ontwikkelde MSN vormen dus een veelbelovende strategie om hMSCs-osteogenese effectief te induceren.

In hoofdstuk 5 werd het belang van ionenconcentratie en -afgifte onderzocht door zink(Zn)-ionen op verschillende manieren in de MSN's op te nemen. In het bijzonder werd Zn opgenomen in de matrix, het oppervlak en in de mesoporiën van afbreekbare en niet-afbreekbare MSN's. De opname-efficiëntie, ionenafgifteprofielen en ALP-activiteit van hMSCs' na blootstelling aan de MSN's en MBG's werden bestudeerd. Ook in deze studie diende de CaP-oppervlaktecoating als een pH-gevoelige laag en voorkwam daarnaast degradatie van MBG's en afbreekbare MSN's in neutrale condities. De resultaten toonden aan dat de ionenconcentratie en het afgifteprofiel, evenals de afbraaksnelheid van nanodeeltjes, een grote invloed hebben op hun effectiviteit bij het bevorderen van osteogenese, waar afbreekbare MSN's het meest effectief waren.

De opname van meerdere ionen in keramische nanodeeltjes is gecompliceerd met behulp van de huidige synthesemethoden. Hoofdstuk 6 onderzocht een nieuwe techniek gebaseerd op laserdoping om meerdere bio-anorganische ionen in nanodeeltjes van bioglas te incorporeren. Hun vermogen om osteogene differentiatie in hMSCs' en angiogenese in menselijke navelstrengendotheelcellen (HUVEC's) te induceren, werd ook geëvalueerd. Laserdoping was succesvol in het incorporeren van Fe, Sr en Cu in bioactieve glazen nanodeeltjes zonder hun morfologie en grootte te beïnvloeden, zij het in kleine hoeveelheden. De bioactieve glazen nanodeeltjes met meerdere ionen hadden een significant hogere angiogene activiteit.

Concluderend, het onderzoek in dit proefschrift toonde het belang aan van de vorm van nanodeeltjes en de toedieningsroute, en verkende het potentieel van MSN's, MBG's en nBG's als effectieve ionenafgiftesystemen om botregeneratie te bevorderen.

List of publications

Pertaining to this thesis

Pichaporn Sutthavas, Pamela Habibovic and Sabine H van Rijt. *The shape-effect of calcium phosphate nanoparticle-based films on their osteogenic properties.* Biomaterials Science, 2021 1754-1766

Pichaporn Sutthavas, Zeinab Tahmasebi Birgani, Pamela Habibovic and Sabine van Rijt. *Calcium Phosphate-Coated and Strontium-Incorporated Mesoporous Silica Nanoparticles can Effectively Induce Osteogenic Stem Cell Differentiation.*Advanced Healthcare Materials, 2021 2192-2640, 2101588

Pichaporn Sutthavas, Matthias Schumacher, Kai Zheng, Pamela Habibović, Aldo Roberto Boccaccini and Sabine van Rijt. *Zn-loaded and calcium phosphate-coated degradable silica nanoparticles can effectively promote osteogenesis in human mesenchymal stem cells.* Nanomaterials, 2022 2079-4991, 2918

Pichaporn Sutthavas, Matthias Schumacher, Martyna Nikody, Vaijayanthi Ramesh, Jurij Jakobi, Elizabeth R. Balmayor, Pamela Habibovic, Christoph Rehbock, Stephan Barcikowski and Sabine van Rijt. *Laser-based ion doping is a suitable alternative to dope biologically active ions into colloidal bioglass nanoparticles.* Materials Advances. *(Underrevision)*

Pichaporn Sutthavas, Pamela Habibovic and Sabine H van Rijt. *Bioceramic nanoparticles for bone regeneration. (In preparation)*

Others

Roger Rosenbrand, David Barata, **Pichaporn Sutthavas**, Ronny Mohren, Berta Cillero-Pastor, Pamela Habibovic and Sabine van Rijt. *Lipid surface modifications increase mesoporous silica nanoparticle labeling properties in mesenchymal stem cells.* International Journal of Nanomedicine, 2018 7711

Lea Andrée, David Barata, **Pichaporn Sutthavas**, Pamela Habibovic and Sabine van Rijt. *Guiding mesenchymal stem cell differentiation using mesoporous silica nanoparticle-based films.* Acta Biomaterialia, 2019 1742-7061, 557-567

Aygul Zengin, **Pichaporn Sutthavas** and Sabine van Rijt. *Inorganic nanoparticle-based biomaterials for regenerative medicine.* Nanostructured Biomaterials for Regenerative Medicine, Elsevier, 2020, 293-312.

Acknowledgements

Firstly, I would like to thank my supervisors Professor Pamela Habibovic and Dr. Sabine van Rijt for the opportunity of doing this phd under their supervision and support. Pamela, who always provides insightful suggestions and attended the meeting despite her busy schedule. She also always listens and gives the opportunity for everyone to explain their opinion and idea which creating the safe and welcoming environment of not just IBE group but also the institute.

As the daily supervisor, Sabine is firm but fair. Thank you for your patience and kindness in guiding me through not only the practical part of chemical synthesis but also other soft skills like writing and presentation. Furthermore, your guidance on project planning and time management has made me not only a better scientist but also a better person in general.

During the first two years of my PhD, I had the pleasure of working closely with David Barata. Thank you, David, for all the analytical techniques you have taught me and those long hours in TENNO. Your suggestion and discussion were also interesting and valuable.

I also would like to thank other both former and current Nanogroup, IBE members and other group within the MERLN. Lea, Aygül, Chloe, Xingzhen, and Lei. I wish you all the best of luck in our own PhD and beyond journey. Mattias and Darragh, thank you for your help throughout our time together in MERLN. Special thanks to Rabeil and Fiona for teaching me through the western blot process. I have pleasure to get to know Floor Ruiter, not only as fellow chemistry lab user but also as Tennis buddy and fellow food adventurers, Marie Jose and our mutual love of wine.

This thesis also would not be possible without help from all our lab managers (Denis, Dennie, Timo, Eva, Marloes) as well as the team from M4I. Especially for Dennis, who had been a great help with SEM, XRD, FTIR, and qPCR thank you so much for all the time including those long days in TENNO. Eva for her expertise and trouble with ICP-MS.

Being far away from home is not easy however, the tight niche group for Thai students a Thai community in Maastricht always bring joy be it through food or the late-night conversation. All of you always step in to help each other and I am proud to be involved in that and hope that our friendship continues beyond the time we spent in Maastricht.

From the deepest of my heart, I would like to express my gratitude toward my family. Special thanks to my parents who always supported me despite the unconventional choice I have made in my educational life. Thank you for your unconditional love and understanding. My dear brother, Pae, who is quiet but always be there for me all my life.

The finally I would like to especially thank Martin Olyschläger. You changed my life in many ways I could not have imagined. Your love and support from the start to finish of my PhD made me who I am today, and I am lucky to be able to call you, my husband.

Biography

Pichporon Sutthavas was born on 11 December 1984 in Chiangmai, City in northern Thailand. Pursuing her passion for engineering and her fascination with human body, she chose to study and completed a bachelor's degree in Bioengineering at Nanyang Technological University, Singapore. With wonderous spirit, she continued to further her studies in Bioengineering in Osaka University, Japan and completed master's degree in biomedical engineering science. While working in Thailand after graduation, she got introduced to stem cells and regenerative medicine and decide that it is the future of biomedical engineering. She decided to pursued another master in Biomedical science to enhance her knowledge of stem cells and biomaterial with the duo program between University of Groningen and RWTH Aachen. In 2017, She moved to Maastricht University to start her her Phd at department of instructive Biomaterials Engineering within the MERLN Institute for Technology-Inspired Regenerative medicine focusing on Bioceramic nanoparticles for bone regeneration purpose which resulting in this thesis.